Fluctuations in Mesoscopic Transport Driven by Thermal, Classical, and Quantum Mechanisms

Dissertation zur Erlangung des
akademischen Grades eines Doktors der
Naturwissenschaften
(Dr. rer. nat.)

vorgelegt von

Hübler, Matthias

an der

MATHEMATISCH-NATURWISSENSCHAFTLICHE SEKTION
FACHBEREICH PHYSIK

Konstanz, 2025

Tag der mündlichen Prüfung:	03.12.2025
Betreuer und Erstprüfer:	Prof. Dr. Wolfgang Belzig
Zweitprüfer:	Prof. Dr. Guido Burkard
Prüfungsvorsitz:	Prof. Dr. Alfred Leitenstorfer

Preface

This thesis was carried out under the supervision of Prof. Dr. Wolfgang Belzig in the Quantum Transport group in the Department of Physics at the University of Konstanz. The text is organized into six chapters, of which the first provides a general introduction to the topic and methods, the last chapter gives a conclusion, and the remaining chapters contain my publications together with a topic-specific introduction. The projects in Sections III.6 and V.4 were conducted in close collaboration with Prof. Dr. Denis Basko and Prof. Dr. Juan Carlos Cuevas, respectively.

Chapter I gives a brief introduction to quantum transport and reviews the methods used in this thesis, including the Keldysh Green's-function formalism and the Landauer–Büttiker scattering approach.

Chapter II presents the peer-reviewed article[1], in which we extend the concept of temperature-difference-induced noise in a normal-metal mesoscopic conductor to the nonsymmetrized current–current correlator at finite frequency, thereby connecting it to light emission.

Chapter III introduces near-field radiative heat transfer (NFRHT), which is described by fluctuational electrodynamics. We discuss the circuit approximation to NFRHT, described by circuit fluctuational electrodynamics, and analyze classical electrical networks as well as their quantization. Section III.6 contains the peer-reviewed work[3], where we formulate the problem of NFRHT as an effective quantum scattering theory of matter excitations. The circuit-related and numerical calculations were carried out by me; the example of a surface-phonon-polariton was a joint effort; the microscopic calculations and the extension to macroscopic bodies were performed by my collaborator, Prof. Dr. Denis Basko.

Chapter IV addresses classical photon-assisted transport in normal-metal mesoscopic conductors and shows how the Landauer–Büttiker approach extends to arbitrary time-dependent voltage drives. In addition, we present an introduction to full counting statistics (FCS) and review the Keldysh action for mesoscopic conductors. Section IV.4 covers the peer-reviewed article[2] on FCS in mesoscopic conductors driven by few-cycle voltage pulses (Gaussian and box-shaped).

Chapter V examines quantum photon-assisted transport in tunnel junctions and introduces dynamical Coulomb blockade, its extension to non-thermal electromagnetic environments, and the basic concepts of circuit quantum electrodynam-

ics. Furthermore, we provide a brief overview of the Josephson effect. Section V.4 contains the peer-reviewed article [4], which presents a theoretical study of the electric current in a Josephson tunnel junction coupled to an arbitrary nonclassical electromagnetic environment, thereby generalizing classical transport phenomena such as photon-assisted tunneling and Shapiro steps to the quantum regime.

Chapter VI provides the overall conclusion of this thesis.

List of Publications

[1] **M. Hübler** and W. Belzig, *Light emission in delta-T-driven mesoscopic conductors*, Phys. Rev. B 107, 155405 (2023)

[2] **M. Hübler** and W. Belzig, *Full counting statistics of ultrafast quantum transport*, Appl. Phys. Lett. 123, 034006 (2023)

[3] **M. Hübler**, D. M. Basko, and W. Belzig, *Scattering approach to near-field radiative heat transfer*, Phys. Rev. B 112, 165428 (2025)

[4] **M. Hübler**, J. C. Cuevas, and W. Belzig, *Nonclassical photon-assisted transport in superconducting tunnel junctions*, Phys. Rev. B 112, 214501 (2025)

Deutsche Zusammenfassung

Moderne Fertigungstechniken ermöglichen die präzise Kontrolle über physikalische Vielteilchensysteme im immer kleineren Maßstab. Ein mesoskopischer Leiter, dessen Ausdehnung kleiner ist als die Phasenkohärenzlänge seiner Elektronenwellen, zeigt Quanteneffekte im Transport und lässt sich durch eine quantenmechanische Streutheorie beschreiben. Der Leiter wird typischerweise durch zwei große Teilchenreservoirs modelliert, die über einen Wellenleiter gekoppelt sind, in dem ein Streupotential (z. B. eine Verengung, ein Defekt oder eine Tunnelbarriere) die kohärente Ausbreitung beeinflusst. Die Leitfähigkeit hängt von der Transmissionswahrscheinlichkeiten der Ladungsträger ab. Dies führt zur Quantisierung der Leitfähigkeit, da Transportkanäle geöffnet oder geschlossen werden können. Transportgrößen wie Strom, Fluktuationen und höhere Kumulanten können genutzt werden, um Informationen über das physikalische System zu gewinnen, beispielsweise über die Ladung und die Streueigenschaften der am Transport beteiligten Teilchen. Im Gleichgewicht, d. h. wenn beide Teilchenreservoirs denselben Zustand haben, fließt kein Strom und die Fluktuationen ergeben sich allein aus dem thermischen Rauschen. Nichtgleichgewichtsfluktuationen können durch verschiedene Mechanismen hervorgerufen werden, zum Beispiel durch das Anlegen einer konstanten Spannung oder durch einen Temperaturunterschied zwischen den Reservoirs. Zeitabhängige und nichtklassische elektromagnetische Felder können ebenfalls Strom und Fluktuationen antreiben, die wiederum charakteristische Signaturen im Transport erzeugen. Quantentransport in elektrischen Leitern weist Parallelen zum Transport anderer Teilchen auf, wie beispielsweise Photonen oder Phononen, deren thermische Leitfähigkeit ebenfalls mit Transmissionswahrscheinlichkeiten identifiziert werden kann.

Alle Körper endlicher Temperatur emittieren aufgrund der thermischen Bewegung ihrer geladenen Bestandteile elektromagnetische Strahlung. Das Plancksche Strahlungsgesetz beschreibt die Emission eines Schwarzen Körpers und ergibt eine breitbandige spektrale Dichte, die ausschließlich von der Temperatur bestimmt ist. Der Strahlungsaustausch zwischen Körpern unterschiedlicher Temperatur bewirkt einen Wärmetransport, der durch das elektromagnetische Feld vermittelt wird. Im Nahfeld kann dieser Wärmetransport die nach dem Planckschen Gesetz erwarteten Beiträge deutlich übersteigen, da in diesem Bereich Beugung, Interferenzeffekte und evaneszente Wellen eine zusätzliche Rolle spielen. Die Fluktuationselektrodynamik bildet ein theoretisches Fundament zur Beschreibung des radiativen Wärmetransports im Fern- und Nahfeld und führt zu einem Wärmestrom mit einer Struktur, die dem elektrischen Strom in mesoskopischen

Leitern ähnelt.

Das erste Kapitel I gibt eine kurze Einführung in den Quantentransport und den Nichtgleichgewichts-Formalismus der Greenschen Funktionen.

Das zweite Kapitel II untersucht die Lichtemission eines mesoskopischen Leiters bei unterschiedlichen Temperaturen der Elektronenreservoirs. Das nicht-symmetrisierte Rauschspektrum bestimmt dabei Emission und Absorption des Leiters. Während spannungsgetriebene Fluktuationen aus einem Beitrag des thermischen Rauschens und einem Beitrag des Schrotrauschens bestehen, lässt sich das Rauschspektrum in thermisch getriebenen Leitern durch einen thermischartigen und einen Delta-T-Beitrag charakterisieren. Zur Veranschaulichung der verschiedenen Beiträge betrachten wir energieunabhängige sowie resonante Streuung.

Das dritte Kapitel III führt in den Nahfeld-radiativen Wärmetransport ein und behandelt die Quantisierung elektrischer Schaltungen. Im Hauptteil entwickeln wir den Streuformalismus für den Nahfeld-radiativen Wärmetransport, der äquivalent zur Fluktuationselektrodynamik ist. Zuerst betrachten wir das Schaltungsmodell, in dem die thermischen Körper durch beliebige Impedanzen dargestellt und ihre Kopplung durch Schaltungselemente beschrieben werden. Prinzipien der Schaltkreis-Quantenelektrodynamik dienen dabei zur quantenmechanischen Modellierung thermischer Fluktuationen und von Dissipation. Aus der Konstruktion der Streuzustände ergibt sich die vollständige Streumatrix. Wir berechnen den Energieflussoperator und untersuchen sowohl die mittlere dissipierte Energie als auch die Energieflussfluktuationen. Reaktive Komponenten innerhalb der thermischen Körper können das Fluktuationsspektrum dominieren, ein Effekt, der von der üblichen Landauer-Büttiker-Theorie nicht erfasst wird. Die Ergebnisse werden anhand von zwei gekoppelten Oberflächen-Phonon-Polaritonen sowie einfachen Schaltungsbeispielen veranschaulicht. Darüber hinaus übertragen wir die Streutheorie auf den radiativen Wärmetransport zwischen makroskopischen Körpern.

Das vierte Kapitel IV behandelt klassischen photonenunterstützten Transport in mesoskopischen Leitern. Es enthält außerdem eine kurze Einführung in die Theorie der Zählstatistik und in den Formalismus der Keldysh-Wirkung. Der Hauptteil widmet sich der Zählstatistik eines mesoskopischen Leiters unter dem Einfluss von Spannungspulsen, insbesondere solcher mit oszillierendem Träger und gaußförmiger oder rechteckiger Hüllkurve. Wir berechnen die Wahrscheinlichkeiten zur Erzeugung von Elektron–Loch-Paaren, welche die Zählstatistik und das Rauschen bestimmen. Dabei zeigt sich, dass das Rauschen stark von der Träger-Einhüllenden-Phase abhängt, also von der relativen Phase zwischen Trägeroszillation und Pulsform.

Das fünfte Kapitel V thematisiert nichtklassischen, photonenunterstützten Transport und enthält eine Einführung in die Theorie der dynamischen Coulomb-Blockade. Die Physik des Josephson-Effekts und der Shapiro-Stufen wird kurz

dargestellt, ergänzt durch einen Überblick über verschiedene Quantenzustände in der Schaltkreis-Quantenelektrodynamik. Im Hauptteil wird der Einfluss einer nichtklassischen elektromagnetischen Umgebung auf den Transport durch einen supraleitenden Tunnelkontakt untersucht. Klassische Transportphänomene wie photonengekoppeltes Tunneln und Shapiro-Stufen werden dabei in das Quantenregime übertragen. Es wird gezeigt, dass der supraleitende Tunnelkontakt den vollständigen Quantenzustand der elektromagnetischen Umgebung erfasst und eine Rekonstruktion ermöglicht. Der Quasiteilchenstrom liefert direkten Zugang zur Wahrscheinlichkeit des Energieaustauschs zwischen Quasiteilchen und Umgebung, während der Cooper-Paar-Strom empfindlich auf die Kohärenzen des Umgebungszustands reagiert, sodass sich Shapiro-Stufen als Indikatoren für diese Kohärenzen nutzen lassen. Als erstes Beispiel für die Umgebung betrachten wir ein Qubit, das in einem beliebigen (reinen oder gemischten) Zustand präpariert ist. Das zweites Beispiel betrachten wir einen LC-Schwingkreis, der entweder in einer Überlagerung aus Vakuum und einem bzw. drei Photonen Zustand, in einem kohärenten Zustand oder in einem gequetschten Zustand initialisiert ist.

Acknowledgement

I would like to thank Prof. Dr. Wolfgang Belzig for his supervision and for the opportunity to pursue my doctoral research in the Quantum Transport group at the University of Konstanz. I am grateful for stimulating ideas, valuable discussions, and the academic freedom to pursue my own directions, as well as for opportunities to present my work at conferences and connect with future collaborators and fellow researchers.
Furthermore, I thank Prof. Dr. Denis Basko (CNRS, Grenoble) for a productive collaboration and stimulating discussions. His clear explanations and careful questions were particularly helpful in refining the analysis. I am also grateful for the opportunity to visit him twice in Grenoble, a beautiful city in a remarkable setting.
Additionally, I would like to thank Prof. Dr. Juan Carlos Cuevas (Universidad Autónoma de Madrid) for insightful discussions and his support. I am grateful for his engagement with our group as a Mercator Fellow, which enriched our exchanges, and for his careful proofreading of the thesis and constructive suggestions.

I would like to thank everyone in the Quantum Transport group and other groups on P10 for creating a friendly and welcoming environment. I especially enjoyed the collegial atmosphere in our office with my officemates Dennis and Sourabh. I am also thankful to Aleksandr and Michael for introducing me to bouldering, a sport that turned out to be a lot of fun. I appreciated that, as a group, we often played sports together, such as basketball and squash. I thank Sabine Wallrabe for many pleasant conversations and for her assistance with organizational issues of all kinds.

In my private life, I am deeply thankful to Katja, who accompanied me throughout my doctoral journey and moved with me to Konstanz to enjoy the lake. She always supported me, especially during stressful periods. I am grateful to my parents, who supported me throughout all the years of my life, and for the endless as well as deep discussions on many topics. I am thankful for my closest friends, Nico, Niclas, Aeneas, Michi (dating back to school), and Felix, Maria, David, Freddy, Melea, Julez, Sophie, Martino, Julia (dating back to my studies). It is truly amazing to have good friends in life. In addition, I found the best volleyball club in the world, SV Litzelstetten, with many wonderful people. I had a lot of fun playing and celebrating with them.

Contents

Chapter I

Introduction: Quantum Transport

Quantum transport describes the coherent propagation of particles or excitations in a physical system, accounting for their wave-like nature and quantum statistics. The concept emerged in the 1980s within the field of mesoscopic physics [1–7], as a framework to describe phase-coherent electron transport in small-scale conductors. As conductors are reduced in size and cooled to low temperatures, Ohm's law no longer applies. The system enters the mesoscopic regime, where quantum effects dominate electron transport and resistance arises from mechanisms other than inelastic scattering. Figure I.1 illustrates several systems exhibiting coherent electronic transport. The physical behaviour of the conductor is governed by its length L in relation to various intrinsic length scales such as the energy relaxation length l_{in}, the coherence length l_ϕ, the elastic mean free path l, and the Fermi wavelength λ_F. The energy relaxation length is the average distance an electron travels before undergoing a significant change in energy. The phase coherence length describes the distance over which an electron maintains its phase coherence. Inelastic scattering processes, such as electron-electron and electron-phonon interactions, can lead to the loss of phase coherence. Apart from scattering by magnetic impurities, elastic scattering does not affect phase coherence. A conductor is said to be in the mesoscopic regime when its physical size is smaller than the phase coherence length. For example, aluminium exhibits a coherence length of approximately $1\,\mu\mathrm{m}$ at $T = 1\,\mathrm{K}$, which decreases to a few tens of nanometres at room temperature [11]. Whether a mesoscopic conductor exhibits diffusive ($l \ll L$) or ballistic ($l > L$) transport is determined by the elastic mean free path, which represents the average distance an electron propagates before scattering off a (static) non-magnetic impurity. Atomic-scale junctions can have dimensions as small as a few nanometers or less, approaching the scale of the Fermi wavelength in metals, namely, the de Broglie wavelength of electrons at the Fermi energy. In this thesis, we consider mesoscopic conductors in the ballistic regime satisfying

$$\lambda_F < L < l < l_\phi \lesssim l_{in}. \tag{I.0.1}$$

Rolf Landauer [1] proposed in the late 1950s that electrical transport, in the absence of inelastic interactions, can be formulated as a scattering problem, thereby establishing the notion that conductance is transmission. The famous Landauer

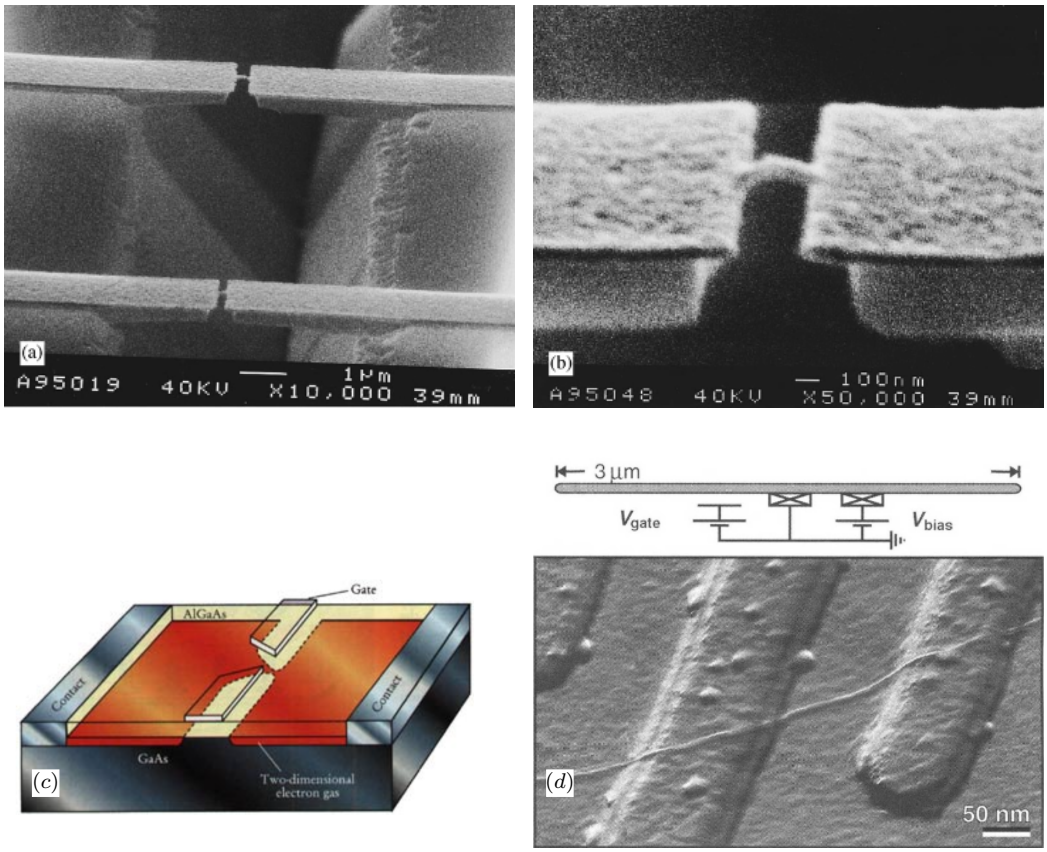

Figure I.1: *Examples of electronic quantum transport*. Scanning electron micrograph [8]: (a) Two microfabricated bridges suspended above a triangular pit in the silicon substrate. (b) Close-up showing two cantilevers ($\sim 700\,\mathrm{nm}$ apart) coated with gold, forming a $\sim 100\,\mathrm{nm}$-wide conducting bridge. Bending the substrate breaks the bridge, resulting in discrete quantum transmission channels. (c) Illustration of a quantum point contact formed in a two-dimensional electron gas (typically at a GaAs/AlGaAs interface) between two contacts acting as electron reservoirs in local equilibrium. A constriction, comparable in width to the electron wavelength, is created by applying a negative voltage to the gate, allowing control over the constriction width [9]. (d) Trapping-mode AFM image of a single-wall carbon nanotube positioned on a Si/SiO_2 substrate with two platinum electrodes, each $15\,\mathrm{nm}$ thick, together with the corresponding circuit diagram. From AFM height profiles, the tube diameter is determined to be $\sim 1\,\mathrm{nm}$, and its total length is $3\,\mu\mathrm{m}$, with a $150\,\mathrm{nm}$ segment located between the biased electrodes [10].

formula for the conductance

$$G = \frac{e^2}{2\pi\hbar} \sum_n \mathcal{T}_n \tag{I.0.2}$$

identifies the relationship between the conductance G and the transmission probabilities $\mathcal{T}_n$ of the electronic modes involved in the transport. The fundamental conductance scale in quantum transport is set by the conductance quantum $G_0 = e^2/(\pi\hbar) \approx 7.74 \times 10^{-5}\,\Omega^{-1}$, which is defined in terms of the elementary charge e and the reduced Planck constant $\hbar$. Equation (I.0.2) captures the essence of conductance quantization, where each newly opened channel contributes a quantized unit of conductance, resulting in a stepwise increase [2, 12, 13]. For example, in a quantum point contact created in a two-dimensional electron gas (see Fig. I.1), the confinement potential controls the transverse quantization of electronic motion and thus the number of open conducting channels. [2, 9, 12]. The Landauer formula for the electric current is

$$\langle \hat{I} \rangle = \frac{e}{2\pi\hbar} \int_{-\infty}^{\infty} dE \sum_n \mathcal{T}_n(E)[f_1(E) - f_2(E)], \tag{I.0.3}$$

and is determined in terms of energy-dependent transmissions $\mathcal{T}_n(E)$, and the occupation difference between the connected terminals, described by the Fermi-Dirac distribution $f_1(E)$ and $f_2(E)$. The terminals act as particle reservoirs, whose behavior can be controlled through external parameters such as temperature, classical voltage drives, or quantum electromagnetic fields.

Although the idea of quantum transport originated in electronic systems, the concept has since been extended to a wide range of carriers. Examples include charged particles such as electrons [2, 6, 14, 15], Cooper pairs [16, 17], and chiral edge states [18–20], as well as neutral excitations such as photons [14, 21, 22], phonons [22–26], magnons [27, 28], and ultracold atomic matter waves in optical lattices [29, 30]. At a fundamental level, quantum transport arises from quantum scattering processes involving the interaction of wave-like particles with potential barriers and interfaces. In many situations, a suitable scattering theory provides an accurate description of transport properties and is especially well suited for non-interacting systems, such as electrons in mesoscopic conductors, photons in optical waveguides, or phonons in nanowires [14, 15, 21, 24]. Accounting for interactions often requires more sophisticated methods, including the nonequilibrium Green's function approach and the Keldysh formalism.

Quantum transport investigates how particles and their associated quantities, energy, charge, or spin, propagate through a system and give rise to measurable observables, including electric, energy, and spin currents and their fluctuations. In many cases, the average current is captured by a Landauer-type formula [24, 31] that expresses transport in terms of transmission probabilities. The scattering theory developed by Landauer and Büttiker (Landauer-Büttiker scattering approach [14]) for electronic transport in mesoscopic conductors can also be applied to bosonic particles propagating through waveguides, and is therefore expected

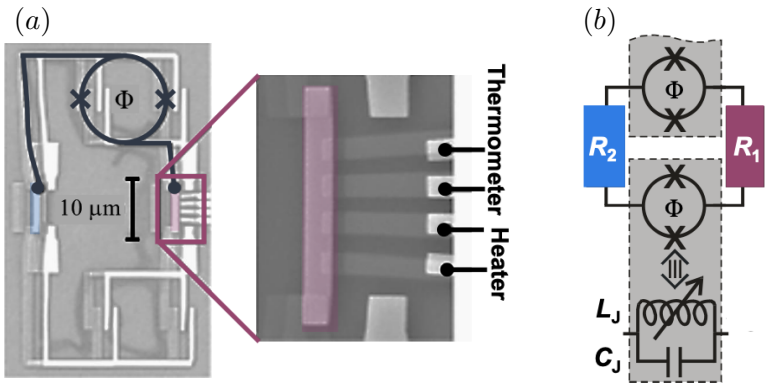

Figure I.2: *Single-channel photonic heat transfer:* (a) image and (b) circuit representation of the device, which consists of two AuPd resistors, R_1 (red) and R_2 (blue), connected via aluminium DC-SQUIDs (superconducting loops interrupted by two Josephson junctions, shown as crosses). A temperature difference between the resistors leads to radiative energy transfer, whose thermal conductance is tuned by the SQUID inductance under external magnetic flux Φ [32].

to also capture photonic and phononic energy transfer. In near-field radiative heat transfer, the average heat current can be described by a Landauer-type formula [21]. Figure I.2 shows an example of single-channel radiative heat transfer in a nanostructure [32]. However, the heat current noise can depart from those predicted by the Landauer-Büttiker scattering approach, as noted recently by Wise et al. [33] for a specific system. In section III.6, we develop a general scattering theory for near-field radiative heat transfer and compare it to the Landauer-Büttiker scattering approach. We demonstrate that the heat current noise spectrum contains information about the thermal bodies that is not captured by the average current.

Nonequilibrium fluctuations can generally contain additional information about the system, since they are not constrained by the fluctuation–dissipation theorem [34]. Shot noise in vacuum tubes [35], for example, was used as an alternative method to the Millikan oil drop experiment [36] for determining the elementary charge of an electron. In mesoscopic electronic conductors, shot noise arises from the stochastic partitioning of charge carriers at scattering potentials and demonstrates the granular nature of charge transport. In fractional quantum Hall systems, it serves as a method to extract the effective charge of transport-related excitations [37–39]. Furthermore, the suppression of mesoscopic shot noise below the Poissonian level, which corresponds to transport by independent, rare events, reveals details about electron transmission probabilities [40]. Historically, shot noise was primarily induced by a voltage bias, but recent studies have shown growing interest in partition noise arising from a thermal bias, commonly termed delta-T noise. We investigate in Chap. II nonsymmetrized current fluctuations in a mesoscopic conductor under thermal bias and show that the delta-T noise spectrum becomes partially negative, a behavior not observed under conventional voltage bias. The nonsymmetrized component of current fluctuations is directly

related to photon emission from the conductor, as it captures the asymmetry between emission and absorption processes [41, 42].

The electromagnetic environment of the mesoscopic conductor influences charge transport and its full statistical properties. The statistical properties of a coherent conductor can be described by full counting statistics (FCS), which provides the probability distribution of transferred charge. FCS enables the identification of the elementary processes of charge transfer. For example, at zero temperature under a classical drive, the transport is governed by single-electron and electron–hole-pair excitations [43–45]. In Sec. IV.4, we investigate the cumulant-generating function, which encodes the FCS, for a mesoscopic conductor driven by few-cycle pulses, and show that the fluctuations depend on the carrier-envelope phase (CEP), i.e., the phase offset between the pulse envelope and its underlying carrier wave.

Photon-assisted transport is sensitive to the characteristics of the surrounding electromagnetic environment and can serve as a probe of its properties. Unlike a classical field, which evolves deterministically, a quantum field inherently fluctuates, with its behavior governed by the specific quantum state it occupies. Advances in (circuit) quantum electrodynamics (QED) now enable the use of nonclassical drives by preparing the electromagnetic environment in arbitrary quantum states. Thermal environments have been extensively studied in the context of dynamical Coulomb blockade [46], whereas more general quantum states, such as squeezed states, have recently been explored in normal-metal tunnel junctions [47]. In such systems, current and noise measurements can be used to infer the nonclassicality of the electromagnetic state. In Sec. V.4, we investigate quantum photon-assisted transport through a superconducting tunnel junction, demonstrating that the quasiparticle and Cooper pair currents encode the complete information about the environmental state, a feature not accessible in normal-metal junctions.

I.1 Photon, Electron and Superconducting Reservoirs

A mesoscopic conductor is connected to macroscopic terminals, acting as reservoirs that supply particles to and remove them from the conductor. The reservoirs are controlled by external parameters, such as voltage, temperature, or a time-dependent classical or quantum drive. When the reservoirs are in different states, a net current flows between them. This thesis considers three types of reservoirs: one consisting of non-interacting photons (see Chap. III), one of non-interacting electrons (see Chap. II and IV), and one of electrons exhibiting superconducting correlations (see Chap. V).

Normal-metal and superconductor.— We begin by considering a system of electrons, described within the formalism of second quantization by the field operator $\hat{\Psi}_\sigma(\boldsymbol{r})$. The field operator $\hat{\Psi}_\sigma(\boldsymbol{r})$ annihilates an electron with spin $\sigma = +$ (up) or $\sigma = -$ (down) at position $\boldsymbol{r}$ within the materials volume $\mathcal{V} \subset \mathbb{R}^3$, and satisfies

the canoncial fermionic anticommutation relations

$$\{\hat{\Psi}_\sigma(\boldsymbol{r}), \hat{\Psi}_{\sigma'}(\boldsymbol{r})\} = 0, \quad \{\hat{\Psi}_\sigma(\boldsymbol{r}), \hat{\Psi}^\dagger_{\sigma'}(\boldsymbol{r}')\} = \delta_{\sigma\sigma'}\delta(\boldsymbol{r}-\boldsymbol{r}'), \tag{I.1.1}$$

where $\{\cdot,\cdot\}$ denotes the anticommutator, $\hat{\Psi}^\dagger_\sigma(\boldsymbol{r})$ is the Hermitian conjugate of $\hat{\Psi}_\sigma(\boldsymbol{r})$, and creates an electron with spin σ at position $\boldsymbol{r}$. The dynamics of the electrons is governed by the Hamiltonian [48, 49]

$$\begin{aligned}\hat{H} = &\sum_{\sigma=\pm}\int_{\mathcal{V}} d^3\boldsymbol{r}\,\hat{\Psi}^\dagger_\sigma(\boldsymbol{r}) h_\sigma(\boldsymbol{r})\hat{\Psi}_\sigma(\boldsymbol{r}) \\ &+\frac{1}{2}\sum_{\sigma,\sigma'=\pm}\iint_{\mathcal{V}} d^3\boldsymbol{r}d^3\boldsymbol{r}'\hat{\Psi}^\dagger_\sigma(\boldsymbol{r})\hat{\Psi}^\dagger_{\sigma'}(\boldsymbol{r}')V(\boldsymbol{r}-\boldsymbol{r}')\hat{\Psi}_{\sigma'}(\boldsymbol{r}')\hat{\Psi}_\sigma(\boldsymbol{r}),\end{aligned} \tag{I.1.2}$$

with $h_\sigma(\boldsymbol{r})$ the local non-interacting Hamiltonian, and $V(\boldsymbol{r}-\boldsymbol{r}')$ a two-body interaction that depends only on the relative distance between particles. Despite the presence of Coulomb interactions, normal metals can often be effectively described using non-interacting electrons ($V(\boldsymbol{r}-\boldsymbol{r}') = 0$) [50]. Hence, the normal state is described by the free-particle Hamiltonian

$$h_\pm(\boldsymbol{r}) = -\frac{\hbar^2}{2m}\nabla^2 - \mu, \tag{I.1.3}$$

with m denoting the electron mass and μ the chemical potential. In a superconducting material, the effective interaction between electrons becomes attractive ($V(\boldsymbol{r}-\boldsymbol{r}') < 0$), allowing the formation of Cooper pairs. To make the problem tractable, a mean-field approximation is typically employed, in which the pairing potential is defined as

$$\Delta(\boldsymbol{r},\boldsymbol{r}') = -|V(\boldsymbol{r}-\boldsymbol{r}')|\langle\hat{\Psi}_-(\boldsymbol{r}')\hat{\Psi}_+(\boldsymbol{r})\rangle, \tag{I.1.4}$$

where $\Delta(\boldsymbol{r},\boldsymbol{r}')$ captures the effective interaction between paired electrons. In this formulation, triplet correlations are discarded, consistent with the assumption of a conventional s-wave superconductor. Additionally, we focus on a translation-invariant pairing potential of the form $\Delta(\boldsymbol{r},\boldsymbol{r}') = \Delta(\boldsymbol{r}-\boldsymbol{r}')$, which includes, as a special case, local potentials given by $\Delta(\boldsymbol{r}-\boldsymbol{r}') = \Delta(\boldsymbol{r})\delta(\boldsymbol{r}-\boldsymbol{r}')$. The field operators can be grouped into a four-component Nambu spinor that acts in the combined Nambu and spin space,

$$\hat{\boldsymbol{\Psi}}^\dagger(\boldsymbol{r}) = (\hat{\Psi}^\dagger_+(\boldsymbol{r}), \hat{\Psi}_-(\boldsymbol{r}), \hat{\Psi}^\dagger_-(\boldsymbol{r}), -\hat{\Psi}_+(\boldsymbol{r})). \tag{I.1.5}$$

This representation allows a compact matrix formulation of the mean-field Hamiltonian, written as

$$\hat{H}_{\text{MF}} = \frac{1}{2}\iint_{\mathcal{V}} d^3\boldsymbol{r}d^3\boldsymbol{r}'\,\hat{\boldsymbol{\Psi}}^\dagger(\boldsymbol{r})\hat{\mathcal{H}}_{\text{MF}}(\boldsymbol{r}-\boldsymbol{r}')\hat{\boldsymbol{\Psi}}(\boldsymbol{r}') + \text{const}, \tag{I.1.6}$$

where $\hat{\mathcal{H}}_{\text{MF}}(\boldsymbol{r})$ is the Bogoliubov-de Gennes Hamiltonian [51]

$$\hat{\mathcal{H}}_{\text{MF}} = \begin{pmatrix} h_+(\boldsymbol{r})\delta(\boldsymbol{r}-\boldsymbol{r}') & \Delta(\boldsymbol{r}-\boldsymbol{r}') & 0 & 0 \\ \Delta^*(\boldsymbol{r}-\boldsymbol{r}') & -h^*_-(\boldsymbol{r})\delta(\boldsymbol{r}-\boldsymbol{r}') & 0 & 0 \\ 0 & 0 & h_-(\boldsymbol{r})\delta(\boldsymbol{r}-\boldsymbol{r}') & \Delta(\boldsymbol{r}-\boldsymbol{r}') \\ 0 & 0 & \Delta^*(\boldsymbol{r}-\boldsymbol{r}') & -h^*_+(\boldsymbol{r})\delta(\boldsymbol{r}-\boldsymbol{r}') \end{pmatrix}. \tag{I.1.7}$$

We consider a cuboidal system of volume $\mathcal{V}$, in which the field operator admits a discrete Fourier expansion of the form

$$\hat{\Psi}_\sigma(\boldsymbol{r}) = \frac{1}{\sqrt{\mathcal{V}}} \sum_{\boldsymbol{k}} e^{i\boldsymbol{k}\cdot\boldsymbol{r}} c_{\boldsymbol{k},\sigma}, \tag{I.1.8}$$

where $\hat{c}_{\boldsymbol{k},\sigma}$ annihilates an electron with momentum $\boldsymbol{k}$ and spin σ. The creation and annihilation operators satisfy the canonical anticommutation relations $\{\hat{c}_{\boldsymbol{k},\sigma}, \hat{c}_{\boldsymbol{k}',\sigma'}\} = 0$ and $\{\hat{c}_{\boldsymbol{k},\sigma}, \hat{c}^\dagger_{\boldsymbol{k}',\sigma'}\} = \delta_{\sigma\sigma'}\delta_{\boldsymbol{k}\boldsymbol{k}'}$. In momentum space, the pairing potential becomes diagonal under the assumption of translation invariance, reducing to

$$\Delta_{\boldsymbol{k}\boldsymbol{k}'} = \frac{1}{\mathcal{V}} \iint_{\mathcal{V}} d^3\boldsymbol{r} d^3\boldsymbol{r}' e^{-i\boldsymbol{k}\cdot\boldsymbol{r}+i\boldsymbol{k}'\cdot\boldsymbol{r}'} \Delta(\boldsymbol{r}-\boldsymbol{r}') = \Delta_{\boldsymbol{k}}\delta_{\boldsymbol{k}\boldsymbol{k}'}. \tag{I.1.9}$$

Accordingly, the mean-field Hamiltonian takes the form

$$\hat{H}_{\mathrm{MF}} = \sum_{\boldsymbol{k}} \hat{\boldsymbol{c}}^\dagger_{\boldsymbol{k}} \hat{H}_{\mathrm{MF},\boldsymbol{k}} \hat{\boldsymbol{c}}_{\boldsymbol{k}} + \text{const}, \quad \hat{H}_{\mathrm{MF},\boldsymbol{k}} = \begin{pmatrix} \xi_{\boldsymbol{k}} & \Delta_{\boldsymbol{k}} \\ \Delta^*_{\boldsymbol{k}} & -\xi_{\boldsymbol{k}} \end{pmatrix} \tag{I.1.10}$$

where $\xi_{\boldsymbol{k}} = \hbar^2\boldsymbol{k}^2/(2m) - \mu$ is the single-particle energy relative to the chemical potential, and the Nambu spinor is defined as $\hat{\boldsymbol{c}}^\dagger_{\boldsymbol{k}} = (\hat{c}^\dagger_{\boldsymbol{k},+}, \hat{c}_{-\boldsymbol{k},-})$. The pairing potential couples electrons with opposite momentum and spin, forming Cooper pairs with zero total momentum and total spin, i.e., in a spin-singlet state. Under the mean-field approximation, the Hamiltonians in Eq. (I.1.6) and Eq. (I.1.10) reduce to a quadratic form, which can be diagonalized via the Bogoliubov transformation. This transformation

$$U_{\boldsymbol{k}} = \begin{pmatrix} u^*_{\boldsymbol{k}} & v_{\boldsymbol{k}} \\ -v^*_{\boldsymbol{k}} & u_{\boldsymbol{k}} \end{pmatrix}, \tag{I.1.11}$$

constructed from the coherence factors $u_{\boldsymbol{k}}$ and $v_{\boldsymbol{k}}$ maps the electronic Nambu spinor $\hat{\boldsymbol{c}}_{\boldsymbol{k}}$ into the quasiparticle spinor $\hat{\boldsymbol{\gamma}}_{\boldsymbol{k}} = (\hat{\gamma}_{\boldsymbol{k},1}, \hat{\gamma}^\dagger_{-\boldsymbol{k},2})^T$ via the relation $\hat{\boldsymbol{\gamma}}_{\boldsymbol{k}} = U_{\boldsymbol{k}}\hat{\boldsymbol{c}}_{\boldsymbol{k}}$. The coherence factors obey $|u_{\boldsymbol{k}}|^2 + |v_{\boldsymbol{k}}|^2 = 1$, and they are given by

$$|u_{\boldsymbol{k}}|^2 = \frac{1}{2}(1 + \frac{\xi_{\boldsymbol{k}}}{E_{\boldsymbol{k}}}), \quad |v_{\boldsymbol{k}}|^2 = \frac{1}{2}(1 - \frac{\xi_{\boldsymbol{k}}}{E_{\boldsymbol{k}}}), \tag{I.1.12}$$

where $E_{\boldsymbol{k}} = \sqrt{\xi^2_{\boldsymbol{k}} + |\Delta_{\boldsymbol{k}}|^2}$ is the quasiparticle energy. The individual phases of the coherence factors are arbitrary, but their relative phase have to reproduce the phase of $\Delta_{\boldsymbol{k}}$. The quasiparticle operators introduced above satisfy the canonical anticommutation relations, and therefore describe fermionic excitations, called Bogoliubov quasiparticles or Bogoliubons. For example, $\hat{\gamma}_{\boldsymbol{k},1}$ is a coherent superposition of an electron annihilation operator with momentum $\boldsymbol{k}$ and spin up, and an electron creation operator with momentum $-\boldsymbol{k}$ and spin down. After the Bogoliubov transformation, the mean-field Hamiltonian takes the diagonal form

$$\hat{H}_{\mathrm{MF}} = \sum_{j=1,2} \sum_{\boldsymbol{k}} E_{\boldsymbol{k}} \hat{\gamma}^\dagger_{\boldsymbol{k},j} \hat{\gamma}_{\boldsymbol{k},j} + \sum_{\boldsymbol{k}} \left(\xi_{\boldsymbol{k}} - E_{\boldsymbol{k}} + \langle \hat{c}^\dagger_{\boldsymbol{k},+} \hat{c}^\dagger_{-\boldsymbol{k},-} \rangle \Delta_{\boldsymbol{k}} \right), \tag{I.1.13}$$

where the second term is independent of the quasiparticle operators and represents the ground-state condensation energy [48]. For a free electron gas ($\Delta_{\boldsymbol{k}} = 0$), the Hamiltonian simplifies to

$$\hat{H}_{\text{el-gas}} = \sum_{\sigma=\pm} \sum_{\boldsymbol{k}} \xi_{\boldsymbol{k}} \hat{c}^{\dagger}_{\boldsymbol{k},\sigma} \hat{c}_{\boldsymbol{k},\sigma}. \tag{I.1.14}$$

There, the ground state corresponds to the Fermi sea, in which all single-particle states are occupied up to the Fermi energy. In contrast, the BCS ground state of a superconductor is given by

$$|\Psi_{\text{G}}\rangle = \Pi_{\boldsymbol{k}} (u_{\boldsymbol{k}} + v_{\boldsymbol{k}} \hat{c}^{\dagger}_{\boldsymbol{k},+} \hat{c}^{\dagger}_{-\boldsymbol{k},-}) \, |0\rangle \, , \tag{I.1.15}$$

where $|0\rangle$ refers to the vacuum state. [52, 53]. Bogoliubov quasiparticles have excitation energies $E_{\boldsymbol{k}}$ above the BCS ground state, with a minimum excitation energy of $|\Delta_{\boldsymbol{k}_F}|$, since $\xi_{\boldsymbol{k}_F} = 0$ at the Fermi surface. Hence, $\Delta_{\boldsymbol{k}}$ is the superconducting gap. In conclusion, the Hamiltonian $\hat{H}_{\text{el-gas}}$ describes a system of non-interacting electrons, while $\hat{H}_{\text{MF}}$ represents non-interacting quasiparticles arising from superconducting correlations.

Electromagnetic field.— The electromagnetic field is a physical field, generated by charges and currents, that mediates electromagnetic forces between charged particles. In regions devoid of matter, the electromagnetic field exists independently and is governed by the source-free Maxwell's equations. The quantization of the free electromagnetic field proceeds by solving Maxwell's equations to identify the mode functions, followed by the promotion of the classical amplitudes to operators satisfying canonical commutation relations. For example, in a cuboidal cavity, the modes of the electromagnetic field are plane waves characterized by discrete wavevectors $\boldsymbol{k}$, whose associated annihilation and creation operators satisfy the canonical commutation relations

$$[\hat{a}_{\boldsymbol{k}}, \hat{a}^{\dagger}_{\boldsymbol{k}'}] = \delta_{\boldsymbol{k},\boldsymbol{k}'}, \quad [\hat{a}_{\boldsymbol{k}}, \hat{a}_{\boldsymbol{k}'}] = 0, \tag{I.1.16}$$

where $[\cdot, \cdot]$ denotes the commutator. The operator $\hat{a}_{\boldsymbol{k}}$ annihilates a photon in the mode with wavevector $\boldsymbol{k}$. For simplicity, the polarization degree of freedom is omitted. The corresponding Hamiltonian of the quantized electromagnetic field is [54]

$$\hat{H}_{\text{ph}} = \sum_{\boldsymbol{k}} \hbar \omega_{\boldsymbol{k}} \left(\hat{a}^{\dagger}_{\boldsymbol{k}} \hat{a}_{\boldsymbol{k}} + \frac{1}{2} \right), \tag{I.1.17}$$

where $\omega_{\boldsymbol{k}} = c|\boldsymbol{k}|$ is the linear dispersion relation for photons, and c is the speed of light. Consequently, each mode of the electromagnetic field behaves as an independent quantum harmonic oscillator. In this thesis, we model the thermal reservoirs involved in near-field radiative heat transfer using semi-infinite transmission lines, which provide an effective electromagnetic representation of the thermal bodies (see Chap. III). Quantization of the transmission line yields the Hamiltonian

$$\hat{H}_{\text{TL}} = \int_0^{\infty} \frac{d\omega}{2\pi} \hbar \omega \left(\hat{a}^{\dagger}(\omega) \hat{a}(\omega) + \frac{1}{2} \right), \tag{I.1.18}$$

which describes a continuum of harmonic oscillators, each labeled by a frequency ω. The annihilation operator $\hat{a}(\omega)$ creates a transmission line excitation of frequency ω.

Equilibrium correlators.— The correlations among particles in the reservoir are determined by its quantum state, described by the density matrix $\hat{\rho}$. Assuming thermal equilibrium, the state of the particles is described by the thermal density matrix

$$\hat{\rho}_{\text{th}} = \frac{1}{\mathcal{Z}} \exp\left(-\beta \hat{H}\right), \tag{I.1.19}$$

where $\hat{H}$ is the Hamiltonian of the particles, $\beta = 1/(k_{\text{B}}T)$ is the inverse thermal energy, T is the temperature of the reservoir, k_{B} is the Boltzmann constant, and the partition function is given by $\mathcal{Z} = \text{Tr}\{\exp(-\beta \hat{H})\}$. We introduce the annihilation operator $\hat{\varsigma}_{\boldsymbol{k}}$, defined to remove a single excitation from the mode corresponding to the quantum number $\boldsymbol{k}$. Depending on the context, the annihilation operator $\hat{\varsigma}_{\boldsymbol{k}}$ may represent the destruction of an electron, a Bogoliubov quasiparticle, or a photon with wavevector $\boldsymbol{k}$, and spin σ or other relevant quantum numbers. The quantum statistical correlations are [49]

$$\langle \hat{\varsigma}^\dagger_{\boldsymbol{k}} \hat{\varsigma}_{\boldsymbol{k}'} \rangle = \frac{1}{\mathcal{Z}} \text{Tr}\{e^{-\beta \hat{H}} \hat{\varsigma}^\dagger_{\boldsymbol{k}} \hat{\varsigma}_{\boldsymbol{k}'}\} = \frac{1}{\mathcal{Z}} \text{Tr}\{e^{-\beta \hat{H}} \hat{\varsigma}_{\boldsymbol{k}'} \hat{\varsigma}^\dagger_{\boldsymbol{k}}\} e^{-\beta \epsilon_{\boldsymbol{k}}} = \frac{1}{\mathcal{Z}} \text{Tr}\{e^{-\beta \hat{H}} [\delta_{\boldsymbol{k}\boldsymbol{k}'} \pm \hat{\varsigma}^\dagger_{\boldsymbol{k}} \hat{\varsigma}_{\boldsymbol{k}'}]\} e^{-\beta \epsilon_{\boldsymbol{k}}}, \tag{I.1.20}$$

leading to

$$\langle \hat{\varsigma}^\dagger_{\boldsymbol{k}} \hat{\varsigma}_{\boldsymbol{k}'} \rangle = \frac{1}{e^{\beta \epsilon_{\boldsymbol{k}}} \mp 1} \delta_{\boldsymbol{k}\boldsymbol{k}'}. \tag{I.1.21}$$

We employed the Baker–Campbell–Hausdorff formula along with the commutation relation $[\hat{H}, \hat{\varsigma}_{\boldsymbol{k}}] = -\epsilon_{\boldsymbol{k}} \hat{\varsigma}_{\boldsymbol{k}}$, which follows from the diagonalization of the Hamiltonian in terms of single-particle energies $\epsilon_{\boldsymbol{k}}$. The difference in sign arises from the use of commutators for bosons and anticommutators for fermions. In Eq. (I.1.21), the negative sign corresponds to bosonic statistics and leads to the Bose–Einstein distribution $n(E) = [e^{\beta E} - 1]^{-1}$, while the positive sign corresponds to fermionic statistics and yields the Fermi–Dirac distribution $f(E) = [e^{\beta E} + 1]^{-1}$ (see Fig. I.3). The same reasoning extends to a continuous spectrum of modes characterized by energy E, resulting in the correlator

$$\langle \hat{\varsigma}^\dagger(E) \hat{\varsigma}(E') \rangle = \frac{1}{e^{\beta E} \mp 1} \delta(E - E'). \tag{I.1.22}$$

In summary, equilibrium correlations of quasiparticles in a reservoir follow the Fermi–Dirac distribution for fermions and the Bose–Einstein distribution for bosons, reflecting their respective exchange statistics.

I.2 Green's Function Approach

Green's functions play a central role in the theoretical treatment of interacting many-body systems in solid-state physics, enabling access to spectral, dynamical, and transport properties. A wide range of observables, including particle

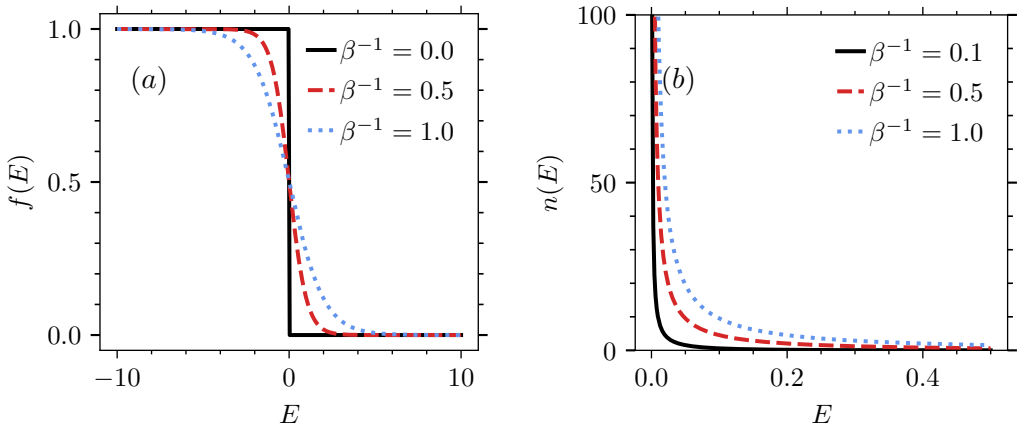

Figure I.3: *Equilibrium correlations*: (a) Fermi–Dirac distribution $f(E)$ for fermions and (b) Bose–Einstein distribution $n(E)$ for bosons, each shown for different temperatures.

densities, currents, correlation functions, and response functions, can be directly obtained. The Green's function formalism provides a systematic perturbative framework, treating interactions diagrammatically and enabling partial resummation of diagrams into blocks. Through the Dyson equation, the Green's function can be expanded in terms of the non-interacting Green's function and the self-energy, which encodes a specific class of diagrams. Systems in thermal equilibrium can be analyzed using imaginary-time Green's functions, either at zero temperature or via the Matsubara formalism. Out of equilibrium, such as under a time-dependent perturbation, nonequilibrium Green's functions, also known as Keldysh Green's functions, provide the appropriate framework to describe the system's dynamics. We briefly introduce the nonequilibrium Green's function formalism and refer the reader to [7, 55–63] for a more detailed treatment.

Keldysh time contour.— Our starting point is a many-body quantum system evolving under a time dependent Hamiltonian $\hat{H}(t)$, which encodes both external driving and internal interactions. The state of the many-body system is described by the density matrix $\hat{\rho}(t)$, which evolves according to the Von Neumann equation $i\hbar\partial_t\hat{\rho}(t) = [\hat{H}(t), \hat{\rho}(t)]$ [64]. The Von Neumann equation admits a formal solution via the time-evolution operator

$$\hat{U}(t, -\infty) = \mathscr{T} \exp\left(-\frac{i}{\hbar}\int_{-\infty}^{t} \hat{H}(\tau)d\tau\right), \tag{I.2.1}$$

leading to $\hat{\rho}(t) = \hat{U}(t, -\infty)\hat{\rho}(-\infty)\hat{U}^\dagger(t, -\infty)$. Here, $\mathscr{T}$ denotes the time-ordering operator, and $\hat{\rho}(-\infty)$ is the density matrix of the system in the distant past. The expectation value of an observable $\hat{\mathcal{O}}$ evolves according to

$$\langle\hat{\mathcal{O}}(t)\rangle = \mathrm{Tr}\{\hat{\mathcal{O}}\hat{\rho}(t)\} = \mathrm{Tr}\{\hat{U}(-\infty, t)\hat{\mathcal{O}}\hat{U}(t, -\infty)\hat{\rho}(-\infty)\} \tag{I.2.2}$$

Therefore, we evolve the system forward in time from $-\infty$ to t, where the observable is inserted, and then backward to $-\infty$ (see Fig. I.4). We extend the time-axis

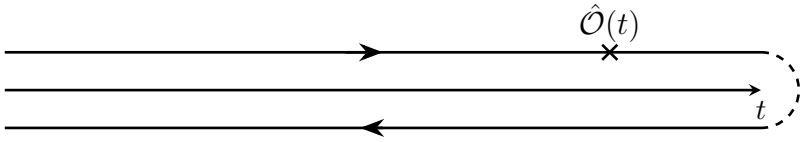

Figure I.4: *Keldysh time contour* as used in the nonequilibrium Green's function formalism.

to infinity by inserting $\hat{U}(t,\infty)\hat{U}(\infty,t) = \mathbb{1}$ into the expectation value, yielding

$$\langle\hat{\mathcal{O}}(t)\rangle = \mathrm{Tr}\{\hat{U}(-\infty,\infty)\hat{U}(\infty,t)\hat{\mathcal{O}}\hat{U}(t,-\infty)\hat{\rho}(-\infty)\} \tag{I.2.3a}$$

$$= \mathrm{Tr}\{\hat{U}(-\infty,t)\hat{\mathcal{O}}\hat{U}(t,\infty)\hat{U}(\infty,-\infty)\hat{\rho}(-\infty)\}. \tag{I.2.3b}$$

This closed time path, running from $-\infty$ to ∞ and back, is referred to as the Keldysh contour. By inserting the identity operator to the left or right of the observable, it is effectively placed on the forward or backward branch of the Keldysh contour, respectively. To capture both cases we extend the time variable t to the Keldysh contour C_K, such that $\langle\hat{\mathcal{O}}(t)\rangle$ with t on the forward branch corresponds to (I.2.3a), and with t on the backward branch to (I.2.3b). While nonequilibrium dynamics require the full Keldysh contour to account for time-asymmetric evolution, the backward branch becomes redundant in equilibrium systems due to the adiabatic switching on and off of interactions [7, 63].

Keldysh Green's functions.— The contour-ordered Green's function is defined by

$$G(x,x') \equiv -i\left\langle \mathscr{T}_{C_\mathrm{K}}\left[\hat{\Psi}_\mathrm{H}(x)\hat{\Psi}^\dagger_\mathrm{H}(x')\right]\right\rangle, \tag{I.2.4}$$

where $x = (\boldsymbol{r},t)$ is the space-time coordinate, $\hat{\Psi}_\mathrm{H}(x)$ is the field operator in the Heisenberg picture with respect to the Hamiltonian $\hat{H}(t)$, and the average is taken with respect to the initial density matrix. The contour-ordering operator $\mathscr{T}_{C_\mathrm{K}}$ is defined as

$$\mathscr{T}_{C_\mathrm{K}}\left[\hat{\Psi}_\mathrm{H}(x)\hat{\Psi}^\dagger_\mathrm{H}(x')\right] \equiv \begin{cases} \hat{\Psi}_\mathrm{H}(x)\hat{\Psi}^\dagger_\mathrm{H}(x') & t >_{C_\mathrm{K}} t' \\ \pm\hat{\Psi}^\dagger_\mathrm{H}(x')\hat{\Psi}_\mathrm{H}(x) & t <_{C_\mathrm{K}} t' \end{cases}, \tag{I.2.5}$$

with the upper sign $(+)$ for bosonic fields and the lower sign $(-)$ for fermionic fields. The relation $t >_{C_\mathrm{K}} t'$ indicates that t occurs after t' along the Keldysh contour. The various cases of contour ordering can be organized into the Keldysh matrix Green's function

$$\check{G}(x,x') = \begin{pmatrix} G^{++}(x,x') & G^{+-}(x,x') \\ G^{-+}(x,x') & G^{--}(x,x') \end{pmatrix}, \tag{I.2.6}$$

with the time-ordered $(++)$, anti-time-ordered $(--)$, greater $(+-)$, and lesser

$(-+)$ Green's functions

$$G^{++}(x,x') = -i\left\langle \mathscr{T}\left[\hat{\Psi}_{\mathrm{H}}(x)\hat{\Psi}^{\dagger}_{\mathrm{H}}(x')\right]\right\rangle \tag{I.2.7a}$$

$$G^{--}(x,x') = -i\left\langle \tilde{\mathscr{T}}\left[\hat{\Psi}_{\mathrm{H}}(x)\hat{\Psi}^{\dagger}_{\mathrm{H}}(x')\right]\right\rangle \tag{I.2.7b}$$

$$G^{+-}(x,x') = \pm i\langle\hat{\Psi}^{\dagger}_{\mathrm{H}}(x')\hat{\Psi}_{\mathrm{H}}(x)\rangle \tag{I.2.7c}$$

$$G^{-+}(x,x') = -i\langle\hat{\Psi}_{\mathrm{H}}(x)\hat{\Psi}^{\dagger}_{\mathrm{H}}(x')\rangle, \tag{I.2.7d}$$

where $\tilde{\mathscr{T}}$ denotes the anti-time-ordering operator. In this representation, the times t and t' lie on the real-time axis rather than on the Keldysh contour. We traded the Keldysh contour for a matrix structure known as Keldysh space, in which matrices are denoted by a check $\check{}$. The components of the Keldysh Green's function are not independent, as they satisfy the identity $G^{++}(x,x')+G^{--}(x,x') = G^{+-}(x,x')+G^{-+}(x,x')$. Therefore, performing a Larkin–Ovchinnikov rotation [63] brings the Green's function into a triangular form

$$\check{L}\check{G}(x,x')\check{L}^{\dagger} = \begin{pmatrix} 0 & G^{\mathrm{a}}(x,x') \\ G^{\mathrm{r}}(x,x') & G^{\mathrm{K}}(x,x') \end{pmatrix} \equiv \breve{G}(x,x'), \tag{I.2.8}$$

with the rotation matrix $\check{L} = (\check{1} - i\check{\sigma}_2)/\sqrt{2}$, constructed from the second Pauli matrix $\check{\sigma}_2$ in Keldysh space. The symbol $\breve{}$ denotes matrices expressed in the retarded–advanced–Keldysh (RAK) basis. At this stage, the Green's function is expressed in terms of the retarded, advanced, and Keldysh component

$$G^{\mathrm{r}}(x,x') = G^{++}(x,x') - G^{+-}(x,x') = G^{-+}(x,x') - G^{--}(x,x') \tag{I.2.9a}$$

$$G^{\mathrm{a}}(x,x') = G^{++}(x,x') - G^{-+}(x,x') = G^{+-}(x,x') - G^{--}(x,x') \tag{I.2.9b}$$

$$G^{\mathrm{K}}(x,x') = G^{++}(x,x') + G^{--}(x,x') = G^{+-}(x,x') + G^{-+}(x,x'). \tag{I.2.9c}$$

Dyson equation.— The Dyson equation relates the Green's function of an interacting system to that of a known non-interacting system via the self-energy, which captures all interaction-induced modifications. Even if the self-energy is determined approximately, the Dyson equation yields a non-perturbative approximation to the full Green's function. To begin, we consider a reference system governed by a single-particle Hamiltonian

$$\hat{H}_0(t) = \iint_{\mathcal{V}} d^3\boldsymbol{r}d^3\boldsymbol{r}'\hat{\Psi}^{\dagger}(\boldsymbol{r})h(\boldsymbol{r},\boldsymbol{r}',t)\hat{\Psi}(\boldsymbol{r}'), \tag{I.2.10}$$

where, for brevity, we omit spin and other internal degrees of freedom. Possible choices for the reference system include the Hamiltonian of a free electron gas (I.1.3) or the mean-field Hamiltonian of a BCS superconductor (I.1.6), depending on the physical system under consideration. The field operators evolve according to the Heisenberg equation of motion, which leads to an equation of motion for the free Green's function,

$$[\check{G}_0^{-1} * \check{G}_0](x,x') = \delta(x-x')\check{\sigma}_3, \tag{I.2.11}$$

where the inverse propagator is defined as

$$\check{G}_0^{-1}(x,x') = [i\hbar\partial_t\delta(\boldsymbol{r}-\boldsymbol{r}') - h(\boldsymbol{r},\boldsymbol{r}',t)]\delta(t-t')\check{1}. \tag{I.2.12}$$

Here, $\check{1}$ denotes the identity matrix, and $\check{\sigma}_3$ the third Pauli matrix in Keldysh space. The symbol $*$ denotes the generalized convolution of two functions $f(x,x')$ and $g(x,x')$, defined by

$$[f*g](x,x') \equiv \int_{\mathcal{V}} d^3\boldsymbol{r}'' \int_{-\infty}^{\infty} dt'' f(x,x'')g(x'',x'). \tag{I.2.13}$$

In expressions involving Keldysh matrices, adjacent terms are also multiplied as matrices.
When interactions are included, the exact evolution of the field operators becomes difficult to track, although it can still be formally expressed using the time-evolution operator. By using the interaction picture, the Green's function is expressed as a time-ordered correlator of the free field operators and the interaction-picture evolution operator. The expansion of the interaction-picture evolution operator yields an infinite series of correlators involving free field operators. Applying Wick's theorem reduces the sum of time-ordered correlators to a convolution sum over products of non-interacting two-point Green's functions $\check{G}_0(x,x')$. To better organize the perturbation series, a diagrammatic representation known as Feynman diagrams is introduced to depict the individual terms. The structure of the diagrams depends on the interaction under consideration. However, Feynman diagrams can be classified according to their structural properties, such as connectivity and particle irreducibility, e.g., connected, disconnected, reducible, or irreducible. A connected diagram is defined by the property that all parts are mutually linked, and no section is disconnected from the rest. Only connected diagrams contribute to the Green's function; disconnected contributions cancel upon normalization. Furthermore, diagrams that differ only by a permutation of internal vertex labels yield the same contribution, so only topologically nonequivalent diagrams contribute. Irreducible diagrams form a distinguished subset of Feynman diagrams that cannot be disconnected by cutting a single internal line. The sum of all such irreducible diagrams defines the self-energy

$$\check{\Sigma}(x,x') = \begin{pmatrix} \Sigma^{++}(x,x') & \Sigma^{+-}(x,x') \\ \Sigma^{-+}(x,x') & \Sigma^{--}(x,x') \end{pmatrix}. \tag{I.2.14}$$

The irreducible diagrams serve as fundamental building blocks for the entire Green's function, which can be expressed through the Dyson equation [65]

$$\check{G}(x,x') = \check{G}_0(x,x') + [\check{G}_0 * \check{\Sigma} * \check{G}](x,x'). \tag{I.2.15}$$

Applying $\check{G}_0^{-1}$ to both sides of the Dyson equation yields the equation of motion for the interacting Green's function

$$[(\check{G}_0^{-1} - \check{\sigma}_3\check{\Sigma}) * \check{G}](x,x') = \delta(x-x')\check{\sigma}_3. \tag{I.2.16}$$

Both the Dyson equation and the equation of motion can be equivalently formulated in the RAK basis, obtained through the Larkin–Ovchinnikov transformation. For a comprehensive treatment of diagrammatic methods and Dyson

equations, see [56, 59].

Reservoir Green's functions.— The thermal reservoirs at the ends of the conductor supply particles, rendering their Green's function essential for determining transport behaviour. Of particular interest are the equilibrium Keldysh Green's functions of a free electron gas and an s-wave BCS superconductor, which are utilized throughout this dissertation. We consider the BCS superconducting reservoir, noting that the free electron gas is recovered in the limit of a vanishing superconducting gap. The Green's functions are constructed from the Nambu spinor (I.1.5), and therefore carry both Nambu and spin structure. Time translation invariance in equilibrium, together with the plane-wave expansion of the field operator (I.1.8), implies that the Green's function depends only on the difference of space-time coordinates, $x - x'$. A Fourier transform in space (to the wavevektor $\boldsymbol{k}$) and time (to the energy E) leads to the equation

$$[E \pm i\eta - \tilde{\mathbb{1}} \otimes \hat{H}_{\mathrm{MF},\boldsymbol{k}}] G^{\mathrm{r/a}}_{\boldsymbol{k}}(E) = 1, \tag{I.2.17}$$

from which the Green's functions are obtained as

$$\begin{aligned} G^{\mathrm{r/a}}_{\boldsymbol{k}}(E) =& [E \pm i\eta - \tilde{\mathbb{1}} \otimes \hat{H}_{\mathrm{MF},\boldsymbol{k}}]^{-1} \\ =& \tilde{\mathbb{1}} \otimes \frac{1}{(E \pm i\eta)^2 - \xi^2_{\boldsymbol{k}} - |\Delta_{\boldsymbol{k}}|^2} \begin{pmatrix} E \pm i\eta + \xi_{\boldsymbol{k}} & \Delta_{\boldsymbol{k}} \\ \Delta^*_{\boldsymbol{k}} & E \pm i\eta - \xi_{\boldsymbol{k}} \end{pmatrix}, \end{aligned} \tag{I.2.18}$$

see Eq. (I.1.10) for the wavevector-resolved mean-field Hamiltonian $\hat{H}_{\mathrm{MF},\boldsymbol{k}}$. The $\pm i\eta$ term ensures causality in the Green's functions and is interpreted as a phenomenological broadening parameter. In a perfect superconductor, it vanishes ($\eta \to 0$), but it can be retained to model simple inelastic scattering mechanisms. Here, $\tilde{\mathbb{1}}$ denotes the identity matrix in spin space, and $\otimes$ indicates the tensor product. In thermal equilibrium, the fluctuation-dissipation theorem constrains the Keldysh component to the form

$$G^{\mathrm{K}}_{\boldsymbol{k}}(E) = (1 - 2f(E))[G^{\mathrm{r}}_{\boldsymbol{k}}(E) - G^{\mathrm{a}}_{\boldsymbol{k}}(E)], \tag{I.2.19}$$

where $f(E)$ is the Fermi distribution. Together with the relations among the Green's function components, these considerations determine the equilibrium Keldysh Green's function $\check{G}_{\boldsymbol{k}}(E)$.

Quasiclassical approximation.— The quasiclassical approximation exploits the fact that, in most systems, the Fermi energy is the dominant energy scale, much larger than other relevant scales such as temperature, applied bias, or the superconducting gap [59, 60]. Since the relevant low-energy processes are concentrated near the Fermi surface, we integrate over $\xi_{\boldsymbol{k}}$, which represents the energy deviation normal to the surface. In terms of the Green's function, the quasiclassical approximation amounts to integrating out the rapid oscillations on the scale of the Fermi wavelength, while retaining only the slow spatial variations. The quasiclassical Green's function is defined by

$$\check{G}_{\mathrm{qc}}(\boldsymbol{R}, \boldsymbol{e}_{\boldsymbol{k}}, E) \equiv \frac{1}{\pi} \int_{-\infty}^{\infty} d\xi_{\boldsymbol{k}} \check{\sigma}_{\mathrm{K}} \check{G}_{\boldsymbol{k}}(\boldsymbol{R}, E), \tag{I.2.20}$$

with $\check{\sigma}_{\mathrm{K}} = \check{\sigma}_3 \otimes \hat{\sigma}_3$, $\boldsymbol{R}$ the center of mass coordinate, $\hat{\sigma}_3$ the third Pauli matrix in Nambu space, and $\boldsymbol{e_k}$ is the unit vector in the direction of the wavevector, accounting for potential angular dependence. The normalization condition of the quasiclassical Green's function,

$$[\check{G}_{\mathrm{qc}}(\boldsymbol{R}, \boldsymbol{e_k}, E)]^2 = \check{\mathbb{1}}, \tag{I.2.21}$$

is central to many calculations, as it constrains the allowable form of solutions and ensures physical consistency. The equilibrium retarded and advanced Green's function of an s-wave BCS superconductor with isotropic gap $\Delta_{\boldsymbol{k}} = \Delta$ take the form

$$G^{\mathrm{r/a}}_{\mathrm{qc}}(E) = \tilde{\mathbb{1}} \otimes \frac{i}{\sqrt{(E \pm i\eta)^2 - |\Delta|^2}} \begin{pmatrix} E \pm i\eta & \Delta \\ \Delta^* & -(E \pm i\eta) \end{pmatrix}. \tag{I.2.22}$$

In the limit $\Delta \to 0$, the BCS Green's function reduces to that of a free electron gas. The retarded and advanced quasiclassical Green's functions become diagonal in Nambu and spin space

$$G^{\mathrm{r/a}}_{\mathrm{qc}}(E) = \pm\tilde{\mathbb{1}} \otimes \hat{\sigma}_3, \tag{I.2.23}$$

leading to

$$\check{G}_{\mathrm{qc}}(E) = \begin{pmatrix} (1 - 2f(E)) & -2f(E) \\ -2(1 - f(E)) & -(1 - 2f(E)) \end{pmatrix}. \tag{I.2.24}$$

Throughout the remainder of this thesis, we work with quasiclassical Green's functions and omit the subscript unless otherwise stated.

I.3 Landauer-Büttiker Scattering Theory

The Landauer-Büttiker scattering approach describes the coherent and elastic transport of electrons through a mesoscopic conductor. This section presents the main principles of the scattering formalism as applied to two-terminal devices with normal-metal leads. For comprehensive treatments and extensions to multiterminal configurations and superconducting contacts, see [5–7, 14, 15].

Scattering states.— The mesoscopic conductor is modelled as a central scattering region connected to macroscopic terminals $\alpha = 1, 2$ via ballistic waveguides (see Fig. I.5). The electrons in the conductor can typically be approximated as non-interacting, allowing the transport problem to be reduced to a single-particle framework. Electrons in the conductor propagate along the z-direction, while their transverse motion is confined by the conductor's geometry, described by a potential $U_{\mathrm{con}}(x, y)$. The electrons experience a localized time-independent scattering potential $U_{\mathrm{scat}}(\boldsymbol{r})$ that vanishes outside a finite region, allowing for free propagation in the asymptotic limits. The single particle Hamiltonian is given by

$$\hat{H} = -\frac{\hbar^2}{2m}\nabla^2 + U_{\mathrm{con}}(x, y) + U_{\mathrm{scat}}(\boldsymbol{r}), \tag{I.3.1}$$

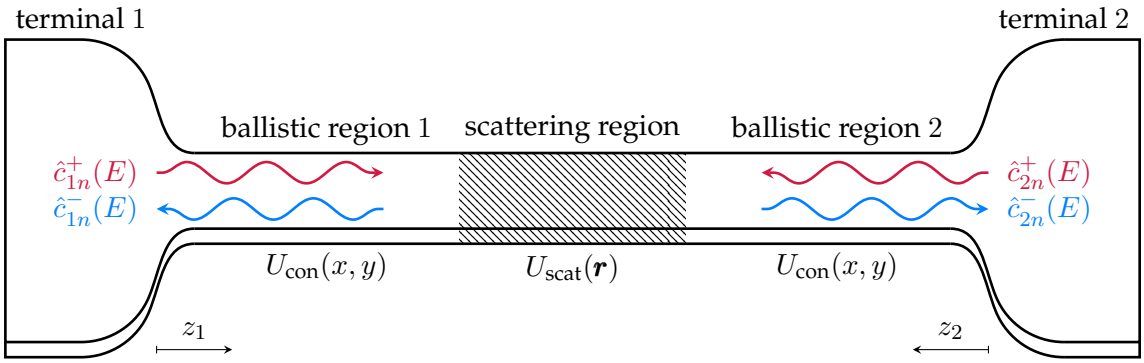

Figure I.5: *Schematic of a coherent conductor* partitioned into three types of regions: reservoirs (terminals), the ballistic region, and the scattering region. Terminals inject incoming electron waves $\hat{c}^+_{\alpha n}$, corresponding to channel n and energy E from terminal α. These waves are scattered within the conductor and emerge as outgoing electron waves $\hat{c}^-_{\beta n}(E)$.

where m corresponds to the electron mass and ∇ to the nabla operator. To analyze the scattering process, we solve the time-independent Schrödinger equation

$$E\psi(\boldsymbol{r}, E) = \hat{H}\psi(\boldsymbol{r}, E), \tag{I.3.2}$$

and construct asymptotic scattering states far from the scattering center. Due to the confinement, the energy levels $E_{\perp\alpha n}$ associated with the transverse wavefunctions $\chi_{\alpha n}(x, y)$ are quantized. Propagation in z-direction remains continuous and is characterised by the longitudinal momentum $k_{\alpha n} = \sqrt{2m(E - E_{\perp\alpha n})}$. For example, a hard-wall waveguide with rectangular cross section of size $L_x \times L_y$ yields transverse wavefunctions $\chi_{\alpha n_x n_y}(x, y) = \sqrt{4/(L_x L_y)}\sin(k_{\alpha x}x)\sin(k_{\alpha y}y)$, with transverse moments $k_{\alpha d} = \pi n_{\alpha d}/L_d, n_{\alpha d} \in \mathbb{Z}, d = x, y$ and confinement energies $E_{\perp\alpha n_x n_y} = (k^2_{\alpha x} + k^2_{\alpha y})/2m$. In general, the energy quantization and the transverse modes depend on the specific form of the confinement potential. For a given energy E, only a finite number of modes propagate, as $k_{\alpha n}$ becomes imaginary for $E_{\alpha n} > E$. Far from the scattering region in terminal α, the wavefunction of mode n with energy E takes the form

$$\psi^\nu_{\alpha n}(\boldsymbol{r}, E) = \frac{1}{\sqrt{v_{\alpha n}}} e^{i\nu k_{\alpha n} z}\chi_{\alpha n}(x, y), \tag{I.3.3}$$

where $\nu = \pm$ denotes forward $(+)$ and backward $(-)$ propagation, and $v_{\alpha n}$ is the mode-dependent group velocity. This set of wavefunctions satisfies the normalization condition

$$\int d\boldsymbol{r}\psi^{\nu *}_{\alpha n}(\boldsymbol{r}, E)\psi^{\nu'}_{\beta k}(\boldsymbol{r}, E') = \delta_{\nu\nu'}\delta_{\alpha\beta}\delta_{nk}\delta(E - E'). \tag{I.3.4}$$

An arbitrary scattering state in terminal α with energy E is described by the wavefunction

$$\psi_\alpha(\boldsymbol{r}, E) = \sum_{n=1}^{N_\alpha(E)} \left[\psi^+_{\alpha n}(\boldsymbol{r}, E)c^+_{\alpha n}(E) + \psi^-_{\alpha n}(\boldsymbol{r}, E)c^-_{\alpha n}(E)\right], \tag{I.3.5}$$

where $c^{\nu}_{\alpha n}(E)$ are the complex amplitudes of the incoming ($\nu = +$) and outgoing ($\nu = -$) modes n in terminal α, and $N_\alpha(E)$ the number of propagating modes. For a given scattering potential, we solve the Schrödinger equation and determine the scattering states by matching the wavefunction and its derivative at the boundaries of the scattering region. In general, this leads to a linear relation between incoming and outgoing mode amplitudes, determined by the scattering matrix $S_{\alpha\beta nm}(E)$,

$$c^{-}_{\alpha n}(E) = \sum_{\beta}\sum_{k} S_{\alpha\beta nk}(E) c^{+}_{\beta k}(E). \tag{I.3.6}$$

Here, the notations $\sum_k$ and $\sum_\beta$ are used as shorthand for $\sum_{k=1}^{N_\beta(E)}$ and $\sum_{\beta=1,2}$, respectively. The scattering matrix encodes the effect of the scattering potential on the asymptotic states. Energy conservation implies elastic scattering, meaning the scattering matrix does not mix incoming and outgoing modes at different energies. Furthermore, the continuity equation implies conservation of probability current, which leads to the unitarity condition of the scattering matrix:

$$\sum_{\gamma}\sum_{l} S^{*}_{\gamma\alpha ln}(E) S_{\gamma\beta lk}(E) = \delta_{\alpha\beta}\delta_{nk}. \tag{I.3.7}$$

Second quantization.— We adopt a second-quantized description to account for many-electron transport, where the Pauli exclusion principle prevents multiple electrons from occupying the same quantum state. The mode amplitudes are promoted to annihilation operators $\hat{c}^{\nu}_{\alpha n}(E)$, with the anticommutation relations $\{\hat{c}^{\nu}_{\alpha n}(E), \hat{c}^{\nu\dagger}_{\beta k}(E')\} = \delta_{\alpha\beta}\delta_{nk}\delta(E - E')$, and $\{\hat{c}^{\nu}_{\alpha n}(E), \hat{c}^{\nu}_{\beta k}(E')\} = 0$. The scattering matrix relates the incoming and outgoing annihilation operators through

$$\hat{c}^{-}_{\alpha n}(E) = \sum_{\beta}\sum_{k} S_{\alpha\beta nk}(E) \hat{c}^{+}_{\beta k}(E). \tag{I.3.8}$$

Within the Heisenberg representation, the field operators are given by

$$\hat{\Psi}_\alpha(\boldsymbol{r}, t) = \sum_{\nu=\pm}\sum_{n}\int_{-\infty}^{\infty} dE \frac{\chi_{\alpha n}(\boldsymbol{r}_\perp)}{\sqrt{2\pi\hbar v_{\alpha n}(E)}} e^{-iEt/\hbar - i\nu k_{\alpha n}(E) z} \hat{c}^{\nu}_{\alpha n}(E) \tag{I.3.9a}$$

$$\hat{\Psi}^{\dagger}_\alpha(\boldsymbol{r}, t) = \sum_{\nu=\pm}\sum_{n}\int_{-\infty}^{\infty} dE \frac{\chi^{*}_{\alpha n}(\boldsymbol{r}_\perp)}{\sqrt{2\pi\hbar v_{\alpha n}(E)}} e^{iEt/\hbar + i\nu k_{\alpha n}(E) z} \hat{c}^{\nu\dagger}_{\alpha n}(E), \tag{I.3.9b}$$

with anticommutation relations

$$\begin{aligned} \{\hat{\Psi}_\alpha(\boldsymbol{r}, t), \hat{\Psi}^{\dagger}_\alpha(\boldsymbol{r'}, t)\} &= \delta(\boldsymbol{r} - \boldsymbol{r'}) \\ \{\hat{\Psi}_\alpha(\boldsymbol{r}, t), \hat{\Psi}_\alpha(\boldsymbol{r'}, t)\} &= 0. \end{aligned} \tag{I.3.9c}$$

Current operator.— The electric current corresponds to the particle current along the z-direction, multiplied by the elementary charge, leading to

$$\hat{I}_\alpha(z,t) = \frac{\hbar e}{2im}\int d\boldsymbol{r}_\perp \left[\hat{\Psi}^\dagger_\alpha(\boldsymbol{r},t)\left(\frac{\partial}{\partial z}\hat{\Psi}_\alpha(\boldsymbol{r},t)\right) - \left(\frac{\partial}{\partial z}\hat{\Psi}^\dagger_\alpha(\boldsymbol{r},t)\right)\hat{\Psi}_\alpha(\boldsymbol{r},t)\right]. \quad \text{(I.3.10)}$$

In terms of the particle creation and annihilation operators, the charge current operator is

$$\begin{aligned}\hat{I}_\alpha(z,t) =& \frac{\hbar e}{m}\sum_{\nu,\nu'=\pm}\sum_n \iint_{-\infty}^{\infty}\frac{dEdE'}{2\pi}e^{i(E-E')t/\hbar}\frac{-\nu k_{\alpha n}(E) - \nu' k_{\alpha n}(E')}{2\sqrt{v_{\alpha n}(E)v_{\alpha n}(E')}} \\ &\times e^{i(\nu k_{\alpha n}(E) - \nu' k_{\alpha n}(E'))z}\hat{c}^{\nu\dagger}_{\alpha n}(E)\hat{c}^{\nu'}_{\alpha n}(E'). \end{aligned} \quad \text{(I.3.11)}$$

The key assumption in electronic transport is that the relevant energies E and E' are close to the Fermi energy, restricting the theory to external perturbations that excite only states near the Fermi energy. Consequently, the wave vector and group velocity are approximately evaluated at the Fermi energy. For example, in the case of a free electron gas, the group velocity is $v_{\alpha n}(E) = \hbar^2 k_{\alpha n}(E)/m$, and the charge current simplifies to

$$\begin{aligned}\hat{I}_\alpha(t) =& e\sum_n\sum_{\nu=\pm}\nu\iint_{-\infty}^{\infty}\frac{dEdE'}{2\pi\hbar}e^{i(E-E')t/\hbar}\hat{c}^{\nu\dagger}_{\alpha n}(E)\hat{c}^{\nu}_{\alpha n}(E') \\ =& e\sum_{\substack{\beta\gamma\\ mk}}\iint_{-\infty}^{\infty}\frac{dEdE'}{2\pi\hbar}e^{i(E-E')t/\hbar}A^\alpha_{\beta\gamma mk}(E,E')\hat{c}^\dagger_{\beta m}(E)\hat{c}_{\gamma k}(E'), \end{aligned} \quad \text{(I.3.12)}$$

with the Landauer-Büttiker A-matrix

$$A^\alpha_{\beta\gamma mk}(E,E') = \delta_{mk}\delta_{\alpha\beta}\delta_{\alpha\gamma} - \sum_n S^\dagger_{\beta\alpha mn}(E)S_{\alpha\gamma nk}(E'), \quad \text{(I.3.13)}$$

and $\hat{c}_{\alpha n}(E) \equiv \hat{c}^+_{\alpha n}(E)$.

Average current.— The current operator is the central object in the Landauer-Büttiker scattering theory and enables the calculation of the average current, noise, and higher-order correlators. A prerequisite for computing current correlators is the evaluation of single-particle correlation functions of the form $\langle \hat{c}^\dagger_{\alpha n}(E)\hat{c}_{\beta m}(E')\rangle$. The electronic correlations of the scattering states are determined by the terminals, therefore the statistical properties of the terminals enter the problem as boundary conditions. External bias and driving applied to the conductor are incorporated through these boundary conditions. The terminals serve as large particle reservoirs that inject and absorb electrons from the conductor. Inelastic scattering within the terminals ensures that they behave as ideal thermal reservoirs, maintaining well-defined temperatures and chemical potentials throughout the transport process. For example, a Fermi gas in thermal equilibrium satisfies the quantum statistical average

$$\langle \hat{c}^\dagger_{\alpha n}(E)\hat{c}_{\beta m}(E')\rangle = \delta_{\alpha\beta}\delta_{nm}\delta(E-E')f_\alpha(E), \quad \text{(I.3.14)}$$

where the Fermi distribution is given by $f_\alpha(E) = [\exp[(E-\mu_\alpha)/(k_\mathrm{B}T_\alpha)]+1]^{-1}$, where T_α and μ_α denote the temperature and chemical potential of terminal α, respectively, while k_B is the Boltzmann constant. A difference in chemical potential ($\mu_1 \neq \mu_2$) corresponds to a voltage bias across the conductor, while a difference in temperature ($T_1 \neq T_2$) gives rise to a thermal bias.
The average current in terminal 1 is given by

$$\begin{aligned}\langle \hat{I}_1(t)\rangle =& \frac{e}{2\pi\hbar}\int_{-\infty}^{\infty} dE \sum_{nk} S^\dagger_{21nk}(E) S_{12kn}(E)[f_1(E)-f_2(E)] \\ =& \frac{e}{2\pi\hbar}\sum_n \int_{-\infty}^{\infty} dE\, \mathcal{T}_n(E)[f_1(E)-f_2(E)],\end{aligned} \tag{I.3.15}$$

which follows from the correlator in Eq.(I.3.14). In the final step, we diagonalized the transmission submatrix $S_{12nm}(E)$ in channel space, yielding the transmission probabilities $\mathcal{T}_n(E)$. At zero temperature and energy-independent transmission, we obtain the Landauer formula (I.0.2) for the conductance.

Noise spectrum.— Noise quantifies the fluctuations of the current around its average value. The deviation from the average current is defined as $\Delta\hat{I}_\alpha(t) \equiv \hat{I}_\alpha(t) - \langle \hat{I}_\alpha(t)\rangle$. The current fluctuations are characterized by the symmetrized correlator

$$S_{\alpha\beta}(t-t') \equiv \frac{1}{2}\left\langle \{\Delta\hat{I}_\alpha(t), \Delta\hat{I}_\beta(t')\}\right\rangle, \tag{I.3.16}$$

and depend on the time difference $t-t'$ for systems without time-dependent drive. The Fourier transform of the symmetrized correlator yields

$$2\pi\delta(\omega+\omega')S_{\alpha\beta}(\omega) \equiv \frac{1}{2}\left\langle \{\Delta\hat{I}_\alpha(\omega), \Delta\hat{I}_\beta(\omega')\}\right\rangle, \tag{I.3.17}$$

with $S_{\alpha\beta}(\omega)$ is the noise spectrum. Current–current correlators involve fourth-order electronic correlations, since the current operator is bilinear in the creation and annihilation operators. Wick's theorem provides a systematic way to express expectation values of products of many creation and annihilation operators in terms of second-order correlation functions, thereby assuming a Gaussian state [66]. As a result the noise spectrum reduces to

$$\begin{aligned}S_{\alpha\beta}(\omega) =& \frac{e^2}{2\pi\hbar}\sum_{\substack{\gamma\delta\\ nm}} \int_{-\infty}^{\infty} dE A^\alpha_{\gamma\delta mn}(E, E+\hbar\omega) A^\beta_{\delta\gamma nm}(E+\hbar\omega, E) \\ & \times \left[f_\gamma(E)(1-f_\delta(E+\hbar\omega)) + (1-f_\gamma(E))f_\delta(E+\hbar\omega))\right].\end{aligned} \tag{I.3.18}$$

In the absence of a voltage bias and at finite temperature, the conductor exhibits thermal noise due to the agitation of charge carriers. Thermal noise is according to the fluctuation-dissipation theorem directly related to the conductance and thus encodes the same information about the system as the current. In contrast, at zero temperature and finite bias, shot noise arises due to quantum partitioning

at the scattering potential. Shot noise is a direct consequence of the quantized transport of charge and reveals the effective charge quantum involved in the process, which can deviate from the elementary charge in interacting or correlated systems [37–39]. In addition, the suppression of shot noise (Fano factor) relative to the Poissonian value provides insight into the distribution of transmission channels. Therefore, shot noise measurements complement conductance measurements by providing additional physical insight. A more detailed discussion of thermal and partition noise is presented in Chapter II.

Bosonic Landauer-Büttiker theory.— Quantum transport of bosonic particles can be described within the Landauer-Büttiker scattering approach, with appropriate modifications. Bosonic particles obey symmetric exchange statistics, in contrast to fermions. As a result, their creation, annihilation, and field operators satisfy analogous relations (compare to Eq. (I.3.9c)), with commutators replacing anticommutators. The expectation values of bosonic creation and annihilation operators are governed by the Bose-Einstein distribution,

$$n_\alpha(E) = [\exp[E/(k_\mathrm{B}T_\alpha)] - 1]^{-1}, \tag{I.3.19}$$

rather than the Fermi-Dirac distribution, reflecting the fact that multiple bosons can occupy the same quantum state. The particle current can be calculated analogously to Eq. (I.3.11), with the bosonic dispersion relation now determining the momentum and group velocity. In the general case, we cannot make the usual approximation that the relevant energies lie near the Fermi energy, which would justify neglecting the energy dependence of the momentum and group velocity. However, if the dispersion relation is linear, the particle current operator takes the form $\hat{J}_\alpha(t) = \hat{I}_\alpha(t)/e$, where $\hat{I}_\alpha(t)$ is the electric current in Eq. (I.3.12). Therefore, the average bosonic particle current and noise share the same structure as the electric current (I.3.15) and noise spectrum (I.3.18), with Bose-Einstein distributions replacing the Fermi-Dirac distributions. In this thesis, we derive the energy current operator in the context of near-field radiative heat transfer. The energy current (III.6.7a) has a structure similar to the electric current (I.3.12), with the reservoir impedance playing a role analogous to the longitudinal electron momentum. The key difference is that a frequency-dependent impedance is generally complex-valued, whereas the momentum is real. For thermal reservoirs with frequency-independent (i.e., purely resistive) impedance, the energy current operator closely resembles the electric current operator. In this case, the scattering theory of near-field radiative heat transfer reduces to a Landauer-Büttiker description.

Chapter II

Delta-T Noise

Thermal fluctuations are unavoidable in practice, since no experiment can achieve exactly zero kelvin, but they can be sufficiently suppressed in the limit of vanishing temperature. Electrical noise in a resistor at thermal equilibrium was first observed by Johnson [67], and later theoretically described by Nyquist [68]. Johnson–Nyquist noise or thermal noise originates from the thermal agitation of charge carriers within the resistor. In a mesoscopic conductor, thermal noise arises because the states incident on the scattering region are not perfectly occupied; instead, their occupation number fluctuates [15]. The occupation becomes noiseless only at zero temperature, as the fluctuations are proportional to $f(E)(1-f(E))$, which vanishes when the Fermi function $f(E)$ becomes a step function. The noise at a tunnel junction can be used for primary thermometry [69]. Schottky [35] theoretically investigated current fluctuations in vacuum tubes and identified another fundamental type of noise known as shot noise. The transfer of electrons occurs through rare, stochastic events, meaning that the total transferred charge is governed by a Poissonian distribution. As a result, a white noise spectrum emerges over a broad frequency range, with the noise power being proportional to the current and the elementary charge serving as the proportionality constant. Shot noise also occurs in mesoscopic conductors, where it arises due to the stochastic partitioning of charge carriers at the scattering center. There, shot noise is suppressed below the Poissonian limit. The degree of suppression is described by the Fano factor, which is for energy-independent transmission $F = \sum_n \mathcal{T}_n(1-\mathcal{T}_n)/\sum_n \mathcal{T}_n$ (see Eq. (I.3.18)), where $\mathcal{T}_n$ is the energy-independent transmission probability of eigenchannel n. Hence, determination of the Fano factor yields insight into the properties of the transmission channels [40]. The total noise spectrum (I.3.18) of a mesoscopic conductor includes both thermal and shot noise, each of which dominates in different regimes, although both types are typically present. The thermal noise spectrum takes the form

$$S_{11}^{\mathrm{th}}(\omega) = 2G\hbar\omega \coth\left(\frac{\hbar\omega}{2k_{\mathrm{B}}T}\right), \tag{II.0.1}$$

where $G = \sum_n \mathcal{T}_n e^2/(2\pi\hbar)$ denotes the conductance. The quantity $S_{11}^{\mathrm{th}}(\omega)$ represents the symmetrized current auto-correlation spectrum at terminal 1. The noise in the conductor is purely thermal when no voltage is applied, i.e., the system is in equilibrium. Although thermal fluctuations vanish at zero temper-

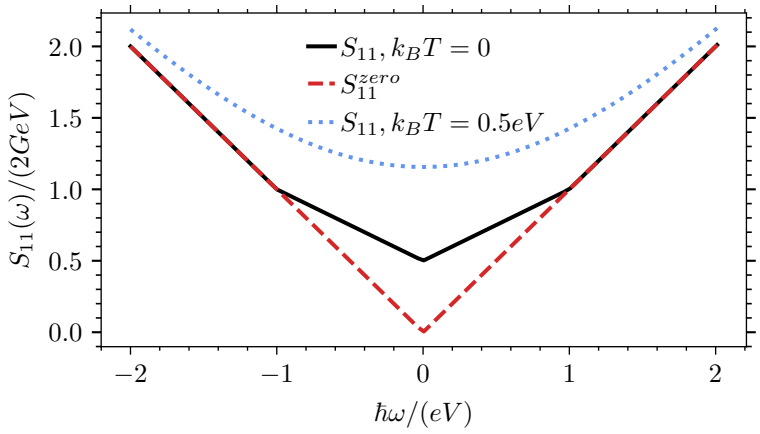

Figure II.1: *Symmetrized current-current noise spectrum* $S_{11}(\omega)$ of a mesoscopic conductor at zero temperature (black, solid) and finite temperature (blue, dotted). The red, dashed curve shows the zero-point contribution. Parameter: Fano factor $F = 1/2$.

ature, the noise spectrum remains finite due to zero-point fluctuations, which yield $S_{11}^{\text{zero}}(\omega) = 2G\hbar|\omega|$. In the opposite regime, where thermal fluctuations are suppressed (zero temperature limit) and a voltage V is applied, the noise reduces to

$$S_{11}(\omega) = 2GF(|eV| - |\hbar\omega|)\Theta(|eV| - \hbar|\omega|) + S_{11}^{\text{zero}}(\omega) \equiv S_{11}^{\text{ex}}(\omega) + S_{11}^{\text{zero}}(\omega) \quad \text{(II.0.2)}$$

At low frequencies, the noise spectrum is dominated by shot noise $S_{11}^{\text{shot}} = 2GFe|V|$, whereas at high frequencies, zero-point fluctuations become the leading contribution. Figure II.1 shows the noise spectrum $S_{11}(\omega)$, decomposed into zero-point fluctuations and excess noise. The excess noise spectrum $S_{11}^{\text{ex}}(\omega)$ represents partition noise, as it vanishes for both perfect transmission ($\mathcal{T}_n = 1$) and perfect reflection ($1 - \mathcal{T}_n = 1$). In this regime, partition noise arises due to the stochastic transmission of charge carriers driven by a voltage drop across the conductor. A temperature gradient across the conductor can also drive transport, a mechanism that remained largely unexplored until recently [70–79]. This raises the question: what are the properties of thermally driven partition noise?

A fundamental nonequilibrium noise arising from a temperature difference ΔT was first demonstrated in atomic-scale junctions by Lumbroso and coworkers [70], and subsequently observed in other mesoscopic platforms [71, 72]. This noise, dubbed delta-T noise, is related to the voltage-driven shot noise and inherits the properties of partition noise [80]. Using the scattering approach, they obtain an approximation of the noise, which is then decomposed into a thermal and a delta-T component. The thermal component corresponds to thermal noise at the average temperature, and the lowest order delta-T component is similar to the quantum shot noise except for different numerical prefactor and scales with $(\Delta T)^2$ instead of the voltage squared. Another study [72] measured and calculated the noise of a voltage-and temperature-biased metallic tunnel junction. This setup operates at a very low temperature and is not restricted to small relative

temperature differences. At the limit, when one terminal is at zero temperature and no voltage is applied, the noise has the form of thermal noise with an additional factor $2\ln 2$ [80].

In a quantum Hall bar furnished with a quantum point contact, the delta-T noise can serve as an instrument to discriminate between electron and quasiparticle tunneling [81, 82]. Tunneling of chiral fractional quantum Hall edge states exhibits a negative delta-T noise, in contrast to a positive contribution in the non-interacting case. A sign inversion, from negative back to positive, may also be forced by changing the transmission of the quantum point contact or applying a voltage. The negative signal is attributed to the scaling dimension of the leading charge tunneling operator [83, 84]. Their results suggest that the negative sign is a property due to many-body interactions. In comparison, a quantum dot in the $SU(2)$ Kondo region has no negative delta-T noise [85], thus the effect does not occur in this case despite the presence of strong correlations. Further, delta-T noise was employed to study experimentally the heat transport of edge modes [86].
An investigation of the relative sizes shows that delta-T noise never exceeds the thermallike noise under the zero-average current condition [31]. In [31] they studied a resonant level as an example for energy-dependent scattering. In the limit of a small resonance width, the size of delta-T noise approaches the thermallike noise. Furthermore, they investigated noise of heat transport, which is not subject to a limit like charge noise. More recently, bounds on the spin and heat current noise were investigated [75].

II.1 Light Emission in Delta-T-Driven Mesoscopic Conductors

At finite frequencies, the noise involves current operators taken at different times. In general, these operators do not commute, so the symmetrized correlator is studied as an observable [15, 42]. A detector that distinguishes between the transfer of an energy quanta $\hbar\omega$ from or to the conductor can access the nonsymmetrized correlator [41, 42]. Indeed, when the fluctuations interact with an electromagnetic field, the energy transfer rate is connected to the nonsymmetrized noise spectrum. Negative frequencies account for the radiated power when one photon is generated in the radiation field and, vice versa, positive frequencies for the absorbed power when one photon is annihilated. In a thermally occupied radiation field, the measured noise power spectrum is a sum of the nonsymmetrized noise spectra at negative and positive frequencies. The prefactors are determined by the Bose-Einstein distribution and, consequently, by the temperature of the electromagnetic field [41, 42].

In this work, we address the nonsymmetrized finite-frequency noise spectrum of a temperature-biased mesoscopic conductor. We are interested in separating the light emission and absorption into a thermallike and delta-T spectrum. Figure II.2 gives an illustrative summary of the considered system and our findings in the case of energy-independent scattering. The mesoscopic conductor is described within the scattering approach, where one terminal assumes a hot temperature and the other a cold temperature. We define the thermallike noise spectrum as the average of the thermal noise spectra at the hot and the cold temperature. Consequently, the delta-T noise spectrum is defined similar to the excess noise spectrum [15, 87, 88]. Two distinct contributions to the delta-T noise are obtained, $S_1^{\Delta T}(\omega)$ comes from the correlations of occupied and free electronic states with different Fermi-Dirac statistics, and $S_2^{\Delta T}(\omega)$ from occupied and free states with the same statistics but associated with a different rate per recombination event than assumed in the thermallike noise. If the scattering is energy-independent or the same from both sides, the latter contribution vanishes. Our main result is that the delta-T noise spectrum can get negative at some frequencies, reducing the thermallike noise spectrum. Below, we investigate the spectra for energy-independent scattering and a single resonant level model. In the resonant case $S_1^{\Delta T}(\omega)$ has a suppressed negative part for the chosen parameters and additionally shows a contribution $S_2^{\Delta T}(\omega)$.

II.1.1 Nonsymmetrized Current Correlations

We consider a mesoscopic two-terminal conductor and model it using the scattering approach [6, 15] discussed in Sec. I.3. Uncorrelated electrons leave the reservoir and transverse through the scattering region, where they are elastically scattered. Interactions between the electrons and charging effects are disregarded. We denote the hot terminal as 1 and the cold one as 2. The Fermi functions $f_\alpha(E) = \{\exp[\beta_\alpha(E-\mu_\alpha)]+1\}^{-1}$ govern the energy distribution of emanating electrons from terminals $\alpha \in \{1,2\}$. The parameters $\beta_1 = 1/k_\mathrm{B}T_h$ and $\beta_2 = 1/k_\mathrm{B}T_c$ are determined by the temperatures T_h and T_c of the hot and cold reservoir, re-

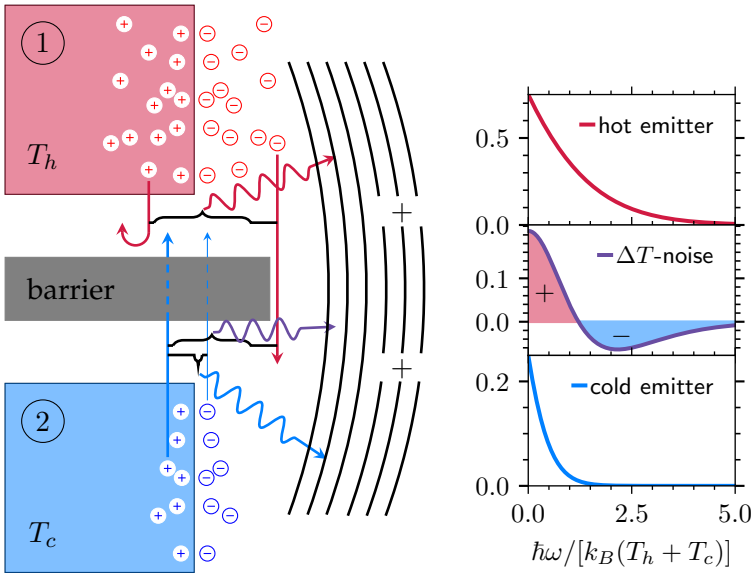

Figure II.2: The mesoscopic conductor consists of a hot reservoir with a temperature T_h and a cold reservoir with a temperature T_c, separated by a potential barrier. In the hot reservoir, more electrons are excited at higher energies, as illustrated by electrons farther away from the surface. The current-current correlator depends on the scattering amplitudes (simplified depicted by the arrows) of electrons (depicted by circles with a minus sign) and holes (depicted by circles with a plus sign) as well as the probability distribution of the terminal from which they originated. Current-current fluctuations are related to the energy transfer rate between the mesoscopic conductor and an electromagnetic field, i.e. to the emission and absorption spectrum. The energy difference $\hbar\omega$ between the electron and the hole corresponds to the energy of the annihilated or excited photon. We separate the spectrum into an equilibrium part (thermallike), a superposition of a hot and cold emitter, and a nonequilibrium part, given by a delta-T noise spectrum. The delta-T noise spectrum is negative at some frequencies, thus diminishing the thermallike noise spectrum. In the shown case, energy-independent scattering is assumed.

spectively. We suppose that there is no applied voltage and set $\mu_1 = \mu_2 = 0$ in the following. The transport is described by the unitary scattering matrix

$$s(E) = \begin{pmatrix} s_{11}(E) & s_{12}(E) \\ s_{21}(E) & s_{22}(E) \end{pmatrix} . \tag{II.1.1}$$

In the submatrix $s_{\alpha\beta}(E)$, the index β indicates where the electrons originated and the left index α where the electrons head to. For a given energy, we assume that a finite number of quantum channels contribute, which determines the size of the submatrices. Overall, the transport properties of the mesoscopic conductor are determined by the scattering matrix and the Fermi distributions of the reservoirs.

The current operator $\hat{I}_\alpha(t)$ describes the electric current in terminal $\alpha \in \{1, 2\}$ at time t [14, 15, 89]. By averaging over the quantum statistical ensemble, the average current $\langle \hat{I}_\alpha(t) \rangle$ is obtained. A positive sign means that the current leaves the reservoir, and vice versa, a negative sign means that it enters. Current fluctuations are characterized by the auto- and cross-correlations of the current operator. We are interested in the nonsymmetrized correlator

$$S_{\alpha\beta}(t, t') = \langle \Delta\hat{I}_\alpha(t) \Delta\hat{I}_\beta(t') \rangle \, , \Delta\hat{I}_\alpha(t) \equiv \hat{I}_\alpha(t) - \langle \hat{I}_\alpha(t) \rangle. \tag{II.1.2}$$

In the absence of a time-dependent external field, the correlations depend only on the time difference $t - t'$. As a result, the Fourier transform of the current correlations yields $S_{\alpha\beta}(\omega, \omega') = 2\pi\delta(\omega + \omega')S_{\alpha\beta}(\omega)$, with

$$S_{\alpha\beta}(\omega) = 2 \int_{-\infty}^{\infty} e^{i\omega t} \langle \Delta\hat{I}_\alpha(t) \Delta\hat{I}_\beta(0) \rangle dt \tag{II.1.3}$$

as the noise spectrum. At different times, the current operators do not commute. This results in an asymmetrical noise spectrum. For $\alpha = 1$, $\beta = 2$, the noise spectrum has the form

$$\begin{aligned} S_{12}(\omega) = \frac{e^2}{\pi\hbar} \int_{-\infty}^{\infty} dE \\ \times \Big[& f_1(E)[1 - f_1(E + \hbar\omega)] \operatorname{Tr} \Big(s_{21}^\dagger(E + \hbar\omega) s_{21}(E) (s_{11}^\dagger(E) s_{11}(E + \hbar\omega) - \mathbb{1}) \Big) \\ & + f_1(E)[1 - f_2(E + \hbar\omega)] \operatorname{Tr} \Big(s_{11}^\dagger(E) s_{12}(E + \hbar\omega) s_{22}^\dagger(E + \hbar\omega) s_{21}(E) \Big) \\ & + f_2(E)[1 - f_1(E + \hbar\omega)] \operatorname{Tr} \Big(s_{12}^\dagger(E) s_{11}(E + \hbar\omega) s_{21}^\dagger(E + \hbar\omega) s_{22}(E) \Big) \\ & + f_2(E)[1 - f_2(E + \hbar\omega)] \operatorname{Tr} \Big(s_{12}^\dagger(E) s_{12}(E + \hbar\omega) (s_{22}^\dagger(E + \hbar\omega) s_{22}(E) - \mathbb{1}) \Big) \Big], \end{aligned} \tag{II.1.4}$$

with e the elementary charge, $\hbar$ the reduced Planck constant, $\dagger$ the conjugate transpose, $\operatorname{Tr}(\cdot)$ the trace over the quantum channels and spin, and $1 - f_\alpha(E)$ the distribution of an unoccupied electronic state (hole). In general, $s^\dagger(E)s(E') \neq 1$

for $E \neq E'$ and thus the noise spectrum can be complex.

We focus on the total current $\hat{I}(t) = [\hat{I}_1(t) - \hat{I}_2(t)]/2$ and investigate the total noise spectrum for this symmetric choice of the currents [90–92]

$$S(\omega) \equiv 2\int_{-\infty}^{\infty} dt e^{i\omega t}\langle \Delta\hat{I}(t)\Delta\hat{I}(0)\rangle = \sum_{\alpha,\beta}\int_{-\infty}^{\infty} dE\, \gamma_{\alpha\beta}(E,\omega) f_\alpha(E)[1 - f_\beta(E+\hbar\omega)], \tag{II.1.5}$$

with

$$\gamma_{\alpha\beta}(E,\omega) = \frac{e^2}{4\pi\hbar}\,\mathrm{Tr}\left(A_{\alpha\beta}(E,\omega)A^\dagger_{\alpha\beta}(E,\omega)\right) \tag{II.1.6}$$

and the matrices

$$\begin{aligned}
A_{11} =& s^\dagger_{21}(E+\hbar\omega)s_{21}(E) + \mathbb{1} - s^\dagger_{11}(E+\hbar\omega)s_{11}(E)\\
A_{22} =& s^\dagger_{12}(E+\hbar\omega)s_{12}(E) + \mathbb{1} - s^\dagger_{22}(E+\hbar\omega)s_{22}(E)\\
A_{12} =& s^\dagger_{21}(E)s_{22}(E+\hbar\omega) - s^\dagger_{11}(E)s_{12}(E+\hbar\omega)\\
A_{21} =& s^\dagger_{22}(E)s_{21}(E+\hbar\omega) - s^\dagger_{12}(E)s_{11}(E+\hbar\omega).
\end{aligned} \tag{II.1.7}$$

Further on, the term total noise spectral density is abbreviated as noise spectrum. The form Eq. (II.1.5) directly implies that the noise spectrum is positive, since for a complex matrix A, the matrix $A^\dagger A$ has only positive eigenvalues and thus a positive trace $\mathrm{Tr}(A^\dagger A) \geq 0$. With the same argument and the monotonic decrease of the Fermi functions, the inequality

$$S(\omega) \geq S(-\omega) \quad \text{for} \quad \omega \geq 0 \tag{II.1.8}$$

follows. This result holds irrespective of the applied voltage or temperature difference. In the next paragraph, we introduce the connection to light emission and absorption, where the inequality has an illustrative interpretation.

The mesoscopic conductor can act as an antenna, where the current fluctuations couple to an electromagnetic field [41, 42, 93]. We assume a linear coupling between the total current operator $\hat{I}(t)$ and the electromagnetic vector potential operator. Fermi's golden rule gives the transition rates for absorption and emission of a photon and thus the rate at which energy is transferred [94]. To establish a connection, we consider the rewritten noise spectrum

$$S(\omega) = 2\pi\sum_{i,f} p_i |\langle i|\,\Delta\hat{I}(0)\,|f\rangle|^2 \delta(E_i - E_f + \hbar\omega), \tag{II.1.9}$$

where p_i is the statistical weight along with E_i the energy of the initial state $|i\rangle$, and E_f the energy of the state $|f\rangle$. The energy transfer rate when emitting one photon from the conductor is proportional to the noise spectrum for $\omega < 0$ and vice versa, when absorbing one photon to the noise spectrum for $\omega > 0$. Therefore, the noise spectrum at negative frequencies is referred to as the emission

spectrum and that of positive frequencies as the absorption spectrum. Utilizing $\Delta\hat{I}(0)$ instead of $\hat{I}(0)$ in expression (II.1.9) differs by a DC component, which contributes nothing to the energy transfer. The inequality (II.1.8) now states that the energy transfer rate at which the conductor absorbs from the electromagnetic field is always greater than or equal to the rate at which it transfers energy to the field.

We follow the interpretation in [95]. The physical processes involve electrons with energy E and holes with energy $E + \hbar\omega$ which are scattered in the mesoscopic conductor and afterwards recombine to emit or absorb energy $\hbar\omega$. When electrons come from terminal α and holes from terminal β, then they contribute $\gamma_{\alpha\beta}(E,\omega)f_\alpha(E)[1 - f_\beta(E + \hbar\omega)]$ to the differential energy transfer rate

$$dS(E,\omega) = \sum_{\alpha,\beta\in\{1,2\}} \gamma_{\alpha\beta}(E,\omega)f_\alpha(E)[1 - f_\beta(E + \hbar\omega)]dE. \tag{II.1.10}$$

On average, there are $f_\alpha(E)$ electrons and $1 - f_\beta(E + \hbar\omega)$ holes participating in $f_\alpha(E)[1 - f_\beta(E + \hbar\omega)]$ recombination events. This is evident by rewriting $f_\alpha(E)[1 - f_\beta(E + \hbar\omega)] = \langle\hat{n}^e_\alpha(E)\hat{n}^h_\beta(E + \hbar\omega)\rangle$ as the expectation value of the electron number operator $\hat{n}^e_\alpha(E)$ and the hole number operator $\hat{n}^h_\beta(E)$. The functions $\gamma_{\alpha\beta}$ correspond to the rates per recombination event. They depend solely on the scattering amplitudes of the electrons and holes traversing the conductor.

Delta-T noise spectrum.— In the tradition of analyzing noise, two distinct contributions of different origins were identified [15, 35, 67, 68]. One is the equilibrium noise (Nyquist-Johnson noise) at thermal equilibrium, attributed to the thermal agitation of the charge carriers, and the other is the nonequilibrium partition noise (shot noise), which arises because an incident charge carrier beam is stochastically divided. Hence, it is a consequence of charge quantization. In the next paragraph, we are concerned with the question how can the noise spectrum be partitioned into an equilibrium (thermallike) and a nonequilibrium (delta-T) component in the presence of a temperature difference.

In the case of zero frequency and an energy-independent scattering matrix, the thermallike noise is given by

$$S^{th}(\omega = 0) = S^{th} = 2Gk_\mathrm{B}T_h + 2Gk_\mathrm{B}T_c, \tag{II.1.11}$$

with $G = G_0\sum_n \mathcal{T}_n$ the conductance, the conductance quantum $G_0 = 2e^2/h$, and $\mathcal{T}_n$ the transmission probability of the n-th eigenchannel [15]. Half of the thermallike noise consists of the Nyquist-Johnson noise at the hot temperature and half at the cold temperature. We interpret that as the thermal agitation of two isolated equilibrium systems and understand the thermallike noise as the average $S^{th} = (S_{T_h} + S_{T_c})/2$ of them, with S_{T_α} the noise at zero frequency and equal temperature T_α in both reservoirs. Following this interpretation, the thermallike noise for finite frequencies is defined as

$$S^{th}(\omega) \equiv \frac{S_{T_h}(\omega) + S_{T_c}(\omega)}{2}, \tag{II.1.12}$$

where $S_{T_\alpha}(\omega)$ is the noise spectrum at equal reservoir temperature T_α. From the standpoint of light emission, the thermallike spectrum manifests as the superposition of independent hot and cold emitters. In [85] an equivalent definition is used to account for the thermallike part in a system with interacting electrons. After some calculation and using the unitary property of the scattering matrix, the thermallike noise can be written as

$$S^{th}(\omega) = \int_{-\infty}^{\infty} dE\, \gamma^{th}(E,\omega) \sum_{\alpha\in\{1,2\}} \frac{f_\alpha(E)[1-f_\alpha(E+\hbar\omega)]}{2}, \tag{II.1.13}$$

with

$$\begin{aligned}\gamma^{th}(E,\omega) =& \gamma_{11}(E,\omega)+\gamma_{12}(E,\omega)+\gamma_{21}(E,\omega)+\gamma_{22}(E,\omega)\\ =& \frac{e^2}{4\pi\hbar}\,\mathrm{Tr}\Big[|s_{11}(E)-s_{11}(E+\hbar\omega)|^2+|s_{22}(E)-s_{22}(E+\hbar\omega)|^2+|s_{12}(E)\\ &+s_{12}(E+\hbar\omega)|^2+|s_{21}(E)+s_{21}(E+\hbar\omega)|^2\Big],\end{aligned} \tag{II.1.14}$$

where $|a|^2 = a^\dagger a$ is implied in the multi-channel case. At zero frequency, the expression coincides with the thermallike noise defined in [31] and reduces to

$$S^{th} = \frac{2e^2}{\pi\hbar}\int_{-\infty}^{\infty} dE \sum_n \mathcal{T}_n(E) \sum_{\alpha=1,2} f_\alpha(E)[1-f_\alpha(E)], \tag{II.1.15}$$

with $\mathcal{T}_n(E)$ the energy-dependent transmission probability.

Equipped with the definition of the thermallike noise, the nonequilibrium contribution is identified as the excess noise spectrum $S^{\Delta T}(\omega) \equiv S(\omega) - S^{th}(\omega)$. This nonequilibrium noise spectrum is referred to as delta-T noise spectrum. We interpret the delta-T noise spectrum by using the picture of recombining electrons and holes. Electrons are denoted as hot or cold if they are distributed according to the Fermi function $f_1 = \langle \hat{n}_1^e \rangle$ with temperature T_h or according to the Fermi function $f_2 = \langle \hat{n}_2^e \rangle$ with temperature T_c, respectively. This designation also applies to holes. The same rates $\gamma_{\alpha\beta}$ are present in the entire noise spectrum (II.1.5) and the thermallike spectrum (II.1.13). The difference manifests itself in the number of recombination events. For example, the actual noise spectrum includes the contribution $\gamma_{12}\langle \hat{n}_1^e \hat{n}_2^h \rangle$, where hot electrons recombine with cold holes. The corresponding term $\gamma_{12}\langle (\hat{n}_1^e \hat{n}_1^h + \hat{n}_2^e \hat{n}_2^h)/2 \rangle$ in the thermallike noise spectrum involves only recombination events of hot electrons with hot holes and cold electrons with cold holes. This is accounted for by a factor $\gamma_{12}\langle (\hat{n}_1^e(\hat{n}_2^h - \hat{n}_1^h) + (\hat{n}_1^e - \hat{n}_2^e)\hat{n}_2^h)/2 \rangle$ in the delta-T noise spectrum, which depends on the excess amount of cold and hot holes $\langle \hat{n}_2^h - \hat{n}_1^h \rangle$ and the excess number of hot and cold electrons $\langle \hat{n}_1^e - \hat{n}_2^e \rangle$. Another example is the noise contribution $\gamma_{11}\langle \hat{n}_1^e \hat{n}_1^h \rangle$, which has the counterpart $\gamma_{11}\langle (\hat{n}_1^e \hat{n}_1^h + \hat{n}_2^e \hat{n}_2^h)/2 \rangle$ in the thermallike noise spectrum. The delta-T contribution assumes the form $\gamma_{11}\langle (\hat{n}_1^e \hat{n}_1^h - \hat{n}_2^e \hat{n}_2^h)/2 \rangle$ and depends on the difference between hot and cold recombination events.

We distinguish between these two cases and split the delta-T noise spectrum into

$$\begin{aligned} S^{\Delta T}(\omega) \equiv& S_1^{\Delta T}(\omega) + S_2^{\Delta T}(\omega) \\ =& \int_{-\infty}^{\infty} dE \sum_{\alpha\neq\beta\in\{1,2\}} \gamma_{\alpha\beta}(E,\omega) F_{\alpha\beta}(E,\omega) \\ &+ \int_{-\infty}^{\infty} dE \left(\gamma_{11}(E,\omega) - \gamma_{22}(E,\omega)\right) F(E,\omega) \end{aligned} \tag{II.1.16}$$

with functions

$$\begin{aligned} \Delta f_{\alpha\beta}(E) =& f_\alpha(E) - f_\beta(E) \\ F_{\alpha\beta}(E,\omega) =& \frac{f_\alpha(E)\Delta f_{\alpha\beta}(E+\hbar\omega) + \Delta f_{\alpha\beta}(E)[1-f_\beta(E+\hbar\omega)]}{2} \\ F(E,\omega) =& \frac{f_1(E)[1-f_1(E+\hbar\omega)] - f_2(E)[1-f_2(E+\hbar\omega)]}{2}. \end{aligned} \tag{II.1.17}$$

The unitary property of the scattering matrix guarantees the symmetry $\mathrm{Tr}\, A_{12} A_{12}^\dagger = \mathrm{Tr}\, A_{21} A_{21}^\dagger$. Moreover, $F_{12}(E,\omega) + F_{21}(E,\omega)$ reduces to $\Delta f_{12}(E)\Delta f_{12}(E+\hbar\omega)$ and the first contribution is given by

$$S_1^{\Delta T}(\omega) = \int_{-\infty}^{\infty} dE\, \gamma_{12}(E,\omega)\Delta f_{12}(E)\Delta f_{12}(E+\hbar\omega). \tag{II.1.18}$$

This contribution stems from recombinations of electrons and holes with different temperatures, e.g., hot electrons with cold holes. It depends only on the excess number of electrons $\langle \hat{n}_1^e - \hat{n}_2^e \rangle$ and holes $\langle \hat{n}_2^h - \hat{n}_1^h \rangle$. In the lowest order, the difference $\Delta f_{12}(E)$ is linear in ΔT and therefore the whole term is quadratic.
The thermallike noise spectrum (II.1.13) includes recombination events of hot electrons with hot holes with a rate γ_{22}. In contrast to the spectrum (II.1.5), where this rate is associated with cold electrons recombining with cold holes. A similar situation arises for the rate γ_{11}, where the thermallike spectrum contains cold recombination events and the actual spectrum contains hot recombination events. These cases are covered by the second contribution $S_2^{\Delta T}(\omega)$. This contribution does not depend on the difference between the Fermi functions but rather on the difference between the number of hot and cold recombination events $\langle \hat{n}_1^e \hat{n}_1^h - \hat{n}_2^e \hat{n}_2^h \rangle$. An expansion in ΔT results in a linear dependence at the lowest order. For the part that depends on the scattering matrix, we find

$$\begin{aligned} \mathrm{Tr}\left[A_{11}A_{11}^\dagger - A_{22}A_{22}^\dagger\right] =& 2\,\mathrm{Re}\,\mathrm{Tr}\Big[s_{22}(E)s_{22}^\dagger(E+\hbar\omega) + s_{21}(E)s_{21}^\dagger(E+\hbar\omega) \\ &- s_{11}(E)s_{11}^\dagger(E+\hbar\omega) - s_{12}(E)s_{12}^\dagger(E+\hbar\omega)\Big], \end{aligned} \tag{II.1.19}$$

with Re denoting the real part. At zero frequency, this expression disappears because of the unitary property of the scattering matrix. The entire spectrum $S_2^{\Delta T}(\omega)$ vanishes in two ways: first, when the scattering properties from both sides are indistinguishable, i.e., $s_{11}(E) = s_{22}(E), s_{12}(E) = s_{21}(E)$, or second, the

reservoirs assume the same temperature.
At zero frequency, the delta-T noise decreases to

$$S^{\Delta T} = \frac{2e^2}{\pi\hbar}\int_{-\infty}^{\infty} dE \sum_n \mathcal{T}_n(E)[1-\mathcal{T}_n(E)][\Delta f_{12}(E)]^2 \tag{II.1.20}$$

and matches with the definition given in [31].

II.1.2 Energy-Independent Scattering

The model is specified further by assuming an energy-independent scattering matrix $s(E) \approx s$. From the well-known equilibrium spectrum [15, 42], we obtain

$$S^{th}(\omega) = G\hbar\omega\left[2 + \coth\left(\frac{\hbar\omega}{2k_B T_h}\right) + \coth\left(\frac{\hbar\omega}{2k_B T_c}\right)\right]. \tag{II.1.21}$$

The thermal spectra $S_{T_h}(\omega), S_{T_c}(\omega)$ are not additive, i.e., $S_{T_h}(\omega)+S_{T_c}(\omega)$ cannot be written as a thermal noise spectrum with adjusted temperature. A consequence of this is that at a fixed average temperature $\tilde{T} = (T_h + T_c)/2$, the thermallike spectrum still changes for different temperature differences $\Delta T = T_h - T_c$. Nevertheless, for convenience, the average temperature and the temperature difference are used hereafter.

The difference between the absorption and emission spectrum obeys $S^{th}(\omega) - S^{th}(-\omega) = 4G\hbar\omega, \omega > 0$. It is sufficient to investigate the emission spectrum since emission and absorption differ only by the zero-point fluctuations. Figure II.3(a) depicts the thermallike spectrum for various ΔT. The curves vary continuously from $\Delta T = 0$ to the maximum $\Delta T = 2\tilde{T}$, where the curve for $\Delta T = 0$ sets a lower bound and for $\Delta T = 2\tilde{T}$ an upper bound.

The examination of the delta-T noise spectrum reveals that $S_2^{\Delta T}(\omega)$ vanishes for energy-independent scattering, and the delta-T component reduces considerably to

$$S^{\Delta T}(\omega) = 2GF\int_{-\infty}^{\infty} dE \Delta f_{12}(E)\Delta f_{12}(E+\hbar\omega), \tag{II.1.22}$$

where $F = \sum_n \mathcal{T}_n(1-\mathcal{T}_n)/\sum_n \mathcal{T}_n$ represents the Fano factor. The Fano factor indicates for the property of a partition noise and is a shared property with the shot noise at zero frequency [15]. If the barrier is completely transparent or reflective, $\mathcal{T}_n = 1$ or $\mathcal{T}_n = 0, \forall n$, then the Fano factor vanishes and so does the delta-T noise spectrum, although a temperature difference might be present. The system consists then of isolated hot and cold electron transport, each in thermal equilibrium, which is why we call the term thermallike.
At the maximal temperature difference $\Delta T = 2\tilde{T}$, it is given as

$$\frac{S^{2\tilde{T}}(\omega)}{GF} = 8k_B\tilde{T}\ln\left[2\cosh\left(\frac{\hbar\omega}{4k_B\tilde{T}}\right)\right] - |\hbar\omega| - \hbar\omega\coth\left(\frac{\hbar\omega}{4k_B\tilde{T}}\right). \tag{II.1.23}$$

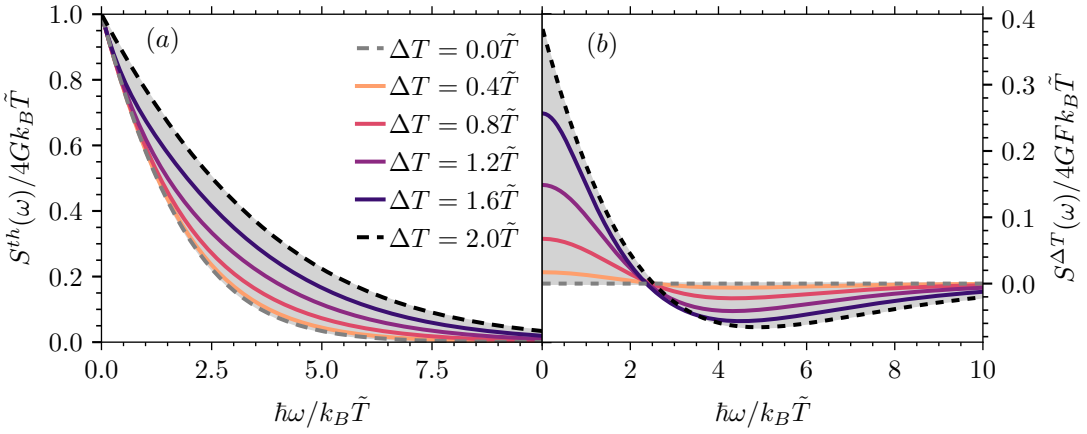

Figure II.3: *Emission spectra* of (a) the thermallike noise (II.1.21) and (b) the delta-T noise (II.1.22) from $\Delta T = 0$ to $2\tilde{T} = T_h + T_c$. The absorption spectrum of (a) results from $S^{th}(\omega) - S^{th}(-\omega) = 4G\hbar\omega$ and of (b) equals the emission spectrum, because of $S^{\Delta T}(\omega) = S^{\Delta T}(-\omega)$. The thermallike spectrum depends on the temperature difference ΔT and all curves lie between the extreme points $\Delta T = 0$ and $\Delta T = 2\tilde{T}$ in the grey area. The delta-T noise changes its sign from positive to negative at a certain frequency (compare to Fig. II.4), which depends on the temperature difference. The curves are not enveloped by the extreme points. The overall noise $S^{th} + S^{\Delta T} \geq 0$ does not change its sign.

In the limit $\omega \to 0$, we get back the factor $2\ln 2$ as in [72]. The delta-T emission and absorption spectrum for different ΔT is shown in Fig. II.3(b). The delta-T noise spectrum starts at a maximum, then decreases and intersects the ω-axis at a certain point. After that, the course reaches a minimum and converges back to zero. Above a certain point, the delta-T noise spectrum is negative and decreases the thermallike noise. Negative delta-T noise (at zero frequency) has been reported for transport in a fractional quantum Hall bar [81]. The decrease in fluctuations is there attributed to interactions and related to the tunneling of quasiparticles. In our case, interactions are not considered by the model. The combination of temperature broadening of the Fermi function and the frequency shift between distributions of the occupied and free states plays the crucial role here. A comparison between the cold and hot distribution shows (see for an example Fig. II.4(b)), that the hot reservoir has fewer occupied states for $E < 0$, more for $E > 0$ and coincides for $E = 0$. This leads to a negative sign of $f_1(E) - f_2(E)$ for $E < 0$ and a positive sign for $E > 0$. The integrand $(f_1(E) - f_2(E))(f_1(E + \hbar\omega) - f_2(E + \hbar\omega))$, i.e., the excess number of recombination events, has a negative sign in the interval $E \in (-\hbar\omega, 0)$. In the complement interval, the signs are equal and the integrand is positive. The delta-T noise spectrum turns negative when the area under the negative part of the integrand exceeds the area under the positive part. Figure II.4(a) depicts the excess number of recombination events for different shifts in the extreme case $T_c = 0$ and $T_h = 2\tilde{T}$.

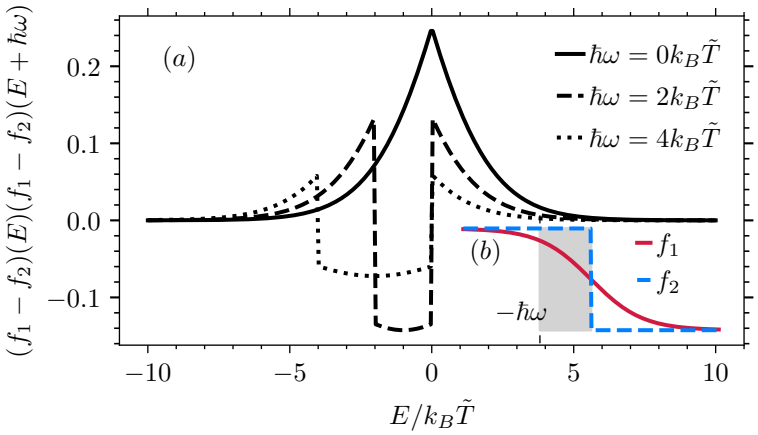

Figure II.4: Illustration (a) shows the *excess number of recombination events* due to recombinations between hot and cold particles, i.e., the integrand in (II.1.22). At a given frequency (here e.g., $\hbar\omega = 0, 2, 4k_B\tilde{T}$), one of the differences Δf_{12} is shifted by $\hbar\omega$ in relation to the other. In the interval $(-\hbar\omega, 0)$, the contribution is negative and outside it is positive. Inset (b) depicts the hot and cold Fermi functions drawn over energy. The gray-shaded area denotes energies where the sign of $f_1(E) - f_2(E)$ and the shifted $f_1(E + \hbar\omega) - f_2(E + \hbar\omega)$ differ. The terminals are assumed to be at temperatures $T_c = 0, T_h = 2\tilde{T}$.

II.1.3 Resonant Level

This paragraph sheds light on the influence of energy-dependent scattering, using a resonant level as an example. We assume a resonance energy of ϵ_0 and a lifetime of $\hbar/\Gamma$. For simplicity, we only consider one open quantum channel. The scattering matrix can be modeled by the Breit-Wigner formula [89, 96]

$$s_{\alpha\beta}(E) = \delta_{\alpha\beta} - \frac{i\sqrt{\Gamma_\alpha\Gamma_\beta}}{E - \epsilon_0 + i\Gamma/2},\ \alpha, \beta \in \{1, 2\} \tag{II.1.24}$$

where Γ_1, Γ_2 are the partial widths, $\Gamma = \Gamma_1 + \Gamma_2$ the total width, and $\delta_{\alpha\beta}$ the Kronecker delta. Inserting this scattering matrix into the thermallike noise spectrum (II.1.13) results in

$$\begin{aligned} S^{th}(\omega) =& \frac{G_0}{4}\int_{-\infty}^{\infty} dE \sum_{\alpha=1,2} f_\alpha(E)[1 - f_\alpha(E + \hbar\omega)]\mathcal{T}(E + \hbar\omega) \\ &\times \mathcal{T}(E)\left[\frac{(\hbar\omega)^2}{\Gamma_1^2} + \frac{(\hbar\omega)^2}{\Gamma_2^2} + 8\frac{(E + \frac{\hbar\omega}{2} - \epsilon_0)^2 + \frac{\Gamma^2}{4}}{\Gamma_1\Gamma_2}\right], \end{aligned} \tag{II.1.25}$$

where

$$\mathcal{T}(E) = \frac{\Gamma_1\Gamma_2}{(E - \epsilon_0)^2 + \Gamma^2/4} \tag{II.1.26}$$

represents the transmission probability through the resonance. Figure II.5 depicts the deviation of thermallike spectrum from the thermal spectrum at average tem-

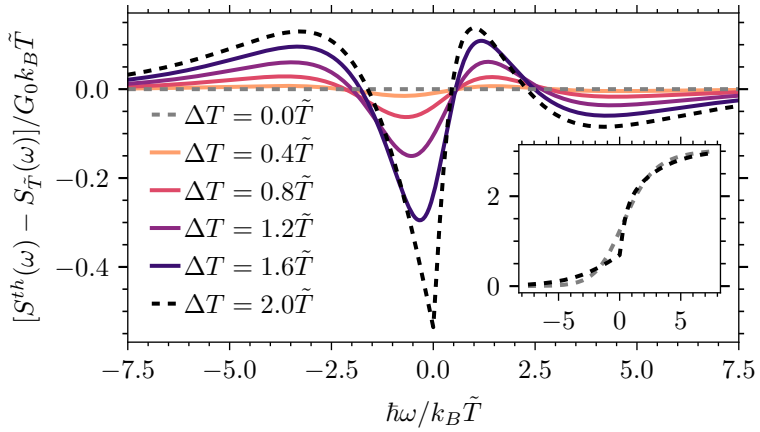

Figure II.5: *The deviation of the thermallike noise spectrum* (II.1.25) from the thermal spectrum at average temperature $S_{\tilde{T}}(\omega)$ is shown for various temperature differences. In the inset, we depict the thermallike noise spectrum at the extremes $\Delta T = 0$, $\Delta T = 2\tilde{T}$ in order to give an idea of its shape and size. The inset uses the same units as the main figure. The resonant level is located at $\epsilon_0 = 0$, i.e., at the terminal's chemical potential, and has the widths $\Gamma_1 = (2/3)k_B\tilde{T}$, $\Gamma_2 = (1/3)k_B\tilde{T}$.

perature. We fix the average temperature and consider different temperature differences for an asymmetric resonance $\Gamma_1 = (2/3)k_B\tilde{T}, \Gamma_2 = (1/3)k_B\tilde{T}$. The curves for $\Delta T \neq 0$ intersect with the curve for $\Delta T = 0$ at three points and have a smaller value in two intervals.

The resonance provides an example where both contributions in the delta-T noise spectrum are relevant. We write the first contribution in the form

$$S_1^{\Delta T}(\omega) = 2G_0 \int_{-\infty}^{\infty} dE \Delta f_{12}(E) \Delta f_{12}(E+\hbar\omega) \mathcal{T}(E) \mathcal{T}(E+\hbar\omega) \times \left[\frac{(E + \frac{\hbar\omega}{2} - \epsilon_0)^2 + \Gamma^2/4}{\Gamma_1 \Gamma_2} - 1 \right]. \tag{II.1.27}$$

Figure II.6 depicts this contribution for several temperature differences. In the integral (II.1.27), the Fermi distributions enter in the same way as for the energy-independent scattering. Temperature broadening in connection with the frequency shift leads again to a negative integrand in the interval $(-\hbar\omega, 0)$. The difference is that the resonance introduces an additional weight, which emphasizes, for the chosen parameters, the positive areas of Fig. II.4(a) and leads to a suppression of the negative contribution.

If the resonance is asymmetric $\Gamma_1 \neq \Gamma_2$, then we obtain a nonvanishing second component

$$S_2^{\Delta T}(\omega) = \frac{G_0}{4} (\hbar\omega)^2 \frac{\Gamma_1^2 - \Gamma_2^2}{\Gamma_1^2 \Gamma_2^2} \int_{-\infty}^{\infty} dE \mathcal{T}(E) \mathcal{T}(E+\hbar\omega) F(E, \omega), \tag{II.1.28}$$

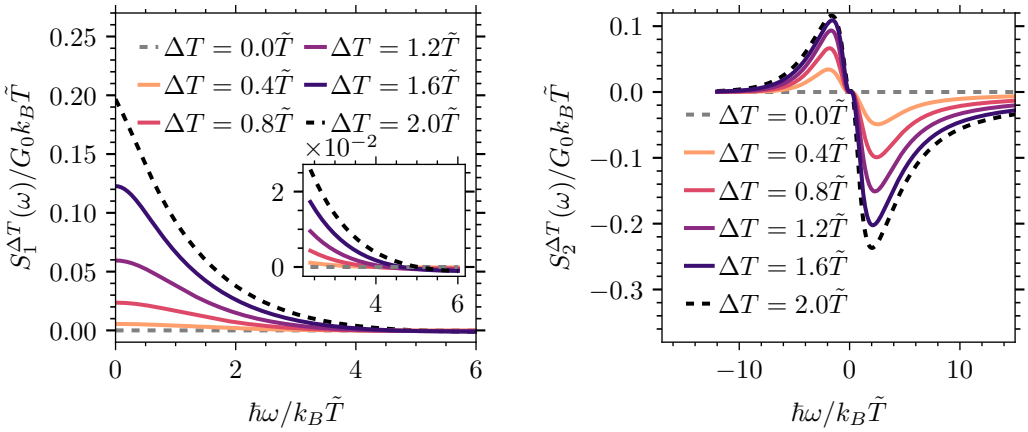

Figure II.6: Left: *Spectra of the contribution* (II.6) at different ΔT. Emission and absorption spectra are identical because this delta-T contribution is symmetric in frequency. The inset shows the spectra at the transition from positive to negative. This negative part is almost suppressed but still present. Right: *Spectra of the second component* (II.1.28) at different temperature differences ΔT. In the emission spectrum, we see an enhancement, and in the absorption spectrum, a reduction. The resonance is assumed to be at $\epsilon_0 = 0$ and has the widths $\Gamma_1 = (2/3)k_B\tilde{T}$, $\Gamma_2 = (1/3)k_B\tilde{T}$.

which is not symmetric in frequency. As a consequence, the emission spectrum differs from the absorption spectrum. The spectrum exhibits a peak at negative frequencies and thus an enhancement in the emission. For positive frequencies, a dip occurs, which results in a reduction of the absorption. It is the other way round if $\Gamma_1 < \Gamma_2$ is used instead of $\Gamma_2 < \Gamma_1$. First and second component are of similar size. In Figure II.6, the second component $S_2^{\Delta T}(\omega)$ is shown for different temperature differences.

II.1.4 Conclusion

We have investigated the nonsymmetrized noise spectral density in mesoscopic conductors subjected to a temperature difference. The thermallike spectrum was identified as the average thermal noise spectrum $(S_{T_h}(\omega) + S_{T_c}(\omega))/2$ and, consequently, the delta-T noise spectrum as the excess spectrum. We further decomposed the delta-T noise spectrum into two contributions, one depending on the frequency-shifted differences of Fermi functions and the other on the difference of the combined Fermi functions. In the case of energy-independent scattering, only the first contribution survived, and the spectrum was proportional to the Fano factor. We have discovered a partially negative delta-T noise spectrum that is positive at low frequencies and becomes negative above a certain frequency. A similar behavior, but with a suppressed negative part, was obtained for a resonant level with the selected parameters. In addition, the second component occurred for an asymmetric resonance.

Chapter III

Near-Field Radiative Heat Transfer

Heat transfer relies on the transport of energy by particles or fields. Basic mechanism are convection, heat conduction or radiation. All these mechanisms can be driven by a temperature difference, resulting in heat flow from a hotter to a colder region, as dictated by the second law of thermodynamics. Convection occurs in fluids or gases, where parts of the material are transferred in bulk, leading to relocation of energy [97]. Heat conduction arises between contacted materials from the diffusive motion of microscopic particles [98], e.g., by the transport of electrons in a metal. Radiative heat transfer is mediated by the electromagnetic field and can bridge vacuum gaps [99], e.g., energy transfer between the sun and the earth (see Fig. III.1) [100]. The fundamental principle of radiative heat transfer is that all bodies at finite temperature emit radiation due to thermal agitation of their charged constituencies. Planck's law describes the radiative emission of a black body, resulting in a broadband spectral density that depends solely on temperature, as illustrated in Fig. III.1 by comparing Planck's law with the measured solar spectrum. A black body corresponds to an idealized object that perfectly absorbs incident radiation of all frequencies and angles. Thermal motion of charged particles lead to a fluctuating charge density and current density, which serve as the sources of the electromagnetic field. The electromagnetic field travels to other bodies and get absorbed there, hence enhancing their internal energy. If two bodies are at the same temperature, the radiative flux in both directions is equal, resulting in no net energy transfer. Energy flux fluctuations are still present and can contain additional information about the system.

Radiative heat transfer can be divided into a near-field and far-field regime, as illustrated in Fig. III.2. In the near-field, heat transfer can significantly exceed the contribution expected from Planck's law [101, 102]. There, diffraction, interference effects, and evanescent waves contribute to heat transport, whereas Planck's law was derived based on ray optics. An evanescent wave travels along the material's surface whilst decaying exponentially in the perpendicular direction. The decay length is often set by the thermal wavelength $\lambda_{th} = 2\pi\hbar c/(k_{\mathrm{B}}T)$, with T the temperature of the emitting body, and c the speed of light. In general, both propagating and evanescent waves contribute to heat transfer, with the dominant mechanism depending on the separation of the bodies. A common rule of thumb is that at separations smaller than the thermal wavelength, evanes-

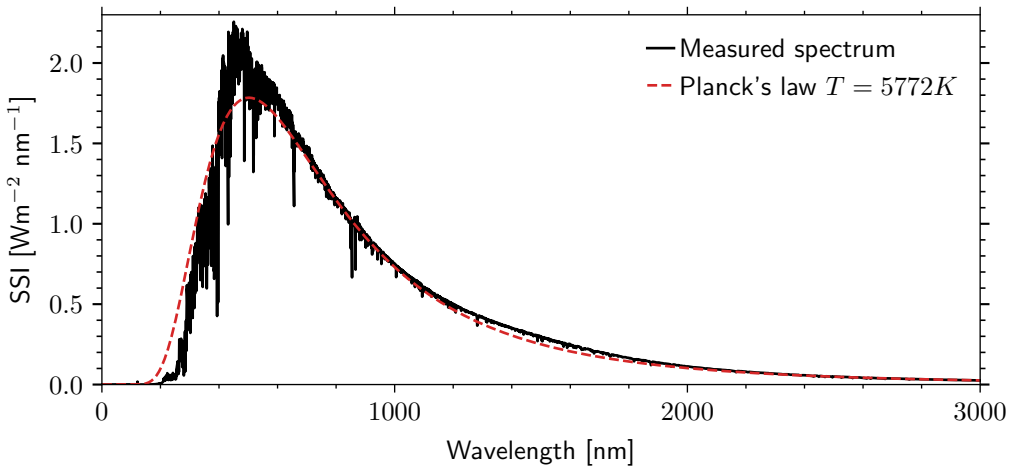

Figure III.1: *Solar spectral irradiance (SSI)*, defined as the solar power received per unit area and per unit wavelength interval at the top of Earth's atmosphere. The spectrum shown was measured by the SOLAR/SOLSPEC instrument aboard the International Space Station (ISS) [100]. While the solar spectrum exhibits numerous absorption features (Fraunhofer lines), its integrated irradiance corresponds to that of a blackbody at $T = 5772\,\mathrm{K}$. For illustration, Planck's radiation law at this temperature is depicted.

cent waves dominate, and significantly enhance heat transfer compared to the far-field [21, 103–105]. Fluctuational electrodynamics (FED) provides a unifying theoretical framework to describe radiative heat transfer in both regimes.

III.1 Fluctuational Electrodynamics

Fluctuational electrodynamics is a semi-classical theory that describes radiative heat transfer. The theory combines Maxwell's equations with Langevin's notion of fluctuating forces [21, 103, 104, 106, 107]. The source terms in Maxwell's equations, charge density and current density, fluctuate due to the thermal motion of charges within the body. The statistics of these fluctuations is evaluated with the fluctuations-dissipation theorem, which connects the response of the material to the random motion in equilibrium. Overall, three essential ingredients are required for fluctuational electrodynamics: Maxwell's equations, material response, and the statistics of the fluctuations.
The dynamics of the electromagnetic field at point $\boldsymbol{r} \in \mathbb{R}^3$ and time $t \in \mathbb{R}$ is captured by Maxwell's equations

$$\nabla \cdot \boldsymbol{E}(\boldsymbol{r},t) = 4\pi\rho(\boldsymbol{r},t) \tag{III.1.1a}$$
$$\nabla \cdot \boldsymbol{B}(\boldsymbol{r},t) = 0 \tag{III.1.1b}$$
$$\nabla \times \boldsymbol{E}(\boldsymbol{r},t) = -\frac{1}{c}\frac{\partial \boldsymbol{B}(\boldsymbol{r},t)}{\partial t} \tag{III.1.1c}$$
$$\nabla \times \boldsymbol{B}(\boldsymbol{r},t) = \frac{1}{c}[4\pi\boldsymbol{j}(\boldsymbol{r},t) + \frac{\partial \boldsymbol{E}(\boldsymbol{r},t)}{\partial t}], \tag{III.1.1d}$$

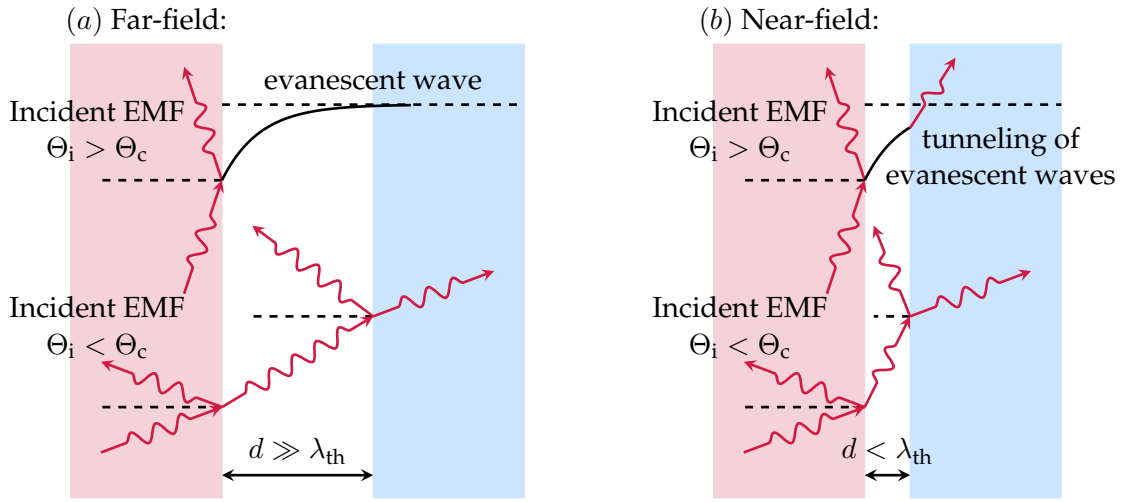

Figure III.2: *Comparison of far- and near-field radiative heat transport.* (a) Far-field regime, with separation $d \gg \lambda_{th}$. Heat transfer is dominated by propagating electromagnetic waves. Evanescent waves, generated by total internal reflection at incident angles Θ_i larger than the critical angle Θ_c, decay rapidly and thus do not reach the other body. (b) Near-field regime, with separation $d < \lambda_{th}$. Evanescent waves can tunnel between the bodies and contribute significantly, leading to strongly enhanced heat transfer [21].

the electric field $\boldsymbol{E}(\boldsymbol{r},t) \in \mathbb{R}^3$, the magnetic field $\boldsymbol{B}(\boldsymbol{r},t) \in \mathbb{R}^3$, and the velocity of light c. The charge density $\rho(\boldsymbol{r},t) \in \mathbb{R}$ and current density $\boldsymbol{j}(\boldsymbol{r},t) \in \mathbb{R}^3$ act as sources of the electromagnetic field. The current density consists of two contributions: the fluctuating current density $\boldsymbol{j}^{\text{fl}}(\boldsymbol{r},t)$ originating from thermal agitation, and the induced current density $\boldsymbol{j}^{\text{ind}}(\boldsymbol{r},t)$, generated by the presence of the electromagnetic field.
How materials react to external perturbations is captured by their constitutive equations, and are material specific. These equations govern the charge and current densities stimulated by an external electromagnetic field. Maxwell's equations in a medium are commonly formulated in terms of the displacement field $\boldsymbol{D}(\boldsymbol{r},t) = \boldsymbol{E}(\boldsymbol{r},t)+4\pi\boldsymbol{P}(\boldsymbol{r},t)$, and the magnetizing field $\boldsymbol{H}(\boldsymbol{r},t) = \boldsymbol{B}(\boldsymbol{r},t)-4\pi\boldsymbol{M}(\boldsymbol{r},t)$-$/c$. The redistribution of charges within the medium is encoded in the polarization vector $\boldsymbol{P}(\boldsymbol{r},t) \in \mathbb{R}^3$, which describes the induced dipole moment per unit volume. Thereby, the magnetization $\boldsymbol{M}(\boldsymbol{r},t) \in \mathbb{R}^3$ represents the induced magnetic dipole moment per unit volume. Induced charge and current densities are related to the polarization and magnetization by

$$\rho^{\text{ind}}(\boldsymbol{r},t) = -\nabla\boldsymbol{P}(\boldsymbol{r},t) \tag{III.1.2a}$$

$$\boldsymbol{j}^{\text{ind}}(\boldsymbol{r},t) = \nabla\times\boldsymbol{M} + \frac{\partial\boldsymbol{P}}{\partial t}. \tag{III.1.2b}$$

In the linear response regime, the polarization is linear to the electric field and the magnetization is linear to the magnetizing field, determined by the electric and magnetic susceptibility. Here, to simplify the discussion, nonmagnetic bodies are considered. There are many ways to express the material's response, such as electric susceptibility, electric permittivity, and conductivity, all of which are

interrelated. The electric permittivity tensor $\boldsymbol{\epsilon}(\boldsymbol{r}, t, \boldsymbol{r}', t') \in M_{3\times3}(\mathbb{R})$ describes the relationship between displacement field and electric field

$$\boldsymbol{D}(\boldsymbol{r}, t) = \int dt' \int d\boldsymbol{r}' \boldsymbol{\epsilon}(\boldsymbol{r}, t, \boldsymbol{r}', t') \boldsymbol{E}(\boldsymbol{r}', t') \tag{III.1.3}$$

and the electric conductivity tensor $\boldsymbol{\sigma}(\boldsymbol{r}, t, \boldsymbol{r}', t') \in M_{3\times3}(\mathbb{R})$ determines the relation between the electric field and the induced current density

$$\boldsymbol{j}^{\text{ind}}(\boldsymbol{r}, t) = \int dt' \int d\boldsymbol{r}' \boldsymbol{\sigma}(\boldsymbol{r}, t, \boldsymbol{r}', t') \boldsymbol{E}(\boldsymbol{r}', t'). \tag{III.1.4}$$

The electric permittivity tensor and conductivity tensor reflects the geometry by being non-zero within the bodies that contain charges. At the interfaces of these bodies, the electromagnetic fields satisfy boundary conditions: the tangential component of the electric field and the normal component of the magnetic field are continuous, while the tangential component of the magnetic field and the normal component of the electric field exhibit jumps dictated by the boundary charge and current densities.
The induced charge density due to the presence of an external potential $\phi(\boldsymbol{r}, t) \in \mathbb{R}$ is described by the density response function $\Pi(\boldsymbol{r}, t, \boldsymbol{r}', t')$, i.e.,

$$\rho^{\text{ind}}(\boldsymbol{r}, t) = \int dt' \int d\boldsymbol{r}' \Pi(\boldsymbol{r}, t, \boldsymbol{r}', t') \phi(\boldsymbol{r}', t'). \tag{III.1.5}$$

Conductivity and density response functions are connected by charge conservation directly expressed by the continuity equation

$$\nabla \boldsymbol{j}(\boldsymbol{r}, t) + \frac{\partial \rho(\boldsymbol{r}, t)}{\partial t} = 0. \tag{III.1.6}$$

Fluctuational electrodynamics describes the field dynamics by stochastic differential equations, with $\boldsymbol{j}^{\text{fl}}(\boldsymbol{r}, t)$ acting as a random source of the electromagnetic fields. This random source resembles a stochastic force in a Langevin equation, which describes the dynamics subject to a combination of deterministic and fluctuating forces. Typically, when the system is driven by an external force, the entire temporal evolution of the force serves as an input to the theory. The stochastic force varies erratically with time and between each realization in the ensemble. It is determined by its temporal force-force correlations, while the average stochastic force vanishes [107]. Analogously, the temporal current-current correlations specify the behaviour of the fluctuating current density. The correlations can be evaluated through application of the fluctuation-dissipation theorem. The fluctuation-dissipation theorem establishes a connection between equilibrium fluctuations and the response to external perturbations. In this context, the polarization characterizes the medium's response to an external field, defined via the electric susceptibility. Polarization fluctuations translate to current density fluctuations of the form

$$\langle j_j^{\text{fl}}(\boldsymbol{r}, \omega) j_k^{\text{fl}*}(\boldsymbol{r}', \omega') \rangle = \hbar\omega \, \text{Re}(\sigma_{jk}(\boldsymbol{r} - \boldsymbol{r}', \omega)) \coth\left(\frac{\hbar\omega}{2k_{\text{B}}T}\right) 2\pi\delta(\omega - \omega'), \tag{III.1.7}$$

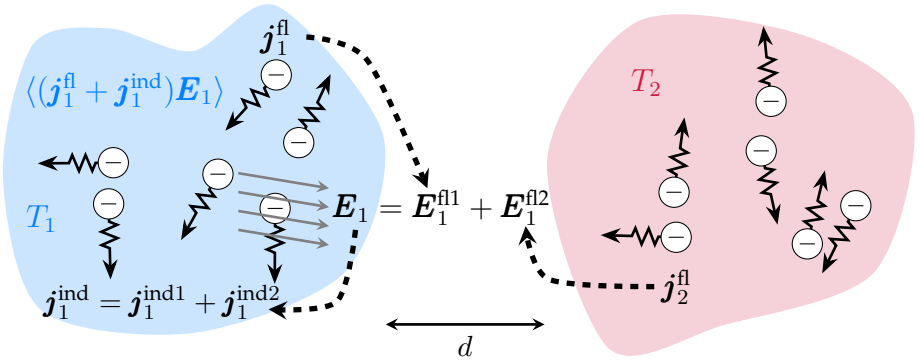

Figure III.3: Sketch of radiative heat transfer within the *framework of fluctuational electrodynamics*. Two thermal bodies, $k = 1, 2$, separated by a distance d, are characterized by their temperatures T_k and their material response (conductivity or permittivity tensor). Heat exchange is mediated by the electromagnetic field generated by fluctuating currents $\boldsymbol{j}_k^{\mathrm{fl}}$ inside the bodies, which originate from thermal agitation of charges and are determined by the fluctuation–dissipation theorem. For example, the electric field E_1 in body 1 results from both its own fluctuations $\boldsymbol{j}_1^{\mathrm{fl}}$ and those $\boldsymbol{j}_2^{\mathrm{fl}}$ of body 2, and in turn self-consistently induces a current density $\boldsymbol{j}_1^{\mathrm{ind1}}$ and $\boldsymbol{j}_1^{\mathrm{ind2}}$, respectively. The local Joule heating is given the local current density times the electric field [108, 109].

with $\hbar$ is the reduced Planck constant, the average $\langle\cdot\rangle$, the angular frequency, and T the temperature of the body. The conductivity tensor is assumed to be space and time invariant such that $\boldsymbol{\sigma}(\boldsymbol{r}, t, \boldsymbol{r'}, t')$ is $\boldsymbol{\sigma}(\boldsymbol{r}-\boldsymbol{r'}, t-t')$, with Fourier transformed conductivity $\boldsymbol{\sigma}(\boldsymbol{r}-\boldsymbol{r}', \omega)$. Ultimately, the complex task boils down to finding the electromagnetic fields by solving Maxwell's equations with boundary conditions, expressing them in terms of the fluctuating current density, and then using the fluctuation-dissipation theorem to calculate the averages.
The radiative heat transferred between two bodies at temperature T_1 and T_2 can be quantified by Joule heating or the Poynting vector. Joule heating describes electrical energy dissipated as heat in a material due to the resistance encountered by moving charge carriers [109]. The deposited energy in body 1 is governed by

$$\mathcal{P}_1 = \int_{B_1} d\boldsymbol{r} \langle \boldsymbol{j}_1(\boldsymbol{r}, t)\boldsymbol{E}_1(\boldsymbol{r}, t)\rangle, \tag{III.1.8}$$

where the integration spans over the whole body B_1. The electric field $\boldsymbol{E}_1 = \boldsymbol{E}_1^{\mathrm{fl1}} + \boldsymbol{E}_1^{\mathrm{fl2}}$ arises from current fluctuations in body 1 and body 2, represented by $\boldsymbol{E}_1^{\mathrm{fl1}}$ and $\boldsymbol{E}_1^{\mathrm{fl2}}$, respectively. The current density $\boldsymbol{j}_1 = \boldsymbol{j}_1^{\mathrm{ind1}} + \boldsymbol{j}_1^{\mathrm{ind2}} + \boldsymbol{j}_1^{\mathrm{fl}}$ consists of the induced current densities due to the electric fields $\boldsymbol{E}_1^{\mathrm{fl1}}$ and $\boldsymbol{E}_1^{\mathrm{fl2}}$, as well as the intrinsically fluctuating current density $\boldsymbol{j}_1^{\mathrm{fl}}$ [109]. The Joule heating is expressed by

$$\mathcal{P}_1 = \int_{B_1} d\boldsymbol{r} \left\langle \left(\boldsymbol{j}_1^{\mathrm{fl}}(\boldsymbol{r}, t) + \int_{B_1} d\boldsymbol{r'} \int dt' \boldsymbol{\sigma}_1(\boldsymbol{r}, \boldsymbol{r'}, t, t')\boldsymbol{E}_1^{\mathrm{fl1}}(\boldsymbol{r'}, t') \right) \boldsymbol{E}_1^{\mathrm{fl1}}(\boldsymbol{r}, t) \right\rangle \tag{III.1.9a}$$

$$+ \int_{B_1} d\boldsymbol{r} \int_{B_1} d\boldsymbol{r'} \int dt' \left\langle \boldsymbol{\sigma}_1(\boldsymbol{r}, \boldsymbol{r'}, t, t')\boldsymbol{E}_1^{\mathrm{fl2}}(\boldsymbol{r'}, t')\boldsymbol{E}_1^{\mathrm{fl2}}(\boldsymbol{r}, t) \right\rangle, \tag{III.1.9b}$$

where we assumed that fluctuating current densities of different bodies are not correlated. The first contribution (III.1.9a) corresponds to the energy emitted by body 1, which includes the energy that escapes to infinity and the energy that is absorbed by the other body. The second contribution (III.1.9b) represents the energy deposited in body 1 due to current density fluctuations in body 2. The Joule heating in body 2 leads to the same formula (III.1.9a) and (III.1.9b), except with indices 1 and 2 swapped. Figure III.3 illustrates radiative heat transfer in the framework of fluctuational electrodynamics. Heat transfer between the bodies captured by the absorption terms, such that the exchanged power is defined by

$$\mathcal{P}_{2\to1} \equiv \int_{B_1} d\boldsymbol{r} \langle \boldsymbol{j}_1^{\mathrm{ind}2}(\boldsymbol{r},t)\boldsymbol{E}_1^{\mathrm{fl}2}(\boldsymbol{r},t)\rangle - \int_{B_2} d\boldsymbol{r} \langle \boldsymbol{j}_2^{\mathrm{ind}1}(\boldsymbol{r},t)\boldsymbol{E}_2^{\mathrm{fl}1}(\boldsymbol{r},t)\rangle, \tag{III.1.10}$$

with

$$\boldsymbol{j}_k^{\mathrm{ind}j}(\boldsymbol{r},t) = \int_{B_k} d\boldsymbol{r}' \int dt' \boldsymbol{\sigma}_k(\boldsymbol{r},\boldsymbol{r}',t,t')\boldsymbol{E}_k^{\mathrm{fl}j}(\boldsymbol{r}',t'). \tag{III.1.11}$$

The first term in (III.1.10) is calculated using Maxwell's equations to determine the electric field in body 1 due to current fluctuations in body 2, and the second term is derived similarly but with the roles of bodies 1 and 2 reversed.
Another method for calculating the heat transfer is based on the Poynting vector. The Poynting vector characterizes the directional energy flux of the electromagnetic field. The power dissipated in a body is obtained by integrating the average Poynting vector over a closed surface containing the body. In the two-body geometry, we can solve Maxwell's equations subject to random currents in body 1 and evaluate the dissipated energy in body 2. Then, we solve the inverse problem and acquire the net transferred heat by subtracting both contributions.

In conclusion, radiative heat transfer reduces to a Landauer-type formula [21]

$$\mathcal{P}_{2\to1} = \int_0^\infty \frac{d\omega}{2\pi} \mathcal{T}(\omega)\hbar\omega[n_2(\omega) - n_1(\omega)], \tag{III.1.12}$$

with $n_\alpha(\omega) = 1/(\exp(\hbar\omega/(k_\mathrm{B}T_\alpha)) - 1)$ the Bose-Einstein distribution of a body $\alpha = 1, 2$ with temperature T_α, and $\mathcal{T}(\omega)$ the total transmission coefficient. A positive heat transfer (III.1.12) indicates heat flux into the body, while a negative value indicates heat flux out of the body. We assumed reciprocal transport such that the transmission coefficient $1 \to 2$ is the same as $2 \to 1$. The transmission coefficient is typically introduced phenomenologically to emphasize its resemblance with the Landauer transport formula in quantum transport. As in quantum transport, the total transmission coefficient $\mathcal{T} = \sum_n \mathcal{T}_n(\omega)$ is constructed from radiation channels n, each with transmission probabilities $0 \leq \mathcal{T}_n(\omega) \leq 1$. The factor $\hbar\omega n_\alpha(\omega)$ could be interpreted as the average energy of a photon with frequency ω. Thus, heat transport presents itself as photon tunnelling, with each photon carrying energy $\hbar\omega$. As we will see later in Sec. III.6 the energy is carried by the electromagnetic field, not by the photons, because the energy current operator and the photon number operator are non-commuting. Our approach derives the energy current operator within a radiative scattering theory, thereby establishing

$\mathcal{T}$ as a transmission coefficient.

The benchmark geometry of near-field radiative heat transfer consists of two filled half spaces separated by a vacuum gap. This simple geometry demonstrates the importance of heat transport by evanescent waves in the near-field regime. We consider optically isotropic and non-magnetic materials $1, 2$, with constant temperature T_1, T_2 and local dielectric permittivities $\epsilon_1(\omega), \epsilon_2(\omega)$. Maxwell's equations in the vacuum gap reduce to the wave equations

$$\nabla^2 \boldsymbol{E}(\boldsymbol{r}, t) + \frac{1}{c}\frac{\partial^2 \boldsymbol{E}(\boldsymbol{r}, \boldsymbol{t})}{\partial t^2} = 0 \tag{III.1.13a}$$

$$\nabla^2 \boldsymbol{B}(\boldsymbol{r}, t) + \frac{1}{c}\frac{\partial^2 \boldsymbol{B}(\boldsymbol{r}, \boldsymbol{t})}{\partial t^2} = 0, \tag{III.1.13b}$$

with plane waves as solutions. The wave vector can be divided into a contribution perpendicular to the surface $k_{\perp v}$, and parallel to the surface $k_\parallel$, while they are related by $k_v^2 = k_{\perp v}^2 + k_\parallel^2$, with the wave number in vacuum $k_v = \omega/c$. The wave is evanescent if $k_{\perp v}$ is complex, i.e., the wave decays exponentially for $k_\parallel > \omega/c$ and propagates for $k_\parallel < \omega/c$.
As pointed out earlier, the transferred heat is obtained by solving the full set of Maxwell's equations, expressing the electromagnetic field in the gap in terms of the fluctuating current density, and evaluating the average Poynting vector. The transferred heat is governed by equation (III.1.12), where the transmission coefficient becomes

$$\mathcal{T}(\omega) = \int_0^\infty \frac{dk_\parallel}{2\pi} k_\parallel [\mathcal{T}_s(\omega, k_\parallel, d) + \mathcal{T}_p(\omega, k_\parallel, d)], \tag{III.1.14a}$$

with the gap size d, and the transmission probabilities $\mathcal{T}_s(\omega, k_\parallel, d), \mathcal{T}_p(\omega, k_\parallel, d)$ of $s-$ or $p-$ polarized waves. Note that the transmission coefficient involves both propagating $(k_\parallel < \omega/c)$ and evanescent electromagnetic waves $(k_\parallel > \omega/c)$. The individual transmissions are given by

$$\mathcal{T}_\alpha(\omega, k_\parallel, d) = \begin{cases} [1 - |r_1^\alpha|^2][1 - |r_2^\alpha|^2]/|D^\alpha|^2 & k_\parallel < k_0 \\ 4\,\mathrm{Im}(r_1^\alpha)\,\mathrm{Im}(r_2^\alpha) e^{-2|k_{\perp v}|d}/|D^\alpha|^2 & k_\parallel > k_0 \end{cases}, \tag{III.1.14b}$$

with $D^\alpha = 1 - r_1^\alpha r_2^\alpha e^{2ik_{\perp v}d}, \alpha = s, p$, and the Fresnel coefficients

$$r_j^s = \frac{k_{\perp v} - k_{\perp j}}{k_{\perp v} + k_{\perp j}} \tag{III.1.14c}$$

$$r_j^p = \frac{\epsilon_j k_{\perp v} - k_{\perp j}}{\epsilon_j k_{\perp v} + k_{\perp j}}, \tag{III.1.14d}$$

with $k_{\perp j} = \sqrt{\epsilon_j(\omega) k_v^2 - k_\parallel^2}, j = 1, 2$. Fresnel coefficients characterize the reflection and transmission of electromagnetic radiation at an interface between media with different permittivities. This demonstrates that the transmission coefficient incorporates geometrical aspects and material properties. A related geometry to the semi-infinite half spaces are two infinite plates in close proximity. There the

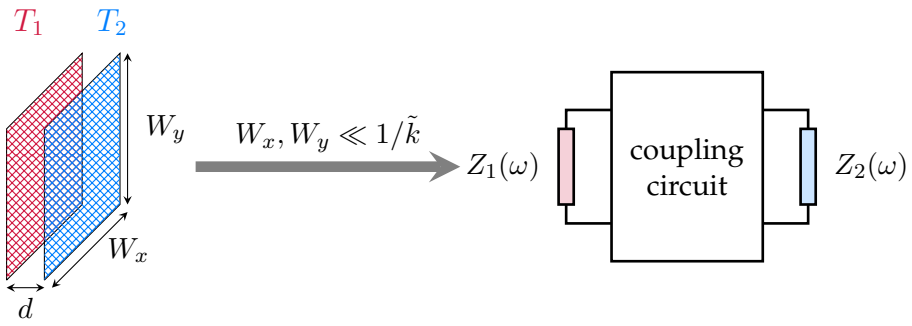

Figure III.4: *Circuit model for nanoscale radiative heat transfer* [109, 127]. Two finite plates of size W_x, W_y support discrete in-plane modes $k_\parallel$. When only a few modes lie in the active band, i.e. when the relevant photon length scale exceeds the object's dimensions ($1/\tilde{k} \gg W_x, W_y$), transport is quasi-static and can be captured by lumped circuit elements. Each thermal body is modeled by an impedance, while electrostatic and magnetostatic couplings are represented by capacitors and inductors, respectively, forming the coupling circuit.

radiative energy can eventually transmit through the plates and escape to infinity. Hence, the absorbed energy of the plate does not corresponds to the average Poynting vector in the gap, but instead to the difference of the Poynting vectors on both sides of the plate. Metals absorb very quickly on the length of the skin depth such that the semi-infinite half space geometry can be a good approximation for plates thicker than the skin depth. The first near-field heat transfer experiments between parallel plates were conducted by [101, 110, 111]. Subsequent research explored various geometries, including scanning thermal profilers [112, 113], scanning thermal microscopes [114, 115], sphere-plate systems [116–120], and integrated microelectromechanical systems (MEMS) [121, 122]. Experimental studies on dielectric materials [105, 123–125] revealed substantial near-field radiative heat transfer exceeding the Planckian limit, attributed to the excitation of surface phonon-polaritons. Metallic layers with macroscopic heat exchange area were investigated in [102, 126].

A complete analytical solution to the radiative heat transfer problem is only available for the geometry of two infinite parallel planar bodies, while other geometries, such as a semi-infinite body and a spherical body, or two spherical bodies, can be treated using approximations [128]. In the realm of heat exchange between nanoscale objects, geometric complexity and material properties can be modelled utilizing an effective circuit approach [127, 129]. To develop a physical intuition for the circuit approach, we examine the case of two finite-sized plates [109]. Heat transfer between infinite plates is described by equation (III.1.12), which incorporates a wave vector and frequency integral. These integrals are dictated by characteristic scales $k_\parallel \sim \tilde{k}, \omega \sim \tilde{\omega}$, for example $\tilde{k} = 1/d, 1/\lambda_{th}, \ldots$ or $\tilde{\omega} = T/\hbar, c/d, \ldots$. Plates of finite size W_x, W_y assume discrete wave vectors $k_x = n\pi/W_x, n \in \mathbb{Z}$, $k_y = m\pi/W_y, m \in \mathbb{Z}$ due to boundary conditions. When the plate size is small compared to the inverse of the characteristic wave vector, i.e., $W_x, W_y \ll 1/\tilde{k}$, then the integral over the wave vector is approximated by a sum over the rele-

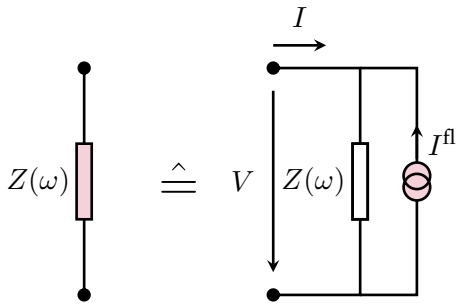

Figure III.5: *Thermal body represented by an impedance* $Z(\omega)$ in parallel with a fluctuating current source I^{fl}, determined by the fluctuation-dissipation theorem.

vant modes. This enables to model the heat transfer by an effective circuit, while each summand represents an extra channel. Or as [109, 127] concludes, a zero-dimensional circuit model is feasible, if the length scale of photons involved in the heat transfer is larger than the system size. The characteristic length scales and the choice of circuit elements require an understanding of the microscopic mechanisms [109]. For example, electrostatic coupling is represented by a capacitor, while magnetostatic coupling is represented by an inductor. Figure III.4 summarizes the equivalent-circuit approach to few-channel near-field radiative heat transfer. In this thesis, we keep the framework general and do not specify a particular circuit model, in order to explore the fundamental structure of near-field radiative heat transfer.

III.2 Circuit Fluctuational Electrodynamics

Fluctuational electrodynamics was extended by [129] to account for radiative heat transfer in circuits. The bodies that absorb and emit heat are modelled as dissipative impedances, with their coupling emulated by linear, passive circuit elements. Absorption is captured by the resistance of the impedance, and the emission by a fictitious fluctuating current source in parallel (see Fig. III.5). Two galvanically connected resistors at different temperatures serve as a fundamental example, originally used by Johnson and Nyquist to investigate thermal noise. Instead of using the electric and magnetic fields, circuit FED employs integrated variables, voltage and current, to describe the operating states of the circuit. The three essential components of circuit FED are: Kirchhoff's laws, which takes the position of Maxwell's equations; dissipative impedances, which represent the material response; and the fluctuating current, which plays an analogous role to the fluctuating current density in FED. To solve the dynamics, we write down Kirchhoff's laws for the circuit (including the fluctuating current sources) and utilize the constitutive equations of the circuit elements. The dynamical equations take the form of a Langevin equation, with the fluctuating currents functioning as the fluctuating forces. The voltage drop $V_j(\omega)$ at impedance $Z_j(\omega)$ induced by the fluctuating

currents $I_k^{\mathrm{fl}}(\omega)$ in impedance k is given by

$$V_j(\omega) = \sum_j \zeta_{jk} I_k^{\mathrm{fl}}(\omega), \tag{III.2.1}$$

with the matrix $\boldsymbol{\zeta}(\omega)$, and the frequency dependence ω obtained by Fourier transformation. The fluctuating current is assumed to obey the fluctuation-dissipation theorem

$$\langle I_j^{\mathrm{fl}}(\omega) I_k^{\mathrm{fl}}(\omega')\rangle = \delta_{jk}\hbar\omega \,\mathrm{Re}\left(\frac{1}{Z_j(\omega)}\right) \coth\left(\frac{\hbar\omega}{2k_{\mathrm{B}}T_j}\right) 2\pi\delta(\omega+\omega'), \tag{III.2.2}$$

while exhibiting vanishing average current. Therefore, the statistics of the fluctuating current depend on the impedance $Z_j(\omega)$ and the temperature T_j at which it originates. The heat deposited into the impedance j is defined by the Joule loss

$$\begin{aligned}
\mathcal{P}_j \equiv& \langle I_j(t) V_j(t)\rangle \\
=& \sum_{k,m} \iint_{-\infty}^{\infty} \frac{d\omega d\omega'}{8\pi^2} e^{-i(\omega+\omega')t} \left(\frac{\zeta_{jk}(\omega)}{Z_j(\omega)} - \delta_{jk}\right) \zeta_{jm}(\omega') \langle I_k^{\mathrm{fl}}(\omega) I_m^{\mathrm{fl}}(\omega')\rangle \\
=& \sum_k \int_{-\infty}^{\infty} \frac{d\omega}{2\pi} \left(\frac{\zeta_{jk}(\omega)}{Z_j(\omega)} - \delta_{jk}\right) \zeta_{jk}^*(\omega) \,\mathrm{Re}\left(\frac{1}{Z_k(\omega)}\right) \hbar\omega \coth\left(\frac{\hbar\omega}{2k_{\mathrm{B}}T_k}\right) \\
=& \sum_k \int_0^{\infty} \frac{d\omega}{2\pi} \mathcal{T}_{jk}(\omega) \hbar\omega [n_k(\omega) - n_j(\omega)]
\end{aligned} \tag{III.2.3}$$

where $V_j(t)$ is the voltage and $I_j(t)$ the current at impedance j, and

$$\mathcal{T}_{jk}(\omega) = 4\,\mathrm{Re}\left(\frac{1}{Z_j(\omega)}\right) \zeta_{jk}(\omega) \zeta_{jk}^*(\omega) \,\mathrm{Re}\left(\frac{1}{Z_k(\omega)}\right) \tag{III.2.4}$$

is the transmission probability between impedance j and k. Here, no radiation leaks to infinity, so $\mathcal{P}_j$ embodies the transferred heat to impedance j by the other impedances. The special case of two dissipative impedances reduces to the Landauer-type formula (III.1.12). The transmission coefficient $\mathcal{T}(\omega)$ depends on the circuit parameters (resistances, capacitances, inductances, etc.), and corresponds to the transmission probability of a single channel.

Superconducting circuits.— The circuit approach can be applied to model radiative heat transfer in superconducting-normal metal structures. These mesoscopic structures consist of normal-metal segments connected by superconducting links, and are designed and operated such that heat transfer by phonons and quasiparticles is suppressed, leaving photons as the prevalent channel for heat transport. Here, the superconducting links provide electrical conductivity while effectively acting as thermal insulators. Andreev reflection prevents subgap energy transfer, and heat conduction takes place via thermally excited quasi-particles [130]. As a result, the thermal conductance is exponentially suppressed at temperatures well below the superconductor's critical temperature [22]. When superconducting links are shorter than the coherence length, subgap energy transport

can contribute to thermal conduction via elastic cotunneling and crossed Andreev reflection [131]. Capacitive coupling between components of the structure additionally suppresses heat conduction, while allowing transport of electromagnetic fields. Another mechanism for heat conduction arises from phonon transport: electron-phonon coupling in the normal metal excites phonons, which carry heat across the structure [32, 132]. Electron-phonon coupling declines significantly at low temperatures. In typical nanoscale systems, the crossover temperature, at which photon contributions dominate over phonon contributions, is typically between $500\,\mathrm{mK} - 100\,\mathrm{mK}$ [132]. At this low temperatures the thermal wavelength is around several centimetres, which warrants the lumped circuit description. Normal-metals are modelled by dissipative impedances or in the simplest case by resistors, and the superconducting components are modelled by linear non-dissipative elements such as capacitors, inductors, finite-length transmission lines. The experiment [133] investigates the century-old Johnson-Nyquist circuit in the quantum regime, featuring two galvanically connected resistors R_1, R_2 held at different temperatures. The photonic thermal conductance $G_{th} = \mathcal{T} G_{Qth}$ consists of one channel, with transmission $\mathcal{T} = 4R_1R_2/(R_1 + R_2)^2$, and the thermal conductance quantum $G_{Qth} = \pi k_\mathrm{B} T/(6\hbar)$. The thermal conductance quantum establishes a fundamental upper limit for the heat conductance per channel [134], and is universally found in quantum heat transfer carried by fermions [135] and bosons [32, 136, 137]. For matched resistors $R_1 = R_2$ the transport is ballistic and the channel perfectly transmitting. Thermal transport by quasiparticles emerged above $\sim 250\,\mathrm{mK}$, while the photon contribution became noticeable below $\sim 200\,\mathrm{mK}$. A more advanced circuit topology incorporates reactive elements between the resistors. Meschke *et al.* [32] demonstrated magnetic flux-control of radiative heat transfer by inserting a DC-SQUID in both connections between the resistors. The DC-SQUIDs provide a flux-tunable inductance, which in turn leads to a flux-tunable transmission, thereby functioning as a heat valve for radiative heat transfer in the system. The flux dependence was washed out for temperatures well above $100\,\mathrm{mK}$. Electric field control of the radiative heat transport was demonstrated in [138], where they added a Cooper-pair transistor, and controlled the gate charge. Heat transport oscillates with the applied gate voltage due to the competing effects of Cooper-pair tunneling and Coulomb repulsion within the island. Photons enable coherent thermal transport over macroscopic distances because they can be guided with minimal scattering in optical fibers or transmission lines. Partanen *et al.* [139] established nearly ballistic radiative quantum transport between mesoscopic-sized resistors (length $\sim 5\,\mu\mathrm{m}$) connected by a one-metre-long waveguide. So far the introduced experiments concentrate on radiative transport between two resistors. Each extra normal-metal segment adds a terminal, enabling the investigation of multiterminal radiative heat transfer. Several proposals exist for multi-terminal setups, such as thermal transistors [140–142], heat amplifiers [143, 144], quantum absorption refrigerators [145, 146], and thermally pumped masers [147]. Gubaydullin et al. [142] engineered a three terminal device interacting through a Xmon qubit, where the qubit frequency is controlled by a magnetic field, which results in flux-dependent radiative heat transfer.

III.3 Classical Electric Networks

Radiative heat transfer in electrical circuits essentially involves determining the voltages and currents within the network. Thereby, we are not interested in every branch voltage and current, but only in those across the dissipative impedances $Z_j(\omega)$ that represent the bodies which absorb and emit heat. The electric network connecting these impedances is summarized as a multi-port network [156], here referred to as the coupling circuit. The port entering the coupling circuit is characterized by its voltage $V_j(\omega)$ and current $I_j(\omega)$, which correspond to those across the associated impedance. At this stage, the coupling circuit is a black box, which is simply determined by the relationships between its external ports. There are several ways to describe the port relations, for example, via the short-circuit admittance, the open-circuit impedance, or, as will be relevant later, the scattering matrix. The open-circuit impedance expresses port voltages in terms of port currents by

$$V_j(\omega) = \sum_k Z^{oc}_{jk}(\omega) I_k(\omega), \tag{III.3.1}$$

with the open-circuit impedance

$$Z^{oc}_{jk}(\omega) = \left.\frac{V_j(\omega)}{I_k(\omega)}\right|_{I_l(\omega)=0, l\neq k}. \tag{III.3.2}$$

The entry $Z^{oc}_{jk}(\omega)$ specifies the voltage $V_j(\omega)$ that develops in response to the current $I_k(\omega)$, while all other ports are open, that is, $I_l(\omega) = 0, k \neq l$. Vice versa, the port currents in terms of port voltages are given by

$$I_j(\omega) = \sum_k Y^{sc}_{jk}(\omega) V_k(\omega), \tag{III.3.3}$$

with the short-circuit admittance

$$Y^{sc}_{jk}(\omega) = \left.\frac{I_j(\omega)}{V_k(\omega)}\right|_{V_l(\omega)=0, l\neq k}. \tag{III.3.4}$$

Here, $Y^{sc}_{jk}(\omega)$ characterizes the current $I_j(\omega)$ due to the voltage $V_k(\omega)$ under the condition that the other ports are shorted, i.e., $V_l(\omega) = 0$ for $l \neq k$. Reciprocal coupling circuits lead to a symmetric short-circuit impedance and open-circuit admittance. An open-circuit impedance or short-circuit admittance representation does not necessarily exist for arbitrary coupling circuits; in some cases, only one of them, or neither, may exists [156].

Scattering parameter.— Energy transfer in electric circuits is naturally treated by scattering parameter [156]. This representation highlights the dual role of the dissipative impedances as both providers of energy (through incident excitations) and absorbers of energy (through scattered excitations). The scattering parameters $A^-_j(\omega)$, $A^+_j(\omega)$ can be interpreted as mode amplitudes of incident $(-)$ and scattered waves $(+)$, respectively, in a transmission line (see section III.6). This

connection enables the description of NFRHT from a quantum transport perspective. To construct the scattering parameters, we begin by defining the scattering currents and voltages

$$V_j^-(\omega) = \frac{1}{2}\frac{Z_j^*(\omega)}{\mathrm{Re}(Z_j(\omega))}[V_j(\omega) - Z_j(\omega)I_j(\omega)] \tag{III.3.5a}$$

$$V_j^+(\omega) = \frac{1}{2}\frac{Z_j(\omega)}{\mathrm{Re}(Z_j(\omega))}[V_j(\omega) + Z_j^*(\omega)I_j(\omega)] \tag{III.3.5b}$$

$$I_j^-(\omega) = \frac{1}{2}\frac{1}{\mathrm{Re}(Z_j(\omega))}[V_j(\omega) - Z_j(\omega)I_j(\omega)] \tag{III.3.5c}$$

$$I_j^+(\omega) = \frac{1}{2}\frac{1}{\mathrm{Re}(Z_j(\omega))}[V_j(\omega) + Z_j^*(\omega)I_i(\omega)], \tag{III.3.5d}$$

with $Z_j(\omega)$ the impedance that terminates port j, and $\mathrm{Re}(Z_j(\omega)) \neq 0$ for all angular frequencies ω. The current and voltage scattering matrix are obtained by

$$S_{jk}^I(\omega) = \left.\frac{I_j^+(\omega)}{I_k^-(\omega)}\right|_{I_l^-(\omega)=0, l\neq k} \tag{III.3.5e}$$

$$S_{jk}^V(\omega) = \left.\frac{V_j^+(\omega)}{V_k^-(\omega)}\right|_{V_l^-(\omega)=0, l\neq k}. \tag{III.3.5f}$$

The conditions $I_l^-(\omega) = 0, V_l^-(\omega) = 0$ impose $V_l(\omega) = Z_j(\omega)I_j(\omega)$, such that the other impedances $Z_l(\omega), l \neq k$ act as dissipative loads for the incident current $I_k^-(\omega)$ or voltage $V_k^-(\omega)$, respectively. For purely resistive impedances $Z_j(\omega) = z_j$, the scattering parameters $A_j^\pm(\omega) \equiv \sqrt{z_j}I_j^\pm(\omega)$ are straightforwardly defined using a frequency-independent normalization. In the case of frequency-dependent impedances [156–162], normalization is achieved by introducing functions $\lambda_{1j}(\omega)$, $\lambda_{2j}(\omega)$, which satisfy $\mathrm{Re}(Z_j(\omega)) = |\lambda_{1j}(\omega)|^2 = |\lambda_{2j}(\omega)|^2$. To respect causality, $\lambda_{1j}(\omega)$, $\lambda_{2j}(\omega)$ and $1/\lambda_{1j}^*(\omega)$, $1/\lambda_{2j}^*(\omega)$ must be holomorphic for $\mathrm{Im}(\omega) > 0$. These conditions do not uniquely determine $\lambda_{1j}(\omega) = \sqrt{\mathrm{Re}(Z_j(\omega))}\, e^{i\vartheta_{1j}(\omega)}$, $\lambda_{1j}(\omega) = \sqrt{\mathrm{Re}(Z_j(\omega))}\, e^{i\vartheta_{2j}(\omega)}$, leaving an arbitrariness in the phase $\vartheta_{1j}(\omega)$, $\vartheta_{2j}(\omega)$. The scattering parameter are obtained by

$$\begin{aligned}\begin{pmatrix} A_j^-(\omega) \\ A_j^+(\omega)\end{pmatrix} &\equiv \begin{pmatrix} \lambda_{1j}^*(\omega) & \\ & \lambda_{2j}(\omega)\end{pmatrix}\begin{pmatrix} I_j^-(\omega) \\ I_j^+(\omega)\end{pmatrix} \\ &= \begin{pmatrix} \lambda_{1j}^*(\omega)/Z_j^*(\omega) & \\ & \lambda_{2j}(\omega)/Z_j(\omega)\end{pmatrix}\begin{pmatrix} V_j^-(\omega) \\ V_j^+(\omega)\end{pmatrix} \\ &= \frac{1}{2}\begin{pmatrix} \lambda_{1j}^{-1}(\omega) & -Z_j(\omega)\lambda_{1j}^{-1}(\omega) \\ \lambda_{2j}^{-*}(\omega) & Z_j^*(\omega)\lambda_{2j}^{-*}(\omega)\end{pmatrix}\begin{pmatrix} V_j(\omega) \\ I_j(\omega)\end{pmatrix},\end{aligned} \tag{III.3.6}$$

which leads to the scattering matrix

$$S_{jk}(\omega) = \left.\frac{A_j^+(\omega)}{A_k^-(\omega)}\right|_{A_l^-(\omega)=0, l\neq k} = \frac{\lambda_{2j}(\omega)}{\lambda_{1k}^*(\omega)}S_{jk}^I(\omega) = \frac{\lambda_{2j}(\omega)Z_j^*(\omega)}{\lambda_{1k}^*(\omega)Z_j(\omega)}S_{jk}^V(\omega). \tag{III.3.7}$$

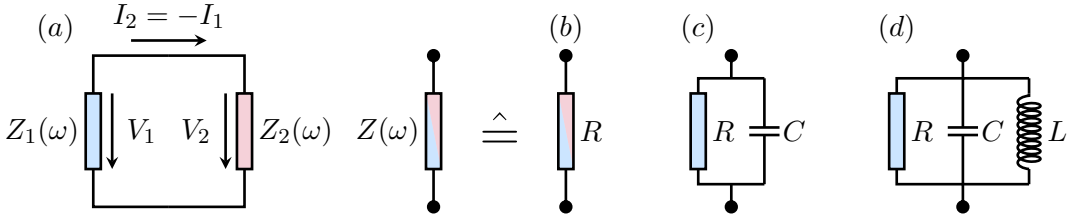

Figure III.6: *Example impedance network*: (a) Two impedances $Z_1(\omega)$ and $Z_2(\omega)$ coupled galvanically. (b-d) Representative realisations for Z_j: (b) pure resistor, (c) low-pass filter, (d) damped RLC resonator.

In terms of the open-circuit impedance matrix $\boldsymbol{Z}^{oc}(\omega)$, we find

$$\boldsymbol{S}(\omega) = \boldsymbol{\lambda}_2^{-*}(\omega)\boldsymbol{\lambda}_1(\omega) + 2\boldsymbol{\lambda}_2(\omega)[\boldsymbol{Z}^{oc}(\omega) - \boldsymbol{Z}(\omega)]^{-1}\boldsymbol{\lambda}_1(\omega), \tag{III.3.8}$$

with diagonal matrices $\boldsymbol{\lambda}_1(\omega) \equiv \mathrm{diag}(\ldots, \lambda_{1j}(\omega), \ldots)$, $\boldsymbol{\lambda}_2(\omega) \equiv \mathrm{diag}(\ldots, \lambda_{2j}(\omega), \ldots)$, $\boldsymbol{Z} \equiv \mathrm{diag}(\ldots, Z_j(\omega), \ldots)$. Equation (III.3.8) directly demonstrates, that the scattering matrix is symmetric, when the electric network and the normalization is reciprocal, i.e., $\boldsymbol{Z}^{oc}(\omega)$ is symmetric and $\boldsymbol{\lambda}_1(\omega) = \boldsymbol{\lambda}_2(\omega)$. Without loss of generality, we adopt a reciprocal normalization $\boldsymbol{\lambda}_1(\omega) = \boldsymbol{\lambda}_2(\omega) = \boldsymbol{\lambda}(\omega)$ in the following, as the measurable quantities are independent of the phases $\vartheta_{1j}(\omega)$ (see section III.6). A fundamental property of the scattering matrix is its unitarity

$$\boldsymbol{S}(\omega)\boldsymbol{S}^\dagger(\omega) = \boldsymbol{S}^\dagger(\omega)\boldsymbol{S}(\omega) = \mathbb{1}. \tag{III.3.9}$$

This guarantees the interpretation of $|S_{jk}(\omega)|^2$ as transmission probability, and $|S_{jj}(\omega)|^2$ as reflection probability.

How to construct the scattering matrix.— The scattering matrix is obtained by the constitutive relations of the circuit elements and Kirchhoff's laws. A circuit element is characterized by its voltage–current relation $V(\omega) = Z(\omega)I(\omega)$, with $Z(\omega)$ its frequency-dependent impedance. For example, a capacitor obeys the constitutive relation $I(\omega) = i\omega CV(\omega)$, while an inductor satisfies $V(\omega) = i\omega LI(\omega)$. Kirchhoff's current law expresses the conservation of charge, stating that the sum of currents entering a node is zero. Kirchhoff's voltage law reflects the conservation of energy, stating that the sum of voltages around any closed loop is zero [163]. In this thesis, we examine radiative heat transfer in several specific circuits and, in the following, demonstrate how to derive their scattering matrices.

Two impedances $Z_1(\omega), Z_2(\omega)$ galvanically connected in a loop constitute a simple and relevant example (see Fig. III.6(a)). Kirchhoff's laws demand $V_1(\omega) = V_2(\omega)$, and $I_1(\omega) = -I_2(\omega)$, therefore equation (III.3.7) leads to the scattering matrix

$$\boldsymbol{S}(\omega) = \frac{1}{Z_1(\omega) + Z_2(\omega)} \begin{pmatrix} \frac{\lambda_1(\omega)[Z_2(\omega) - Z_1^*(\omega)]}{\lambda_1^*(\omega)} & 2\lambda_1(\omega)\lambda_2(\omega) \\ 2\lambda_1(\omega)\lambda_2(\omega) & \frac{\lambda_2(\omega)[Z_1(\omega) - Z_2^*(\omega)]}{\lambda_2^*(\omega)} \end{pmatrix}. \tag{III.3.10}$$

The corresponding transmission probability is given by

$$\mathcal{T}(\omega) = S_{21}^\dagger(\omega)S_{12}(\omega) = \frac{4\,\mathrm{Re}(Z_1(\omega))\,\mathrm{Re}(Z_2(\omega))}{|Z_1(\omega) + Z_2(\omega)|^2}. \tag{III.3.11}$$

If $Z_1(\omega) = R_1$, $Z_2(\omega) = R_2$, we recover the transmission $\mathcal{T} = 4R_1R_2/(R_1 + R_2)^2$ of the Johnson-Nyquist circuit [133] (see Fig. III.6(a) and (b)). Note that while the scattering matrix depends on the complex normalization, the transmission coefficient does not. The unitarity of the scattering matrix is verified by the relations $S_{11}^\dagger(\omega)S_{11}(\omega) + S_{12}^\dagger(\omega)S_{21}(\omega) = \mathbb{1}$ and $S_{11}^\dagger(\omega)S_{12}(\omega) + S_{12}^\dagger(\omega)S_{22}(\omega) = 0$.
A parallel RC-element (see Fig. III.6(a) and (c)) with impedance $Z_1(\omega) = R/(1 - i\omega RC)$, $\lambda_1(\omega) = \sqrt{R}/(1 - i\omega RC)$ coupled galvanically to a resistor $Z_2(\omega) = R$, $\lambda_2(\omega) = \sqrt{R}$ results in the scattering matrix

$$\boldsymbol{S}(\omega) = \frac{1}{1 - i\omega RC/2}\begin{pmatrix} i\omega RC/2 & 1 \\ 1 & i\omega RC/2 \end{pmatrix}, \tag{III.3.12}$$

with the transmission function

$$\mathcal{T}(\omega) = \frac{1}{1 + \omega^2R^2C^2/4}. \tag{III.3.13}$$

The transmission function corresponds to a Lorentzian centred at $\omega = 0$,where the inverse of the RC-time defines the damping parameter. Therefore, radiation with frequency $\omega RC/2 \ll 1$ is transmitted, while radiation with $\omega RC/2 \gg 1$ is reflected, realizing a low-pass filter.
A parallel RLC-element(see Fig. III.6(a) and (d)) with impedance $Z_1(\omega) = 1/(1/R - 1/(i\omega L) - i\omega C)$, $\lambda_1(\omega) = -i\omega L/[\sqrt{R}(1 - \omega^2LC - i\omega L/R)]$ coupled to a resistor with $Z_2(\omega) = R$, $\lambda_2(\omega) = \sqrt{R}$ posses the scattering matrix

$$\boldsymbol{S}(\omega) = \frac{1}{2\omega\gamma - i(\omega^2 - \omega_0^2)}\begin{pmatrix} i(\omega^2 - \omega_0^2) & 2\omega\gamma \\ 2\omega\gamma & i(\omega^2 - \omega_0^2) \end{pmatrix} \tag{III.3.14}$$

and the transmission function

$$\mathcal{T}(\omega) = \frac{(2\omega\gamma)^2}{(\omega^2 - \omega_0^2)^2 + (2\omega\gamma)^2}, \tag{III.3.15}$$

with $\omega_0 \equiv 1/\sqrt{LC}$, $\gamma \equiv 1/(RC)$. Radiation with frequency around ω_0 can pass from resistor 1 to resistor 2, with the RC-time determining the bandwidth. We refer to this configuration as resonant-pass filter. The RLC element may model a small metallic particle hosting a plasmonic resonance (reflected by the LC resonator) together with electron-hole pair excitations (the resistor).

Two coupled surface phonon-polariton modes can be modelled by the circuit III.7. This example is discussed in depth in Sec. III.6. The surface phonon-polariton is mimicked by the impedances

$$Z_1(\omega) = Z_2(\omega) = \left[-i\omega C_\mathrm{c} - \frac{i\omega C_T}{1 - \omega^2LC_T - i\omega RC_T}\right]^{-1} = \frac{1}{-i\omega C_\mathrm{c}}\frac{\omega_T^2 - \omega^2 - 2i\omega\gamma}{\omega_L^2 - \omega^2 - 2i\omega\gamma}, \tag{III.3.16a}$$

with

$$\mathrm{Re}(Z_1(\omega)) = \mathrm{Re}(Z_2(\omega)) = \frac{R/(LC_\mathrm{c})^2}{(\omega_L^2 - \omega^2)^2 + (2\omega\gamma)^2}, \tag{III.3.16b}$$

$$\lambda_1(\omega) = \lambda_2(\omega) = \frac{\sqrt{R}/(LC_\mathrm{c})}{\omega_L^2 - \omega^2 - 2i\omega\gamma}. \tag{III.3.16c}$$

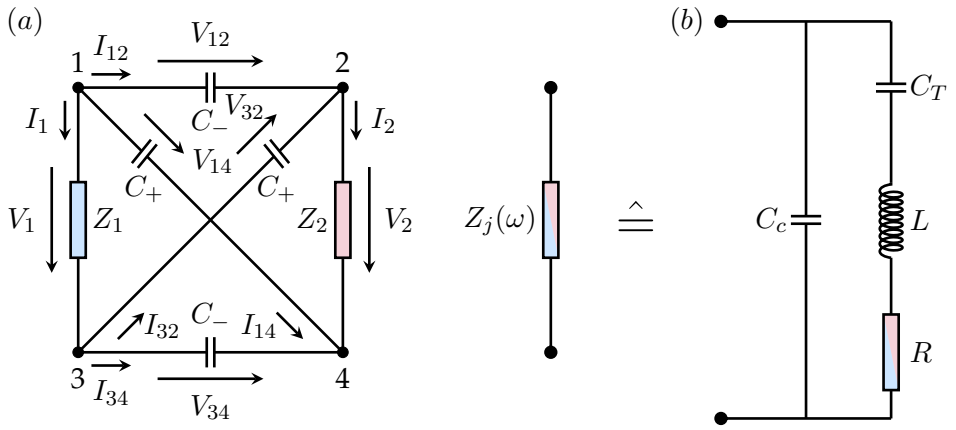

Figure III.7: (a) *circuit representation of two coupled surface-phonon-polariton modes*, each modelled as a damped LC resonator (b) with impedance $Z_j(\omega), (j = 1, 2)$, capacitively coupled via C_+ and C_-.

Symmetric and antisymmetric coupling of the modes is captured by the capacitances $C_\pm$. To obtain the scattering matrix, we solve the dynamic equations of the coupling circuit (illustrated in Fig. III.7(a)) to obtain the voltages and currents at the impedances. Kirchhoff's laws lead to the equations

$$\begin{aligned}
I_1(\omega) + I_{12}(\omega) + I_{14}(\omega) &= 0, & V_1(\omega) + V_{32}(\omega) - V_{12}(\omega) &= 0 && \text{(III.3.17a)}\\
-I_1(\omega) + I_{32}(\omega) + I_{34}(\omega) &= 0, & V_1(\omega) + V_{34}(\omega) - V_{14}(\omega) &= 0 && \text{(III.3.17b)}\\
-I_2(\omega) + I_{12}(\omega) + I_{32}(\omega) &= 0, & V_2(\omega) + V_{12}(\omega) - V_{14}(\omega) &= 0 && \text{(III.3.17c)}\\
I_2(\omega) + I_{14}(\omega) + I_{34}(\omega) &= 0, & V_2(\omega) + V_{34}(\omega) - V_{32}(\omega) &= 0 && \text{(III.3.17d)}
\end{aligned}$$

and utilizing the constitutive laws gives the relations

$$\begin{aligned}
I_1(\omega) + I_2(\omega) &= i\omega C^+(V_1(\omega) + V_2(\omega)) && \text{(III.3.18a)}\\
I_1(\omega) &= \frac{i\omega}{2}(C^+ + C^-)V_1(\omega) + \frac{i\omega}{2}(C^+ - C^-)V_2(\omega) && \text{(III.3.18b)}\\
I_1(\omega) - I_2(\omega) &= i\omega C^-(V_1(\omega) - V_2(\omega)) && \text{(III.3.18c)}\\
I_2(\omega) &= \frac{i\omega}{2}(C^+ - C^-)V_1(\omega) + \frac{i\omega}{2}(C^+ + C^-)V_2(\omega). && \text{(III.3.18d)}
\end{aligned}$$

For example, the reflection amplitude $S_{11}(\omega)$ is calculated by

$$\begin{aligned}
S_{11}(\omega) &= \frac{\lambda_1(\omega)}{\lambda_1^*(\omega)} \frac{V_1(\omega) + Z_1^*(\omega)I_1(\omega)}{V_1(\omega) - Z_1(\omega)I_1(\omega)}\bigg|_{V_2(\omega)=Z_2(\omega)I_2(\omega)}\\
&= \frac{\lambda_1(\omega)}{\lambda_1^*(\omega)} \frac{1 - i\omega(Z_2(\omega) - Z_1^*(\omega))(C^+ + C^-)/2 + \omega^2 Z_1^*(\omega)Z_2(\omega)C^+C^-}{1 - i\omega(Z_2(\omega) + Z_1(\omega))(C^+ + C^-)/2 - \omega^2 Z_1(\omega)Z_2(\omega)C^+C^-},
\end{aligned} \qquad \text{(III.3.19a)}$$

and derived from equations (III.3.18) under the condition $V_2(\omega) = Z_2(\omega)I_2(\omega)$. The other elements are determined in an analogous manner, resulting in the sec-

ond reflection amplitude

$$S_{22}(\omega) = \frac{\lambda_2(\omega)}{\lambda_2^*(\omega)} \frac{1 - i\omega(Z_1(\omega) - Z_2^*(\omega))(C^+ + C^-)/2 + \omega^2 Z_2^* Z_1(\omega) C^+ C^-}{1 - i\omega(Z_1(\omega) + Z_2(\omega))(C^+ + C^-)/2 - \omega^2 Z_2(\omega) Z_1(\omega) C^+ C^-}, \tag{III.3.19b}$$

and the transmission amplitudes

$$S_{12}(\omega) = \frac{i\omega\lambda_1(\omega)\lambda_2(\omega)(C^+ - C^-)}{1 - i\omega(Z_1(\omega) + Z_2(\omega))(C^+ + C^-)/2 - \omega^2 Z_2(\omega) Z_1(\omega) C^+ C^-} \tag{III.3.19c}$$

$$S_{21}(\omega) = \frac{i\omega\lambda_1(\omega)\lambda_2(\omega)(C^+ - C^-)}{1 - i\omega(Z_1(\omega) + Z_2(\omega))(C^+ + C^-)/2 - \omega^2 Z_2(\omega) Z_1(\omega) C^+ C^-}, \tag{III.3.19d}$$

which lead to the transmission coefficient

$$\mathcal{T}(\omega) = \frac{\omega^2 \operatorname{Re}(Z_1(\omega)) \operatorname{Re}(Z_2(\omega))(C^+ - C^-)^2}{N(\omega)}, \tag{III.3.20}$$

with

$$\begin{aligned} N(\omega) =& |1 - \omega^2 Z_1(\omega) Z_2(\omega) C^+ C^-|^2 + \omega(C^+ + C^-) \operatorname{Im}((Z_1(\omega) \\ &+ Z_2(\omega))(1 - \omega^2 Z_1^*(\omega) Z_2^*(\omega) C^+ C^-)) + \omega^2 |Z_2(\omega) + Z_1(\omega)|^2 (C^+ + C^-)^2/4. \end{aligned} \tag{III.3.21}$$

Indeed, the reflection coefficients satisfy $|S_{11}(\omega)|^2 = |S_{22}(\omega)|^2 = 1 - \mathcal{T}(\omega)$, as demanded by the unitarity of the scattering matrix.

III.4 Quantum Electric Networks: Circuit Quantum Electrodynamics

Quantum electric networks, described within the framework of circuit quantum electrodynamics, represent the low-frequency approximation of quantum electrodynamics. A phenomenological approach is employed to describe electric networks in the quantum regime. Charges and magnetic fluxes of circuit components are viewed as collective coordinates, emerging from the cooperative motion of many electrons, and are directly quantized rather than being derived from a full first-principles treatment of the underlying material [164]. Quantum effects in electric circuits become observable when thermal fluctuations are suppressed and the energy levels are well resolved, such that the linewidths remain smaller than the level spacing [165]. This phenomenological approach led, for example, to noiseless amplifiers, mixer configurations, and back-action-evading detectors [164]. Quantization requires deriving the Hamiltonian of the circuit, where the canonical variables are the branch charge, defined as the time integral of the current, and the branch flux, defined as the time integral of the voltage. The branch variables are not independent due to constitutive equations and Kirchhoff's laws, which impose constraints on the system. The constraints are satisfied by eliminating degrees of freedom till they are all independent or using the Dirac-Bergmann algorithm [166–168]. The Lagrangian is formulated from the energy

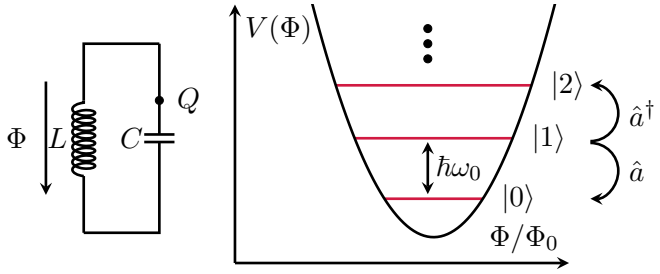

Figure III.8: Left: *LC circuit* consisting of a capacitor in parallel with an inductor, representing a harmonic oscillator. The system can be described equivalently by the magnetic flux linked to the inductor or by the charge on the capacitor. Right: The quadratic potential energy $V(\Phi)$ gives rise to equidistant *energy levels* with spacing set by the resonator frequency ω_0. The annihilation operator $\hat{a}$ lowers, and the creation operator $\hat{a}^\dagger$ raises, the excitation number of the resonator [108].

expressions of the circuit elements, and the Hamiltonian is then derived via Legendre transformation. The Hamiltonian is constructed such that the Heisenberg equations reproduce Kirchhoff's laws. Therefore, the scattering matrix (III.3.7) remains the same in both the quantum and classical regimes. For a comprehensive discussion of circuit quantization, we refer the reader to [108, 165, 169]. In the following, we discuss the quantization of an LC resonator and a resistor, as they represent the relevant examples for this thesis.

Harmonic oscillator.— The LC resonator consists of an inductance L, and a capacitance C (see Fig. III.8). The energy of the inductor is given by $E_L = \Phi^2/(2L)$, and that of the capacitor by $E_C = Q^2/(2C)$, where Φ corresponds to the magnetic flux through the inductor, and Q to the charge on the capacitor. To construct the Lagrangian, we need to decide which energy constitutes the kinetic energy and which the potential energy. When E_C is treated as the kinetic energy, the flux variable plays the role of the position variable of a particle in a harmonic potential. Conversely, when E_L is taken as the kinetic energy, the charge variable corresponds to the position variable. Both choices lead to the same equations of motions, and we choose here E_L as the kinetic energy. The Lagrangian is then defined as $\mathcal{L} = E_L - E_C$, which leads to the corresponding Hamiltonian

$$\mathcal{H} = \frac{\Phi^2}{2L} + \frac{Q^2}{2C}. \tag{III.4.1a}$$

Charge and flux are conjugate variables, and quantization is achieved by promoting the Poisson brackets to commutators, thereby introducing the canonical commutation relations.

$$[\hat{Q}, \hat{\Phi}] = i\hbar. \tag{III.4.1b}$$

It is instructive to introduce the annihilation operator $\hat{a}$ and creation operator $\hat{a}^\dagger$, defined by

$$\hat{a} = \frac{1}{2}\left(Q_{\text{zpf}}^{-1}\hat{Q} + i\Phi_{\text{zpf}}^{-1}\hat{\Phi}\right), \quad \hat{a}^\dagger = \frac{1}{2}\left(Q_{\text{zpf}}^{-1}\hat{Q} - i\Phi_{\text{zpf}}^{-1}\hat{\Phi}\right), \tag{III.4.2}$$

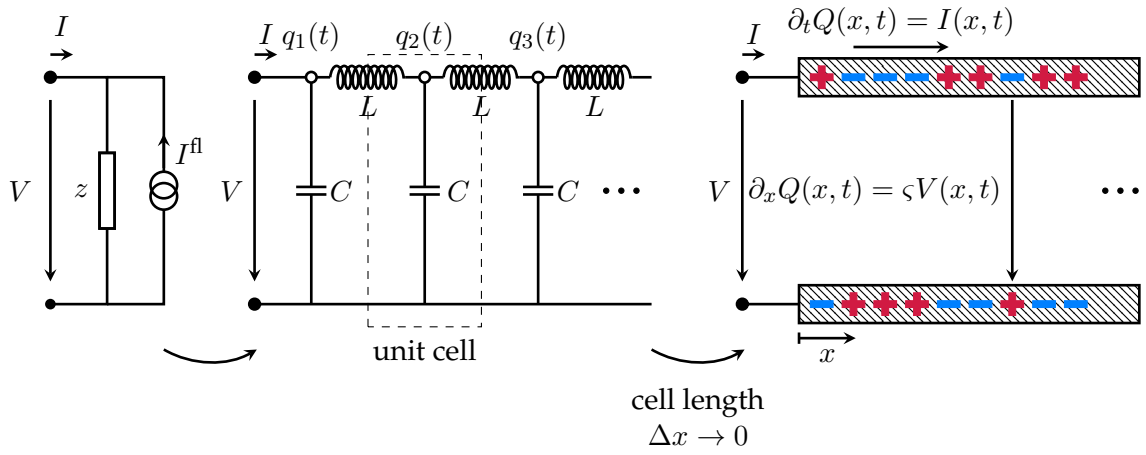

Figure III.9: *From resistor to (continuum) transmission line.* Left: A resistor z in parallel with a fluctuating current source, inducing the current I^{fl}. Centre: LC ladder; unit cell (dotted rectangle) n comprises two series inductors $L/2$ and a shunt capacitor C. The node (capacitor) charge is $q_n(t)$. Right: Taking $\Delta x \to 0$ with $\varsigma = C/\Delta x$ and $l = L/\Delta x$ fixed yields a continuous line described by the polarization coordinate $Q(x,t)$, i.e. the accumulated line charge to the left of x with $q(x,t) = \partial_x Q(x,t)$.

with the magnitude of the zero-point fluctuations $Q_{\mathrm{zpf}} = \sqrt{\hbar/(2Z_r)}$, $\Phi_{\mathrm{zpf}} = \sqrt{\hbar Z_r/2}$, and the characteristic impedance $Z_r = \sqrt{L/C}$. The Hamiltonian assumes the form

$$\hat{H} = \hbar\omega_0 \left(\hat{a}^\dagger \hat{a} + \frac{1}{2}\right), \tag{III.4.3}$$

with the resonance frequency $\omega_0 = 1/\sqrt{LC}$. The eigenstates $\hat{a}^\dagger\hat{a}\,|n\rangle = n\,|n\rangle$, with $n \in \mathbb{N}_0$, of the number operator diagonalize the Hamiltonian, yielding eigenenergies $E_n = \hbar\omega_0(n + 1/2)$. The energy levels are equally spaced, so that transitions between states require integer multiples of the resonance quantum $\hbar\omega_0$. The annihilation operator $\hat{a}$ destroys an excitation of frequency ω_0, while the creation operator $\hat{a}^\dagger$ creates one. The energy levels are broadened due to interactions with environmental degrees of freedom, introducing a linewidth κ. The quality factor $\mathcal{Q} = \omega_0/\kappa$ quantifies the resolution of the energy levels, with large values ranging from $\mathcal{Q} \sim 10^3$ to 10^8 achievable in experiments [170–172]. Another requirement to observe the quantum effects is that the thermal energy $k_{\mathrm{B}}T$ be much smaller than the energy quantum $\hbar\omega_0$, ensuring that thermal transitions are suppressed. Superconductors operated far below their critical temperature $\sim 1 - 10\,\mathrm{K}$ on low-loss dielectric substrates are optimal platforms for accessing the quantum regime. Additionally, voltage vacuum fluctuations are typically relatively large, resulting in stronger electric dipole interactions than those encountered in conventional quantum optics [173].

Resistor/transmission line.— In electric circuits, resistors play a twofold role: on one hand, they inject energy into the coupled circuit elements via thermal noise;

on the other hand, they dissipate energy from those elements. According to the fluctuation-dissipation theorem, thermal noise generated by a resistor or impedance element depends on its resistance and the temperature. Thus, a transmission line that accurately reproduces the resistor's electrical response is sufficient for modeling purposes, and the microscopic structure does not need to be considered. This phenomenological approach neglects electrical noise that stems from microscopic or nonequilibrium processes, such as flicker noise [165]. In contrast to a resistor, a transmission line is amenable to quantization. A quantum system evolving under a hermitian Hamiltonian is inherently reversible, such that no energy escapes from the system. To accurately model a dissipative quantum system, an environment with infinitely many degrees of freedom is required to ensure that energy, once transferred, is not reabsorbed by the system. A resistor can be modelled by a semi-infinite transmission line, as illustrated in Fig. III.9, with the Lagrangian

$$\mathcal{L}(t) = \frac{1}{2}\int_0^\infty dx \left[l(\partial_t Q(x,t))^2 - \frac{1}{\varsigma}(\partial_x Q(x,t))^2 \right], \tag{III.4.4}$$

expressed by the polarization field $Q(x,t)$ with inductance l and capacitance ς per unit length. A similar Lagrangian is obtained when formulating the theory in terms of the flux field $\Phi(x,t)$, where $l \leftrightarrow \varsigma$ are interchanged. The classical dynamics is governed by the Euler-Lagrange equation

$$\partial_t^2 Q(x,t) - c^2 \partial_x^2 Q(x,t) = 0, \tag{III.4.5}$$

with the propagation velocity $c = 1/\sqrt{l\varsigma}$. The evolution of the polarization field is described by a wave equation, and can thus be decomposed into left- and right-travelling waves, i.e. an incident and scattered polarization field. Hence, heat transfer in electric circuits can be formulated as a scattering theory. To construct the scattering theory, we express the equations of motion in terms of the scattering states

$$A^\sigma(x,t) = \frac{1}{2}\left(\sqrt{\frac{c}{\varsigma}}\partial_x Q(x,t) - \sigma\sqrt{z}\partial_t Q(x,t) \right), \tag{III.4.6}$$

with $\sigma = -$ the left and $\sigma = +$ right propagating transmission line excitation, and the transmission line impedance $z = \sqrt{l/\varsigma}$. The equations of motions reduce to

$$(\partial_t - \sigma c \partial_x) A^\sigma(x,t) = 0, \tag{III.4.7}$$

with the solution

$$A^\sigma(x,t) = \frac{1}{\sqrt{2\pi}}\int_{-\infty}^\infty d\omega \sqrt{\frac{|\hbar\omega|}{2}} e^{-i\omega(t-\sigma x/c)} \alpha_\omega^\sigma. \tag{III.4.8}$$

At the endpoint $x = 0$, the transmission line is coupled to the rest of the circuit elements, which imposes a boundary condition. A field theory can be subject to different boundary conditions, such as Von Neumann, Dirichlet or Cauchy boundary conditions. These boundary conditions restrict the phase space, as they

only allow for fields that satisfy the boundary condition. We first resolve the constraints within classical field theory to obtain the reduced phase space, laying the groundwork for quantization [167]. This approach is commonly used, for example, to quantize the electromagnetic field in a box, where the E-and B-fields are expressed by their Fourier components, which are then quantized. Alternatively, one may treat constrained Hamiltonians using the Dirac procedure, which involves replacing the Poisson bracket with the Dirac bracket [166, 167].
Assuming the resistor is open-ended, the boundary condition enforces that the current $\partial_t Q(0,t)$ vanishes, which implies $A^+(0,t) = A^-(0,t)$ in the time domain, and consequently $\alpha^+_\omega = \alpha^-_\omega$ in the frequency domain. Incident excitations are totally reflected back without a phase shift. For a shorted resistor, the boundary condition $\partial_x Q(0,t) = 0$ implies $\alpha^+_\omega = -\alpha^-_\omega$, corresponding to total reflection of the incident wave with a phase shift of π. The boundary condition eliminates the field α^+_ω, leaving α^-_ω as the only independent degree of freedom. The Hamiltonian of the open and short circuited transmission line is

$$\begin{aligned}\mathcal{H}(t) =& \frac{1}{2}\int_0^\infty dx\left[l(\partial_t Q(x,t))^2 + \frac{1}{\varsigma}(\partial_x Q(x,t))^2\right] = \frac{1}{c}\sum_{\sigma=\pm}\int_0^\infty dx[A^\sigma(x,t)]^2 \\ =& \int_{-\infty}^\infty d\omega \frac{\hbar|\omega|}{2}\alpha^{-*}_\omega\alpha^-_\omega = \int_0^\infty d\omega\hbar\omega\left(\alpha^{-*}_\omega\alpha^-_\omega + \frac{1}{2}\right)\end{aligned} \tag{III.4.9}$$

with the Poisson brackets

$$\{A^\sigma(x,t), A^{\sigma'}(x',t)\}_P = -\frac{\delta_{\sigma\sigma'}\sigma c^2}{2}\partial_{x-x'}\delta(x-x'), \tag{III.4.10}$$

which are obtained from the canonical Possion brackets $\{Q(x,t),\Phi(x',t)\}_P = \delta(x-x')$. The Hamiltonian resembles that of a free harmonic oscillator. Quantization of the field theory is accomplished by replacing the Poisson bracket with the commutator, i.e.,

$$\{\alpha^-_\omega, \alpha^-_{\omega'}\}_P = -\frac{i}{\hbar}\operatorname{sgn}(\omega)\delta(\omega+\omega') \to [\hat{\alpha}^-_\omega, \hat{\alpha}^-_{\omega'}] = \operatorname{sgn}(\omega)\delta(\omega+\omega'). \tag{III.4.11}$$

The quantum Hamiltonian is obtained by replacing α^-_ω with the annihilation/-creation operator $\hat{\alpha}^-_\omega$ of a transmission line excitation in equation (III.4.9).

Electric networks.— We are now equipped to quantize the linear classical networks discussed in Section III.3. As in the classical case, we assume that the initial conditions of the coupling circuit elements have decayed, such that the currents and voltages in the coupling circuit are solely determined by thermal fluctuations in the resistors or by external sources attached to the resistors. Each resistor j possesses a Lagrangian $\mathcal{L}_j$, given by (III.4.4). The boundary condition demands that the transmission line fields $A^\sigma_j(x=0,\omega)$ equal the scattering parameters $A^\sigma_j(\omega)$ from section III.3. Therefore, the coupling circuit imposes the relation

$$\alpha^+_{j,\omega} = \sum_k S_{jk}(\omega)\alpha^-_{k,\omega}, \tag{III.4.12}$$

between incident $\alpha^{-}_{j,\omega}$, and scattered $\alpha^{+}_{j,\omega}$ excitations, leaving the incident fields as the independent degrees of freedom. All information about the coupling is condensed into the scattering matrix, which completely determines the scattered states. The total Hamiltonian is given by

$$\begin{aligned}\hat{H}(t) =& \sum_{j,k,l} \iint_{-\infty}^{\infty} d\omega d\omega' \sqrt{\frac{|\hbar\omega||\hbar\omega'|}{4}} e^{-i(\omega+\omega')t} \left[\delta_{jk}\delta_{jl} D_{\omega+\omega'} + S_{jk}(\omega) S_{jl}(\omega') D_{-\omega-\omega'}\right] \\ & \times \hat{\alpha}_{k,\omega}\hat{\alpha}_{l,\omega'} \\ =& \int_0^{\infty} d\omega \hbar\omega \sum_j \left(\hat{\alpha}^{\dagger}_{j,\omega}\hat{\alpha}_{j,\omega} + \frac{1}{2}\right) \qquad \text{(III.4.13a)} \\ & + i \sum_{j,k,l} \text{P.V.} \iint_{-\infty}^{\infty} \frac{d\omega d\omega'}{2\pi} \sqrt{\frac{|\hbar\omega||\hbar\omega'|}{4}} e^{-i(\omega+\omega')t} \frac{\delta_{jk}\delta_{jl} - S_{jk}(\omega) S_{jl}(\omega')}{\omega+\omega'} \hat{\alpha}_{k,\omega}\hat{\alpha}_{l,\omega'} \qquad \text{(III.4.13b)}\end{aligned}$$

with $\hat{\alpha}_{j,\omega} \equiv \hat{\alpha}^{-}_{j,\omega}$, and

$$D_{\omega} = \lim_{\eta\to 0} \int_0^{\infty} \frac{d\tau}{2\pi} e^{i(\omega+i\eta)\tau} = \lim_{\eta\to 0} \frac{1}{2\pi} \frac{i}{\omega+i\eta} = \frac{1}{2}\delta(\omega) + \frac{i}{2\pi}\text{P.V.}\left(\frac{1}{\omega}\right), \qquad \text{(III.4.14)}$$

where P.V. is the principal value. The term in (III.4.13a) represents the energy of the transmission-line excitations, whereas the term in (III.4.13b) takes into account the energy stored in the coupling circuit. In the ideal galvanic-coupling limit where the scattering matrix is frequency independent, the coupling network introduces no internal dynamics. Hence the term in Eq. (III.4.13b) vanishes. The commutation relations governing the incident field modes are

$$[\hat{\alpha}_{j,\omega}, \hat{\alpha}_{k,\omega'}] = \delta_{jk}\,\text{sgn}(\omega)\delta(\omega+\omega'). \qquad \text{(III.4.15)}$$

This Hamiltonian does not commute with the particle number operators,such that the particle number is not conserved under time evolution.

III.5 Heat Current Fluctuations

A deeper understanding of near-field radiative heat transfer can be achieved by extending the analysis beyond the average heat transfer to include its fluctuations [33, 148–150]. The detection of heat current fluctuations is constrained not only by experimental limitations but also by fundamental physical principles [151–154]. Whether fluctuations can be detected depends on the time scale at which they occur. The requirement on the experimental level is that the measurement system must have a time resolution finer than the time scale of the fluctuations; otherwise, the signal is averaged out. On the fundamental level, heat is a path-dependent thermodynamic quantity exchanged when a system undergoes a non-adiabatic transition between equilibrium states. The system of interest consists of a thermal body absorbing energy from a fluctuating heat current emitted by another thermal body, thereby changing its internal energy. In

accordance with the first law of thermodynamics, the change in internal energy equals the heat dQ absorbed by the body, provided that the incident heat current performs no mechanical work. Although the actual absorption process may be irreversible or out of equilibrium, the change in internal energy between the initial and final equilibrium states can still be computed by invoking a hypothetical quasi-static path, thereby enabling the assignment of a well-defined temperature change dT. In total, the absorbed heat is given by $dQ = C_{\mathrm{V}} dT$, where C_{V} is the heat capacity at constant volume. If the heat current fluctuates on a timescale much longer than the body's equilibration time, the system can be viewed as a random succession of equilibrium states, enabling the heat current fluctuations to be measured in terms of temperature fluctuations. Since the inverse equilibration rate is typically much smaller than the thermal frequency scale $\tau_{\mathrm{th}}^{-1} = k_{\mathrm{B}} T/\hbar$, experimental observations are generally restricted to low- or zero-frequency heat current fluctuations. Karimi [155] reported a direct, time-resolved measurement of electron temperature fluctuations induced by a fluctuating heat current from a phonon bath. Electron–electron interactions lead to rapid thermalization on nanosecond timescales ($\sim 10^{-9}\,\mathrm{s}$), while energy exchange with the environment and especially with the phonon bath occurs over much longer timescales, typically around $\sim 10^{-5}\,\mathrm{s}$, due to weak electron–phonon coupling. As a result of the separation of timescales, the fluctuating electron temperature accurately reflects the heat current exchanged with the environment. The equilibrium temperature fluctuations are governed by the fluctuation–dissipation theorem, which sets a fundamental limit to temperature detection sensitivity, a limit that was reached in the experiment. The authors propose that their quantum calorimetry technique could be applied to measure microwave-energy transport in the gigahertz regime, as relevant for circuit QED platforms. The electron reservoir is then subject to a fluctuating radiative heat current, thereby driving the electrons out of equilibrium with the phonon bath. When the fluctuations in the radiative heat current are comparable to or exceed those in the phononic channel, they may become experimentally detectable. Further details on how to model temperature fluctuations can be found in [22, 109].

III.6 Scattering Approach to Near-Field Radiative Heat Transfer

Mesoscopic transport of electrons, phonons, and photons is associated with quantum-mechanical scattering processes [22, 24, 174]. The Landauer-Büttiker scattering approach [4, 6] expresses average currents between two or more particle reservoirs in terms of the particle scattering matrix.
Moreover, the scattering approach gives a general prediction for current noise [14], which is known to contain additional valuable information beyond the average signal [34]. This is widely utilized in the field of electronic quantum transport, where current noise is employed to characterize conduction mechanisms and the nature of charge carriers [15]. Besides the field of electronic transport, a Landauer-type formula for the average current is also found in quantum heat transport conveyed by phonons or photons [24, 175].
Near-field radiative heat transfer (NFRHT) occurs between closely spaced bodies and is mediated by electromagnetic field rather than carried by particles. The natural and common tool for its description is fluctuational electrodynamics (FED) [176, 177], which also results in a Landauer-type formula for the average heat current [103, 104, 106, 178]. The analogy between the FED formulation of NFRHT and Landauer-Büttiker approach was pushed further in Refs. [179, 180], where thermal reservoirs and transmission channels were identified. Still, we are not aware of any work where scattering states for reservoir excitations and the corresponding scattering matrix would be constructed for the NFRHT problem.
The need for such construction becomes especially pressing in the context of recent studies of heat current noise in NFRHT [33, 148–150, 181]. It has been noted [33] that the NFRHT noise spectrum does not fit the general form obtained from the scattering approach for bosonic particles in Ref. [14]. It is therefore important to clarify what type of scattering problem NFRHT corresponds to.
In this work, we show how to formulate the quantum-mechanical scattering problem for NFRHT, focusing on its circuit version [129] for simplicity. Effective circuits of lumped elements (resistors, capacitors, inductors) can be used to model NFRHT between nanoscale objects at low temperatures [32, 127, 129, 182], when the full set of Maxwell's equations separates into electrostatic and magnetostatic sectors with few relevant modes. In the circuit picture, thermal reservoirs associated with different bodies at different temperatures are represented as dissipative resistors, which include fluctuating current sources (Nyquist-Johnson noise at the corresponding temperature) and are coupled by non-dissipative linear circuit elements (capacitors and inductors, modeling electrostatic and magnetostatic coupling, respectively), as schematically represented in Fig. III.10. Instead of Maxwell's equations, one solves Kirchhoff's laws, and all geometrical details of the structure are encoded in a few circuit parameters [127]. Such circuit models are more tractable than the standard Maxwellian FED, while being conceptually equivalent.
Using an equivalent representation of each reservoir by a microwave transmission line (TL) hosting bosonic excitations, we construct scattering states for these excitations. The corresponding scattering matrix can be determined from the linear circuit equations (Kirchhoff's laws), just like the response to fluctuating sources in FED. The scattering theory enables one to determine arbitrary high-

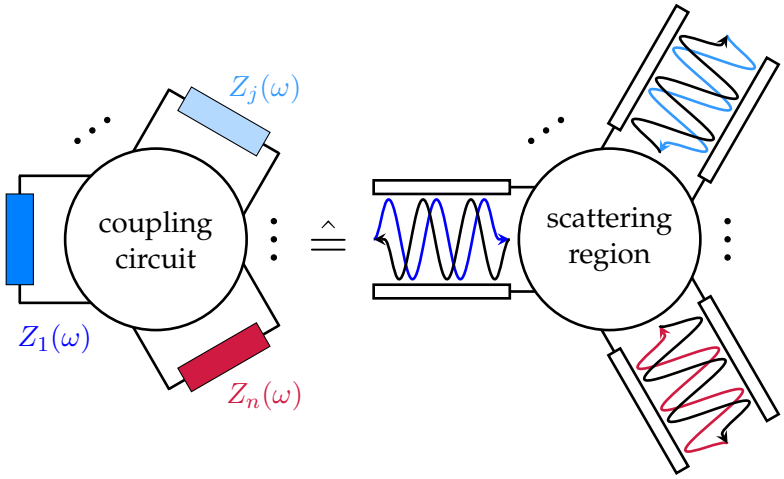

Figure III.10: Left: *Circuit representation of near-field radiative heat transfer* (NFRHT) between thermal reservoirs at different temperatures. The reservoirs are modeled as resistors, characterized by their frequency-dependent impedances, $Z_j(\omega)$. Right: An equivalent *scattering representation* of NFRHT, where transmission lines (TL's) couple through a scattering region. Incoming TL excitations are either reflected back or transmitted to other TL's through the scattering region.

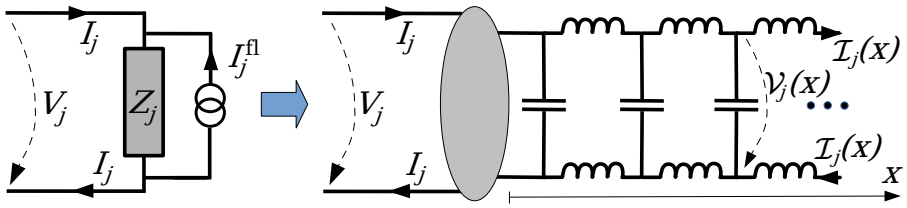

Figure III.11: *Representation of a resistor $Z_j(\omega)$ by an extended semi-infinite TL*, modeled by a sequence of infinitesimal inductors and capacitors, connected to the rest of the circuit via a linear 4-terminal element ("filter") which transforms a constant impedance of the TL into the given impedance $Z_j(\omega)$.

order correlation functions of the NFRHT energy current. We obtain a general expression for the energy current, which extends Büttiker's formula for the particle current [14, 15]. We find that frequency dependence of reservoir's impedance results in an additional reactive contribution to the energy current, which has no counterpart in Büttiker's theory for particle current. This reactive contribution is absent in the average energy current, but can give a dominant contribution to its finite-frequency noise.

III.6.1 Scattering Approach to Radiative Heat Transfer in Circuits

We employ the mesoscopic approach of circuit quantum electrodynamics [164, 165], directly quantizing circuit fluxes and charges, which yield currents and voltages. It is equivalent to the Green's function approach in the random-phase ap-

proximation [33, 150], where currents and voltages emerge as collective variables of electronic or ionic motion. Our main step is to represent each resistor j having an arbitrary complex impedance $Z_j(\omega)$ as a semi-infinite TL with some real constant impedance z_j (thus purely dissipative), combined with a purely reactive element which yields the required total impedance $Z_j(\omega)$ [157]. The TL is characterized by the inductance ℓ_j and capacitance ς_j per unit length, and can be viewed as a chain of infinitesimal unit cells of length $\Delta x \to 0$, each unit cell containing two inductances $\ell_j\,\Delta x/2$ and a capacitance $\varsigma_j\,\Delta x$ (Fig. III.11). The TL's impedance is $z_j = \sqrt{\ell_j/\varsigma_j}$ and the wave velocity $c_j = 1/\sqrt{\ell_j\varsigma_j}$. The voltage and current profiles

$$\hat{\mathcal{V}}_j(x,t) = \int_0^\infty d\omega \sqrt{\frac{\hbar\omega z_j}{4\pi}} \sum_{\sigma=\pm} \left[\hat{a}^\sigma_{j,\omega} e^{-i\omega(t-\sigma x/c_j)} + \text{h.c.}\right], \tag{III.6.1a}$$

$$\hat{\mathcal{I}}_j(x,t) = \int_0^\infty d\omega \sqrt{\frac{\hbar\omega}{4\pi z_j}} \sum_{\sigma=\pm} \left[\sigma\hat{a}^\sigma_{j,\omega} e^{-i\omega(t-\sigma x/c_j)} + \text{h.c.}\right], \tag{III.6.1b}$$

are expressed in terms of bosonic creation/annihilation operators $\hat{a}^{\sigma\,\dagger}_{j,\omega}, \hat{a}^\sigma_{j,\omega}$, for left- ($\sigma = -$) and right- ($\sigma = +$) propagating excitations at frequency ω with the commutator $[\hat{a}^\sigma_{j,\omega}, \hat{a}^{\sigma\,\dagger}_{k,\omega'}] = \delta_{jk}\delta(\omega-\omega')$. The scattered excitations, $\sigma = +$, are determined by the incident excitations and by the coupling circuit, so the operators $\hat{a}^+_{j,\omega}$ are related to $\hat{a}^-_{k,\omega'}$. Quantization of fluxes and charges in the circuit constitutes the circuit analog of quantizing the electric and magnetic fields in the Maxwellian electrodynamics.

At $x = 0$ the TL is connected to a fictitious linear reciprocal 4-terminal element ("filter") in order to reproduce the required impedance $Z_j(\omega)$. The filter transforms voltage and current Fourier components as [157]

$$\begin{pmatrix} \hat{V}_j(\omega) \\ \hat{I}_j(\omega) \end{pmatrix} = \begin{pmatrix} \operatorname{Re}\frac{Z_j(\omega)}{\lambda_j(\omega)} & i\operatorname{Im}\frac{Z_j(\omega)}{\lambda_j(\omega)} \\ i\operatorname{Im}\frac{1}{\lambda_j(\omega)} & \operatorname{Re}\frac{1}{\lambda_j(\omega)} \end{pmatrix} \begin{pmatrix} z_j^{-1/2}\hat{\mathcal{V}}_j(0,\omega) \\ z_j^{1/2}\hat{\mathcal{I}}_j(0,\omega) \end{pmatrix}. \tag{III.6.2}$$

The function $\lambda_j(\omega)$ is determined by the physical realization of the filter (the so-called network synthesis [156, 157]). It must satisfy $|\lambda_j(\omega)|^2 = \operatorname{Re} Z_j(\omega)$. To respect causality, $\lambda_j(\omega)$ and $1/\lambda_j^*(\omega)$ must be holomorphic for $\operatorname{Im}\omega > 0$. These conditions do not uniquely determine $\lambda_j(\omega) = \sqrt{\operatorname{Re} Z_j(\omega)}\, e^{i\vartheta_j(\omega)}$, leaving an arbitrariness in the phase $\vartheta_j(\omega)$. For example, one may include a piece of transmission line of length l into the filter, which amounts to $\vartheta_j \to \vartheta_j + \omega l/c_j$. We do not need the explicit construction, since measurable quantities are phase-independent.
The resulting expressions of the voltage and current at the resistor j in terms of the bosonic mode operators,

$$\hat{V}_j(t) = \int_0^\infty d\omega \sqrt{\frac{\hbar\omega}{4\pi}} \left[\frac{Z_j(\omega)}{\lambda_j(\omega)}\,\hat{a}^+_{j,\omega} + \frac{Z_j^*(\omega)}{\lambda_j^*(\omega)}\,\hat{a}^-_{j,\omega}\right] e^{-i\omega t} + \text{h.c.}, \tag{III.6.3a}$$

$$\hat{I}_j(t) = \int_0^\infty d\omega \sqrt{\frac{\hbar\omega}{4\pi}} \left[\frac{1}{\lambda_j(\omega)}\,\hat{a}^+_{j,\omega} - \frac{1}{\lambda_j^*(\omega)}\,\hat{a}^-_{j,\omega}\right] e^{-i\omega t} + \text{h.c.}, \tag{III.6.3b}$$

will be our main tool in the following. We investigate the heat exchange between the resistors while maintaining their temperatures at T_j. Accordingly, the reservoirs are assumed to have thermal populations $\langle \hat{a}^{-\dagger}_{j,\omega} \hat{a}^{-}_{k,\omega'} \rangle = \delta_{jk} n_j(\omega) \delta(\omega - \omega')$, where $n_j(\omega) = 1/(e^{\hbar\omega/T_j} - 1)$ being the Bose-Einstein distribution (the Boltzmann constant $k_\mathrm{B} = 1$). In thermal equilibrium, the expectation values $\langle \hat{a}^{-}_{j,\omega} \rangle$ vanish, resulting in zero average currents and voltages. However, other quantum states of the TL's can give rise to nonzero average currents and voltages. Applying a classical voltage drive to the resistor means imposing $\hat{V}_j(t) = V_\mathrm{ext} e^{-i\omega_\mathrm{ext} t} + \text{c.c.}$. Then we obtain $\hat{a}^{+}_{j,\omega} = V_\mathrm{ext}[\lambda_j(\omega)/Z_j(\omega)] \sqrt{4\pi/(\hbar\omega)} \delta(\omega - \omega_\mathrm{ext}) - [Z_j^*(\omega)/Z_j(\omega)] e^{2i\vartheta_j(\omega)} \hat{a}^{-}_{j,\omega}$ from Eq. (III.6.3a), and Eq. (III.6.3b) yields $\langle \hat{I}_j(t) \rangle = V_\mathrm{ext} e^{-i\omega_\mathrm{ext} t}/Z_j(\omega_\mathrm{ext}) + \text{c.c.}$, consistent with the definition of $Z_j(\omega)$ (see Sec. III.7.1).

Scattering matrix.— The operators $\hat{a}^{+}_{j,\omega}$ of scattered excitations are related to those of incident excitations. In a linear coupling circuit without external drives, this relation must be linear and frequency-conserving, $\hat{a}^{+}_{j,\omega} = \sum_k S_{jk}(\omega) \hat{a}^{-}_{k,\omega}$, where $S_{jk}(\omega)$ is the scattering matrix [1]. It must be holomorphic for $\mathrm{Im}(\omega) > 0$ by causality; otherwise, the scattered excitation $\hat{a}^{+}_j(t) = \sum_k \int dt' S_{jk}(t - t') \hat{a}^{-}_k(t')$ would depend on $\hat{a}^{-}_j(t')$ in the future. Since the coupling circuit is lossless (all dissipative elements must be included as reservoirs), the scattering matrix must be unitary, $\sum_k S^*_{kj}(\omega) S_{kl}(\omega) = \delta_{jl}$ [183]. It is sufficient to solve the linear circuit equations (Kirchhoff's laws), with no need to specify the circuit Hamiltonian, to find the scattering matrix

$$S_{jk}(\omega) = \frac{a^{+}_{j,\omega}}{a^{-}_{k,\omega}}\bigg|_{\substack{a^{-}_{l,\omega}=0,\\ l\neq k}} = \frac{\lambda_j(\omega)}{\lambda_k^*(\omega)} \frac{I_j^{+}(\omega)}{I_k^{-}(\omega)}\bigg|_{\substack{I_l^{-}(\omega)=0,\\ l\neq k}} \tag{III.6.4}$$

where $I_j^{-}(\omega) \equiv [V_j(\omega) - Z_j(\omega) I_j(\omega)]/[2\,\mathrm{Re}\, Z_j(\omega)]$ is the incident current and $I_j^{+}(\omega) \equiv [V_j(\omega) + Z_j^*(\omega) I_j(\omega)]/[2\,\mathrm{Re}\, Z_j(\omega)]$ the scattered current.

Circuit FED.— In the scattering approach, fluctuations emerge from the incident TL excitations, whereas in circuit FED [129], they originate from fictitious fluctuating current sources $I_j^{\mathrm{fl}}(t)$ attached in parallel to each resistor (Fig. III.11). $I_j^{\mathrm{fl}}(t)$ represents the Johnson-Nyquist noise of the resistor, dictated by the fluctuation-dissipation theorem, and induces the fluctuating voltage $V_j(\omega) = Z_j(\omega)[I_j(\omega) + I_j^{\mathrm{fl}}(\omega)]$. In the scattering approach, Eqs. (III.6.3) lead to the fluctuating voltage $V_j(\omega) = Z_j(\omega) I_j(\omega) + [2\,\mathrm{Re}\, Z_j(\omega)] I_j^{-}(\omega)$. Thus, the incident current plays the same role as the fluctuating current, and both approaches induce the identical voltage if $Z_j(\omega)\, I_j^{\mathrm{fl}}(\omega) = [2\,\mathrm{Re}\, Z_j(\omega)] I_j^{-}(\omega)$. We recover the standard Johnson-Nyquist expression for the average anticommutator $\langle \{\hat{I}_j^{-}(t), \hat{I}_j^{-}(0)\} \rangle$. Additionally, we can apply the circuit FED approach [129] to determine the scattering

[1] Typically, the coupling circuit does not conserve the number of excitations; indeed, electrostatic/magnetostatic coupling enters the circuit Hamiltonian via charges/fluxes which involve linear combinations of creation and annihilation operators. However, this non-conservation may occur only transiently in the scattering region, but not in the asymptotic scattering states. Mixing creation and annihilation operators in the scattering relation would allow for production of excitation pairs out of vacuum, which is forbidden in a stable harmonic system without external drives.

matrix. The fluctuating current source $I_j^{\rm fl}(\omega)$ at the resistor k induces a voltage $V_j(\omega) = \sum_k \zeta_{jk}(\omega)\, I_k^{\rm fl}(\omega)$ on resistor j, where the matrix $\zeta_{jk}(\omega)$ is found by using Kirchhoff's laws. (The matrix $\zeta_{jk}(\omega)$ should not be confused with the impedance matrix which relates the total currents, not the fluctuating sources.) Then, using Eqs. (III.6.3), (III.6.4) and the relation $Z_j(\omega)\, I_j^{\rm fl}(\omega) = [2\,\mathrm{Re}\, Z_j(\omega)] I_j^-(\omega)$, we can express the scattering matrix as

$$S_{jk}(\omega) = \frac{2\lambda_j(\omega)\lambda_k(\omega)}{Z_j(\omega)\, Z_k(\omega)}\, \zeta_{jk}(\omega) - \delta_{jk}\, \frac{\lambda_j(\omega) Z_j^*(\omega)}{\lambda_j^*(\omega) Z_j(\omega)}. \tag{III.6.5}$$

In a reciprocal circuit, the matrix $\zeta_{jk}(\omega)$ is symmetric, and so is $S_{jk}(\omega)$. Non-reciprocity can be included via non-reciprocal circuit elements such as circulators [183].

Energy current.— We define the power, injected into the j-th resistor from the rest of the circuit, as $\hat{\mathcal{P}}_j(t) \equiv \{\hat{I}_j(t), \hat{V}_j(t)\}/2$. For its time average, Eqs. (III.6.3) give the natural expression

$$\int_{-\tau/2}^{\tau/2} \frac{dt}{\tau}\, \hat{\mathcal{P}}_j(t) \underset{\tau\to\infty}{\sim} \frac{1}{\tau} \int_0^\infty d\omega\, \hbar\omega \sum_{\sigma=\pm} \sigma\, \hat{a}_{j,\omega}^{\sigma\,\dagger} \hat{a}_{j,\omega}^{\sigma}, \tag{III.6.6}$$

which is determined by the number operator of incident and scattered excitations, each carrying energy $\hbar\omega$. The same expression is obtained for the time average of the power $\{\hat{\mathcal{I}}_j(0,t), \hat{\mathcal{V}}_j(0,t)\}/2$ injected into the j-th TL from Eqs (III.6.1). Thus, the introduced filter is indeed non-dissipative, although it can accumulate some energy for a finite interval of time, as any reactive element.
We express the dissipated power (energy current) operator in terms of the incident creation/annihilation operators $\hat{\alpha}_{j,\omega>0} \equiv \hat{a}_{j,\omega}^-$ and $\hat{\alpha}_{j,\omega<0} \equiv \hat{a}_{j,\omega}^{-\dagger}$, which then reads

$$\hat{\mathcal{P}}_j(t) = -\iint_{-\infty}^{\infty} \frac{d\omega\, d\omega'}{4\pi}\, \hbar\sqrt{|\omega\omega'|}\, e^{i(\omega-\omega')t} \sum_{k,l} A_{kl}^j(\omega,\omega')\, \hat{\alpha}_{k,\omega}^\dagger \hat{\alpha}_{l,\omega'}, \tag{III.6.7a}$$

where we defined $S_{ij}(\omega<0) = S_{ij}^*(\omega)$, and the matrix $A_{kl}^j(\omega,\omega')$ is given by

$$\begin{aligned} A_{kl}^j(\omega,\omega') = &-\frac{Z_j^*(\omega)+Z_j(\omega')}{2\lambda_j^*(\omega)\lambda_j(\omega')}\, S_{jk}^*(\omega)\, S_{jl}(\omega') - \frac{Z_j(\omega)-Z_j(\omega')}{2\lambda_j(\omega)\lambda_j(\omega')}\, \delta_{jk} S_{jl}(\omega') \\ &+ \frac{Z_j^*(\omega)-Z_j^*(\omega')}{2\lambda_j^*(\omega)\lambda_j^*(\omega')}\, S_{jk}^*(\omega)\, \delta_{jl} + \frac{Z_j(\omega)+Z_j^*(\omega')}{2\lambda_j(\omega)\lambda_j^*(\omega')}\, \delta_{jk}\delta_{jl}. \end{aligned} \tag{III.6.7b}$$

These expressions can be viewed as the extension of the general Büttiker's formula [14, 15] to the case of energy current, and represent the main formal result of our work. The energy current operator does not conserve the particle number, as it contains terms $\hat{a}_{j,\omega}^{-\dagger}\hat{a}_{k,\omega'}^{-\dagger}, \hat{a}_{j,\omega}^{-}\hat{a}_{k,\omega'}^{-}$. This highlights a difference between mesoscopic electronic transport and radiative energy transport, where energy is carried by the electromagnetic field rather than by particles [184, 185], leading to these additional terms.

To understand the origin of the difference between Eqs. (III.6.7) and the simpler Büttiker's formula, we note that the latter is recovered if instead of the power flowing into the whole impedance $Z_j(\omega)$, one considers the power flowing into its TL part; it is obtained by setting $Z_j, Z_j^* \to z_j$ and $\lambda_j \to \sqrt{z_j}$ in Eq. (III.6.7b) with the same scattering matrix. This Büttiker-like energy current $\hat{\mathcal{P}}_j^B(t)$ matches that in Refs. [14, 15], where the effective particle velocity $v_j \propto 1/z_j$. Here, the frequency dependence of $Z_j(\omega)$ necessarily implies $\mathrm{Im}\, Z_j(\omega) \neq 0$ due to Kramers-Kronig relations and results in a reactive component of the reservoir, where energy can be stored temporarily. The reactive contribution $\hat{\mathcal{P}}_j - \hat{\mathcal{P}}_j^B$ has no counterpart in the particle current since particle velocity must be real, even if energy-dependent.
Equations (III.6.7) result in a Landauer-type expression for the average dissipated power (or average energy current),

$$\langle \hat{\mathcal{P}}_j \rangle = \sum_k \int_0^\infty \frac{d\omega}{2\pi}\, \hbar\omega |S_{jk}(\omega)|^2 \left[n_k(\omega) - n_j(\omega)\right], \tag{III.6.8}$$

well-known in the context of NFRHT; here we see how the transmission coefficient $|S_{jk}(\omega)|^2$, usually introduced phenomenologically, arises explicitly from the scattering framework. The added value of Eqs. (III.6.7) is that they enable one to calculate all higher-order correlation functions of the energy current, just like the Büttiker's formula for the electric current. Indeed, the incident excitations being in the thermal state, arbitrary averages of the $\hat{\alpha}_{j,\omega}$ operators can be evaluated from the pair average $\langle \hat{\alpha}_{j,\omega} \hat{\alpha}_{k,\omega'} \rangle = \delta_{jk}\delta(\omega+\omega')\, n_j(\omega')\, \mathrm{sgn}\,\omega'$ using Wick's theorem [2]. Note that the correlations $\langle \hat{a}^{-\dagger}_{j,\omega} \hat{a}^{-\dagger}_{k,\omega'} \rangle, \langle \hat{a}^{-}_{j,\omega} \hat{a}^{-}_{k,\omega'} \rangle$ vanish, ensuring that all observables depend solely on the occupation number. Power correlations cannot be computed in the semiclassical FED framework, which contains only the average anticommutator of fluctuating currents, since correlators of order 2 and higher also involve commutators.

Heat current noise spectrum.— Energy current correlations between two reservoirs j and k are given by

$$\begin{aligned} W_{jk}(\Omega) &= \int_{-\infty}^{\infty} dt\, e^{i\Omega t} \left[\frac{1}{2} \left\langle \{\hat{\mathcal{P}}_j(t), \hat{\mathcal{P}}_k(0)\} \right\rangle - \langle \hat{\mathcal{P}}_j \rangle \langle \hat{\mathcal{P}}_k \rangle \right] \\ &= \sum_{l,m} \int_{-\infty}^{\infty} \frac{d\omega}{16\pi} \hbar^2 \omega(\omega+\Omega) A^j_{lm}(\omega, \omega+\Omega) A^k_{ml}(\omega+\Omega, \omega) \\ &\quad \times \left[\coth \frac{\hbar\omega}{2T_l} \coth \frac{\hbar(\omega+\Omega)}{2T_m} - 1 \right]. \end{aligned} \tag{III.6.9}$$

A similar expression $W^B_{jk}(\Omega)$, matching the one in Refs. [14, 15], can be constructed for the the correlations of energy currents $\hat{\mathcal{P}}_j^B(t)$ between TLs, by re-

[2] Wick's theorem guarantees that energy current correlators do not depend on the phases $\vartheta_j(\omega)$. Indeed, $S_{jk}(\omega) \propto e^{i\vartheta_j(\omega)+i\vartheta_k(\omega)}$ and $A^j_{kl}(\omega,\omega') \propto e^{-i\vartheta_k(\omega)+i\vartheta_l(\omega')}$, so each annihilation/creation operator $\hat{\alpha}_{j,\omega}$ in Eq. (III.6.7a) is accompanied by the corresponding phase factor. Since $\vartheta_j(\omega) = -\vartheta_j(-\omega)$, the phase factors cancel out upon averaging.

placing $Z_j, Z_j^* \to z_j$ and $\lambda_j \to \sqrt{z_j}$ in Eq. (III.6.7b) for $A^j_{kl}(\omega,\omega')$ [3]. In contrast to Eq. (III.6.9), thus defined $W^B_{jk}(\Omega)$ depends on the phases $\vartheta_j(\omega)$, unlike the average $\langle\hat{\mathcal{P}}^B_j(t)\rangle = \langle\hat{\mathcal{P}}_j(t)\rangle$.
The simple physical reason for such behavior is that a reactive element can accumulate some energy for a finite amount of time, and thus affect finite-frequency heat current fluctuations, while a finite average current can only be accommodated by a dissipative element. Which reactive elements must be included into the reservoirs and which belong to the external circuit depends on their microscopic nature and on how the energy current is actually measured. Typically, one measures changes in electronic temperatures and its fluctuations [155]. For example, a small piece of metal with the Drude conductivity $\sigma(\omega) = \sigma_0/(1-i\omega\tau)$ (τ being the momentum relaxation time) can be effectively represented as a resistor and an inductor in series. A tunnel junction is equivalent to a resistor and a capacitor in parallel. However, in both cases the reactive and the dissipative components are effectively made of the same electrons, there is no way to physically separate them, so $\hat{\mathcal{P}}^B(t)$ is not measurable. Importance of the reactive contribution to the noise can be illustrated in some simple circuits (see Sec. III.7.2), and is particularly manifest in fluctuations of NFRHT between two dielectrics via coupled surface phonon-polaritons [148]. This physics (electric coupling between two polarization oscillators) can be mimicked by the effective circuit with two RLC contours, hosting weakly damped resonances at frequency $\omega_L = \sqrt{1/(LC_T)+1/(LC_c)}$, and coupled by the capacitances $C_\pm$(Fig. III.12 and Sec. III.7.3). The frequency of the coupled symmetric (antisymmetric) mode is $\omega_\pm = \sqrt{1/(LC_T)+1/(LC_c+LC_\pm)}$, and their amplitude decay rate $\gamma = R/(2L)$. The Poynting vector in the vacuum gap separating the two dielectrics corresponds to the power deposited into each RLC contour, which is thus treated as a dissipative bath with impedance

$$Z(\omega) = \left(-i\omega C_c - \frac{i\omega C_T}{1-\omega^2 LC_T - i\omega RC_T}\right)^{-1}, \tag{III.6.10}$$

while the capacitances $C_\pm$ make the coupling circuit. We choose $\lambda(\omega) = [\sqrt{R}/(LC_c)]/(\omega_L^2-\omega^2-2i\omega\gamma)$ and find (see Sec. III.7.3)

$$|S_{12}(\omega)|^2 = \frac{(2\gamma\omega)^2(\omega_+^2-\omega_-^2)^2}{\prod_{\sigma=\pm}[(\omega_\sigma^2-\omega^2)^2+(2\gamma\omega)^2]}. \tag{III.6.11}$$

Generally, fluctuations are more important in smaller systems, for which the circuit description is also expected to be most suitable. In Fig. III.12 we plot $W_{11}(\Omega)$ and $W^B_{11}(\Omega)$ for the circuit parameters representative of two pieces of dielectric of volume $(30\,\text{nm})^3$, separated by a vacuum gap of size $d = 30\,\text{nm}$: the typical capacitance $C_T = 1$ aF, $1/\sqrt{LC_T}, \omega_L = (1.5, 1.8)\times 10^{14}\ \text{s}^{-1}$ (transverse and longitudinal optical phonons in SiC, respectively), $\omega_+, \omega_- = (1.7, 1.6)\times 10^{14}\text{s}^{-1}$, $\gamma = 5\times 10^{11}\text{s}^{-1}$, which fix all circuit parameters, and $T_2 = 300\ \text{K} \gg T_1$. The reactive contribution

[3] A minor difference from the particle current fluctuations in Refs. [14, 15] is the contribution from averages $\langle\hat{\alpha}_{k,\omega_1}\hat{\alpha}_{l,\omega_2}\rangle\langle\hat{\alpha}^\dagger_{k',\omega_1'}\hat{\alpha}^\dagger_{l',\omega_2'}\rangle$ coming from Wick's theorem. Due to the symmetry $A^j_{kl}(-\omega,-\omega') = A^j_{lk}(\omega',\omega)$, this only produces a factor of 2 in $W_{ij}(\Omega)$.

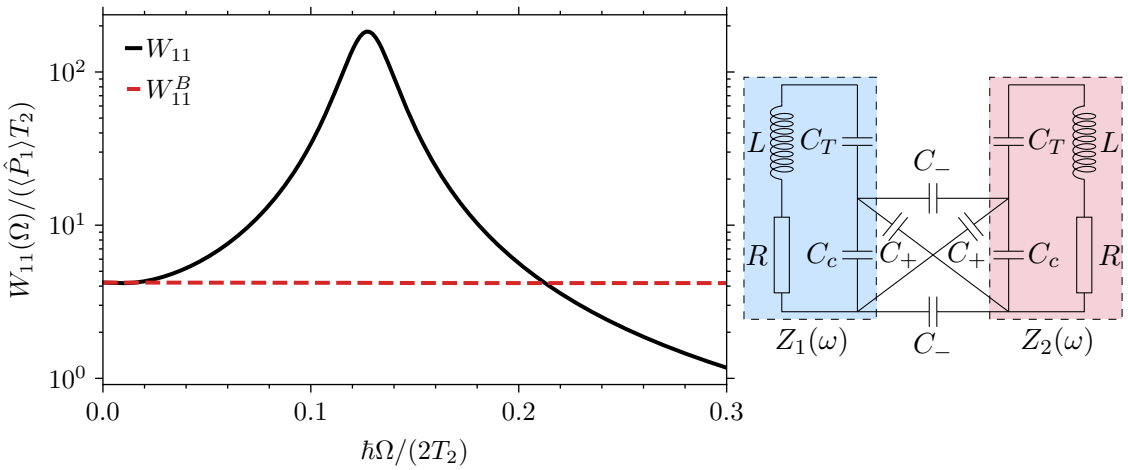

Figure III.12: *Heat current noise spectrum* $W_{11}(\Omega)$ (solid line) and the Büttiker-like contribution $W_{11}^B(\Omega)$ (dashed line), for the circuit mimicking heat transfer via surface polaritons (right of panel) with $L = 44$pH, $C_T = 1$aF, $C_c = 2.3$aF, $C_+ = 1.5$aF, $C_- = 1.0$aF, $R = 44\Omega$ at $T_1 \to 0$, $T_2 = 300$ K.

dominates in a wide range of Ω and has a prominent peak at $\Omega = |\omega_+ - \omega_-|$. This peak corresponds to oscillations in the time domain, found in Ref. [148].

To prove that the circuit in Fig. III.12 does indeed provide a correct model for the NFRHT via coupled surface phonon-polaritons, in Appendix III.7.4 we present a microscopic calculation for two dielectrics separated by a planar vacuum gap, using non-equilibrium Green's functions. By comparing the two calculations, one can see that each heat conduction channel (in the planar geometry specified by the in-plane wave vector) behaves exactly as the effective circuit. This confirms the common knowledge that the circuit representation works when the electromagnetic coupling is dominated by just a few modes (which is often the case for small objects at low temperatures). At the same time, the Green's function calculation is much heavier, and the relation to the standard Landauer-Büttiker framework is not manifest. In a similar fashion, equivalence of scattering approach to the Green's function formalism can be established rather straightforwardly for each specific system (since the use of Green's functions is always based on a specific microscopic model with a certain Hamiltonian).

III.6.2 Scattering Approach to Radiative Heat Transfer Between Extended Bodies

The scattering problem developed for heat transfer in circuits can be straightforwardly extended to the standard picture of radiative heat transport between spatially extended bodies and fields described by Maxwell's equations. Let us focus on structures described by a position-dependent local isotropic optical conductivity $\sigma(\mathbf{r}, \omega)$ (or, equivalently, dielectric function $\varepsilon(\mathbf{r}, \omega) = 1 + 4\pi i\sigma(\mathbf{r}, \omega)/\omega$) without spatial dispersion, which covers most of situations studied in the literature. The crucial step to construct the scattering problem is to note that each

spatial point $\mathbf{r}$ where $\operatorname{Re}\sigma(\mathbf{r},\omega) > 0$ effectively represents an independent dissipative bath, uncorrelated with those at neighboring points. All subsequent steps are quite analogous to the circuit case, even though some short-distance regularization is required to make them well-defined mathematically. Obviously, $\sigma(\mathbf{r},\omega)$ of the material plays the same physical role as the admittance $1/Z_j(\omega)$ of circuit elements.

First of all, we define a function $\kappa(\mathbf{r},\omega)$, holomorphic for $\operatorname{Im}\omega > 0$ and such that $|\kappa(\mathbf{r},\omega)|^2 = \operatorname{Re}\sigma(\mathbf{r},\omega)$. For a Drude metal,

$$\sigma(\omega) = \frac{\sigma_{\mathrm{dc}}}{1-i\omega\tau}, \quad \kappa(\omega) = \frac{\sqrt{\sigma_{\mathrm{dc}}}}{1-i\omega\tau}, \tag{III.6.12}$$

while for an insulator with an optical phonon resonance, described by the Drude-Lorentz model,

$$\sigma(\omega) = \frac{\omega_L^2-\omega_T^2}{4\pi}\,\frac{i\omega}{\omega^2+2i\gamma\omega-\omega_T^2}, \tag{III.6.13a}$$

$$\kappa(\omega) = \sqrt{\frac{\gamma(\omega_L^2-\omega_T^2)}{4\pi}}\,\frac{i\omega}{\omega^2+2i\gamma\omega-\omega_T^2}. \tag{III.6.13b}$$

Instead of the current and voltage at each resistor, we have the current density and the electric field at each point $\mathbf{r}$ with Cartesian components labeled by $k,l = x,y,z$:

$$\hat{j}_k(\mathbf{r},t) = \int_0^\infty d\omega \sqrt{\frac{\hbar\omega}{4\pi}}\left[\frac{\sigma(\mathbf{r},\omega)}{\kappa(\mathbf{r},\omega)}\,\hat{a}^+_{k,\mathbf{r},\omega} + \frac{\sigma^*(\mathbf{r},\omega)}{\kappa^*(\mathbf{r},\omega)}\,\hat{a}^-_{k,\mathbf{r},\omega}\right]e^{-i\omega t} + \text{h.c.}, \tag{III.6.14a}$$

$$\hat{E}_k(\mathbf{r},t) = \int_0^\infty d\omega \sqrt{\frac{\hbar\omega}{4\pi}}\left[\frac{1}{\kappa(\mathbf{r},\omega)}\,\hat{a}^+_{k,\mathbf{r},\omega} - \frac{1}{\kappa^*(\mathbf{r},\omega)}\,\hat{a}^-_{k,\mathbf{r},\omega}\right]e^{-i\omega t} + \text{h.c.}. \tag{III.6.14b}$$

The bosonic operators $\hat{a}^-_{k,\mathbf{r},\omega}$ of the incident matter excitations have the commutation relations $[\hat{a}^-_{k,\mathbf{r},\omega}, \hat{a}^{-\dagger}_{l,\mathbf{r}',\omega'}] = \delta_{kl}\,\delta(\mathbf{r}-\mathbf{r}')\,\delta(\omega-\omega')$, and thermal averages $\langle \hat{a}^{-\dagger}_{k,\mathbf{r},\omega}\,\hat{a}^-_{l,\mathbf{r}',\omega'}\rangle = \delta_{kl}\,\delta(\mathbf{r}-\mathbf{r}')\,\delta(\omega-\omega')\,n(\mathbf{r},\omega)$, where $n(\mathbf{r},\omega) = [e^{-\hbar\omega/T(\mathbf{r})}-1]^{-1}$ is the Bose-Einstein distribution with the local temperature $T(\mathbf{r})$. The operators $\hat{a}^+_{k,\mathbf{r},\omega}$ of the scattered excitations are related to the incident ones via the scattering matrix, which now also involves integration over spatial variables:

$$\hat{a}^+_{k,\mathbf{r},\omega} = \sum_l \int d^3\mathbf{r}'\,\mathcal{S}_{kl}(\mathbf{r},\mathbf{r}',\omega)\,\hat{a}^-_{l,\mathbf{r}',\omega}. \tag{III.6.15}$$

The scattering matrix can be found by solving Maxwell's equations in the given structure. To see how it works, let us represent the total current density as a sum of the fluctuating (quantum Langevin) source and the current induced by the electric field, which is conveniently done in the frequency domain: $\hat{\mathbf{j}}(\mathbf{r},\omega) = \sigma(\mathbf{r},\omega)\hat{\mathbf{E}}(\mathbf{r},\omega) + \hat{\mathbf{j}}^{\mathrm{fl}}(\mathbf{r},\omega)$. Eq. (III.6.14a) then gives

$$\hat{j}^{\mathrm{fl}}_k(\mathbf{r},t) = \int_0^\infty d\omega \sqrt{\frac{\hbar\omega}{4\pi}}\,2\kappa(\mathbf{r},\omega)\,\hat{a}^-_{k,\mathbf{r},\omega}e^{-i\omega t} + \text{h.c.}. \tag{III.6.16}$$

The electric field operator satisfies the Maxwell's equations with the total current as a source. Separating the fluctuating part, we arrive at the familiar equation

$$\boldsymbol{\nabla}\times\boldsymbol{\nabla}\times\hat{\mathbf{E}}(\mathbf{r},\omega)-\frac{\omega^2}{c^2}\left[1+\frac{4\pi\sigma(\mathbf{r},\omega)}{-i\omega}\right]\hat{\mathbf{E}}(\mathbf{r},\omega)=\frac{4\pi i\omega}{c^2}\,\hat{\mathbf{j}}^{\text{fl}}(\mathbf{r},\omega), \tag{III.6.17}$$

which relates the electric field to the fluctuating current sources (the expression in the square brackets is nothing but the dielectric function of the medium). Its solution in a given structure can be written as

$$\hat{E}_k(\mathbf{r},\omega)=-\sum_l\int d^3\mathbf{r}'\,\frac{\mathcal{D}^R_{kl}(\mathbf{r},\mathbf{r}',\omega)}{-i\omega}\,\hat{j}^{\text{fl}}_l(\mathbf{r}',\omega), \tag{III.6.18}$$

where $\mathcal{D}^R_{kl}(\mathbf{r},\mathbf{r}',\omega)$ is the same Green's function of the electric field as in the microscopic description in Sec. III.7.4. Note that $\mathcal{D}^R_{kl}(\mathbf{r},\mathbf{r}',\omega)/(i\omega)$ plays the same role as the matrix $\zeta_{ij}(\omega)$ played for circuits (response of the voltages to external current sources). Matching Eq. (III.6.14b), we relate the scattering matrix to the electric field Green's function:

$$\mathcal{S}_{kl}(\mathbf{r},\mathbf{r}',\omega)=2\kappa(\mathbf{r},\omega)\,\frac{\mathcal{D}^R_{kl}(\mathbf{r},\mathbf{r}',\omega)}{i\omega}\,\kappa(\mathbf{r}',\omega)+\delta_{kl}\,\delta(\mathbf{r}-\mathbf{r}')\,\frac{\kappa(\mathbf{r},\omega)}{\kappa^*(\mathbf{r},\omega)}. \tag{III.6.19}$$

The dissipated power density $\hat{\mathcal{P}}(\mathbf{r})$ at each point $\mathbf{r}$ is given by the usual Joule losses:

$$\begin{aligned}\hat{\mathcal{P}}(\mathbf{r},t)&=\frac{1}{2}\left[\hat{\mathbf{E}}(\mathbf{r},t)\cdot\hat{\mathbf{j}}(\mathbf{r},t)+\hat{\mathbf{j}}(\mathbf{r},t)\cdot\hat{\mathbf{E}}(\mathbf{r},t)\right]\\&=-\int_{-\infty}^{\infty}\frac{d\omega'\,d\omega''}{4\pi}\,\hbar\sqrt{|\omega'\omega''|}\,e^{i(\omega'-\omega'')t}\sum_{l',l''}\int d^3\mathbf{r}'\,d^3\mathbf{r}''\,\mathcal{A}_{l'l''}(\mathbf{r},\mathbf{r}',\mathbf{r}'';\omega',\omega'')\\&\quad\times\hat{\alpha}^\dagger_{l',\mathbf{r}',\omega'}\hat{\alpha}_{l'',\mathbf{r}'',\omega''},\end{aligned} \tag{III.6.20a}$$

$$\begin{aligned}\mathcal{A}_{l'l''}(\mathbf{r},\mathbf{r}',\mathbf{r}'';\omega',\omega'')&=-\frac{\sigma^*(\mathbf{r},\omega')+\sigma(\mathbf{r},\omega'')}{2\kappa^*(\mathbf{r},\omega')\,\kappa(\mathbf{r},\omega'')}\sum_k\mathcal{S}^*_{kl'}(\mathbf{r},\mathbf{r}',\omega')\,\mathcal{S}_{kl''}(\mathbf{r},\mathbf{r}'',\omega'')\\&\quad-\frac{\sigma(\mathbf{r},\omega')-\sigma(\mathbf{r},\omega'')}{2\kappa(\mathbf{r},\omega')\,\kappa(\mathbf{r},\omega'')}\,\delta(\mathbf{r}-\mathbf{r}')\,\mathcal{S}_{l'l''}(\mathbf{r},\mathbf{r}'',\omega'')\\&\quad+\frac{\sigma^*(\mathbf{r},\omega')-\sigma^*(\mathbf{r},\omega'')}{2\kappa^*(\mathbf{r},\omega')\,\kappa^*(\mathbf{r},\omega'')}\,\mathcal{S}^*_{l''l'}(\mathbf{r},\mathbf{r}',\omega')\,\delta(\mathbf{r}-\mathbf{r}'')\\&\quad+\frac{\sigma(\mathbf{r},\omega')+\sigma^*(\mathbf{r},\omega'')}{2\kappa(\mathbf{r},\omega')\,\kappa^*(\mathbf{r},\omega'')}\,\delta_{l'l''}\,\delta(\mathbf{r}-\mathbf{r}')\,\delta(\mathbf{r}-\mathbf{r}'')\\&=-2\,\kappa^*(\mathbf{r}',\omega')\,\kappa(\mathbf{r}'',\omega'')[\sigma^*(\mathbf{r},\omega')+\sigma(\mathbf{r},\omega'')]\\&\quad\times\sum_k\frac{\mathcal{D}^{R*}_{kl}(\mathbf{r},\mathbf{r}',\omega')\,\mathcal{D}^R_{kl''}(\mathbf{r},\mathbf{r}'',\omega'')}{\omega'\omega''}\\&\quad-2\,\kappa^*(\mathbf{r}',\omega')\,\kappa(\mathbf{r}'',\omega'')\left[\delta(\mathbf{r}-\mathbf{r}')\,\frac{\mathcal{D}^R_{l'l''}(\mathbf{r},\mathbf{r}'',\omega'')}{-i\omega''}\right.\\&\quad\left.+\frac{\mathcal{D}^{R*}_{l''l'}(\mathbf{r},\mathbf{r}',\omega')}{i\omega'}\,\delta(\mathbf{r}-\mathbf{r}'')\right],\end{aligned} \tag{III.6.20b}$$

where we defined $\hat{\alpha}_{k,\mathbf{r},\omega>0} \equiv \hat{a}^{-}_{k,\mathbf{r},\omega}$ and $\hat{\alpha}_{k,\mathbf{r},\omega<0} \equiv \hat{a}^{-\dagger}_{k,\mathbf{r},\omega}$. Then, one can calculate arbitrary correlators of the power density, like $\langle \hat{\mathcal{P}}(\mathbf{r},t)\,\hat{\mathcal{P}}(\mathbf{r}',t')\rangle$, etc.
The scattering matrix $\mathcal{S}_{kl}(\mathbf{r},\mathbf{r}',\omega)$, even though a natural object in any scattering problem, in the present setting may lead to mathematically ill-defined expressions, which should be handled with care. For example, in the average dissipated power we have to deal with the square of the δ function,

$$\begin{aligned}\langle \hat{\mathcal{P}}(\mathbf{r})\rangle &= \int_0^\infty \frac{d\omega}{4\pi}\,\hbar\omega \int d^3\mathbf{r}'\,[2n(\mathbf{r}',\omega)+1]\left[\sum_{k,l}|\mathcal{S}_{kl}(\mathbf{r},\mathbf{r}',\omega)|^2 - 3\delta^2(\mathbf{r}-\mathbf{r}')\right]\\ &= \int_0^\infty \frac{d\omega}{2\pi}\,\hbar\omega \int d^3\mathbf{r}' \sum_{k,l}|\mathcal{S}_{kl}(\mathbf{r},\mathbf{r}',\omega)|^2[n(\mathbf{r}',\omega)-n(\mathbf{r},\omega)] \qquad \text{(III.6.21)}\end{aligned}$$

where we used $n(\mathbf{r}',\omega)\,\delta^2(\mathbf{r}-\mathbf{r}') = n(\mathbf{r},\omega)\,\delta^2(\mathbf{r}-\mathbf{r}')$, as well as the unitarity of the scattering matrix in the form

$$\sum_l \int d^3\mathbf{r}'\,|\mathcal{S}_{kl}(\mathbf{r},\mathbf{r}',\omega')|^2 = \delta(\mathbf{r}=0) = \int d^3\mathbf{r}'\,\delta^2(\mathbf{r}-\mathbf{r}'). \qquad \text{(III.6.22)}$$

Thus, the transmission probability $|S_{12}(\mathbf{q},\omega)|^2$, found in the microscopic description in Sec. III.7.4, is related to the scattering matrix which has a natural block structure in the in-plane momentum:

$$|S_{12}(\mathbf{q},\omega)|^2 = \sum_{k,l}\int_{d/2}^{\infty} dz \int_{-\infty}^{-d/2} dz'\,|\mathcal{S}_{kl}(z,z',\mathbf{q},\omega)|^2. \qquad \text{(III.6.23)}$$

From the practical point of view, it is more convenient to equivalently express the result in terms of $\mathcal{D}^R_{kl}(\mathbf{r},\mathbf{r}',\omega)$, which does not suffer from short-distance singularities:

$$\begin{aligned}\langle \hat{\mathcal{P}}(\mathbf{r})\rangle = &\int_0^\infty \frac{d\omega}{\pi}\,\hbar\omega \sum_{k,l}\int d^3\mathbf{r}'\,[2n(\mathbf{r}',\omega)+1]\,\frac{\mathrm{Re}\,\sigma(\mathbf{r},\omega)}{\omega}\\ &\times\left[|\mathcal{D}^R_{kl}(\mathbf{r},\mathbf{r}',\omega')|^2\,\frac{\mathrm{Re}\,\sigma(\mathbf{r}',\omega)}{\omega} + \mathrm{Im}\,\mathcal{D}^R_{kk}(\mathbf{r},\mathbf{r},\omega)\,\delta_{kl}\,\delta(\mathbf{r}-\mathbf{r}')\right]. \qquad \text{(III.6.24)}\end{aligned}$$

Using the relation

$$\mathrm{Im}\,\mathcal{D}_{kk}(\mathbf{r},\mathbf{r},\omega) = -\sum_l \int d^3\mathbf{r}\,|\mathcal{D}^R_{kl}(\mathbf{r},\mathbf{r}',\omega')|^2\,\frac{\mathrm{Re}\,\sigma(\mathbf{r}',\omega)}{\omega}, \qquad \text{(III.6.25)}$$

which can be obtained from Eq. (III.6.17) and its complex conjugate, we arrive at the standard Caroli formula for the dissipated power:

$$\langle \hat{\mathcal{P}}(\mathbf{r})\rangle = \int_0^\infty \frac{d\omega}{\pi}\,2\hbar\omega \sum_{k,l}\int d^3\mathbf{r}'\,[n(\mathbf{r}',\omega)-n(\mathbf{r},\omega)]\,\frac{\mathrm{Re}\,\sigma(\mathbf{r},\omega)}{\omega}\,|\mathcal{D}^R_{kl}(\mathbf{r},\mathbf{r}',\omega')|^2\,\frac{\mathrm{Re}\,\sigma(\mathbf{r}',\omega)}{\omega}. \qquad \text{(III.6.26)}$$

Note that $\sigma(\mathbf{r},\omega)/(-i\omega)$ is nothing but the retarded polarization operator of the medium, see Eq. (III.7.54a). In the same way, one can obtain equivalent expressions for higher-order correlators of dissipated power in terms of the scattering matrix or in terms of the matter and field Green's functions.
The presented scattering problem construction is fully analogous to that in circuits. The situation becomes a bit less straightforward if the spatial dispersion should be taken into account in the optical conductivity. In this case, it becomes an integral operator with the kernel $\sigma_{kl}(\mathbf{r},\mathbf{r}',\omega)$, and one cannot treat each spatial point as an independent bath. Instead, at each ω one should diagonalize the operator $\mathrm{Re}\,\sigma_{kl}(\mathbf{r},\mathbf{r}',\omega)$, and each eigenmode of this operator can be represented as an independent scattering channel with incident and scattered excitation. Then the construction again becomes analogous, although solution of the Maxwell's equations becomes quite difficult, as is usually the case in the presence of spatial dispersion.
Another complication arises from the fact that besides the absorbing bodies, the system may have one more dissipative bath, corresponding to radiation at $|\mathbf{r}| \to \infty$. This depends on the geometry of the problem: while for the textbook example of heat transfer between two semi-infinite half-spaces (metallic or dielectric), separated by a vacuum gap, all radiation is eventually absorbed by the material, the case of two spheres involves photons that can escape to infinity, as well as thermal photons incident from infinity. These represent additional scattering channels, and only upon inclusion of these channels the scattering matrix becomes unitary. More detailed study of this issue is beyond the scope of our work.

III.6.3 Conclusions

We have developed a quantum-mechanical scattering theory for NFRHT problem, which enables one to calculate fluctuations of the energy current. Our general expression differs from Büttiker's formula for particle current fluctuations in the presence of reactive components in the energy reservoir. We show that this reactive contribution can dominate the energy current fluctuations at finite frequencies. To determine it correctly, it is important to precisely define how the energy current is measured. Our construction describes scattering of matter excitations due to their coupling to the electromagnetic field, and has some limitations. Temperature dependence of the scattering matrix is not naturally included, similarly to the Landauer-Büttiker approach to electron transport; temperature dependence arises from many-body effects inside the material (such as electron-electron interactions or phonon anharmonicity), so a description in terms of scattering of single excitations is, at best, approximate, if valid at all. Heat transfer via phonons or electrons is far beyond our construction (in the same way as it is beyond FED), since it represents a totally different physical mechanism involving matter excitations themselves.

III.7 Appendix

III.7.1 Resistor Under a Classical Drive

Here we show that Eqs. (III.6.3) for the voltage and current operators are consistent with the standard definition of the impedance. The impedance $Z(\omega)$ of a circuit element can be defined either via the response of the current through this element to an externally applied monochromatic voltage source, or via the response of the voltage to an external current source.
Let us connect an external voltage source $V_{\text{ext}}e^{-i\omega_{\text{ext}}t} + V^*_{\text{ext}}e^{i\omega_{\text{ext}}t}$ to the jth resistor. This means that the voltage operator $\hat{V}_j(t)$ is constrained to have this value, thus becoming a pure number. Interpreting this condition,

$$\int_0^\infty d\omega \sqrt{\frac{\hbar\omega}{4\pi}} \left[\frac{Z_j(\omega)}{\lambda_j(\omega)}\, \hat{a}^+_{j,\omega} + \frac{Z^*_j(\omega)}{\lambda^*_j(\omega)}\, \hat{a}^-_{j,\omega} \right] e^{-i\omega t} + \text{h.c.} = V_{\text{ext}} e^{-i\omega_{\text{ext}}t} + \text{c.c.}, \tag{III.7.1}$$

as an equation for $\hat{a}^+_{j,\omega}$, we apply Fourier transform on both sides, and find

$$\hat{a}^+_{j,\omega} = V_{\text{ext}}\, \frac{\lambda_j(\omega)}{Z_j(\omega)} \sqrt{\frac{4\pi}{\hbar\omega}}\, \delta(\omega - \omega_{\text{ext}}) - \frac{Z^*_j(\omega)}{Z_j(\omega)}\, \frac{\lambda_j(\omega)}{\lambda^*_j(\omega)}\, \hat{a}^-_{j,\omega}. \tag{III.7.2}$$

Such linear shift of the bosonic operators in the Heisenberg picture implies for the Schrödinger picture that if the incident excitations were in the vacuum state, then the scattered excitations are in the coherent state, resulting in a non-zero expectation value of the current. This expectation value can be easily found by averaging the Heisenberg operator $\hat{I}_j(t)$ [Eq. (2a) of the main text] over the vacuum state. Only the first term in Eq. (III.7.2) contributes to this non-zero average, yielding

$$\langle \hat{I}_j(t) \rangle = \frac{V_{\text{ext}}}{Z_j(\omega_{\text{ext}})}\, e^{-i\omega_{\text{ext}}t} + \text{c.c.}, \tag{III.7.3}$$

so that the impedance is indeed $Z_j(\omega)$. The same result is obtained if the incident excitations are in a thermal state.
If we connect an external current source $I_{\text{ext}}e^{-i\omega_{\text{ext}}t} + I^*_{\text{ext}}e^{i\omega_{\text{ext}}t}$, this results in imposing

$$\int_0^\infty d\omega \sqrt{\frac{\hbar\omega}{4\pi}} \left[\frac{1}{\lambda_j(\omega)}\, \hat{a}^+_{j,\omega} - \frac{1}{\lambda^*_j(\omega)}\, \hat{a}^-_{j,\omega} \right] e^{-i\omega t} + \text{h.c.} = I_{\text{ext}} e^{-i\omega_{\text{ext}}t} + \text{c.c.}. \tag{III.7.4}$$

Again, this condition enables us to express the scattered excitation operator as

$$\hat{a}^+_{j,\omega} = I_{\text{ext}} \lambda_j(\omega) \sqrt{\frac{4\pi}{\hbar\omega}}\, \delta(\omega - \omega_{\text{ext}}) + \frac{\lambda_j(\omega)}{\lambda^*_j(\omega)}\, \hat{a}^-_{j,\omega}, \tag{III.7.5}$$

yielding the average voltage

$$\langle \hat{V}_j(t) \rangle = I_{\text{ext}} Z_j(\omega_{\text{ext}})\, e^{-i\omega_{\text{ext}}t} + \text{c.c.}, \tag{III.7.6}$$

again corresponding to the impedance $Z_j(\omega)$.
In this picture, the Joule losses in the resistor correspond to emission of excitations into the transmission line. This can be checked by employing Eq. (III.7.2) or Eq. (III.7.5) to calculate the average of the power $\langle \hat{P}_j(t) \rangle$.

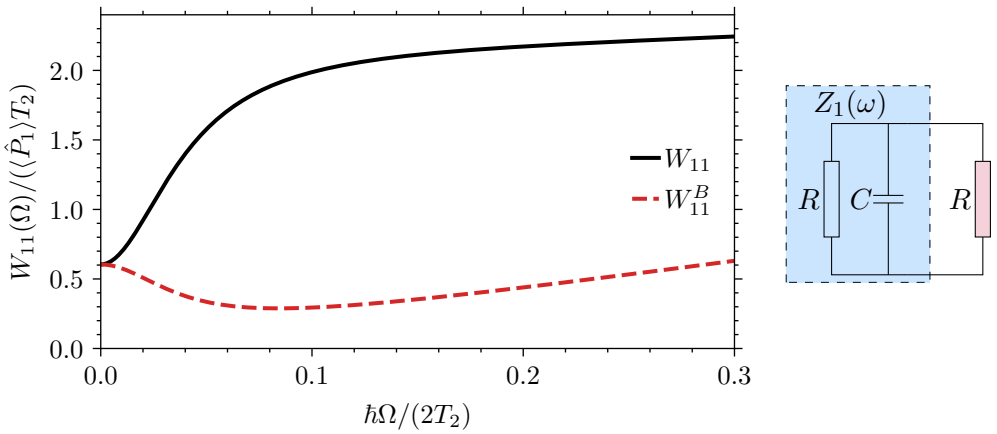

Figure III.13: *Heat current noise spectrum* $W_{11}(\Omega)$ (solid line) and the Büttiker-like contribution $W_{11}^B(\Omega)$ (dashed line) for the circuit shown in the inset. The impedance $Z_1(\omega)$ consists of a parallel RC element galvanically coupled to the second resistor R. Here, the RC time is chosen as $T_2RC/\hbar = 50$. Impedance temperature T_1 is assumed to be much smaller than the temperature T_2 of the second resistor.

III.7.2 Simple Circuits

Here we discuss simple circuits to illustrate the impact of reactive elements within the thermal reservoir, which becomes evident in the heat current noise spectrum but not in the average heat current. We calculate the noise spectrum for the specific examples of a low-pass and resonant-pass filter. Both cases can be viewed as two impedances $Z_{1,2}(\omega)$, galvanically connected in a loop. The scattering matrix for this configuration is straightforwardly found from Eqs. (III.6.3) of the main text and the conditions $\hat{V}_1 = \hat{V}_2$, $\hat{I}_1 = -\hat{I}_2$:

$$S = \frac{1}{Z_1 + Z_2}\begin{pmatrix} \lambda_1(Z_2 - Z_1^*)/\lambda_1^* & 2\lambda_1\lambda_2 \\ 2\lambda_1\lambda_2 & \lambda_2(Z_1 - Z_2^*)/\lambda_2^* \end{pmatrix}. \tag{III.7.7}$$

We focus on the power flowing into reservoir 1 and calculate $W_{11}(\Omega)$ assuming for simplicity $T_1 \ll T_2$. The Büttiker-like contribution $W_{11}^B(\Omega)$ matches with the total heat current noise spectrum $W_{11}(\Omega)$ when the reactive elements are excluded from the reservoir and included in the coupling circuit. In these specific examples, the heat current noise spectra $W_{11}(\Omega)$ and $W_{22}(\Omega)$ coincide, since the current and voltage across the impedance $Z_1(\omega)$ are the same as those across the resistor R.
According to Eq. (III.6.9), $W_{11}(\Omega)$ is given by a sum of four terms, $\sum_{l,m} W_{11}^{(lm)}(\Omega)$, each containing a factor $\coth[\hbar\omega/(2T_l)]\coth[\hbar(\omega+\Omega)/(2T_m)] - 1$ in the integrand for $l, m = 1, 2$. The term $W_{11}^{(22)}(\Omega)$ is due to excitations originating in the reservoir with temperature T_2, $W_{11}^{(11)}(\Omega)$ is due to excitations from the reservoir with temperature $T_1 \ll T_2$, and thus is negligibly small. The terms $W_{11}^{(12)}(\Omega)$ and $W_{11}^{(21)}(\Omega)$ are due to interference.

The low-pass filter consists of a parallel RC element with the impedance $Z_1(\omega) = R/(1-i\omega RC)$, coupled galvanically to a second resistor $Z_2(\omega) = R$ (see Fig. III.13).

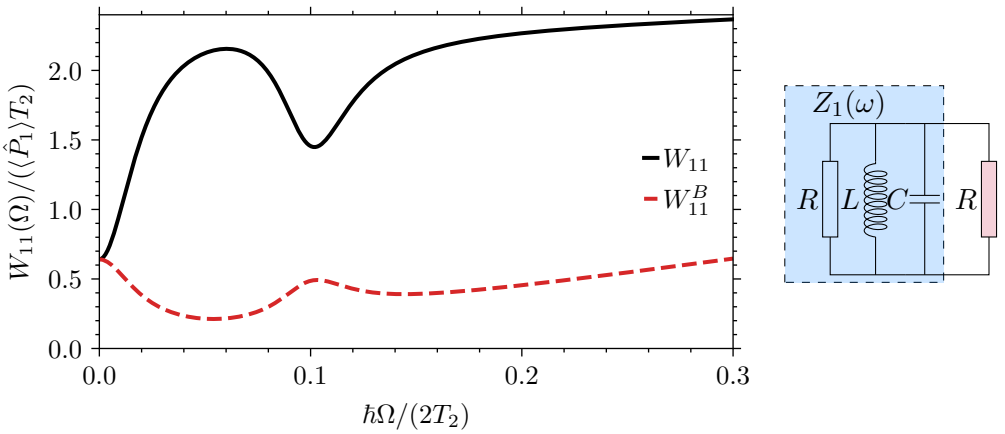

Figure III.14: *Heat current noise spectrum* $W_{11}(\Omega)$ (solid line) and the Büttiker-like contribution $W_{11}^B(\Omega)$ (dashed line) for the circuit shown in the inset. The impedance $Z_1(\omega)$ consists of a parallel RLC element galvanically coupled to the second resistor R. The RC time is chosen as $T_2RC/\hbar = 50$ and the resonance frequency as $T_2\sqrt{LC}/\hbar = 10$. Impedance temperature T_1 is assumed to be much smaller than the temperature T_2 of the second resistor.

Such circuit may represent an electronic tunnel junction. Choosing $\lambda_1(\omega) = \sqrt{R}/(1-i\omega RC)$, $\lambda_2(\omega) = \sqrt{R}$, we find the transmission function given by a Lorentzian

$$|S_{12}(\omega)|^2 = \frac{1}{1+\omega^2R^2C^2/4}, \tag{III.7.8}$$

where the RC-time corresponds to the inverse of the damping parameter. For $\hbar/(RC) \ll T_2$, the transmission function is sharply peaked around $\omega = 0$, and the average power is approximately $\langle\hat{P}_1\rangle \approx T_2/(2RC)$.
Assuming $\hbar\Omega \ll T_2$, we evaluate the frequency integral in Eq. (III.6.9), and find the Büttiker-like contribution given by

$$W_{11}^{B(22)}(\Omega) \approx \frac{T_2^2}{4RC}\frac{1}{1+(\Omega RC/4)^2}. \tag{III.7.9}$$

The full $W_{11}^{(22)}(\Omega)$ contains an additional factor

$$\frac{|Z_1(\omega)+Z_1^*(\omega+\Omega)|^2}{4\,\mathrm{Re}\,Z_1(\omega)\,\mathrm{Re}\,Z_1(\omega+\Omega)} = 1+(\Omega RC/2)^2,$$

which leads to

$$W_{11}^{(22)}(\Omega) \approx \frac{T_2^2}{4RC}\frac{1+(\Omega RC/2)^2}{1+(\Omega RC/4)^2}. \tag{III.7.10}$$

The two expressions behave quite differently; the Büttiker-like contribution peaks at $\Omega = 0$ and decays for $\Omega RC \gg 1$, while $W_{11}^{(22)}(\Omega)$ exhibits a dip at $\Omega = 0$. The interference terms $W_{11}^{B(12)}(\Omega) = W_{11}^{B(21)}(\Omega)$ are subleading in the limit $T_2 \gg \hbar\Omega$, but they grow linearly with frequency, $W_{11}^{B(12)}(\Omega) \approx T_2\hbar|\Omega|/(4RC)$, in the limit $\Omega RC \gg 1$. The interference terms play a minor role in the total spectrum $W_{11}(\Omega)$,

where $W_{11}^{(22)}(\Omega)$ dominates the behavior.
In the second example, two resistors are coupled via an LC resonator (see Fig. III.14), which may model a small metallic particle hosting a plasmonic resonance (represented by the LC resonator) together with electron-hole pair excitations (the resistor). The circuit partitioning is then determined by the energy measurement protocol, which may be either sensitive to electron-hole pairs only, or to the plasmonic energy as well. Let us calculate $W_{11}(\Omega)$ assuming that the LC resonator is included in the cold reservoir whose impedance is thus

$$Z_1(\omega) = \left(\frac{1}{R} - \frac{1}{i\omega L} - i\omega C\right)^{-1}, \tag{III.7.11}$$

then the Büttiker-like contribution $W_{11}^B(\Omega)$ will correspond to the first reservoir including only the resistor. We can choose

$$\lambda_1(\omega) = \frac{-i\omega L/\sqrt{R}}{1 - \omega^2 LC - i\omega L/R}, \tag{III.7.12}$$

which results in the transmission function

$$|S_{12}(\omega)|^2 = \frac{(2\omega\gamma)^2}{(\omega^2 - \omega_0^2)^2 + (2\omega\gamma)^2}, \tag{III.7.13}$$

where we denoted $\omega_0 \equiv 1/\sqrt{LC}$, $\gamma \equiv 1/(RC)$. The transmission function exhibits peaks at $\omega = \pm\omega_0$ resulting in peaks at $\Omega = 0, \pm 2\omega_0$ in the Büttiker component $W_{11}^{B(22)}(\Omega)$ [33] Again, the increase of $W_{11}^B(\Omega)$ for $\Omega \gtrsim 2\omega_0$ stems from the interference terms $W_{11}^{B(12)}(\Omega) = W_{11}^{B(21)}(\Omega)$. The full noise spectrum $W_{11}(\Omega)$ is quite different from $W_{11}^B(\Omega)$. Instead of peaks, $W_{11}(\Omega)$ displays dips at the locations $\Omega = 0, \pm 2\omega_0$. Its shape is primarily determined by $W_{11}^{(22)}(\Omega)$ and not by the interference terms $W_{11}^{(12)}(\Omega) = W_{11}^{(21)}(\Omega)$.

III.7.3 Effective Circuit for Coupled Surface Polaritons

Two coupled surface polariton modes can arise in the planar geometry in the TM polarization when two semi-infinite half-spaces with dielectric function $\varepsilon(\omega)$ are separated by a vacuum gap of width d. In the quasi-static limit, corresponding to the speed of light $c \to \infty$, the dispersion $\omega_\pm(q)$ of the symmetric/antisymmetric mode as a function of the in-plane wave vector q is determined by the equation

$$\varepsilon(\omega) = -\frac{1 \mp e^{-qd}}{1 \pm e^{-qd}}. \tag{III.7.14}$$

For the Drude-Lorentz model of optical phonon resonance in a dielectric,

$$\varepsilon(\omega) = \varepsilon_\infty \frac{\omega^2 - \omega_L^2}{\omega^2 - \omega_T^2}, \tag{III.7.15}$$

the frequencies of the symmetric and antisymmetric modes are given by

$$\omega_\pm^2(q) = \frac{\varepsilon_\infty \omega_L^2 + \omega_T^2 \pm (\varepsilon_\infty \omega_L^2 - \omega_T^2)e^{-qd}}{\varepsilon_\infty + 1 \pm (\varepsilon_\infty - 1)e^{-qd}}. \tag{III.7.16}$$

Here ω_T is the mechanical frequency of the triply degenerate polar optical phonon, and ω_L is the Coulomb frequency of the longitudinal optical phonon (both in the bulk). A finite damping γ of the optical phonon can be included by replacing $\omega^2 \to \omega^2 + 2i\gamma\omega$ in Eq. (III.7.15). At $d \to \infty$ the splitting vanishes, and the two surfaces are decoupled, each hosting its own weakly damped surface polariton. This situation can be modeled by the circuit in Fig. III.12. Here each RLC contour hosts a weakly damped resonance at frequency $\omega_L = \sqrt{\omega_T^2 + 1/(LC_c)}$, where we denoted $\omega_T^2 \equiv 1/(LC_T)$. The two contours are coupled by capacitances $C_\pm$. The frequency of the coupled symmetric/antisymmetric mode is determined by the equation

$$-i\omega C_c - \frac{i\omega C_T}{1 - \omega^2 LC_T - i\omega RC_T} = i\omega C_\pm. \tag{III.7.17}$$

We are interested in the regime when the damping is smaller than the splitting, so that the doublet is well resolved. Then the solutions for the frequencies are approximately given by

$$\omega_\pm - i\gamma \equiv \sqrt{\frac{1}{LC_T} + \frac{1}{L(C_c + C_\pm)}} - i\,\frac{R}{2L}, \tag{III.7.18}$$

where $\omega_\pm$ are the hybridized mode frequencies, and γ is their amplitude decay rate. For the condition $\gamma \ll |\omega_+ - \omega_-|$ to hold, the circuit parameters should satisfy

$$R \ll \frac{|C_+ - C_-|}{\omega_L (C_c + C_+)(C_c + C_-)}. \tag{III.7.19}$$

The Poynting vector in the middle of the vacuum gap between the two dielectrics corresponds to the power deposited into the RLC contour, which is thus treated as a dissipative bath with impedance

$$Z(\omega) = \left[-i\omega C_c - \frac{i\omega C_T}{1 - \omega^2 LC_T - i\omega RC_T}\right]^{-1} = \frac{1}{-i\omega C_c}\,\frac{\omega_T^2 - \omega^2 - 2i\omega\gamma}{\omega_L^2 - \omega^2 - 2i\omega\gamma}, \tag{III.7.20}$$

while the capacitances $C_\pm$ represent the coupling circuit. According to the general construction in the main text, this association leads to

$$\operatorname{Re} Z(\omega) = \frac{R/(LC_c)^2}{(\omega_L^2 - \omega^2)^2 + (2\omega\gamma)^2}, \tag{III.7.21}$$

$$\lambda(\omega) = \frac{\sqrt{R}/(LC_c)}{\omega_L^2 - \omega^2 - 2i\omega\gamma}, \tag{III.7.22}$$

and

$$\zeta_{11} = \zeta_{22} = \frac{2/Z - i\omega(C_+ + C_-)}{2(1/Z - i\omega C_+)(1/Z - i\omega C_-)}, \tag{III.7.23a}$$

$$\zeta_{12} = \zeta_{21} = \frac{i\omega(C_+ - C_-)}{2(1/Z - i\omega C_+)(1/Z - i\omega C_-)}. \tag{III.7.23b}$$

According to Eq. (III.6.4) and Sec. III.3, the scattering matrix is given by

$$S_{11} = S_{22} = \frac{\lambda}{\lambda^*} \frac{1 + \omega(C_+ + C_-)\,\mathrm{Im}\,Z + \omega^2 C_+ C_- |Z|^2}{(1 - i\omega C_+ Z)(1 - i\omega C_- Z)}, \tag{III.7.24a}$$

$$S_{12} = S_{21} = \frac{i\omega\lambda^2 (C_+ - C_-)}{(1 - i\omega C_+ Z)(1 - i\omega C_- Z)}, \tag{III.7.24b}$$

leading to the transmission and reflection coefficients

$$\begin{aligned} |S_{12}(\omega)|^2 &= \frac{[\omega(C_+ - C_-)\,\mathrm{Re}\,Z(\omega)]^2}{|1 - i\omega C_+ Z(\omega)|^2 |1 - i\omega C_- Z(\omega)|^2} \\ &= \frac{(2\gamma\omega)^2(\omega_+^2 - \omega_-^2)^2}{[(\omega_+^2 - \omega^2)^2 + (2\gamma\omega)^2][(\omega_-^2 - \omega^2)^2 + (2\gamma\omega)^2]}, \end{aligned} \tag{III.7.25a}$$

$$\begin{aligned} |S_{11}(\omega)|^2 &= 1 - |S_{12}(\omega)|^2 \\ &= \frac{[(\omega_+^2 - \omega^2)(\omega_-^2 - \omega^2) + (2\gamma\omega)^2]^2}{[(\omega_+^2 - \omega^2)^2 + (2\gamma\omega)^2][(\omega_-^2 - \omega^2)^2 + (2\gamma\omega)^2]}. \end{aligned} \tag{III.7.25b}$$

Due to the condition $|\omega_+ - \omega_-| \gg \gamma$, we can approximating $|S_{12}(\omega)|^2$ by a sum of four Lorentzians,

$$|S_{12}(\omega)|^2 \approx \sum_{\sigma,\sigma'=\pm} \frac{\gamma^2}{(\omega + \sigma\omega_{\sigma'})^2 + \gamma^2}. \tag{III.7.26}$$

In this approximation, the average power is given by

$$\langle \hat{\mathcal{P}}_1 \rangle = \sum_{\sigma=\pm} \frac{\gamma}{2} \left(\frac{\hbar\omega_\sigma}{e^{\hbar\omega_\sigma/T_2} - 1} - \frac{\hbar\omega_\sigma}{e^{\hbar\omega_\sigma/T_1} - 1} \right). \tag{III.7.27}$$

This expression can also be obtained from the simple rate equations for the bosonic occupation of the coupled resonant modes.

We are interested in the correlator $W_{11}(\Omega)$ of the power dissipated into the impedance 1 in the limit $T_2 \gg T_1, \hbar\Omega$. According to Eq. (III.6.9), $W_{11}(\Omega)$ is given by a sum of four terms, $\sum_{l,m} W_{11}^{(lm)}(\Omega)$, each containing a factor $\coth[\hbar\omega/(2T_l)]\coth[\hbar(\omega+\Omega)/(2T_m)] - 1$ in the integrand for $l, m = 1, 2$. Let us analyze these contributions one by one.

For the contribution with $l = m = 2$ we use the identity $\coth x \coth(x+y) - 1 = \cosh y/[\sinh x \sinh(x+y)]$ and write it as

$$\begin{aligned} W_{11}^{(22)}(\Omega) = \cosh\frac{\hbar\Omega}{2T_2} \int_{-\infty}^{\infty} \frac{d\omega}{16\pi} \frac{\hbar\omega |S_{12}(\omega)|^2}{\sinh[\hbar\omega/(2T_2)]} \frac{\hbar(\omega+\Omega)|S_{12}(\omega+\Omega)|^2}{\sinh[\hbar(\omega+\Omega)/(2T_2)]} \\ \times \frac{|Z(\omega) + Z^*(\omega+\Omega)|^2}{4\,\mathrm{Re}\,Z(\omega)\,\mathrm{Re}\,Z(\omega+\Omega)}. \end{aligned} \tag{III.7.28}$$

The Büttiker part $W_{11}^{B(22)}(\Omega)$ is given by the same expression, but without the last line. Since $|S_{12}(\omega)|^2$ is peaked around $\omega = \omega_\pm, -\omega_\pm$, the frequency integral in Eq. (III.7.28) can be particularly large for such Ω that the peaks in the two factors $|S_{12}(\omega)|^2$ and $|S_{12}(\omega+\Omega)|^2$ overlap. This happens near $\Omega = 0, \pm|\omega_+ - \omega_-|$.

Let us first calculate the Büttiker contribution $W_{11}^{B(22)}(\Omega)$, which is simpler. Using the Lorentzian approximation (III.7.26) together with the fact that the convolution of two Lorentzians is a Lorentzian with a double width, and assuming $T_2 \sim \hbar\omega_\pm \gg \hbar|\omega_+ - \omega_-|$, we find

$$W_{11}^{B(22)}(\Omega) = \left[\frac{\hbar\omega_\pm/2}{\sinh[\hbar\omega_\pm/(2T_2)]}\right]^2 \left[\frac{2\gamma^3}{\Omega^2+4\gamma^2} + \frac{\gamma^3}{(\Omega+\omega_+-\omega_-)^2+4\gamma^2} \times \frac{\gamma^3}{(\Omega+\omega_--\omega_+)^2+4\gamma^2}\right], \tag{III.7.29}$$

where $\hbar\omega_\pm$ in the first factor means that either of the two frequencies can be taken within the made approximation. To evaluate the full spectrum, $W_{11}^{(22)}(\Omega)$, we rewrite the last factor in Eq. (III.7.28) as

$$\frac{|Z(\omega)+Z^*(\omega+\Omega)|^2}{4\,\mathrm{Re}\,Z(\omega)\,\mathrm{Re}\,Z(\omega+\Omega)} = 1 + \frac{|Z(\omega+\Omega)-Z(\omega)|^2}{4\,\mathrm{Re}\,Z(\omega+\Omega)\,\mathrm{Re}\,Z(\omega)} \approx 1 + \frac{\Omega^2}{4\gamma^2}, \tag{III.7.30}$$

where the last line is written in the approximation $|\omega-\omega_L|, \Omega, \gamma \ll (LC_\mathrm{c})^{-1/2}$,-$(LC_T)^{-1/2}$. Then, we have a very simple relation

$$W_{11}^{(22)}(\Omega) = \frac{\Omega^2+4\gamma^2}{4\gamma^2}\, W_{11}^{B(22)}(\Omega), \tag{III.7.31}$$

which shows a rather dramatic effect of the reactive contribution: the central peak around $\Omega = 0$ is fully suppressed, while the two peaks at $\Omega = \pm(\omega_+ - \omega_-)$ are strongly enhanced.

Let us now consider the contribution $W_{11}^{(12)}(\Omega)$ with $l = 1$ and $m = 2$ [the other one is just $W_{11}^{(21)} = W_{11}^{(12)}(-\Omega)$]. The Büttiker contribution $W_{11}^{B(12)}(\Omega)$ is calculated quite analogously to $W_{11}^{B(22)}(\Omega)$, in the limit $T_1, \hbar\Omega \ll T_2$ and the Lorentzian approximation (III.7.26):

$$W_{11}^{B(12)}(\Omega) = \int_{-\infty}^{\infty} \frac{d\omega}{8\pi} \frac{\hbar^2\omega(\omega+\Omega)|S_{11}(\omega)|^2|S_{12}(\omega+\Omega)|^2}{e^{\mathrm{sgn}(\omega)\hbar(\omega+\Omega)/T_2}-1}$$
$$= \frac{\hbar^2\omega_\pm^2/2}{e^{\hbar\omega_\pm/T_2}-1} \times \left[\frac{\Omega^2\gamma+2\gamma^3}{\Omega^2+4\gamma^2} - \frac{\gamma^3}{(\Omega+\omega_+-\omega_-)^2+4\gamma^2} - \frac{\gamma^3}{(\Omega+\omega_--\omega_+)^2+4\gamma^2}\right]. \tag{III.7.32}$$

For the full spectrum $W_{11}^{(12)}(\Omega)$, we cannot give a simple compact analytical expression because of interference terms. Still, at $\Omega = 0$ it obviously coincides with $W_{11}^{B(12)}(\Omega = 0)$, while at $\Omega \gg \gamma$ it differs from $W_{11}^{B(12)}(\Omega)$ by a large factor, of the same origin as in $W_{11}^{(22)}(\Omega)$.

Finally, the contribution $l = m = 1$ is negligibly small. Indeed, the factor $\coth[\hbar\omega/$-$(2T_1)]\coth[\hbar(\omega+\Omega)/(2T_1)] - 1$ is non-vanishing only in a narrow region $|\omega| \sim \max\{\Omega, T_1/\hbar\}$, so it misses the peaks at $|\omega| \approx \omega_\pm$. The rest of the integrand is regular at low frequencies, so the whole integral is small.

III.7.4 Non-Equilibrium Green's Functions for Coupled Surface Polaritons

Here we study how the results for heat current noise obtained from the circuit scattering approach are related to those found using non-equilibrium Green's functions. This latter approach is always based on a specific microscopic model for the involved materials, so we choose to model the specific situation of heat transfer via surface polaritons between two thick dielectric slabs separated by a planar vacuum gap of thickness d, so that the half-spaces $z > d/2$ and $z < -d/2$ are occupied by dielectrics with a dielectric function $\varepsilon(\omega)$ and held at temperatures T_1 and T_2, respectively. The circuit mimicking this situation was studied in detail in Sec. III.7.3. For a metallic system, the Green's functions' treatment is analogous, and can be found in Ref. [33].

Microscopic model.— We need a microscopic model for a dielectric that would produce an isotropic Drude-Lorentz dielectric function of the bulk material,

$$\varepsilon(\omega) = \varepsilon_\infty \frac{\omega_L^2 - \omega^2 - 2i\gamma\omega}{\omega_T^2 - \omega^2 - 2i\gamma\omega}, \tag{III.7.33}$$

where the spatial dispersion is neglected. Since our goal is to illustrate the Green's function approach rather than to quantitatively describe a specific material, we aim at the simplest model with a minimal number of ingredients. When a specific example is needed, we will have in mind the tetrahedral SiC with two atoms per unit cell (3C-SiC) and point group T_d. For simplicity, we will set the high-frequency value of the dielectric function $\varepsilon_\infty = 1$. Its difference from unity is due to a contribution from high-frequency polarizable degrees of freedom. We do not include them explicitly, but briefly discuss the procedure at the end of the next subsection.

The first ingredient of the model is the triply degenerate polar optical phonon mode, assumed to be dispersionless. It is described by a vector field $\boldsymbol{\xi}(\mathbf{r})$ of the relative displacements of two inequivalent atoms, with the Hamiltonian

$$\hat{H}_{\text{op}} = \int_{|z|>d/2} d^3\mathbf{r} \left[\frac{\hat{\eta}_j(\mathbf{r})\,\hat{\eta}_j(\mathbf{r})}{2\varrho_{\text{op}}} + \frac{\varrho_{\text{op}}\omega_T^2}{2}\,\hat{\xi}_j(\mathbf{r})\,\hat{\xi}_j(\mathbf{r}) \right]. \tag{III.7.34a}$$

Here $\hat{\boldsymbol{\eta}}(\mathbf{r})$ is the momentum canonically conjugate to the displacement operator $\hat{\boldsymbol{\xi}}(\mathbf{r})$, so that $[\hat{\xi}_j(\mathbf{r}), \hat{\eta}_k(\mathbf{r}')] = i\hbar\delta_{jk}\delta(\mathbf{r}-\mathbf{r}')$. Summation over repeated Cartesian indices $j,k = x,y,z$ is implied. ϱ_{op} is the density of the reduced mass, corresponding to the optical phonon. For 3C-SiC, it is related to the total mass density ϱ_0 of the crystal by a factor involving the masses of silicon and carbon atoms, $\varrho_{\text{op}} = \varrho_0 m_{\text{Si}} m_{\text{C}}/(m_{\text{Si}} + m_{\text{C}})^2$. Finally, ω_T is the mechanical frequency of the optical phonon.

The second ingredient is the coupling of optical phonons to the electromagnetic field. It is due to the fact that the polar phonon displacement $\boldsymbol{\xi}(\mathbf{r})$ is associated with electric polarization in the material, $\mathbf{P}(\mathbf{r}) = \theta(|z| - d/2)\,\rho\,\boldsymbol{\xi}(\mathbf{r})$, with $\theta(z)$ being the Heaviside step function. Such local relation is valid under the same assumptions as neglecting the spatial dispersion in the dielectric function (III.7.33), that is, at length scales well exceeding the atomic scale. The coefficient ρ has

the dimensionality of the charge density and is determined by the microscopic charge distribution in the atomic bond. Coupling between the polarization and the electromagnetic field is taken in the electrostatic (Coulomb) limit, valid for heat transfer between dielectrics at distances much smaller than the wavelength of thermal photons (in contrast to metals, where the dominant mechanism is magnetostatic [106, 186–188]). Recalling that the charge density is given by $-\boldsymbol{\nabla}\cdot\hat{\mathbf{P}}(\mathbf{r})$, we write

$$\hat{H}_{\mathrm{C}} = \frac{1}{2}\int d^3\mathbf{r}\, d^3\mathbf{r}'\, \frac{(-\boldsymbol{\nabla}\cdot\hat{\mathbf{P}}(\mathbf{r}))\,(-\boldsymbol{\nabla}'\cdot\hat{\mathbf{P}}(\mathbf{r}'))}{|\mathbf{r}-\mathbf{r}'|} \equiv \frac{\rho^2}{2}\int d^3\mathbf{r}\, d^3\mathbf{r}'\, D_{ij}(\mathbf{r}-\mathbf{r}')\,\hat{P}_i(\mathbf{r})\,\hat{P}_j(\mathbf{r}'). \tag{III.7.34b}$$

With this definition, the function $-D_{ij}(\mathbf{r}-\mathbf{r}')$ gives the response of the electric field to the polarization, as determined by Maxwell's equations in the quasi-static limit, and describes the dipole-dipole interaction.

The third ingredient has to account for the optical phonon damping γ, appearing as the imaginary term in the dielectric function (III.7.33). Such damping can result from optical phonon decay into a pair of acoustic phonons due to anharmonicity [189, 190], provided that the optical phonon frequency is not too high and can be matched by two acoustic phonon frequencies (which is the case in SiC [191–193]). The acoustic phonons are described by the vector field of atomic displacements $\mathbf{u}(\mathbf{r})$. In the long-wavelength limit, the change in the elastic energy is expressed in terms of the strain tensor $u_{ij} \equiv (1/2)(\partial u_i/\partial x_j + \partial u_j/\partial x_i)$ [194]. The simplest model for acoustic phonons is that of a fully isotropic elastic medium; however, such high symmetry prohibits local anharmonic coupling between a vector ξ_i (transforming according to angular momentum 1) and a product of two symmetric tensors u_{ij} (each transforming according to angular momentum 0 or 2, so their product having components of angular momentum 0, 2, and 4). Thus, we write the elastic energy in terms of invariants of the T_d point group, whose lower symmetry allows for the sought anharmonic coupling in the form

$$\begin{aligned}\hat{H}_{\mathrm{anh}} =& \Upsilon\int_{|z|>d/2} d^3\mathbf{r}\,\Big[\hat{\xi}_x\hat{u}_{yz}(2\hat{u}_{xx}-\hat{u}_{yy}-\hat{u}_{zz}) + \hat{\xi}_y\hat{u}_{zx}(2\hat{u}_{yy}-\hat{u}_{zz}-\hat{u}_{xx})\hat{\xi}_z\hat{u}_{xy} \\ &\times(2\hat{u}_{zz}-\hat{u}_{xx}-\hat{u}_{yy})\Big] \\ \equiv& \int_{|z|>d/2} d^3\mathbf{r}\,\frac{\Upsilon_{ijklm}}{2}\,\hat{\xi}_i(\mathbf{r})\,\hat{u}_{jk}(\mathbf{r})\,\hat{u}_{lm}(\mathbf{r}),\end{aligned} \tag{III.7.34c}$$

where Υ is the corresponding coupling constant, and the x, y, z axes are directed along the edges of the cube centered at the position of a Si atom, while the four C atoms forming the tetrahedron are located at four (out of eight) cube's vertices, so that the six edges of the tetrahedron coincide with diagonals of each of the six cube's faces.

The harmonic part of the acoustic phonon Hamiltonian is written in terms of the strain tensor operator $\hat{u}_{ij}(\mathbf{r})$ and of the vector momentum operator $\hat{\boldsymbol{\pi}}(\mathbf{r})$, canonically conjugate to the displacement operator $\hat{\mathbf{u}}(\mathbf{r})$, such that $[\hat{u}_j(\mathbf{r}), \hat{\pi}_k(\mathbf{r}')] = i\hbar\delta_{jk}$-$\delta(\mathbf{r}-\mathbf{r}')$. To be consistent, here we also assume the tetrahedral symmetry instead

of the full isotropy. This gives three terms in the elastic deformation energy:

$$\begin{aligned}\hat{H}_{\text{ac}} &= \int_{|z|>d/2} d^3\mathbf{r} \left[\frac{\hat{\pi}_i(\mathbf{r})\,\hat{\pi}_i(\mathbf{r})}{2\varrho_0} + \varrho_0 \frac{v_l^2 - 2v_t^2}{2} \left[\hat{u}_{ii}(\mathbf{r})\right]^2 + \varrho_0 v_t^2 \hat{u}_{ij}(\mathbf{r})\hat{u}_{ij}(\mathbf{r}) \right. \\ &\qquad \left. + \frac{\varrho_0 v_\Delta^2}{2} \left[\hat{u}_{xx}^2(\mathbf{r}) + \hat{u}_{yy}^2(\mathbf{r}) + \hat{u}_{zz}^2(\mathbf{r})\right] \right] \\ &\equiv \int_{|z|>d/2} d^3\mathbf{r} \left[\frac{\hat{\pi}_i(\mathbf{r})\,\hat{\pi}_i(\mathbf{r})}{2\varrho_0} + \frac{\mathcal{K}_{jklm}}{2}\,\hat{u}_{jk}(\mathbf{r})\,\hat{u}_{lm}(\mathbf{r}) \right]. \end{aligned} \tag{III.7.34d}$$

Here ϱ_0 is the mass density of the crystal, v_l and v_t are the longitudinal and transverse acoustic phonon velocities in the isotropic approximation (which corresponds to keeping only the first two terms in the elastic energy), while v_Δ plays the role of the coupling constant in the last term, which is absent in the isotropic approximation. This last term splits the two transverse phonon branches for wave vectors which are not directed along high-symmetry axes.

Phonon propagators and the dielectric function.— In order to verify that the model of Eqs. (III.7.34) indeed corresponds to the dielectric function (III.7.33) with $\varepsilon_\infty = 1$, let us consider an infinite bulk crystal and calculate the response of the polarization to an external oscillating electric field $\mathbf{E}^{\text{ext}} e^{i\mathbf{kr}-i\omega t} + \text{c.c.}$, which couples to the polarization via the Hamiltonian

$$\hat{H}_{\text{ext}} = -\int d^3\mathbf{r}\,\hat{\mathbf{P}}(\mathbf{r}) \cdot \left(\mathbf{E}^{\text{ext}} e^{i\mathbf{kr}-i\omega t} + \text{c.c.}\right). \tag{III.7.35}$$

The Kubo formula expresses the corresponding response function $\tilde{\chi}_{ij}(\mathbf{k},\omega)$ as the retarded correlator of the polarizations:

$$\tilde{\chi}_{ij}(\mathbf{k},\omega) = \frac{i}{\hbar}\int_0^\infty dt \int d^3\mathbf{r}\, e^{i\omega t - i\mathbf{kr}} \left\langle [\hat{P}_i(\mathbf{r},t), \hat{P}_j(\mathbf{0},0)] \right\rangle, \tag{III.7.36}$$

where we used the fact that in the infinite medium two-point correlators depend only on the difference of the spatial and temporal coordinates.
To evaluate this correlator, we consider $\hat{H}_{\text{op}} + \hat{H}_{\text{ac}}$ [Eqs. (III.7.34a) and (III.7.34d)] as the zero-approximation Hamiltonian, while $\hat{H}_{\text{C}}$ and $\hat{H}_{\text{anh}}$ [Eqs. (III.7.34b) and (III.7.34c), respectively] are included by summing perturbation series. Accordingly, the operators of the optical and acoustic phonon displacements are expressed in terms of the phonon creation and annihilation operators:

$$\hat{\xi}_j(\mathbf{r}) = \sum_{\mathbf{k}} \sqrt{\frac{\hbar}{2V\varrho_{\text{op}}\omega_T}} \left(\hat{b}_{\mathbf{k}j} e^{i\mathbf{kr}} + \hat{b}_{\mathbf{k}j}^\dagger e^{-i\mathbf{kr}}\right), \tag{III.7.37a}$$

$$\hat{\mathbf{u}}(\mathbf{r}) = \sum_{\mathbf{k},\mu} \sqrt{\frac{\hbar}{2V\varrho_0\omega_{\mathbf{k},\mu}^{\text{ac}}}}\, \mathbf{e}_{\mathbf{k}\mu} \left(\hat{a}_{\mathbf{k}\mu} e^{i\mathbf{kr}} + \hat{a}_{\mathbf{k}\mu}^\dagger e^{-i\mathbf{kr}}\right), \tag{III.7.37b}$$

where V is the crystal volume. The index μ labels the three acoustic phonon branches, while the degenerate optical phonon branches can be labeled by the

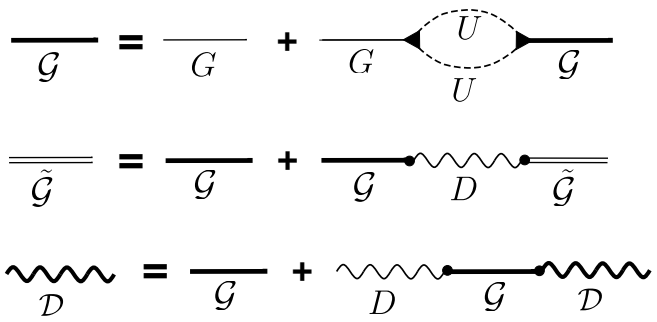

Figure III.15: *Feynamnn diagrams* representing the Dyson series for the phonon Green's functions. Solid, dashed and wavy lines represent the Green's function for the optical phonons, acoustic phonons, and the electric field, respectively. Triangles and thick dots represent the Υ and ρ vertices appearing in the Hamiltonians $\hat{H}_{\text{anh}}$ and $\hat{H}_{\text{C}}$, respectively.

Cartesian index $j = x, y, z$. The unit vectors $\mathbf{e}_{\mathbf{k}\mu}$ give the directions of the atomic displacements for each acoustic normal mode. The corresponding non-interacting retarded, advanced, and Keldysh Green's functions (propagators) for the optical phonons are given by

$$\begin{aligned} G^R_{jl}(\mathbf{r}-\mathbf{r}',t-t') &= -\frac{i}{\hbar}\,\theta(t-t')\langle[\hat{\xi}_j(\mathbf{r},t),\hat{\xi}_l(\mathbf{r}',t')]\rangle \\ &= \int \frac{d^3\mathbf{k}\,d\omega}{(2\pi)^4}\,\frac{\delta_{jl}}{\varrho_{\text{op}}}\,\frac{e^{i\mathbf{k}(\mathbf{r}-\mathbf{r}')-i\omega(t-t')}}{(\omega+i0^+)^2-\omega_T^2}, \qquad \text{(III.7.38a)} \\ G^A_{jl}(\mathbf{r}-\mathbf{r}',t-t') &= \frac{i}{\hbar}\,\theta(t'-t)\langle[\hat{\xi}_j(\mathbf{r},t),\hat{\xi}_l(\mathbf{r}',t')]\rangle \\ &= \int \frac{d^3\mathbf{k}\,d\omega}{(2\pi)^4}\,\frac{\delta_{jl}}{\varrho_{\text{op}}}\,\frac{e^{i\mathbf{k}(\mathbf{r}-\mathbf{r}')-i\omega(t-t')}}{(\omega-i0^+)^2-\omega_T^2}, \qquad \text{(III.7.38b)} \\ G^K_{jl}(\mathbf{r}-\mathbf{r}',t-t') &= -\frac{i}{\hbar}\langle\{\hat{\xi}_j(\mathbf{r},t),\hat{\xi}_l(\mathbf{r}',t')\}\rangle \\ &= \int \frac{d^3\mathbf{k}\,d\omega}{(2\pi)^4}\,\frac{\delta_{jl}}{\varrho_{\text{op}}}e^{i\mathbf{k}(\mathbf{r}-\mathbf{r}')-i\omega(t-t')}\,\frac{2\pi i}{2\omega_T} \\ &\quad\times[\delta(\omega+\omega_T)-\delta(\omega-\omega_T)]\coth\frac{\hbar\omega}{2T}, \qquad \text{(III.7.38c)} \end{aligned}$$

where $\{\cdot,\cdot\}$ denotes the anticommutator, and T is the crystal temperature. In the similar way we define the Green's functions $U^{R,A,K}_{jklm}(\mathbf{r}-\mathbf{r}',t-t')$ for the acoustic phonons, building them from the strain operators $\hat{u}_{jk}(\mathbf{r},t),\hat{u}_{lm}(\mathbf{r}',t')$. These Green's functions can be straightforwardly evaluated in the Fourier space from the Hamiltonian (III.7.34d); we do not give the explicit expressions because they are too cumbersome.

The next step is to dress the optical phonon Green's function by the self-energy originating from the coupling (III.7.34c) to the acoustic phonons (Fig. III.15). To

the leading (i. e, second) order in $\hat{H}_{\text{anh}}$, the retarded self-energy is given by

$$\Sigma^R_{jj'}(\mathbf{K},\Omega) = \int \frac{d^3\mathbf{k}\,d\omega}{(2\pi)^4}\,\frac{i\hbar}{4}\,\Upsilon_{jklmn}\Upsilon_{j'k'l'm'n'}\left[U^R_{klk'l'}(\mathbf{K}+\mathbf{k},\Omega+\omega)\,U^K_{m'n'mn}(\mathbf{k},\omega)\right.$$
$$\left. + U^K_{klk'l'}(\mathbf{K}+\mathbf{k},\Omega+\omega)\,U^A_{m'n'mn}(\mathbf{k},\omega)\right]. \tag{III.7.39}$$

This self-energy can be calculated explicitly using the Green's functions built from the Hamiltonian (III.7.34d). Note, however, that what we really need is the limit $\operatorname{Im}\Sigma^R_{jj'}(\mathbf{k}\to 0,\omega)$, because we are interested in the damping of long-wavelength optical phonons. By symmetry, $\Sigma^R_{jj'}(\mathbf{k}\to 0,\omega)\propto\delta_{jj'}$, so its real part gives an overall frequency shift which is the same for the three phonon branches, without lifting the degeneracy, so it can be absorbed into ω_T. Thus, we approximate

$$\Sigma^R_{jl}(\mathbf{k},\omega) = -2i\varrho_{\text{op}}\omega\,\gamma(\omega)\,\delta_{jl}, \tag{III.7.40}$$

where the damping rate $\gamma(\omega)$ is frequency-dependent. This frequency dependence is determined by the two-phonon density of states for acoustic phonons, as well as by the momentum dependence of the coupling matrix elements. Equations (III.7.34d) and (III.7.34c), although provide a specific model where $\gamma(\omega)$ can be calculated, do not describe any material quantitatively. The reason is that an optical phonon with small momentum decays into two acoustic phonons whose momenta are not small at all, they are of the order of the inverse lattice constant. Equations (III.7.34d) and (III.7.34c) represent an expansion in the acoustic phonon momenta around $\mathbf{k}=0$, and lose their validity deep in the Brillouin zone. Thus, we keep $\gamma(\omega)$ as a parameter of the theory (the simplest assumption, implied in the Drude-Lorentz model, is to take $\gamma=$ const in the frequency region of interest). Summing up the Dyson series, we find the optical phonon Green's function, dressed by the anharmonic coupling to acoustic phonons:

$$\mathcal{G}^R_{jl}(\mathbf{k},\omega) = \frac{\delta_{jl}}{\varrho_{\text{op}}}\,\frac{1}{\omega^2-\omega_T^2+2i\omega\gamma(\omega)}. \tag{III.7.41}$$

Finally, we dress this Green's function by the self-energy originating from the Coulomb interaction (III.7.34b), taken for the infinite medium:

$$\tilde{\Sigma}_{jl}(\mathbf{k}) = \rho^2 D_{jl}(\mathbf{k}) = 4\pi\rho^2\,\frac{k_jk_l}{k^2}. \tag{III.7.42}$$

This gives the fully dressed optical phonon retarded Green's function (Fig. III.15),

$$\tilde{\mathcal{G}}^R_{jl}(\mathbf{k},\omega) = \left(\delta_{jl}-\frac{k_jk_l}{k^2}\right)\frac{1/\varrho_{\text{opt}}}{\omega^2-\omega_T^2+2i\omega\gamma(\omega)} + \frac{k_jk_l}{k^2}\,\frac{1/\varrho_{\text{opt}}}{\omega^2-\omega_L^2+2i\omega\gamma(\omega)}, \tag{III.7.43}$$

where $\omega_L\equiv\sqrt{\omega_T^2+4\pi\rho^2/\varrho_{\text{op}}}$ is the Coulomb frequency of the longitudinal optical phonon.

To relate the Green's functions to the dielectric function $\varepsilon(\omega)$, we recall that the latter determines the response of the electric displacement $\mathbf{E}+4\pi\mathbf{P}$ to the *total* electric field $\mathbf{E}$, which is the sum of the external field $\mathbf{E}^{\text{ext}}$ and the field produced by

the polarization $\mathbf{P}$ itself, so that $E_j = E_j^{\text{ext}} - D_{jl}P_l = (\delta_{jm} - D_{jl}\tilde{\chi}_{lm})E_m^{\text{ext}}$. We can also define the electric susceptibility $\chi(\mathbf{k},\omega)$, which determines the response of the polarization $\mathbf{P}$ to the total field $\mathbf{E}$, so that the dielectric function $\varepsilon_{ij} = \delta_{ij} + 4\pi\chi_{ij}$. Equating $\tilde{\chi}\mathbf{E}^{\text{ext}} = \chi(\mathbf{E}^{\text{ext}} - D\tilde{\chi}\mathbf{E}^{\text{ext}})$, we find the relation $\chi = \tilde{\chi}(1 - D\tilde{\chi})^{-1}$. At the same time, Eq. (III.7.36) gives $\tilde{\chi}_{ij}(\mathbf{k},\omega) = -\rho^2\tilde{\mathcal{G}}^R_{ij}(\mathbf{k},\omega)$, and the Dyson series for $\tilde{\mathcal{G}}^R$ yields $(\tilde{\mathcal{G}}^R)^{-1} = (\mathcal{G}^R)^{-1} - \rho^2 D$, from which we deduce $\chi_{ij}(\mathbf{k},\omega) = -\rho^2\mathcal{G}^R_{ij}(\mathbf{k},\omega)$. As a result, from Eq. (III.7.41) with $\gamma(\omega) = \text{const}$ we recover Eq. (III.7.33) with $\varepsilon_\infty = 1$. Thus, the Hamiltonian presented in the previous subsection indeed describes a dielectric material with the Drude-Lorentz dielectric function.
To reproduce Eq. (III.7.33) with an asymptotic high-frequency value $\varepsilon_\infty > 1$, one has to include additional polarizable degrees of freedom resonating at much higher frequencies (for example, electronic contribution to atomic polarizabilities). The propagator for these degrees of freedom should be included (i) as an additive contribution to $\tilde{\chi}_{ij}(\omega)$, and (ii) in the dressing of the dipole-dipole interaction $D_{ij}(\mathbf{r} - \mathbf{r}')$. Then the Drude-Lorentz dielectric function with a single resonance at $\omega = \omega_T$ is recovered for frequencies well below those of the higher resonances.

Energy and current operator.— To define the energy current operator $\hat{\mathbf{J}}(\mathbf{r})$, one must first define the energy density operator $\hat{\mathcal{E}}(\mathbf{r})$, such that the Hamiltonian $\hat{H} = \int d^3\mathbf{r}\,\hat{\mathcal{E}}(\mathbf{r})$, and then define an operator $\hat{\mathbf{J}}(\mathbf{r})$ which satisfies the energy continuity equation,

$$\frac{\partial\hat{\mathcal{E}}(\mathbf{r})}{\partial t} = \frac{i}{\hbar}\left[\hat{H}, \hat{\mathcal{E}}(\mathbf{r})\right] = -\boldsymbol{\nabla}\cdot\hat{\mathbf{J}}(\mathbf{r}). \tag{III.7.44}$$

The energy densities $\hat{\mathcal{E}}_{\text{op}}(\mathbf{r}), \hat{\mathcal{E}}_{\text{ac}}(\mathbf{r}), \hat{\mathcal{E}}_{\text{anh}}(\mathbf{r})$ are naturally defined as the integrands in Eqs. (III.7.34a), (III.7.34d) and (III.7.34c), respectively. Since the Coulomb energy (III.7.34b) is non-local, it is possible to find many operators $\hat{\mathcal{E}}_{\text{C}}(\mathbf{r})$ which give $\hat{H}_{\text{C}} = \int d^3\mathbf{r}\,\hat{\mathcal{E}}_{\text{C}}(\mathbf{r})$. The gauge-invariant definition is [195]

$$\begin{aligned}\hat{\mathcal{E}}(\mathbf{r}) = &\left[\hat{\mathcal{E}}_{\text{op}}(\mathbf{r}) + \hat{\mathcal{E}}_{\text{ac}}(\mathbf{r}) + \hat{\mathcal{E}}_{\text{anh}}(\mathbf{r})\right]\theta(|z| - d/2)\\ &+ \frac{1}{8\pi}\left|\int d^3\mathbf{r}'\,\boldsymbol{\nabla}\frac{1}{|\mathbf{r}-\mathbf{r}'|}\boldsymbol{\nabla}'\cdot\rho\hat{\boldsymbol{\xi}}(\mathbf{r}')\theta(|z'| - d/2)\right|^2.\end{aligned} \tag{III.7.45}$$

Indeed, the identity

$$-\nabla^2\frac{1}{|\mathbf{r}-\mathbf{r}'|} = 4\pi\delta(\mathbf{r}-\mathbf{r}') \tag{III.7.46}$$

ensures that the integral over $\mathbf{r}$ of the last term in Eq. (III.7.45) gives Eq. (III.7.34b). Then, the energy current operator $\hat{\mathbf{J}}(\mathbf{r})$ satisfying Eq. (III.7.44) is given by

$$\hat{J}_i(\mathbf{r}) = \frac{1}{2}\left\{\hat{\varsigma}_{ik}(\mathbf{r}), \frac{\hat{\pi}_k(\mathbf{r})}{\varrho_0}\right\}\theta(|z| - d/2) + \frac{\hat{\mathbf{E}}(\mathbf{r})\times\hat{\boldsymbol{\beta}}(\mathbf{r}) - \hat{\boldsymbol{\beta}}(\mathbf{r})\times\hat{\mathbf{E}}(\mathbf{r})}{8\pi} \equiv \hat{J}_i^S + \hat{J}_i^S, \tag{III.7.47}$$

where the first line represents the elastic energy current, expressed in terms of the stress tensor,

$$\hat{\varsigma}_{ik}(\mathbf{r}) = \left(\Lambda_{iklm} + \hat{\xi}_j(\mathbf{r})\Upsilon_{jiklm}\right)\hat{u}_{lm}(\mathbf{r}), \tag{III.7.48}$$

while the second line in Eq. (III.7.47) is nothing but the Poynting vector, expressed in terms of the electric and "magnetic" fields,

$$\hat{\mathbf{E}}(\mathbf{r}) = -\boldsymbol{\nabla} \int d^3\mathbf{r}' \, \frac{-\boldsymbol{\nabla}' \cdot \rho\hat{\boldsymbol{\xi}}(\mathbf{r}')\theta(|z'| - d/2)}{|\mathbf{r} - \mathbf{r}'|}, \tag{III.7.49a}$$

$$\hat{\boldsymbol{\beta}}(\mathbf{r}) = \boldsymbol{\nabla} \times \int d^3\mathbf{r}' \, \frac{(\rho/\varrho_{\text{op}})\hat{\boldsymbol{\eta}}(\mathbf{r}')\theta(|z'| - d/2)}{|\mathbf{r} - \mathbf{r}'|}, \tag{III.7.49b}$$

which satisfy the following equations:

$$\boldsymbol{\nabla} \cdot \hat{\mathbf{E}}(\mathbf{r}) = -4\pi \boldsymbol{\nabla} \cdot \hat{\mathbf{P}}(\mathbf{r}), \tag{III.7.50a}$$

$$\boldsymbol{\nabla} \times \hat{\mathbf{E}}(\mathbf{r}) = 0, \tag{III.7.50b}$$

$$\boldsymbol{\nabla} \cdot \hat{\boldsymbol{\beta}}(\mathbf{r}) = 0, \tag{III.7.50c}$$

$$\boldsymbol{\nabla} \times \hat{\boldsymbol{\beta}}(\mathbf{r}) = 4\pi \, \frac{i}{\hbar} \left[\hat{H}, \hat{\mathbf{P}}(\mathbf{r})\right] + \frac{i}{\hbar} \left[\hat{H}, \hat{\mathbf{E}}(\mathbf{r})\right]. \tag{III.7.50d}$$

The first two equations are the Maxwell's equations for the electrostatic electric field $\mathbf{E}$, while the last two equations are the Maxwell's equations for the magnetic field $\mathbf{B}$, up to the factor $1/c$ on the right-hand side of the last equation. Indeed, the two terms with the commutators in the last equation become $4\pi(\partial\hat{\mathbf{P}}/\partial t) \equiv 4\pi\mathbf{j}$ and $\partial\hat{\mathbf{E}}/\partial t$ in the Heisenberg representation, where

$$\hat{\mathbf{j}}(\mathbf{r}) = \frac{\rho}{\varrho_{\text{op}}} \hat{\boldsymbol{\eta}}(\mathbf{r}) = -i\omega_T \sum_{\mathbf{k},l} \sqrt{\frac{\hbar\rho^2}{2V\varrho_{\text{op}}\omega_T}} \, \mathbf{e}_l \left(\hat{b}_{\mathbf{k}l} e^{i\mathbf{kr}} - \hat{b}^\dagger_{\mathbf{k}l} e^{-i\mathbf{kr}}\right) \tag{III.7.51}$$

is the operator of the electric current density.

The appearance of the magnetic field may look somewhat surprising in our problem with purely electrostatic interactions. Strictly speaking, the electrostatic limit is obtained by sending the speed of light $c \to \infty$ in the Maxwell's equations, so the magnetic field $\mathbf{B} = O(1/c)$ vanishes, but the "magnetic" field $\boldsymbol{\beta} = c\mathbf{B}$ stays finite, and so does the Poynting vector. The only term in the Maxwell's equations that vanishes in the limit $c \to \infty$ is $-(1/c^2)\partial\hat{\boldsymbol{\beta}}/\partial t$, which would stand on the right-hand side of Eq. (III.7.50b).

Using Eqs. (III.7.50), it is rather straightforward to verify that the continuity equation (III.7.44) is satisfied. Indeed, we have

$$\begin{aligned}
&[\hat{H}_{\text{op}} + \hat{H}_{\text{anh}}, \hat{\mathcal{E}}_{\text{op}} + \hat{\mathcal{E}}_{\text{anh}}] = 0, \\
&[\hat{H}_{\text{C}}, \hat{\mathcal{E}}_{\text{anh}}] = [\hat{H}_{\text{anh}} + \hat{H}_{\text{C}}, \hat{E}^2/(8\pi)] = 0, \\
&\frac{i}{\hbar}[\hat{H}_{\text{ac}}, \hat{\mathcal{E}}] + \frac{i}{\hbar}[\hat{H}_{\text{op}} + \hat{H}_{\text{anh}} + \hat{H}_{\text{C}}, \hat{\mathcal{E}}_{\text{ac}}] = -\boldsymbol{\nabla} \cdot \hat{\mathbf{J}}^{\text{S}}, \\
&\frac{i}{\hbar}[\hat{H}_{\text{op}}, \hat{E}^2/(8\pi)] = -\boldsymbol{\nabla} \cdot \hat{\mathbf{J}}^{S} - \frac{\hat{\mathbf{j}} \cdot \hat{\mathbf{E}} + \hat{\mathbf{E}} \cdot \hat{\mathbf{j}}}{2}, \\
&\frac{i}{\hbar}[\hat{H}_{\text{C}}, \hat{\mathcal{E}}_{\text{op}}] = \frac{\hat{\mathbf{j}} \cdot \hat{\mathbf{E}} + \hat{\mathbf{E}} \cdot \hat{\mathbf{j}}}{2}.
\end{aligned}$$

Polarization operator.— Instead of working with the phonon Green's functions, it

is convenient to introduce retarded, advanced and Keldysh components of the polarization operator,

$$\tilde{\Pi}^R_{jk}(\mathbf{r},\mathbf{r}',t-t') = -\frac{i}{\hbar}\,\theta(t-t')\langle[\hat{P}_j(\mathbf{r},t),\hat{P}_k(\mathbf{r}',t')]\rangle, \tag{III.7.52a}$$

$$\tilde{\Pi}^A_{jk}(\mathbf{r},\mathbf{r}',t-t') = \frac{i}{\hbar}\,\theta(t'-t)\langle[\hat{P}_j(\mathbf{r},t),\hat{P}_k(\mathbf{r}',t')]\rangle, \tag{III.7.52b}$$

$$\tilde{\Pi}^K_{jk}(\mathbf{r},\mathbf{r}',t-t') = -\frac{i}{\hbar}\langle\{\hat{P}_j(\mathbf{r},t),\hat{P}_k(\mathbf{r}',t')\}\rangle, \tag{III.7.52c}$$

where the time dependence is determined by the full Hamiltonian. These are proportional to the corresponding Green's functions of the displacements $\hat{\boldsymbol{\xi}}(\mathbf{r})$: $\tilde{\Pi}^{R,A,K}_{jk}(\mathbf{r},\mathbf{r}',t-t') = \rho^2\tilde{\mathcal{G}}^{R,A,K}_{jk}(\mathbf{r},\mathbf{r}',t-t')$. The Green's functions of the momenta $\hat{\boldsymbol{\eta}}(\mathbf{r})$ can also be expressed in terms of the polarization operator using the fact that $\hat{\boldsymbol{\eta}}(\mathbf{r},t) = \varrho_{\text{op}}\,\partial\hat{\boldsymbol{\xi}}(\mathbf{r},t)/\partial t$:

$$\begin{aligned}\frac{\mp i}{\hbar}\,\theta(\pm(t-t'))\langle[\hat{\eta}_j(\mathbf{r},t),\hat{\eta}_k(\mathbf{r}',t')]\rangle =& \frac{\varrho_{\text{op}}^2}{\rho^2}\frac{\partial^2\tilde{\Pi}^{R,A}_{jk}(\mathbf{r},\mathbf{r}',t-t')}{\partial t\,\partial t'} \\ &- \rho_{\text{op}}\delta_{jk}\delta(t-t')\delta(\mathbf{r}-\mathbf{r}')\theta(|z|-d/2),\end{aligned} \tag{III.7.53a}$$

$$-\frac{i}{\hbar}\langle\{\hat{\eta}_j(\mathbf{r},t),\hat{\eta}_k(\mathbf{r}',t')\}\rangle = \frac{\varrho_{\text{op}}^2}{\rho^2}\frac{\partial^2\tilde{\Pi}^{K}_{jk}(\mathbf{r},\mathbf{r}',t-t')}{\partial t\,\partial t'}. \tag{III.7.53b}$$

The reason for introducing the polarization operator rather than working directly with the phonon Green's functions is that the subsequent steps will not rely on the specific model for the material that we used in the previous subsections. Whatever excitations contribute to the dielectric response of the material, the subsequent steps involve only the polarization operator, and thus are more general than the specific model. For example, for a metal the polarization operator is expressed in the random-phase approximation in terms of density-density and current-current electronic bubbles, and the whole subsequent treatment is quite analogous [33].

Together with the full polarization operator $\tilde{\Pi}$ constructed from operators in the Heisenberg representation involving the entire Hamiltonian including interaction (III.7.34b) with the electric field, we also introduce the mechanical polarization operator Π, where the time dependence does not include this interaction. It is related to the optical phonon Green's functions as $\Pi^{R,A,K}_{jk}(\mathbf{r},\mathbf{r}',t-t') = \rho^2\mathcal{G}^{R,A,K}_{jk}(\mathbf{r},\mathbf{r}',t-t')$, and in the frequency space is given by

$$\Pi^R_{jk}(\mathbf{r},\mathbf{r}',\omega) = \delta_{jk}\delta(\mathbf{r}-\mathbf{r}')\,\frac{1-\varepsilon(\omega)}{4\pi}\,\theta(|z|-d/2), \tag{III.7.54a}$$

$$\Pi^A_{jk}(\mathbf{r},\mathbf{r}',\omega) = \delta_{jk}\delta(\mathbf{r}-\mathbf{r}')\,\frac{1-\varepsilon^*(\omega)}{4\pi}\,\theta(|z|-d/2), \tag{III.7.54b}$$

$$\begin{aligned}\Pi^K_{jk}(\mathbf{r},\mathbf{r}',\omega) = \delta_{jk}\delta(\mathbf{r}-\mathbf{r}')\,&\frac{\varepsilon^*(\omega)-\varepsilon(\omega)}{4\pi} \\ &\times\left[\theta(z-d/2)\coth\frac{\hbar\omega}{2T_1} + \theta(-z-d/2)\coth\frac{\hbar\omega}{2T_2}\right].\end{aligned} \tag{III.7.54c}$$

These expressions are also more general than the specific model for the material that we used in the previous subsections [196]. The conditions for their validity coincide with those for the spatially local dielectric response of the material, supplemented by the requirement of thermal equilibrium in the material on each side of the vacuum gap. In other words, heat conduction inside the material should be more efficient than the near-field radiative heat transfer across the vacuum gap [197, 198]. The relation between the mechanical and the Coulomb-dressed polarization operators at a given frequency ω is

$$\tilde{\Pi}^{R,A} = \Pi^{R,A} + \Pi^{R,A}\, D\, \tilde{\Pi}^{R,A}, \tag{III.7.55a}$$

$$\tilde{\Pi}^{R} - \tilde{\Pi}^{A} = \left(\mathbb{1} + \Pi^{R}\mathcal{D}^{R}\right)\left(\Pi^{R} - \Pi^{A}\right)\left(\mathbb{1} + \mathcal{D}^{A}\Pi^{A}\right), \tag{III.7.55b}$$

$$\tilde{\Pi}^{K} = \left(\mathbb{1} + \Pi^{R}\mathcal{D}^{R}\right)\Pi^{K}\left(\mathbb{1} + \mathcal{D}^{A}\Pi^{A}\right), \tag{III.7.55c}$$

where the products are understood in the matrix sense (convolutions over the Cartesian indices and over the spatial variables), $\mathbb{1}$ is a shorthand notation for $\delta_{ij}\delta(\mathbf{r}-\mathbf{r}')$, and the dressed retarded and advanced Green's functions of the electric field are defined as (Fig. III.15)

$$\mathcal{D}^{R,A} = D + D\,\Pi^{R,A}\mathcal{D}^{R,A}. \tag{III.7.55d}$$

While $-D$ gives the electric field produced by an external polarization, as determined by Maxwell's equations in the empty space, the dressed Green's function $-\mathcal{D}^{R}$ does the same, but from the solution of Maxwell's equations in the full dielectric environment. This dielectric environment is encoded in Π^{R} [57, 196].

Heat current fluctuations.— As in most of the literature on near-field radiative heat transfer, we will be interested in the energy current $\hat{J}_z(\mathbf{r})$ inside the vacuum gap separating the two materials, where the Poynting vector represents the only contribution. Specifically, Ref. [148] focused on fluctuations of $\hat{J}_z(\mathbf{r})$ at a given point $\mathbf{r} = (0, 0, d/2 - 0^+)$. We believe that a more relevant quantity would be the total power flowing to the upper body, assumed to have a finite size $L_x \times L_y$ in the in-plane directions:

$$\hat{\mathcal{P}}_1 = \int_0^{L_x} dx \int_0^{L_y} dy\, \hat{J}_z(x, y, d/2 - 0^+). \tag{III.7.56}$$

Indeed, in experiments it is not the heat current that is measured directly, but rather fluctuations in the sample's temperature [155]. Conversion of the heat current into a temperature change necessarily involves heat transport inside the material, which is assumed to be efficient. Thus, local fluctuations of the heat current will quickly spread out across the sample, so fluctuations of the global energy stored in the finite-size sample seem to be a more relevant quantity for experimental observation. Of course, the relative magnitude of the global fluctuations is inversely proportional to the sample area $L_x L_y$, so the sample should be small enough. We assume $L_x, L_y \gg d$ so that one can neglect boundary effects at the sample edges. At the same time, we assume $L_x, L_y \ll c/\omega_T$ so that the Coulomb approximation is valid. In practice, for $\omega_T \sim 10^{14}$ s^{-1} we have $c/\omega_T \sim 10$ μm, while the separation can be $d \sim 10$ nm, so these assumptions are quite realistic.

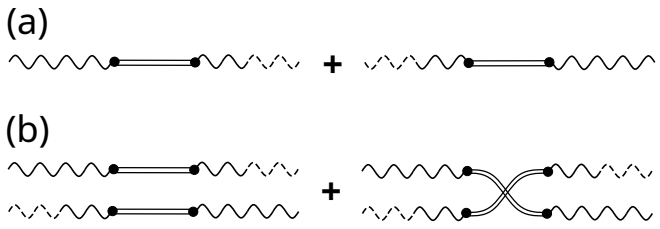

Figure III.16: *Feynamnn diagrams* representing (a) the average Poynting vector, and (b) its fluctuations. Double solid lines represent the polarization operator $\tilde{\Pi}$, solid wavy lines represent the electric field Green's function D, while dashed-solid and solid-dashed wavy lines represent the magnetic field response $-i(\omega/c)\Lambda$ and $i(\omega/c)\Lambda^\dagger$, respectively.

Technically, we need to calculate various averages of electric and magnetic field operators in the Heisenberg representation. It is convenient to reformulate Eqs. (III.7.49) as

$$\hat{E}_i(\mathbf{r}) = -\int d^3\mathbf{r}'\, D_{ik}(\mathbf{r}-\mathbf{r}')\,\hat{P}_k(\mathbf{r}') = -\int d^3\mathbf{r}'\,\hat{P}_k(\mathbf{r}')\,D_{ki}(\mathbf{r}'-\mathbf{r}), \tag{III.7.57a}$$

$$\hat{B}_i(\mathbf{r}) = -\frac{1}{c}\int d^3\mathbf{r}'\,\Lambda_{ik}(\mathbf{r}-\mathbf{r}')\,\hat{j}_k(\mathbf{r}') = -\frac{1}{c}\int d^3\mathbf{r}'\,\hat{j}_k(\mathbf{r}')\,\Lambda_{ki}(\mathbf{r}'-\mathbf{r}). \tag{III.7.57b}$$

These linear relations between the fields and the polarization $\hat{\mathbf{P}}$ (recalling that the current $\hat{\mathbf{j}} = \partial\hat{\mathbf{P}}/\partial t$) enable us to express correlators of the fields in terms of correlators of the polarization given by Eqs. (III.7.52), as shown diagrammatically in Fig. III.16. To simplify the algebra keeping track of different combinations of the fields (giving 4 terms for $\langle\hat{J}_i(\mathbf{r},t)\rangle$ and 32 terms for $\langle\{\hat{J}_i(\mathbf{r},t),\hat{J}_k(\mathbf{r}',t')\}\rangle$), we arrange all components of the fields in a single 6-vector $(f_1,\ldots,f_6)\equiv(E_x,E_y,E_z,$-$B_x,B_y,B_z)$ and consider a generic observable

$$\hat{O}(\mathbf{r}) = \sum_{\alpha,\beta=1}^{6} O_{\alpha\beta}\,\hat{f}_\alpha(\mathbf{r})\,\hat{f}_\beta(\mathbf{r}), \tag{III.7.58}$$

with some matrix $O_{\alpha\beta} = O^*_{\beta\alpha}$. We also combine the two 3×3 matrices $D_{jk}(\mathbf{r}-\mathbf{r}')$ and $-i(\omega/c)\Lambda_{jk}(\mathbf{r}-\mathbf{r}')$, which determine response of the electric and magnetic fields to the external polarization, into a single 6×3 matrix $D_{\alpha j}(\mathbf{r},\mathbf{r},\omega)$. Then the average and the fluctuations of $\hat{O}(\mathbf{r},t)$, shown diagrammatically in Fig. III.16, can

be written as

$$\langle\hat{O}(\mathbf{r},t)\rangle = \frac{i\hbar}{2}\sum_{\alpha,\beta} O_{\alpha\beta}\int d^3\mathbf{r}_1\, d^3\mathbf{r}_2 \int \frac{d\omega}{2\pi}\, D_{\beta j}(\mathbf{r},\mathbf{r}_1,\omega)\,\tilde{\Pi}^{K-R+A}_{jk}(\mathbf{r}_1,\mathbf{r}_2,\omega)$$
$$\times D^*_{k\alpha}(\mathbf{r}_2,\mathbf{r}',\omega), \tag{III.7.59a}$$
$$\int d(t-t')\, e^{i\Omega(t-t')}\left[\frac{1}{2}\langle\{\hat{O}(\mathbf{r},t),\hat{O}(\mathbf{r}',t')\}\rangle - \langle\hat{O}(\mathbf{r},t)\rangle\langle\hat{O}(\mathbf{r}',t')\rangle\right]$$
$$= -\frac{\hbar^2}{4}\sum_{\alpha,\beta,\alpha',\beta'}(O_{\alpha\beta}O_{\alpha'\beta'} + O_{\alpha\beta}O_{\beta'\alpha'})\int d^3\mathbf{r}_1\ldots d^3\mathbf{r}_4 \int\frac{d\omega}{2\pi}$$
$$\times\Big[D_{\alpha i}(\mathbf{r},\mathbf{r}_1,\omega+\Omega)\,\tilde{\Pi}^K_{ij}(\mathbf{r}_1,\mathbf{r}_2,\omega+\Omega)\,D^*_{j\alpha'}(\mathbf{r}_2,\mathbf{r}',\omega+\Omega)\,D_{\beta' k}(\mathbf{r}',\mathbf{r}_3,\omega)\,\tilde{\Pi}^K_{kl}(\mathbf{r}_3,\mathbf{r}_4,\omega)$$
$$\times D^*_{l\beta}(\mathbf{r}_4,\mathbf{r},\omega)\left(\tilde{\Pi}^K\to\tilde{\Pi}^R-\tilde{\Pi}^A\right)\Big], \tag{III.7.59b}$$

where we introduced a compact notation $\tilde{\Pi}^{K-R+A} = \tilde{\Pi}^K - (\tilde{\Pi}^R - \tilde{\Pi}^A)$. Instead of the dressed polarization operators $\tilde{\Pi}$ and the empty-space field Green's functions D, it is convenient to work with the mechanical polarization operators Π and the dressed field Green's functions $\mathcal{D}$. Similarly to Eqs. (III.7.55b), (III.7.55c), in Eqs. (III.7.59) we can replace

$$D_{\alpha i}\tilde{\Pi}^K_{ij}D^*_{j\beta} = \mathcal{D}^R\Pi^K_{ij}\mathcal{D}^A_{j\beta}, \tag{III.7.60a}$$
$$D_{\alpha i}(\tilde{\Pi}^R_{ij} - \tilde{\Pi}^A_{ij})D^*_{j\beta} = \mathcal{D}^R(\Pi^R_{ij} - \Pi^A_{ij})\mathcal{D}^A_{j\beta}. \tag{III.7.60b}$$

The mechanical polarization operators have a very simple structure (III.7.54), while the dressed field Green's function $\mathcal{D}^R_{\alpha j}$ can be found from Maxwell's equations in the given dielectric structure.

In the planar geometry we are considering here (vacuum for $|z| < d/2$, spatially uniform dielectric for $|z| > d/2$), it is natural to work in the Fourier space with respect to the in-plane coordinates $\mathbf{r}_\parallel \equiv (x,y)$, introducing the in-plane wave vector $\mathbf{q}$. Let us place a layer of an external polarization at $z = z' < -d/2$, so that

$$\mathbf{P}^{\text{ext}}(\mathbf{r},t) = \mathbf{P}e^{i\mathbf{q}\mathbf{r}_\parallel - i\omega t}\delta(z-z'). \tag{III.7.61}$$

Then, Maxwell's equations in the quasi-static limit $c\to\infty$ give the electrostatic potential φ together with the electric and magnetic fields in the region $|z| < d/2$:

$$\varphi(\mathbf{r},t) = \frac{4\pi(i\mathbf{q}\mathbf{P}/q - P_z)e^{q(z'+d/2)+i\mathbf{q}\mathbf{r}_\parallel - i\omega t}}{(\varepsilon+1)^2e^{qd} - (\varepsilon-1)^2e^{-qd}}\left[(\varepsilon-1)e^{q(z-d/2)} - (\varepsilon+1)e^{-q(z-d/2)}\right], \tag{III.7.62a}$$

$$\mathbf{E}(\mathbf{r},t) = i\mathbf{q}\,\frac{4\pi(i\mathbf{q}\mathbf{P}/q - P_z)e^{q(z'+d/2)+i\mathbf{q}\mathbf{r}_\parallel - i\omega t}}{(\varepsilon+1)^2e^{qd} - (\varepsilon-1)^2e^{-qd}}\left[(\varepsilon+1)e^{-q(z-d/2)} - (\varepsilon-1)e^{q(z-d/2)}\right]$$
$$+ q\mathbf{e}_z\,\frac{4\pi(i\mathbf{q}\mathbf{P}/q - P_z)e^{q(z'+d/2)+i\mathbf{q}\mathbf{r}_\parallel - i\omega t}}{(\varepsilon+1)^2e^{qd} - (\varepsilon-1)^2e^{-qd}}$$
$$\times\left[(\varepsilon+1)e^{-q(z-d/2)} + (\varepsilon-1)e^{q(z-d/2)}\right], \tag{III.7.62b}$$

$$\mathbf{B}(\mathbf{r},t) = \frac{\omega}{c}\,\frac{\mathbf{e}_z\times\mathbf{q}}{q}\,\frac{4\pi(i\mathbf{q}\mathbf{P}/q - P_z)e^{q(z'+d/2)+i\mathbf{q}\mathbf{r}_\parallel - i\omega t}}{(\varepsilon+1)^2e^{qd} - (\varepsilon-1)^2e^{-qd}}$$
$$\times\left[(\varepsilon+1)e^{-q(z-d/2)} + (\varepsilon-1)e^{q(z-d/2)}\right], \tag{III.7.62c}$$

where $\mathbf{e}_z$ is the unit vector along the z axis. Thus, if for each given $\mathbf{q}$ we rotate the basis $(x, y, z) \to (L, T, Z)$ with unit vectors $\mathbf{e}_L = \mathbf{q}/q$, $\mathbf{e}_T = \mathbf{e}_z \times \mathbf{q}/q$, $\mathbf{e}_Z = \mathbf{e}_z$, the field Green's function $\mathcal{D}^R_{\alpha j}$ has a direct product structure with only 4 non-zero components out of 18:

$$\mathcal{D}^R(-d/2 < z < d/2, z' < -d/2, \mathbf{q}, \omega) = \frac{4\pi e^{q(d/2+z')}}{\nu_+(0)\,\nu_-(0)} \begin{pmatrix} iq\nu_-(z) \\ 0 \\ q\nu_-(z) \\ 0 \\ (\omega/c)\nu_+(z) \\ 0 \end{pmatrix} \begin{pmatrix} -i & 0 & 1 \end{pmatrix}, \tag{III.7.63a}$$

$$\nu_\pm(z) \equiv (\varepsilon + 1)e^{-q(z-d/2)} \pm (\varepsilon - 1)e^{q(z-d/2)}. \tag{III.7.63b}$$

If the source polarization is placed at $z' > d/2$, the fields are easily found from the previous solution by symmetry: flipping the signs $z \to -z$, $z' \to -z'$ implies $(P_x, P_y, P_z) \to (P_x, P_y, -P_z)$, $(E_x, E_y, E_z) \to (E_x, E_y, -E_z)$, $(B_x, B_y, B_z) \to (-B_x, -B_y, B_z)$:

$$\mathcal{D}^R(-d/2 < z < d/2, z' > d/2, \mathbf{q}, \omega) = \frac{4\pi e^{q(d/2-z')}}{\nu_+(0)\,\nu_-(0)} \begin{pmatrix} -iq\nu_-(-z) \\ 0 \\ q\nu_-(-z) \\ 0 \\ (\omega/c)\nu_+(-z) \\ 0 \end{pmatrix} \begin{pmatrix} i & 0 & 1 \end{pmatrix}. \tag{III.7.63c}$$

For $z = d/2 - 0^+$ we are mainly interested in, we have simply $\nu_+(d/2) = 2\varepsilon$, $\nu_-(d/2) = 2$.

For a finite-size sample, the in-plane momentum $\mathbf{q}$ takes discrete values, spaced by $\pi/L_x, \pi/L_y$. However, for $L_x, L_y \gg d$ we can neglect this discretization and replace discrete summation $\sum_{\mathbf{q}} \to L_x L_y \int d^2\mathbf{q}/(2\pi)^2$. The matrix $O_{\alpha\beta}$ corresponding to the Poynting vector has the same simple form in the original (x, y, z) basis and in the rotated (L, T, Z) basis (since $\hat{J}_z$ is invariant under rotations around the z axis):

$$O = \frac{c}{8\pi} \begin{pmatrix} 0 & 0 & 0 & 0 & 1 & 0 \\ 0 & 0 & 0 & -1 & 0 & 0 \\ 0 & 0 & 0 & 0 & 0 & 0 \\ 0 & -1 & 0 & 0 & 0 & 0 \\ 1 & 0 & 0 & 0 & 0 & 0 \\ 0 & 0 & 0 & 0 & 0 & 0 \end{pmatrix}. \tag{III.7.64}$$

All matrix products, spatial convolutions and z integrations in Eqs. (III.7.59) with replacements (III.7.60) can be straightforwardly performed now.

For the average power, the result is

$$\frac{\langle\hat{\mathcal{P}}_1\rangle}{L_xL_y}=\int\frac{d^2\mathbf{q}}{(2\pi)^2}\int_0^\infty\frac{d\omega}{2\pi}\left(\frac{\hbar\omega}{e^{\hbar\omega/T_2}-1}-\frac{\hbar\omega}{e^{\hbar\omega/T_1}-1}\right)\frac{16(\operatorname{Im}\varepsilon)^2}{|(\varepsilon+1)^2e^{qd}-(\varepsilon-1)^2e^{-qd}|^2}. \tag{III.7.65}$$

Using Eq. (III.7.16), we can rewrite the last line identically in terms of the surface mode frequencies $\omega_\pm(q)$ as

$$\begin{aligned}|S_{12}(\mathbf{q},\omega)|^2\equiv&\frac{16(\operatorname{Im}\varepsilon)^2}{|(\varepsilon+1)^2e^{qd}-(\varepsilon-1)^2e^{-qd}|^2}\\=&\frac{(2\gamma\omega)^2[\omega_+^2(q)-\omega_-^2(q)]^2}{[(\omega_+^2(q)-\omega^2)^2+(2\gamma\omega)^2][(\omega_-^2(q)-\omega^2)^2+(2\gamma\omega)^2]},\end{aligned} \tag{III.7.66}$$

which is identical to Eq. (III.6.11) for the effective circuit. In fact, $|S_{12}(\mathbf{q},\omega)|^2$ appearing here is identical to $|S_{12}(\omega)|^2$ in Eq. (III.6.11) for any frequency dependence of $\varepsilon(\omega)$, if one makes a substitution

$$Z(\omega)\to-\frac{1}{i\omega C_*}\frac{1}{\varepsilon(\omega)},\quad C_\pm\to C_*\frac{e^{qd}\mp1}{e^{qd}\pm1}, \tag{III.7.67}$$

where C_* is an arbitrary constant having the dimensionality of capacitance.
For the correlator of the power $\hat{\mathcal{P}}_1$, we find [denoting $\omega'\equiv\omega+\Omega$, and the prime at $\nu'_\pm(z)$ indicating that it contains $\varepsilon(\omega')$]

$$\begin{aligned}\frac{W_{11}(\Omega)}{L_xL_y}=&\int_{-\infty}^\infty\frac{d\omega}{16\pi}\int\frac{d^2\mathbf{q}}{(2\pi)^2}\frac{2\hbar\operatorname{Im}\varepsilon(\omega')}{|\nu'_+(0)\,\nu'_-(0)|^2}\frac{2\hbar\operatorname{Im}\varepsilon(\omega)}{|\nu_+(0)\,\nu_-(0)|^2}\times\\
\times\Bigg[&\left(\coth\frac{\hbar\omega'}{2T_2}\coth\frac{\hbar\omega}{2T_2}-1\right)\left|\nu_-^*(d/2)\,\omega'\nu'_+(d/2)-\omega\nu_+^*(d/2)\,\nu'_-(d/2)\right|^2+\\
&+\left(\coth\frac{\hbar\omega'}{2T_1}\coth\frac{\hbar\omega}{2T_2}-1\right)\left|\nu_-^*(d/2)\,\omega'\nu'_+(-d/2)+\omega\nu_+^*(d/2)\,\nu'_-(-d/2)\right|^2+\\
&+\left(\coth\frac{\hbar\omega'}{2T_2}\coth\frac{\hbar\omega}{2T_1}-1\right)\left|\nu_-^*(-d/2)\,\omega'\nu'_+(d/2)+\omega\nu_+^*(-d/2)\,\nu'_-(d/2)\right|^2+\\
&+\left(\coth\frac{\hbar\omega'}{2T_1}\coth\frac{\hbar\omega}{2T_1}-1\right)\left|\nu_-^*(-d/2)\,\omega'\nu'_+(-d/2)-\omega\nu_+^*(-d/2)\,\nu'_-(-d/2)\right|^2\Bigg].\end{aligned} \tag{III.7.68}$$

Again, at each $\mathbf{q}$ the integrand of this expression is identical to Eq. (III.6.9) if one takes the scattering matrix (III.7.24) and makes the substitution (III.7.67). That is, each in-plane momentum $\mathbf{q}$, which takes discrete values for finite L_x, L_y, represents an independent scattering channel admitting an equivalent circuit representation. Since for $q\gg1/d$ the integrand is exponentially suppressed, the effective number of channels contribution to the heat current and its fluctuations is of the order of L_xL_y/d^2. Thus, a single circuit can qualitatively represent heat transfer between two pieces of dielectric whose size $L_x, L_y\sim d$, where the number of channels is of the order of 1.

Chapter IV

Classical Photon-Assisted Transport

A mesoscopic conductor in equilibrium exhibits no net current and solely thermal fluctuations. Placing the conductor in an electromagnetic environment, or driving it with a time-dependent voltage, modifies the current and its fluctuations. In a broader context, photon-assisted transport can be understood as the transfer of charged particles that exchange energy with the electromagnetic environment or the drive. The concept underlying photon-assisted transport was originally introduced by Tien and Gordon [199], who investigated the effect of a microwave radiation on electron tunneling between superconducting films. Pedersen and Büttiker [91] later developed the description of photon-assisted transport in normal-metal mesoscopic conductors by incorporating time-dependent voltages into the Landauer-Büttiker scattering framework. Here, we follow the arguments of Pedersen and Büttiker, while allowing for an arbitrary drive profile. The influence of the drive can be understood either as a modification of the occupation distribution in the terminals or, equivalently, as a modification of the scattering matrix, resulting in inelastic tunneling. Inelastic scattering processes can arise under periodic modulation of system parameters (e.g. the voltage, barrier height) and are captured by the Floquet scattering theory of quantum pumps [200, 201]. Quantum noise induced by an AC drive has been investigated in [200, 202–208], while nonsymmetrized quantum noise is related to light emission [41, 42, 209]. Beyond the noise, the full counting statistics of charge transfer was studied by Vanević *et al.* [43, 44], who analyzed various voltage drive profiles including square, cosine, triangular, sawtooth, and Lorentzian shapes. The full counting statistics (FCS) approach provides detailed insight into the elementary charge transfer processes in mesoscopic conductors. In particular, it reveals that time-dependent drives disturbs the Fermi sea and generates single-electron and electron-hole pairs, which subsequently scatter at the conductor [45]. The field of electron quantum optics focuses on the creation, manipulation, and measurement of these excitations in solid-state analogues of optical systems [45, 210–215] .

IV.1 Driven Landauer–Büttiker Scattering Approach

We begin by adopting the Landauer-Büttiker formalism and subsequently incorporate time-dependent drives into the framework [14, 15, 91]. A time-dependent voltage $V_\alpha(t)$ modulates the chemical potential at terminal α. These voltages are introduced into the Hamiltonian (I.3.1) via the scalar potential $V(z,t)$, which asymptotically approaches $V_1(t)$ in terminal 1 and $V_2(t)$ in terminal 2. As a result, the single-particle Hamiltonian is modified to

$$\hat{H} = -\frac{\hbar^2}{2m}\nabla^2 - eV(z,t) + U_{\text{con}}(x,y) + U_{\text{scat}}(\boldsymbol{r}). \tag{IV.1.1}$$

The dynamics of the system is governed by the time-dependent Schrödinger equation

$$i\hbar\frac{d\psi(\boldsymbol{r},t)}{dt} = \hat{H}(t)\psi(\boldsymbol{r},t). \tag{IV.1.2}$$

To handle the time-dependent drive, we apply a gauge transformation, which corresponds to moving to a driven frame. The transformed wavefunction is

$$\psi'(\boldsymbol{r},t) = \Upsilon(z,t)\psi(\boldsymbol{r},t), \tag{IV.1.3}$$

where the unitary transformation

$$\Upsilon(z,t) \equiv \exp\left(-i\phi(z,t)\right), \tag{IV.1.4}$$

satisfies $\partial_t\phi(z,t) = eV(z,t)/\hbar$. Throughout the thesis, we employ this transformation to account for the drive by absorbing its effect into the phase of the wavefunction or field operators (compare to the Green's function (IV.3.13)). Furthermore, the Hamiltonian transforms according to [216]

$$\hat{H}' = \hat{\Upsilon}(z,t)\hat{H}(t)\hat{\Upsilon}^\dagger(z,t) + i\hbar\frac{d\hat{\Upsilon}(z,t)}{dt}\hat{\Upsilon}^\dagger(z,t) \tag{IV.1.5}$$

which yields

$$\hat{H}' = \frac{\hbar^2}{2m}(i\nabla + \nabla\phi(z,t))^2 + U_{\text{con}}(x,y) + U_{\text{scat}}(\boldsymbol{r}). \tag{IV.1.6}$$

By assuming that the voltage drop between terminal 1 and 2 is distributed over a long distance, the gradient $\nabla\phi(z,t)$ becomes negligible, and we recover the static Hamiltonian (I.3.1). The adiabatic approximation holds when the spatial variation of the field is slow on the scale of the Fermi wavelength, preventing additional scattering [91]. Thus, transforming to the driven frame casts the problem into the form of the standard Landauer-Büttiker scattering formalism. Overall, the scattering states in the undriven frame are

$$\psi_\alpha(\boldsymbol{r},t) = e^{i\phi_\alpha(t)}\int_{-\infty}^{\infty}\frac{dE}{\sqrt{2\pi\hbar}}e^{-iEt/\hbar}\sum_n\left[\psi'^{+}_{\alpha n}(\boldsymbol{r},E)c'^{+}_{\alpha n}(E) + \psi'^{-}_{\alpha n}(\boldsymbol{r},E)c'^{-}_{\alpha n}(E)\right], \tag{IV.1.7}$$

where $\psi'^{\nu}_{\alpha n}(\boldsymbol{r}, E)$ are the wavefunctions defined in Eq. (I.3.3), and $c'^{\nu}_{\alpha n}(E)$ the mode amplitudes in the driven frame. We assume that transport is dominated by states near the Fermi energy E_F, and thus approximate the scattering wavefunction as $\psi'_{\alpha n}(\boldsymbol{r}, E) \approx \psi'_{\alpha n}(\boldsymbol{r}, E_F)$. In the second quantization formalism, the mode amplitudes are promoted to annihilation operators, yielding the field operators

$$\hat{\Psi}_\alpha(\boldsymbol{r}, t) = \sum_{\nu=\pm}\sum_n \psi'_{\alpha n}(\boldsymbol{r}, E_F)\hat{c}^{\nu}_{\alpha n}(t) \tag{IV.1.8}$$

$$\hat{\Psi}^\dagger_\alpha(\boldsymbol{r}, t) = \sum_{\nu=\pm}\sum_n \psi'_{\alpha n}(\boldsymbol{r}, E_F)\hat{c}^{\nu\dagger}_{\alpha n}(t), \tag{IV.1.9}$$

where the operators in the undriven frame are related to those in the driven frame by the transformation $\hat{c}^{\nu}_{\alpha n}(t) = e^{i\phi_\alpha(t)}\hat{c}'^{\nu}_{\alpha n}(t)$. Note that in the undriven frame, the creation and annihilation operators also satisfy the anticommutation relations $\{\hat{c}^{\nu}_{\alpha n}(E), \hat{c}^{\nu\dagger}_{\beta k}(E')\} = \delta_{\alpha\beta}\delta_{nk}\delta(E-E')$ and $\{\hat{c}^{\nu}_{\alpha n}(E), \hat{c}^{\nu}_{\beta k}(E')\} = 0$. The transformation leaves the current operator invariant, so that $\hat{I}_\alpha(t) = \hat{I}'_\alpha(t)$. As a result, the current operator takes the same form as in the static Landauer-Büttiker formalism (I.3.12), and is given by

$$\begin{aligned}\hat{I}_\alpha(t) =& e\sum_{\nu=\pm}\sum_n \nu\hat{c}^{\nu\dagger}_{\alpha n}(t)\hat{c}^{\nu}_{\alpha n}(t) = e\sum_n\sum_{\nu=\pm}\nu\hat{c}'^{\nu\dagger}_{\alpha n}(t)\hat{c}'^{\nu}_{\alpha n}(t)\\ =& e\sum_{\substack{\beta\gamma\\ mk}}\iint_{-\infty}^{\infty}\frac{dEdE'}{2\pi\hbar}e^{i(E-E')t/\hbar}A^{\alpha}_{\beta\gamma mk}(E,E')\hat{c}'^{\dagger}_{\beta m}(E)\hat{c}'_{\gamma k}(E').\end{aligned} \tag{IV.1.10}$$

Here, $\hat{c}'_{\beta m}(E) \equiv \hat{c}'^{+}_{\beta m}(E)$ denotes the annihilation operator for incoming scattering states in the driven frame, and $A^{\alpha}_{\beta\gamma mk}(E,E')$ is the Landauer-Büttiker A-matrix (I.3.13). Therefore, the average current and noise spectrum retain the same form as Eqs. (I.3.15) and (I.3.18), but with the correlations $\langle c'^{\dagger}_{\beta m}(E)c'_{\gamma k}(E')\rangle$ evaluated in the driven frame. To compute the physical observables, we need to transform back to the undriven frame. The particle correlators in the undriven frame, such as $\langle\hat{c}^{\dagger}_{\beta m}(E)\hat{c}_{\gamma k}(E')\rangle$, are assumed to obey standard thermal averages consistent with the equilibrium statistics of the reservoirs. Consequently, the correlators in the driven frame acquire a time-dependent modulation and no longer obey equilibrium statistics, so that the reservoir in the driven frame must be treated as a nonequilibrium reservoir. To describe the nonequilibrium reservoir, we introduce the Wigner function [217], defined as

$$\begin{aligned}W_\alpha(\bar{t},\overline{E}) \equiv& \int_{-\infty}^{\infty}d\Delta t e^{-i\overline{E}\Delta t/\hbar}\langle\hat{c}'^{\dagger}_{\alpha n}(\bar{t}+\Delta t/2)\hat{c}'_{\alpha n}(\bar{t}-\Delta t/2)\rangle\\ =& \int_{-\infty}^{\infty}d\Delta t e^{-i\overline{E}\Delta t/\hbar}e^{i\phi_\alpha(\bar{t}+\Delta t/2)}e^{-i\phi_\alpha(\bar{t}-\Delta t/2)}\langle\hat{c}^{\dagger}_{\alpha n}(\bar{t}+\Delta t/2)\hat{c}_{\alpha n}(\bar{t}-\Delta t/2)\rangle\\ =& \int_{-\infty}^{\infty}\frac{d\Delta t}{2\pi\hbar}\int_{-\infty}^{\infty}d\epsilon' e^{-i\epsilon'\Delta t/\hbar}e^{i\phi_\alpha(\bar{t}+\Delta t/2)}e^{-i\phi_\alpha(\bar{t}-\Delta t/2)}f_\alpha(\overline{E}-\epsilon'),\end{aligned} \tag{IV.1.11}$$

where the Wigner function is expressed in terms of the center time $\bar{t} \equiv (t+t')/2$ and the center energy $\overline{E} \equiv (E+E')/2$, with time difference $\Delta t \equiv t-t'$ and energy

difference $\epsilon \equiv E - E'$. The Wigner function characterizes the time-dependent quasidistribution of electronic occupations under the drive [217]. It is a quasidistribution because it can take on negative values or exceed one, corresponding to an apparent under- or over-occupation of fermionic states. In the absence of the drive, the Wigner function reproduces the standard Fermi-Dirac distribution. When a constant voltage is applied, it reflects the expected energy shift in the distribution. The Wigner function can be reconstructed experimentally from shot noise measurements, as demonstrated for levitons by [218]. Levitons are minimal-noise states, consisting solely of single-electron excitations above the Fermi sea, created by Lorentzian voltage pulses [212, 219]. Vanević *et al.* [45] investigated the many-body state generated by a mesoscopic conductor subject to a periodic arbitrary time-dependent drive. Using a full counting statistics approach, in particular the cumulant generating function (IV.4.1), the authors identified the independent single-electron and electron–hole excitations. The many-body state corresponds to the Fermi sea dressed by the quasiparticle excitations induced by the drive. Injecting time-delayed excitations from both terminals into the quantum contact causes interference of the fermionic wave functions, whose overlap can be determined via shot noise measurements. The experimentally obtained overlap between a single-electron wave packet generated by a constant voltage and electron–hole pairs generated by a harmonic drive was in quantitative agreement with the theoretical predictions.
Overall, the nonequilibrium correlations within the electron reservoir reduce to

$$\langle \hat{c}'^{\dagger}_{\beta m}(E)\hat{c}'_{\gamma k}(E')\rangle = \frac{1}{2}\delta_{\beta\gamma}\delta_{mk}\int_{-\infty}^{\infty}\frac{d\bar{t}}{2\pi\hbar}e^{-i(E-E')\bar{t}/\hbar}W_{\beta}(\bar{t},(E+E')/2). \tag{IV.1.12}$$

Diagonal elements $E = E'$ correspond to electron populations, proportional to the number of electrons per unit energy, whereas off-diagonal elements $E \neq E'$ encode the coherence [214]. Therefore, averaging the Wigner function over the center time yields the effective occupation function. For notational convenience, we define the Wigner transform of the A-matrix with respect to the energy difference as

$$A^{\alpha}_{\beta\gamma mk}(\bar{t},\overline{E}) \equiv \int_{-\infty}^{\infty}\frac{d\epsilon}{2\pi\hbar}e^{i\epsilon\bar{t}/\hbar}A^{\alpha}_{\beta\gamma mk}(E+\epsilon/2, E-\epsilon/2). \tag{IV.1.13}$$

The average current is then given by

$$\langle \hat{I}_{\alpha}(t)\rangle = \frac{e}{2\pi\hbar}\sum_{\beta m}\int_{-\infty}^{\infty}d\overline{E}\int_{-\infty}^{\infty}d\bar{t}A^{\alpha}_{\beta\beta mm}(t-\bar{t},\overline{E})W_{\beta}(\bar{t},\overline{E}), \tag{IV.1.14}$$

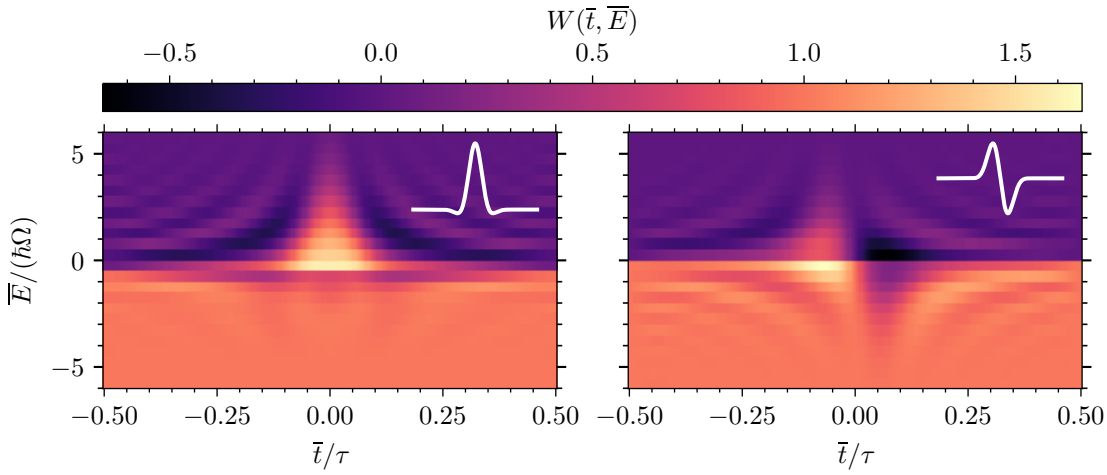

Figure IV.1: *Wigner functions* (IV.1.19) for periodic single-cycle ($\sigma\omega = 1$) Gaussian voltage pulses (IV.1.23b), repeated with period $\tau/(\sqrt{2}\sigma) = 10$, and amplitude $eV_0/(\hbar\omega) = 5$. Left: carrier–envelope phase $\varphi = 0$, Right: $\varphi = \pi/2$. Insets: corresponding temporal pulse shapes. The electron reservoir is assumed to be at zero temperature.

involving a time integral over the center time, and the center energy $\overline{E}$. Furthermore, the instantaneous noise spectrum is expressed as

$$\begin{aligned} S_{\alpha\beta}(\bar{t},\omega) \equiv& \frac{1}{2}\int_{-\infty}^{\infty} d\Delta t e^{i\omega\Delta t}\langle\{\hat{I}_\alpha(\bar{t}+\Delta t/2),\hat{I}_\beta(\bar{t}-\Delta t/2)\}\rangle \\ =& \frac{e^2}{8\pi^2\hbar^2}\sum_{\substack{\gamma\delta\\ mk}}\int_{-\infty}^{\infty} d\overline{E}\iint_{-\infty}^{\infty} d\bar{t}_1 d\bar{t}_2 K^{\alpha\beta}_{\gamma\delta mk}(\bar{t}-\bar{t}_1,\bar{t}-\bar{t}_2,\overline{E},\overline{E}+\hbar\omega) \\ &\times\left[W_\beta(\bar{t}_1,\overline{E})[1-W_\delta(\bar{t}_2,\overline{E}+\hbar\omega)]+[1-W_\beta(\bar{t}_1,\overline{E})]W_\delta(\bar{t}_2,\overline{E}+\hbar\omega)\right] \end{aligned} \tag{IV.1.15}$$

where the kernel function

$$\begin{aligned} K^{\alpha\beta}_{\gamma\delta mk}(\bar{t}_1,\bar{t}_2,\overline{E}_1,\overline{E}_2) \equiv& \iint_{-\infty}^{\infty}\frac{d\epsilon_1 d\epsilon_2}{(2\pi\hbar)^2}e^{i\epsilon_1\bar{t}_1/\hbar+i\epsilon_2\bar{t}_2/\hbar}A^{\alpha}_{\gamma\delta mk}(\overline{E}_1+\epsilon_1/2,\overline{E}_2-\epsilon_2/2) \\ &\times A^{\beta}_{\delta\gamma km}(\overline{E}_2+\epsilon_2/2,\overline{E}_1-\epsilon_1/2) \end{aligned} \tag{IV.1.16}$$

characterizes the scattering processes. Without drive, we rediscover the noise spectrum in Eq. (I.3.18). In the general case of energy-dependent scattering, the kernel (IV.1.16) cannot be expressed in terms of independently-Wigner-transformed A-matrices (IV.1.13), but rather mixes them.

Periodic drives.— In the special case of periodic drives with angular frequencies Ω_α, we can write the phase factors in terms of the Fourier series

$$e^{i\phi_\alpha(t)} = \sum_{l=-\infty}^{\infty} a_{\alpha l}e^{il\Omega_\alpha t},\quad a_{\alpha l} = \frac{1}{\tau_\alpha}\int_0^{\tau_\alpha} e^{il\Omega_\alpha t+i\phi_\alpha(t)}dt, \tag{IV.1.17}$$

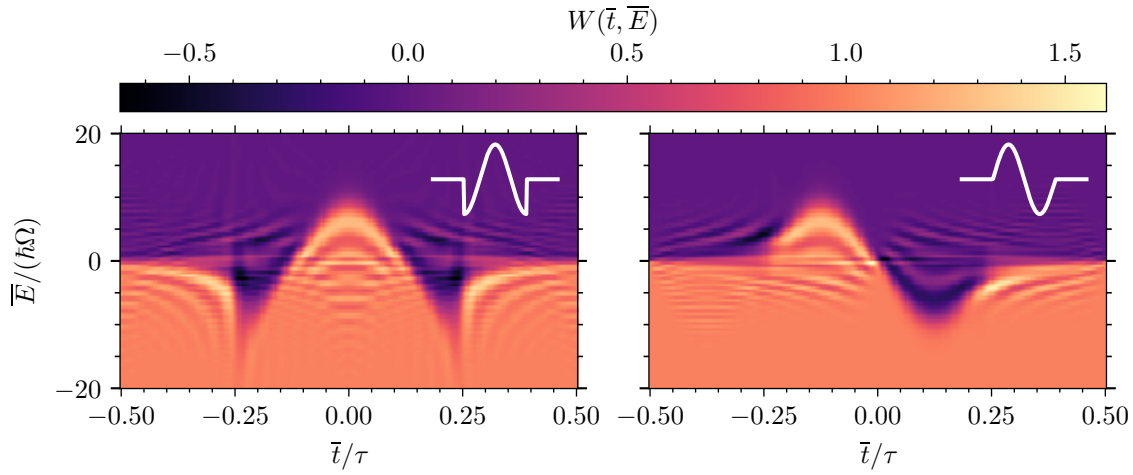

Figure IV.2: *Wigner functions* (IV.1.19) for periodic single-cycle ($N = 1$) voltage pulses (IV.1.23c) with a box-shaped envelope. The box width relative to the repetition period is $\tau_\omega/\tau = 1/2$, and amplitude $eV_0/(\hbar\omega) = 5$. Left: carrier–envelope phase $\varphi = 0$, Right: $\varphi = \pi/2$. Insets: temporal pulse shapes. Temperature is set to zero.

with the period $\tau_\alpha = 2\pi/\Omega_\alpha$. The Fourier coefficients satisfy the conditions

$$\sum_{l=-\infty}^{\infty} a_{\alpha n+l} a^*_{\alpha m+l} = \delta_{nm}, \tag{IV.1.18}$$

which allows $p_{\alpha l} = |a_{\alpha l}|^2$ to be interpreted as a probability distribution over l. Overall, the Wigner function reduces to

$$W_\alpha(\bar{t},\overline{E}) = \sum_{l,l'=-\infty}^{\infty} a_{\alpha l} a^*_{\alpha l'} e^{i(l-l')\Omega_\alpha \bar{t}} f_\alpha\left(\overline{E} - [l+l']\frac{\hbar\Omega_\alpha}{2}\right), \tag{IV.1.19}$$

which leads to the average current

$$\begin{aligned}\langle \hat{I}_\alpha(t)\rangle =& \frac{e}{2\pi\hbar}\sum_{\beta m}\sum_{l,l'=-\infty}^{\infty} a_{\alpha l} a^*_{\alpha l} e^{i(l-l')\Omega_\beta t}\int_{-\infty}^{\infty} d\overline{E} f_\beta\left(\overline{E} - [l+l']\frac{\hbar\Omega_\beta}{2}\right)\\ &\times A^\alpha_{\beta\beta mm}\left(\overline{E} + [l-l']\frac{\hbar\Omega_\beta}{2}, \overline{E} - [l-l']\frac{\hbar\Omega_\beta}{2}\right).\end{aligned} \tag{IV.1.20}$$

The noise spectrum has a complicated form, which is omitted here for brevity, but can be obtained by inserting the Wigner function into Eq. (IV.1.15). Under harmonic driving, both the average current and noise spectrum are consistent with the expressions reported by Pedersen [91]. The time-averaged current is determined by the time-averaged Wigner function

$$\overline{W}_\alpha(\overline{E}) \equiv \lim_{\overline{T}\to\infty}\frac{1}{\overline{T}}\int_{-\overline{T}/2}^{\overline{T}/2} W_\alpha(\bar{t},\overline{E})d\bar{t} = \sum_{l=-\infty}^{\infty} p_{\alpha l} f_\alpha(\overline{E} - l\hbar\Omega_\alpha) \equiv \overline{f}_\alpha(\overline{E}), \tag{IV.1.21}$$

and can be interpreted as an effective occupation $\overline{f}_\alpha$ that captures the time-averaged influence of the drive. The effective occupation distribution is a valid distribution respecting the Pauli principle and is larger than zero. For terminal 1, the average current is given by

$$\begin{aligned}\overline{I}_1 =& \frac{e}{2\pi\hbar}\sum_n \int_{-\infty}^{\infty} dE \mathcal{T}_n(E)[\overline{f}_1(E) - \overline{f}_2(E)] \\ =& \sum_{l=-\infty}^{\infty} p_l I_0(V + l\hbar\Omega_1/e),\end{aligned} \tag{IV.1.22}$$

where $I_0(V)$ denotes the static current–voltage characteristic, and we assumed in the second line that a time-dependent drive is applied only to terminal 1. In a conductor with energy-independent transmission $\mathcal{T}_n(E) = \mathcal{T}_n$, the current-voltage characteristic is linear. Therefore, If the average voltage $\overline{V}_1$ over one cycle of the drive vanishes and no external static voltage V is applied, the average current vanishes, since on average no energy quanta are exchanged, i.e. $\sum_l l p_l = 0$ [43] (see Eq. (IV.1.18)). For energy-dependent scattering, a nonzero average current can arise even when both V and $\overline{V}_1$ vanish. This effect was exploited in the experiments in the Leitenstorfer group [220–222] to demonstrate carrier-envelope phase control of the average transport, as we will discuss in Sec. IV.4. For illustration, we consider the Wigner functions resulting from voltage pulses with an oscillating carrier modulated by an envelope function (see Sec. IV.4). The pulses occur periodically, with repetition frequency $\Omega = 2\pi/\tau$. In particular, the voltage pulse during one period is given by

$$V(t) = E(t)V_0 \cos(\omega t + \varphi) - V_{\text{off}}, \tag{IV.1.23a}$$

with the envelope $E(t)$, the ac amplitude V_0, the carrier frequency ω, the carrier-envelope phase φ, the offset V_{off} which ensures vanishing average voltage. The Wigner function $W(\bar{t}, \overline{E})$ for a Gaussian envelope

$$E(t) = \frac{1}{\sqrt{2\pi}} \exp\left(-\frac{t^2}{2\sigma^2}\right) \tag{IV.1.23b}$$

is shown in Fig. IV.1, while the corresponding result for a box-shaped envelope,

$$E(t) = \Theta(t + N\tau_\omega/2)(1 - \Theta(t - N\tau_\omega/2)) \tag{IV.1.23c}$$

is depicted in Fig. IV.2. The Wigner functions clearly reflect the temporal pulse shape. Figure IV.3 shows the effective occupation distribution $\overline{f}(\overline{E})$ obtained by time-averaging over the full pulse. Further details and illustrative examples of the Wigner function can be found in [217].

Non-periodic drives.— A non-periodic drive complicates the notion of drive-induced quasiparticle excitations: the driven single-electron operator

$$\hat{c}'_{\alpha n}(E) = \hat{c}_{\alpha n}(E) + \int_{-\infty}^{\infty} \frac{dE'}{\sqrt{2\pi\hbar}} \mathcal{F}[(e^{-i\phi_\alpha(t)} - 1)](E')\hat{c}_{\alpha n}(E - E') \tag{IV.1.24}$$

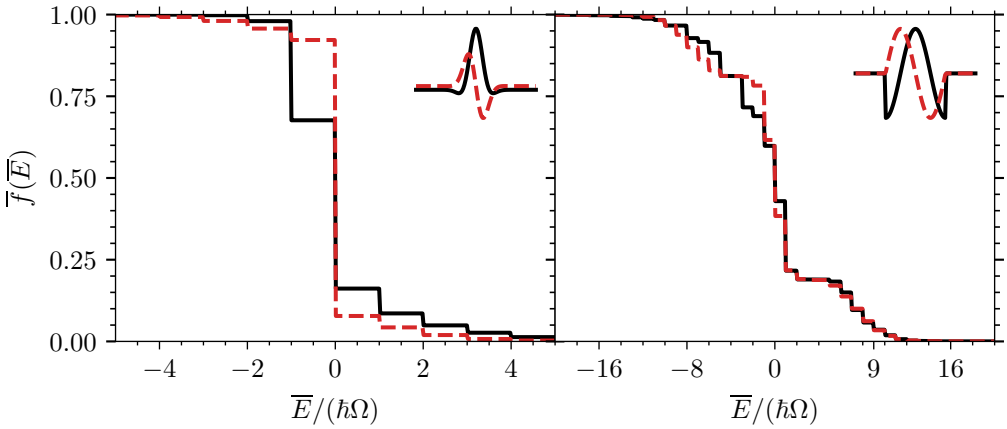

Figure IV.3: *Effective occupation* (IV.1.21). Left: single-cycle ($\sigma\omega = 1$) Gaussian-shaped pulse with amplitude $eV_0/(\hbar\omega) = 5$, period $\tau/(\sqrt{2}\sigma) = 10$, and carrier-envelope phase $\phi = 0, \pi/2$. Right: single-cycle ($N = 1$) box-shaped pulse with amplitude $eV_0/(\hbar\omega) = 5$, width $\tau_\omega/\tau = 1/2$, and carrier-envelope phase $\varphi = 0, \pi/2$. Insets show the corresponding pulse shapes. Zero temperature assumed.

is not straight forward to evaluate when the phases $\phi_\alpha(-\infty), \phi_\alpha(\infty)$ are not an integer multiple of 2π. In that case, the Fourier transform $\mathcal{F}[e^{i\phi_\alpha(t)} - 1]$ does not exist as an ordinary function, but may still be defined in the distributional sense. Levitov et al. [219, 223, 224] demonstrated that in this situation the charge fluctuations exhibit a logarithmic divergence, indicating the occurrence of a dynamical orthogonality catastrophe. For a constant voltage bias, the phase factor is $\phi_\alpha(t) = eV_\alpha t/\hbar$, yielding $\mathcal{F}[e^{-i\phi_\alpha(t)}](E) = \sqrt{2\pi\hbar}\delta(E - eV)$ and shifting the occupation $\langle \hat{c}'_{\alpha n}(E)\hat{c}'_{\beta m}(E')\rangle = f(E - eV)$ by the applied voltage bias. Similarly, for a periodic drive $V_\alpha(t)$, we obtain $\mathcal{F}[e^{-i\phi_\alpha(t)}](E) = \sqrt{2\pi\hbar}\sum_{l=-\infty}^{\infty} a_{\alpha l}\delta(E - l\hbar\Omega_\alpha)$. The drive generates a wavepacket of the form $\hat{c}'_{\alpha n}(E) = \sum_{l=-\infty}^{\infty} a_{\alpha l}\hat{c}_{\alpha n}(E - l\hbar\Omega_\alpha)$ centered around E, which corresponds to the particles energy in the driven frame. Thus, the drive gives rise to sidebands at energies $E + l\hbar\Omega_\alpha$, representing electrons that have absorbed ($l > 0$) or emitted ($l < 0$) $|l|$ energy quanta $\hbar\Omega_\alpha$. For example, a harmonic drive yields $a_{\alpha l} = J_l(eV_\alpha/(\hbar\Omega_\alpha))$, with V_α denoting the drive amplitude and $J_l(\cdot)$ the Bessel function of the first kind of order l.
Nevertheless, the Wigner function can also be calculated in the non-periodic case using the Fourier transformation of the Fermi-Dirac distribution. The thermal correlator in the Wigner function (IV.1.11) is given by

$$\begin{aligned}\langle \hat{c}^\dagger_{\alpha n}(\bar{t} + \Delta t/2)\hat{c}_{\alpha n}(\bar{t} - \Delta t/2)\rangle &= \int_{-\infty}^{\infty} \frac{d\overline{E}}{2\pi\hbar} e^{-i\overline{E}\Delta t/\hbar} f(\overline{E}) \\ &= \frac{1}{2\pi i}\left(\pi i\delta(\Delta t) + \frac{1}{\Delta t}\frac{\pi\Delta t k_B T/\hbar}{\sinh(\pi\Delta t k_B T/\hbar)}\right), \quad \text{(IV.1.25)}\end{aligned}$$

where T is the temperature. Therefore, the Wigner function reduces to

$$W_\alpha(\bar{t},\overline{E}) = f(\overline{E}) + \int_{-\infty}^{\infty} \frac{d\Delta t}{2} e^{-i\overline{E}\Delta t/\hbar} \left[e^{i\phi_\alpha(\bar{t}+\Delta t/2)-i\phi_\alpha(\bar{t}-\Delta t/2)} - 1 \right] \frac{k_\mathrm{B}T/\hbar}{\sinh(\pi \Delta t k_\mathrm{B}T/\hbar)}, \tag{IV.1.26}$$

which can be evaluated numerically. We consider the same pulses as before, but focus on a single pulse rather than a train of pulses. The Gaussian envelope leads to a phase

$$\phi(t) = \phi_\mathrm{eff}\,\mathrm{Re}\left(e^{i\varphi}\,\mathrm{erf}\left(\frac{t}{\sqrt{2}\sigma} - i\frac{\omega\sigma}{\sqrt{2}} \right) + 1 \right), \quad \phi_\mathrm{eff} = \frac{eV_0\sigma}{2\hbar} e^{-\omega^2\sigma^2/2}, \tag{IV.1.27}$$

where $\mathrm{erf}(\cdot)$ is the error function and we discarded the offset voltage $V_\mathrm{off} \equiv 0$, while the box envelope yields

$$\phi(t) = \phi_\mathrm{eff}\left(\sin(\omega t + \varphi) - \sin(\varphi - \pi N)\right), \quad \phi_\mathrm{eff} = eV_0/(\hbar\omega). \tag{IV.1.28}$$

Figures IV.4 and IV.5 display the Wigner function for the Gaussian and Box envelopes, respectively, with the shape of the drive being imprinted in the Wigner function. The Wigner functions clearly resemble those of periodic pulses in Figs. IV.1 and IV.5. Figure IV.6 illustrates the effective occupation $\overline{f}(\overline{E})$ obtained from $\int_{-\infty}^{\infty} W(t,\overline{E})dt$ for both a single-cycle Gaussian pulse and a box pulse. The small overshoot near zero energy arises from the finite resolution and averaging time used in the numerical calculation.

IV.2 Full Counting Statistics: Beyond Average and Noise

Charge transport through nanostructures is inherently non-deterministic, exhibiting fluctuations that stem from thermal and quantum mechanical origins, as well as imperfections in the measurement process. Besides limiting the precision of detection, out-of-equilibrium fluctuations carry information about the system that is not captured by the average alone [34, 40]. Complete information about the intrinsic charge transport is contained in the full counting statistics (FCS), which describes the entire probability distribution of transferred charge. [225]. The concept of full counting statistics was adopted from quantum optics, where its counterpart, the photon counting statistics, has played a key role in characterizing quantum states of light [226]. A major difference is that photons are typically absorbed during detection, whereas charges are counted non-destructively, which leads to a different operator ordering scheme [219]. At a fundamental level, charge transport is inherently discrete, since it involves the transfer of particles carrying quantized charge. For example, shot noise [15] originates from the discrete nature of charge and results from the stochastic transport of particles through the nanostructure. While most experiments have focused on the average current and noise, measurements of higher-order cumulants [227] and direct counting of single-electron transfers have also been realized [228–230]. From a theoretical perspective, FCS is particularly intriguing because it provides insights into the elementary processes underlying charge transport [43, 44, 219, 231–236] .

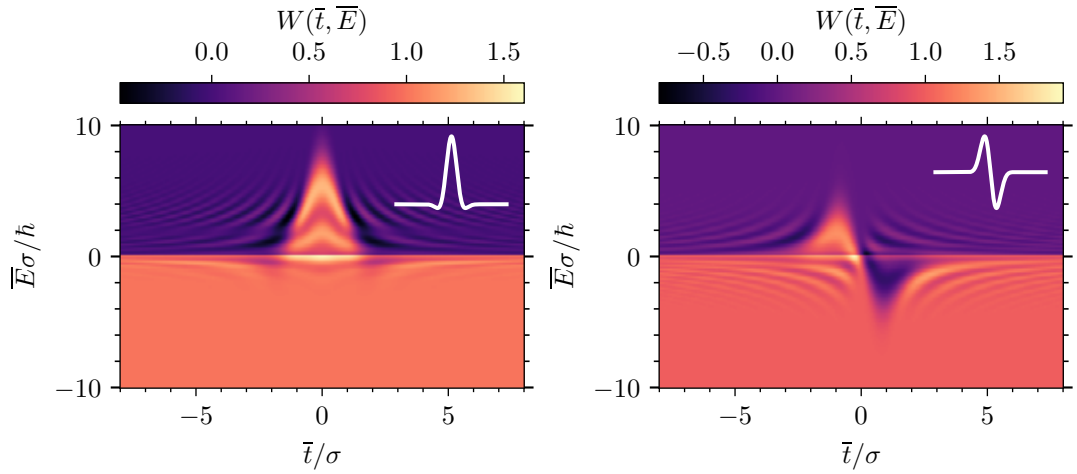

Figure IV.4: *Wigner functions* (IV.1.26) for one single-cycle ($\sigma\omega = 1$) Gaussian voltage pulse (IV.1.23b) (with $V_{\text{off}} \equiv 0$), $\phi_{\text{eff}} = 2\pi$. Left: carrier–envelope phase $\varphi = 0$, Right: $\varphi = \pi/2$. Insets: corresponding temporal pulse shapes. The electron reservoir is assumed to be at zero temperature.

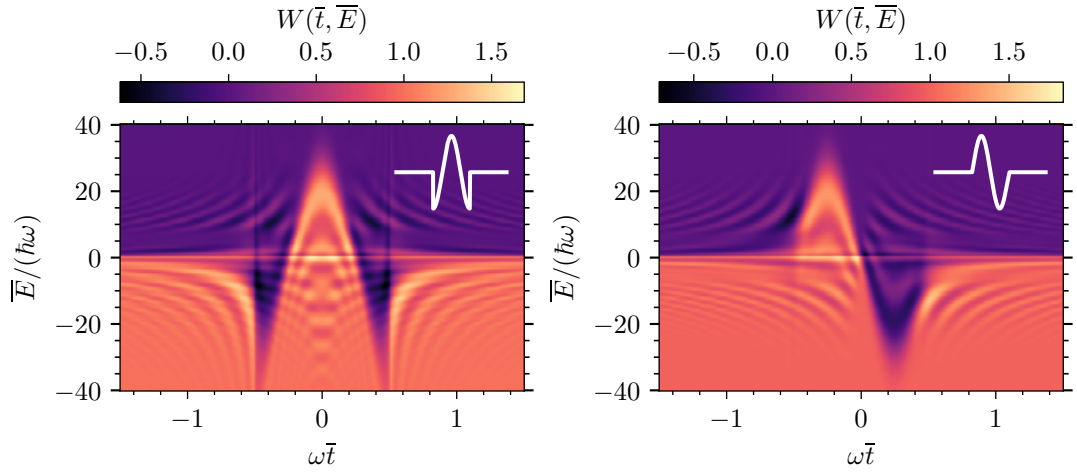

Figure IV.5: *Wigner functions* (IV.1.26) for one single-cycle ($N = 1$) voltage pulses (IV.1.23c) with a box-shaped envelope. The box envelope exactly span one period of the oscillating carrier, and amplitude $eV_0/(\hbar\omega) = 5$. Left: carrier–envelope phase $\varphi = 0$, Right: $\varphi = \pi/2$. Insets: temporal pulse shapes. Temperature is set to zero.

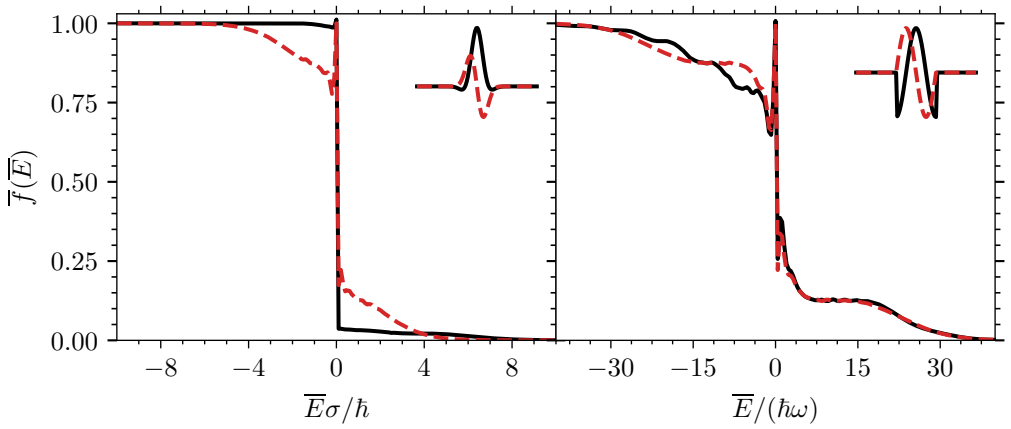

Figure IV.6: *Effective occupation* of a single pulse. Left: single-cycle ($\sigma\omega = 1$) Gaussian-shaped pulse with amplitude $eV_0/(\hbar\omega) = 5$, and carrier-envelope phase $\varphi = 0, \pi/2$. Right: single-cycle ($N = 1$) box-shaped pulse with amplitude $eV_0/(\hbar\omega) = 5$, and carrier-envelope phase $\varphi = 0, \pi/2$. Insets show the corresponding pulse shapes. Zero temperature assumed.

Charge distribution.— At the heart of FCS lies the charge transfer distribution $\mathcal{P}(N)$, which describes the probability that N charges are transferred over a finite measurement time. Once the charge probability distribution is known, the k-th moment can be obtained from

$$\mathcal{M}_k = \overline{N^k} \equiv \sum_N N^k \mathcal{P}(N). \tag{IV.2.1}$$

While moments capture the overall shape of a probability distribution, cumulants refine this description by removing redundant correlations and highlighting statistically independent contributions. The first four cumulants are given by

$$\mathcal{C}_1 = \overline{N} \equiv \sum_N \mathcal{P}(N) N \tag{IV.2.2a}$$

$$\mathcal{C}_2 = \overline{(N-\overline{N})^2} = \sum_N \mathcal{P}(N)(N-\overline{N})^2 \tag{IV.2.2b}$$

$$\mathcal{C}_3 = \overline{(N-\overline{N})^3} = \sum_N \mathcal{P}(N)(N-\overline{N})^3 \tag{IV.2.2c}$$

$$\begin{aligned}\mathcal{C}_4 &= \overline{(N-\overline{N})^4} - 3\overline{(N-\overline{N})^2}^2 \\ &= \sum_N \mathcal{P}(N)(N-\overline{N})^4 - 3\left(\sum_N \mathcal{P}(N)(N-\overline{N})^2\right)^2 .\end{aligned} \tag{IV.2.2d}$$

The first cumulant corresponds to the mean, whereas the second cumulant represents the variance and characterizes the width of the distribution. The asymmetry of the probability distribution is captured by the third cumulant and quantified

by the skewness, defined as $\mathcal{C}_3/\mathcal{C}_2^{3/2}$. A positive skewness indicates a long tail of the distribution extending toward large values, whereas a negative skewness implies the tail is toward smaller values. Zero skewness corresponds to a symmetric distribution. The fourth cumulant signals the peakedness of the distribution, quantified by the kurtosis excess $\mathcal{C}_4/\mathcal{C}_2^2$. Positive kurtosis excess indicates a distribution with a pronounced central peak and heavier tails compared to a Gaussian distribution. For a Gaussian distribution, the kurtosis excess is zero [237].

Cumulant generating function.— All cumulants can be derived from the cumulant-generating function (CGF) $\mathcal{S}(\chi)$ via

$$\mathcal{C}_k = (-i)^k \frac{\partial^k \mathcal{S}(\chi)}{\partial \chi^k}\bigg|_{\chi=0}, \tag{IV.2.3}$$

where χ is the counting field. The CGF is related to the FCS by

$$\mathcal{S}(\chi) = \ln\left(\sum_N \mathcal{P}(N)\exp(iN\chi)\right). \tag{IV.2.4}$$

The CGF provides an alternative representation of the charge transfer statistics that contains the identical information and is more tractable for theoretical treatment. Typically, the CGF or partition function is first computed, and the FCS is then obtained via an inverse Fourier transform (see Eq. (IV.2.4)). The probability of transferring N charges corresponds to the coefficient in front of $e^{iN\chi}$, and can be directly extracted from the CGF in Eq. (IV.2.4). This reveals the elementary charge transfer processes and establishes a connection to particle transport. Independent processes contribute additively to the total CGF, appearing as a sum of individual CGFs. This indicates that the FCS can be represented as a convolution of the probability distributions associated with independent events. Therefore, deviations from additivity in the CGF signal the presence of correlations between processes.

Examples.— We begin by presenting the CGF and FCS of illustrative examples, and subsequently discuss the microscopic calculation in the following section IV.3. A simple mesoscopic system involves an electron reservoir sending uncorrelated electrons to a scattering region, where each electron is transmitted with probability $\mathcal{T}$ to the other reservoir or reflected by $\mathcal{R} = 1 - \mathcal{T}$. The probability of transferring N elementary charges to the other reservoir is found to be binomial [6, 219, 225]

$$\mathcal{P}(N) = \binom{M}{N}\mathcal{T}^N\mathcal{R}^{M-N}, \tag{IV.2.5}$$

for $N = 0, \ldots, M$ and $\mathcal{P}(N) = 0$ otherwise. M corresponds to the number of elementary charges send from the reservoir within the measurement time t_0. The binomial coefficient corresponds to the number of distinct ways to transmit N and reflect $M - N$ elementary charges out of M attempts. Figure IV.7 shows the

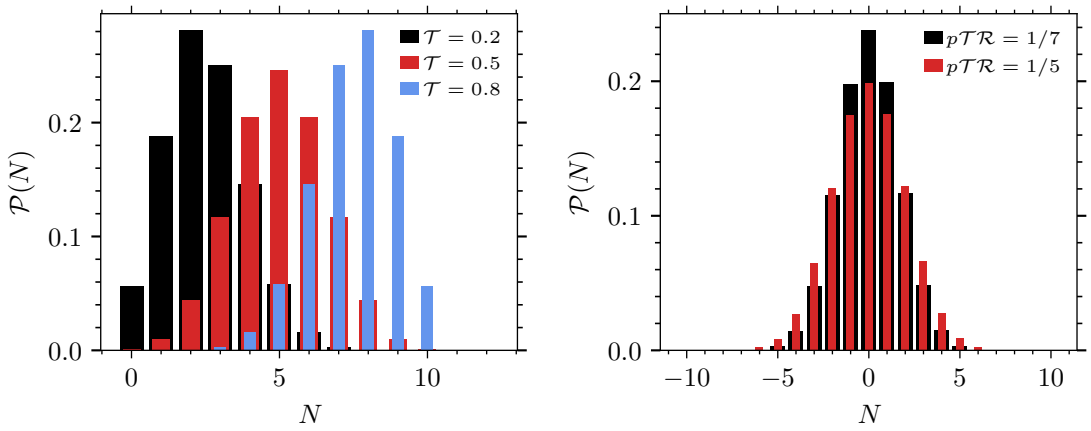

Figure IV.7: *Charge transfer distribution*. Left: Binomial distribution of a single-channel mesoscopic conductor for varying transmissions, with $M = 10$ attempts. Right: Hypergeometric distribution [237] arising under time-dependent voltage driving, evaluated for two different charge-transfer probabilities $p\mathcal{TR}$, with $M = 10$.

binomial distribution for various transmissions. The CGF is obtained by

$$\mathcal{S}(\chi) = \ln\left[\sum_N \binom{M}{N} \mathcal{T}^N \mathcal{R}^{M-N} e^{iN\chi}\right] = \ln\left[(\mathcal{R} + \mathcal{T}e^{i\chi})^M\right] = M\ln[1 + \mathcal{T}(e^{i\chi} - 1)], \tag{IV.2.6}$$

where we used the binomial formula. This CGF arises for a single-channel normal-metal mesoscopic conductor at zero temperature, with the number of transmission attempts $M = et_0V/(\pi\hbar)$ is set by the applied voltage V [232]. In the multichannel case, each channel n contributes independently, and the total CGF is the sum of the single-channel CGFs, each with its distinct transmission probability $\mathcal{T}_n$. At finite temperature, transport in the reverse direction becomes possible. The CGF takes the form

$$\mathcal{S}(\chi) = \frac{t_0}{2\pi\hbar}\sum_n \int dE \ln[1 + \mathfrak{p}_{1n}(e^{i\chi} - 1) + \mathfrak{p}_{-1n}(e^{-i\chi} - 1)], \tag{IV.2.7}$$

where each electron, with energy E and channel n, contributes independently to the charge transfer. The factor $\mathfrak{p}_{1n} = \mathcal{T}_n f_1(E)[1 - f_2(E)]$ represents the probability of transferring an electron from terminal 1 to terminal 2, with the Fermi distribution $f_j(E) = [1 + \exp((E - \mu_j)/(k_B T_j))]^{-1}$ of terminal j, determined by the temperature T_j, and the chemical potential μ_j. Charge is transferred from terminal 1 to 2 when the state in terminal 1 is occupied (described by $f_1(E)$) and an unoccupied state is available in terminal 2 (described by $1 - f_2(E)$), with the electron being transmitted with probability $\mathcal{T}_n$ (illustrated in Fig. IV.8). The transport in the reverse direction is described by $\mathfrak{p}_{-1n} = \mathcal{T}_n[1 - f_1(E)]f_2(E)$. Equation (IV.2.7) directly indicates that transport in both directions are correlated.

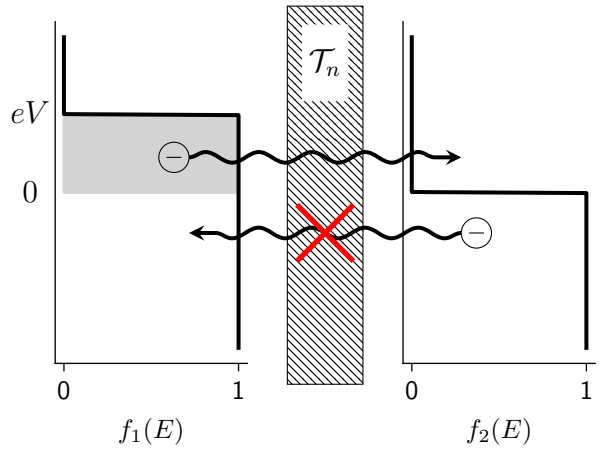

Figure IV.8: *Electron transfer probability* in a voltage-biased mesoscopic conductor at zero temperature. Transfer occurs when one terminal is occupied and the other is empty.

A tunnel junction possess the CGF

$$\mathcal{S}(\chi) = N_{12}(e^{i\chi} - 1) + N_{21}(e^{-i\chi} - 1), \tag{IV.2.8}$$

which is derived from Eq. (IV.2.7) by expanding to first order in the transmission probabilities $\mathcal{T}_n \ll 1$, with the average number of transferred charge

$$N_{12} = \frac{t_0 G_T}{e^2} \int dE[1 - f_1(E)]f_2(E) \tag{IV.2.9a}$$

$$N_{21} = \frac{t_0 G_T}{e^2} \int dE f_1(E)[1 - f_2(E)], \tag{IV.2.9b}$$

and the tunnel conductance $G_T = e^2 \sum_n \mathcal{T}_n/(\pi\hbar)$. All odd cumulants $C_{2k+1} = N_{12} - N_{21}$ and even cumulants $C_{2k} = N_{12} + N_{21}$ are identical and are determined by the transferred charge from one side to the other. Transport form one side to the other is uncorrelated and follows a Poisson distribution

$$\mathcal{P}_{jk}(N) = \frac{N_{jk}^N}{N!} e^{-N_{jk}}, \quad j, k = 1, 2, \ j \neq k. \tag{IV.2.10}$$

The total FCS results from the convolution of two Poisson distributions and takes the form of a generalized Poisson distribution [238]. Therefore, charge transfer in a tunnel junction corresponds to the successive transport of uncorrelated electrons [6].
Multiparticle transfer involves the transfer of several particles in each attempt. During a transfer event, there is a probability p_k of transferring a group of k-particles, where $\sum_{k=-\infty}^{\infty} p_k = 1$. Given M total attempts, the CGF is given by

$$\mathcal{S}(\chi) = M \ln \left(\sum_{k=-\infty}^{\infty} p_k e^{ik\chi} \right). \tag{IV.2.11}$$

Multiparticle transfer occurs, for example, in a mesoscopic conductor at finite temperature subjected to a time-dependent voltage drive [44]. For simplicity, we consider a normal-metal conductor at zero temperature with a single channel and transmission probability $\mathcal{T}$. The drive creates electron-hole pairs in the terminal, which are emitted towards the scatterer. The electron-hole pair contributes to charge transport when the electron is transmitted with probability $\mathcal{T}$ and the hole is reflected with probability $\mathcal{R} = 1-\mathcal{T}$, or vice versa. In total one elementary charge is transferred with probability $\mathfrak{p}_1 = \mathcal{T}\mathcal{R}p$, with p the probability to create an electron-hole pair by the drive. The inverse process, in which the hole is transferred, possesses the identical the probability $\mathfrak{p}_{-1} = \mathfrak{p}_1$. No charge is transferred with probability $\mathfrak{p}_0 = 1 - \mathfrak{p}_1 - \mathfrak{p}_{-1}$, following from the normalization condition. Overall, the CGF reduces to

$$\mathcal{S}(\chi) = M \ln\left[1 + p\mathcal{T}\mathcal{R}(e^{i\chi} + e^{-i\chi} - 2)\right]. \tag{IV.2.12}$$

Electrons and holes are transmitted with equal probability, causing all odd cumulants to cancel out, resulting in no net charge transport. Fluctuations are still present, resulting in the cumulants

$$\mathcal{C}_2 = 2Mp\mathcal{T}\mathcal{R} \tag{IV.2.13a}$$
$$\mathcal{C}_4 = 2Mp\mathcal{T}\mathcal{R}(1 - 6p\mathcal{T}\mathcal{R}). \tag{IV.2.13b}$$

An ideal creation of electron-hole pairs, $p = 1$, yields independent contributions from electrons and holes, thereby splitting the CGF into independent unidirectional components with CGFs given by $\mathcal{S}_\pm(\chi) = \ln[1 + \mathcal{T}(e^{\pm i\chi} - 1)]$. The corresponding FCS can be formulated in terms of a hypergeometric function, and is symmetric around $N = 0$, with a sharper peak for $0 < p\mathcal{T}\mathcal{R} < 1/6$ and a flatter peak for $1/6 < p\mathcal{T}\mathcal{R} < 1/4$, as indicated by the kurtosis excess [237]. The charge transfer distribution of a single-channel mesosocopic conductor under time-dependent drive is depicted in Fig. IV.7.

IV.3 Keldysh-Action Approach

Over the years, multiple approaches have been developed to calculate the full counting statistics. Nagaev et al. [239, 240] introduced a semiclassical cascade approach, based on the Boltzmann-Langevin equations, to calculate higher-order current correlators, and a stochastic path integral approach was developed in [241, 242]. Levitov et al. [243] proposed the first theory of full counting statistics. There, the authors approached the problem by computing current moments $\langle[\int_0^t dt' \hat{I}(t')]^k\rangle$, which led to an unphysical result: a fractional electron charge for the particles involved in the transport. The difficulty arises from the non-commutativity of the current operator at different times, which renders the transmitted charge operator $\hat{Q}(t) = \int_0^t dt' \hat{I}(t')$ ill-defined. Therefore, time ordering is essential when computing higher-order correlators. To resolve this issue, Levitov et al. [219] introduced a quantum detector, a spin-$1/2$ particle that precesses in the magnetic field induced by the current, serving as a quantum galvanometer. The FCS and the associated CGF are independent of the galvanometer, which merely provides

a convenient and rigorous quantum-mechanical definition of counting that resolves the operator-ordering ambiguities. Superconducting constrictions raise an additional subtlety, as the full counting statistics can become negative under certain conditions [231], thereby undermining their interpretation as a probability distribution. Here, the measuring device plays a decisive role in the interpretation. Kindermann et al. [233] proposed a static detector to study the FCS of a general quantum mechanical variable. They demonstrated that the FCS captures the transformation of the detectors density matrix due to the measurement. The detector's quantum state cannot be interpreted as a probability distribution, since its Wigner function can take on negative values. Consequently, the FCS does not need to be strictly positive either. In the following, we analyze the cumulant-generating functional using the Keldysh Green's function formalism [232, 233, 244, 245].

Partition functional.— The central object of interest is the moment generating functional

$$\mathcal{Z}[\chi] = \left\langle \tilde{\mathcal{T}} \left[\exp\left(\frac{i}{e} \int_{t_s}^{\infty} dt \chi^{-}(t) \hat{I}_{\mathrm{H}}(t) \right) \right] \mathcal{T} \left[\exp\left(-\frac{i}{e} \int_{t_s}^{\infty} dt \chi^{+}(t) \hat{I}_{\mathrm{H}}(t) \right) \right] \right\rangle, \tag{IV.3.1}$$

where $\hat{I}_H(t)$ is the current operator in the Heisenberg picture, evolving according to the Hamiltonian $\hat{H}(t)$. The time ordering and anti-time ordering operator are denoted as $\mathcal{T}$ and $\tilde{\mathcal{T}}$, respectively. We introduced the counting fields $\chi^{\pm}(t)$,where $\chi^{+}(t)$ is defined on the forward Keldysh contour and $\chi^{-}(t)$ on the backward contour. The Keldysh contour runs from the initial time t_s to infinity and back to t_s. The corresponding cumulant-generating functional is obtained by

$$\mathcal{S}[\chi] \equiv \ln \mathcal{Z}[\chi]. \tag{IV.3.2}$$

Functional derivation of the moment-generating functional and cumulant-generating functional creates the time ordered current correlators

$$\langle \tilde{\mathcal{T}}[\Pi_{k=1}^{j} \hat{I}_{\mathrm{H}}(t_k)] \mathcal{T}[\Pi_{l=j+1}^{n} \hat{I}_{\mathrm{H}}(t_l)] \rangle = \left. \frac{(-1)^j (ie)^n \delta^n \mathcal{Z}[\chi]}{\delta\chi^{-}(t_1) \dots \delta\chi^{-}(t_j) \delta\chi^{+}(t_{j+1}) \dots \delta\chi^{+}(t_n)} \right|_{\chi=0} \tag{IV.3.3a}$$

$$\langle\langle \tilde{\mathcal{T}}[\Pi_{k=1}^{j} \hat{I}_{\mathrm{H}}(t_k)] \mathcal{T}[\Pi_{l=j+1}^{n} \hat{I}_{\mathrm{H}}(t_l)] \rangle\rangle = \left. \frac{(-1)^j (ie)^n \delta^n \mathcal{S}[\chi]}{\delta\chi^{-}(t_1) \dots \delta\chi^{-}(t_j) \delta\chi^{+}(t_{j+1}) \dots \delta\chi^{+}(t_n)} \right|_{\chi=0}, \tag{IV.3.3b}$$

where $\Pi_{k=1}^{n} \hat{I}_{\mathrm{H}}(t_j)$ denotes the product $\hat{I}_{\mathrm{H}}(t_1) \cdot \ldots \cdot \hat{I}_{\mathrm{H}}(t_n)$, and $\langle\langle \cdot \rangle\rangle$ is the cumulant averaging. Accordingly, all correlation functions and the full counting statistics can be derived from the moment-generating functional.
The moment-generating functional is connected to non-equilibrium field theory, where it corresponds to the Keldysh partition functional. This connection becomes clear by introducing the auxiliary Hamiltonians

$$\hat{H}_{\mathrm{aux}}^{\pm} = \hat{H} + (\hbar/e)\chi^{\pm}(t)\hat{I}, \tag{IV.3.4}$$

which differ on the forward and backward branches of the Keldysh contour due to the contour-dependent counting fields. The interaction picture relates the time evolution operators by

$$\hat{U}^{\pm}_{\mathrm{H_{aux}}}(t,t_s) = \hat{U}_{\mathrm{H}}(t,t_s)\hat{U}^{\pm}_{\mathrm{int}}(t,t_s), \tag{IV.3.5}$$

with $\hat{U}^{\pm}_{\hat{H}_{\mathrm{aux}}}(t,t_s)$ the time evolution operator of the extended system, $\hat{U}_H(t,t_s)$ the time evolution operator of the physical subsystem $\hat{H}$, and

$$\hat{U}^{\pm}_{\mathrm{int}}(t,t_s) = \mathscr{T}\exp\left(-\frac{i}{e}\int_{t_s}^{t} dt'\chi^{\pm}(t')\hat{I}_{\mathrm{H}}(t')\right). \tag{IV.3.6}$$

Thus, the Heisenberg-picture formulation in (IV.3.1) can be recast in terms of a Schrödinger picture with an extended Hamiltonian $\hat{H}_{\mathrm{aux}}$. The moment-generating function is given by the Keldysh partition functional [63]

$$\mathcal{Z}[\chi] = \left\langle \tilde{\mathscr{T}}\left[\exp\left(\frac{i}{\hbar}\int_{t_s}^{\infty} dt\hat{H}^{-}_{\mathrm{aux}}(t)\right)\right]\mathscr{T}\left[\exp\left(-\frac{i}{\hbar}\int_{t_s}^{\infty} dt\hat{H}^{+}_{\mathrm{aux}}(t)\right)\right]\right\rangle. \tag{IV.3.7}$$

If the counting fields are equal on both contours, then partition function reduces to $\mathcal{Z}[\chi^+ = \chi^-] = 1$. Especially, the partition functional is normalized at $\chi^{\pm}(t) = 0$. A comprehensive treatment of the Keldysh path integral formalism is provided in [63].

Counting fields.— It is instructive to consider the interaction Hamiltonians $\hat{H}^{\pm}_{\mathrm{int}}(t) = (\hbar/e)\chi^{\pm}(t)\hat{I}$ in greater detail. The counting fields $\chi^{\pm}(t)$ are dimensionless, whereas $(\hbar/e)\chi^{\pm}(t)$ has the dimension of a magnetic flux. Hence, the Hamiltonians effectively mediate an interaction between the system's current and a fictitious magnetic flux introduced via the counting fields. A classical time-dependent drive $V(t)$ induces an magnetic flux $\Phi(t) = \int_{t_s}^{t} dt'V(t')$, which corresponds to a phase $\phi(t) = e\Phi(t)/\hbar$. To account for a physically imposed phase $\phi(t)$, the counting fields are shifted as $\chi^{\pm}(t) \to \chi^{\pm}(t) + \phi(t)$. Therefore, the current correlators in the presence of a classical drive can be obtained from (IV.3.3) by evaluating the functional derivative at $\chi^{\pm}(t) = \phi(t)$ instead of zero. Furthermore, a quantum mechanical environment imposing a phase $\hat{\phi}$ on the system is modelled by

$$\hat{H}^{\pm}_{\mathrm{hybrid}} = \hat{H}^{\pm}_{\mathrm{aux}} + \hat{H}_{\mathrm{env}} + \hat{H}^{\mathrm{int}}_{\mathrm{env}}, \tag{IV.3.8}$$

with $\hat{H}_{\mathrm{env}}$ the Hamiltonian of the electromagnetic environment, and the interaction Hamiltonian $\hat{H}^{\mathrm{int}}_{\mathrm{env}} = (\hbar/e)\hat{\phi}\hat{I}$. The partition functional now incorporates an average over both the electromagnetic environment and the system. If the initial state is separable, the expectation value factorizes as $\langle\cdot\rangle = \langle\langle\cdot\rangle_{\mathrm{env}}\rangle_{\mathrm{sys}}$. The electromagnetic environment is typically modelled as a collection of harmonic oscillators with a quadratic Hamiltonian [233]. The phase operator is linear in the bosonic creation and annihilation operators of the modes. Transitioning to a path integral description introduces the fields $\phi^{\pm}(t)$, which represent the phase

operator on the forward and backward branches of the Keldysh contour [63]. The partition functional of the coupled system is given by

$$\mathcal{Z}_{\text{hybrid}}[\chi] = \int D[\phi^{\pm}]\mathcal{Z}_{\text{env}}[\phi]\mathcal{Z}_{\text{sys}}[\chi+\phi], \tag{IV.3.9}$$

with $\int D[\phi^{\pm}]$ denotes the path integral measure over the forward and backward phase fields, and $\mathcal{Z}_{\text{env}}[\phi]$ the partition functional of the isolated electromagnetic environment [63]. This highlights the intimate connection of the counting fields both with the Keldysh quantum field of the electromagnetic environment and with an externally applied classical drive.

Green-function formalism.— We examine the Keldysh action of a two-terminal coherent conductor, outlining the key aspects, while the details can be found in [232–234, 244, 246]. Let us briefly recapitulate the basic modeling perspective of a mesoscopic conductor outlined in Chap. I. A mesoscopic conductor is a nanoscale constriction that allows particles to traverse it without undergoing inelastic processes, such as electron-electron collisions or interactions with phonons. The conductor acts as a one-dimensional fermionic waveguide, inside which a potential hinders free propagation and induces elastic scattering. Due to confinement within the waveguide, electron motion becomes quantized and is described by transverse modes, or channels. Incoming and outgoing modes are related through the scattering matrix, which encapsulates how they scatter off the potential. Outside the ballistic region, electrons are exchanged with independent particle reservoirs $j = 1, 2$. Each reservoir is characterized by a quasiclassical Green's function $\check{G}_j(t,t')$, which is a matrix in Keldysh, Nambu and spin space. The terminal Green's functions are constant in space and isotropic in momentum space as they are calculated in the diffusive approximation [247]. The key property of the quasiclassical Green's function, where most calculations rely on [244, 246], is the normalization condition

$$[\check{G}_j\check{G}_j](t,t') = \int dt''\check{G}_j(t,t'')\check{G}_j(t'',t') = \delta(t-t')\check{1}, \tag{IV.3.10}$$

where multiplication involves matrix multiplication and time integration. All regions are assumed to be much shorter than the coherence length, allowing the current to be evaluated within the ballistic region, as the matrix current is conserved [245]. The current through the mesoscopic conductor is determined by the Green's function in the ballistic region, which in turn depends on the reservoir Green's functions and the scattering matrix [245, 246]. The Green's function framework can be extended to multiterminal devices [246] and to circuits with multiple mesoscopic conductors [234, 245], separating the circuit into nodes (isotropic particle reservoirs) and connectors (mesoscopic conductors) characterized by their transmission probabilities.

Incorporating Counting.— A central question that remains is how charge transfer through the conductor is counted and how the counting field is incorporated. The counting field can be transformed either to the scattering matrix or to the reservoir Green's functions [231, 237, 246]. In the former case, the scattering potential

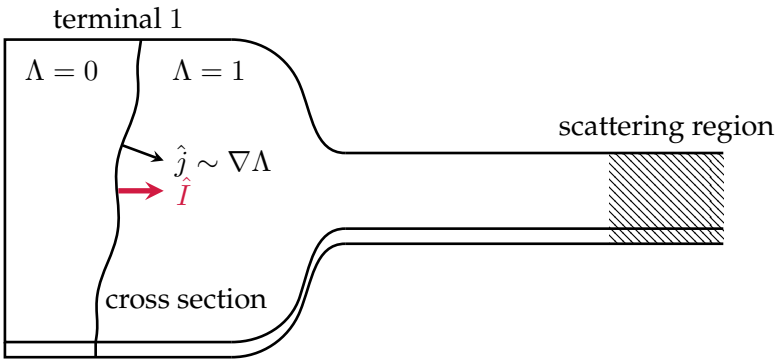

Figure IV.9: *Charge counting* in terminal 1. The counting field couples to the current $\hat{I}$ across the cross section to generate its statistics.

is modified to incorporate the coupling (Eq. (IV.3.4)) between the counting field and the current, where the counting field appears as a phase factor in the scattering matrix [246]. In the latter case, a cross section cutting through terminal 1 is introduced, which counts the charge transferred between terminal 1 and 2. The current density operator through this cross section is given by

$$\hat{j}(\boldsymbol{r}) = [\nabla\Lambda(x)] \lim_{\boldsymbol{r}\to\boldsymbol{r}'} \frac{ie}{2m}(\nabla_{\boldsymbol{r}} - \nabla_{\boldsymbol{r}'})\hat{\sigma}_3, \tag{IV.3.11}$$

where $\hat{\sigma}_3$ acts in Nambu space and reflects the particle-hole structure relevant for a superconducting terminal. $\Lambda(\boldsymbol{r})$ is an auxiliary function that approaches one on the side facing the scatterer and zero on the opposite side of the cross section, with the transition occurring near the cross section over a length scale larger than the Fermi wavelength but smaller than both the impurity mean free path and the superconducting coherence length (see Fig. IV.9). The current density leads to the current

$$\hat{I} = \int_{\mathcal{V}} d^3\boldsymbol{r}\hat{j}(\boldsymbol{r})\hat{\boldsymbol{\Psi}}_1^\dagger(\boldsymbol{r}')\hat{\boldsymbol{\Psi}}_1(\boldsymbol{r}), \tag{IV.3.12}$$

where $\hat{\boldsymbol{\Psi}}_1(\boldsymbol{r})$ is the spinor defined in Eq. (I.1.5) of the particles in terminal 1. Because $\nabla\Lambda(\boldsymbol{r})$ is sharply localized at the cross section, it effectively acts as a Dirac delta distribution, reducing the volume integral in (IV.3.12) to a surface integral. Consequently, the current operator yields the total current through the cross section, and the Keldysh partition functional generates the statistics of this current. The stationary Eilenberger equation or the non-stationary Eliashberg equation is used to determine the reservoir Green's function near the cross section [232, 237], incorporating the counting field as

$$\check{G}_1(t,t';\chi) = \begin{pmatrix} e^{-i\chi^+(t)\hat{\sigma}_3} & 0 \\ 0 & e^{-i\chi^-(t)\hat{\sigma}_3} \end{pmatrix} \check{G}_1(t,t') \begin{pmatrix} e^{i\chi^+(t')\hat{\sigma}_3} & 0 \\ 0 & e^{i\chi^-(t')\hat{\sigma}_3} \end{pmatrix}, \tag{IV.3.13}$$

where $\check{G}_1(t,t')$ is the equilibrium Green's function in the absence of the counting fields [232, 237]. Since the Green's function (IV.3.13) satisfies the normalization condition, the current through the mesoscopic conductor can be obtained using

the identical procedure as in [245].
The same gauge-like condition can be obtained from a different perspective by noting that $\dot{\chi}^{\pm}(t)$ correspond to externally applied fields. A time-dependent drive modulates the chemical potential and thereby influences the electronic occupation in the terminal. The fields are introduced into the kinetic energy, explicitly shown in the Hamiltonian

$$\hat{H}^{\pm}_{\text{aux}}(\chi) = \sum_{\sigma=\pm} \int_{\mathcal{V}} d\boldsymbol{r}\, \hat{\Psi}^{\dagger}_{1\sigma}(\boldsymbol{r}) \left[-\frac{\hbar^2\nabla^2}{2m} - \mu - \hbar\dot{\chi}^{\pm}(t) \right] \hat{\Psi}_{1\sigma}(\boldsymbol{r}) + \hat{H}_{\text{coup+int}}, \quad \text{(IV.3.14)}$$

where the first term describes the kinetic energy of the electrons in terminal 1 and $\hat{H}_{\text{coup+int}}$ contains the coupling with terminal 2 through the conductor plus interactions between the electrons in terminal 1. The effect of the external field is incorporated into the phase of the field operators through the gauge-like transformation (IV.1.4), where the counting fields $\chi^{\pm}(t)$ correspond to the time-dependent phases acquired by electrons propagating along the forward $(+)$ and backward $(-)$ contour. In the transformed frame, the Hamiltonian becomes time-independent, enabling the use of established methods to compute the current [245] or the action [219, 246] of the mesoscopic conductor. Expressing the transformed Green's function in terms of the counting fields and the equilibrium Green's function recovers the transformation given in Eq. (IV.3.13). In this context, the cumulant generating functional (IV.3.7) encodes the statistics of occupation changes in terminal 1, as described by the time derivative of the number operator

$$\partial_t \hat{N}_1(t) = \sum_{\sigma=\pm} \int_{\mathcal{V}} d\boldsymbol{r}\, \partial_t \left(\hat{\Psi}^{\dagger}_{\sigma}(\boldsymbol{r},t) \hat{\Psi}_{\sigma}(\boldsymbol{r},t) \right). \quad \text{(IV.3.15)}$$

Using the gauge-like transformation in Eq. (IV.3.13), the counting field can equivalently be understood as coupling to either the current across a cross section of the terminal or to the temporal change of its fermionic occupation.

Conductor action.— The action is determined from variation of the partition functional (IV.3.7), and related to the Green's function in the ballistic region. After tracing out the channel structure, Nazarov and collaborators [244, 246, 248] obtain the effective action

$$\mathcal{S}[\chi] = \frac{1}{4} \sum_{n} \operatorname{Tr} \ln \left[1 + \frac{\mathcal{T}_n}{4} \left(\{ \check{G}_1(\chi) \overset{\otimes}{,} \check{G}_2 \} - 2 \right) \right], \quad \text{(IV.3.16)}$$

with the transmission values $\mathcal{T}_n$, and the trace running over Keldysh, Nambu, spin, and time space. The anti-commutator $\{\cdot \overset{\otimes}{,} \cdot\}$ involves integration over the time arguments of the adjacent Green's functions. Compared to the normal-metal case, the superconducting action carries a prefactor of $1/4$ rather than $1/2$, as a result of the state doubling in Nambu space [248]. This action provides a versatile framework for quantum transport analysis and admits generalizations to both multiterminal configurations and energy-dependent scattering matrices [246, 248].

IV.4 Full Counting Statistics of Ultrafast Quantum Transport

Oscillating electric fields impact the electron transport in mesoscopic conductors, which leads to features at multiples of the driving frequency [199, 202, 203]. A mesoscopic conductor divides the incident electron stream from the terminals according to its total transmission probabilities [15]. These charge carriers are distributed by the equilibrium Fermi function, i.e., by the chemical potentials and temperatures of their departure terminals. Photon-assisted transport describes electron tunneling driven by an oscillating chemical potential [91, 249]. The electron wave function at energy E exhibits side bands at energies $E + n\hbar\omega, n \in \mathbb{Z}$ weighted by Bessel functions [15, 91, 249]. This leads to kinks at voltages $n\hbar\omega/e$ in the zero-temperature noise. The step height in the differential noise depends on the ac amplitude through the Bessel functions [15, 202]. This field is complemented by the dynamical response of the shot noise [206, 250].

Going beyond the noise and analyzing the full counting statistics (FCS) gives insight into the elementary processes involved in electron transport [219, 225, 231, 251]. Classical charge carriers would obey a Poisson distribution, while electrons in a mesoscopic conductor follow a binomial distribution due to the Pauli exclusion principle [219, 225]. This manifests itself in a suppression of noise, indicated by the Fano factor. In superconducting junctions, the probability distribution can assume negative values, which torpedoes the notion of a probability distribution [231]. Never the less, this function accounts for all elementary processes and can be measured in an experiment. The same information about the charge transport is contained in the cumulant generating function (CGF). Dismantling the CGF into a sum of binomials or multinomials unveils the independent elementary processes at play. This shows, for instance, that the charge transfer in spin-sensitive tunnel junctions is carried by single electrons and spin-singlet pairs when the electron source is a mesoscopic conductor in series [251].

Time-dependent voltage pulses generate collective excitations of the Fermi sea, which are realized as a superposition of electron and hole excitations [45, 219, 223]. For example, Levitions are solition-like electron excitations, created by Lorenzian voltage pulses with a quantized flux [219, 223]. These states minimize the noise, which is reduced to a corresponding dc noise. Furthermore, the entire full counting statistic shortens to a corresponding dc statistic [43, 44]. Levitions have been realized experimentally [212] and analyzed via quantum state tomography [218]. In general, many body electronic states generated by a time-dependent voltage are built from single-electron and electron-hole quasiparticle excitations [45]. The amplitudes and probabilities of these elementary excitations depend on the details of the drive and can be examined experimentally [45]. The entanglement can be addressed by a continuous-variable entanglement test [208].

Arbitrary time-dependent voltages can be treated by the non-equilibrium Green's function method [43, 44, 231, 245]. The work [43, 44] investigated the FCS for cosine, square, triangle, sawtooth, and Lorentzian pulses. Apart from a dc statistic, there appears to be a bidirectional part that depends on the scattering of electron-

hole pairs. The probabilities of creating these electron-hole pairs enter the CGF and are determined by the shape of the pulses. A similar CGF structure is found for a superconductor (S)-normal-metal (N) contact, because the problem can be mapped onto a NN contact by replacing the transmission probabilities with the Andreev reflection probabilities and doubling the counting field as well as the applied voltage [252].

Nowadays, light fields can be manipulated on femtosecond time scales, leading to ultrafast electron transport in mesoscopic constrictions. The experiments [220–222] harnessed the nonlinear $I-V$ characteristic of their bowtie antenna to establish carrier-envelope phase (CEP) control of electron transfer. For a cosine-shaped carrier to envelope configuration (CEP$=0$), the average current is maximal, while for a sine-shaped configuration (CEP$=\pi/2$), the average current vanishes. The near-field in the gap is distorted compared to the far-field, leading to a strong field enhancement and a shift in the effective carrier-envelope phase [221]. A minor dc bias can be exploited to direct the photocurrent [222].

This work extends the investigations [43, 44] to include pulses that are a few cycles long and modulated by a Gauss- or box-shaped envelope. We are interested in the zero-temperature noise and how the carrier-envelope phase manifests therein. As expected, the differential noise shows oscillations with increasing ac amplitude. For both envelopes, the carrier-envelope phase clearly affects these oscillations. The influence of the carrier-envelope phase attenuates for rising number of carrier cycles under the Gauss. This trend is not seen for the box pulse, probably because the temporal behavior at the edges of the box is fundamentally different for a sine and cosine carrier.

IV.4.1 Driven Full Counting Statistic

The full counting statistic is concerned with the probability of charge transfer [219, 225]. The transfer of N charges in a given measurement time t_0 is described by the probability density $P_{t_0}(N)$. For uncorrelated and unidirectional transport, we get a Poissonian distribution that exhibits Schottky's shot noise. In contrast, for a degenerated electron gas at zero temperature, we obtain a binomial distribution.

All information about the cumulants is encoded in the cumulant generating function (CGF) $\mathcal{S}(\chi)$, which is related to the probability density by

$$\exp(-\mathcal{S}(\chi)) = \sum_N P_{t_0}(N)\exp(iN\chi),$$

with the counting field χ, and the imaginary unit i [219, 225]. The normalization of the distribution requires $\mathcal{S}(0)=0$. The cumulants are attained by

$$\mathcal{C}_n = -(-i)^n \frac{\partial^n}{\partial\chi^n}\mathcal{S}(\chi)\bigg|_{\chi=0},$$

where the first cumulant $C_1 = \overline{N} := \sum_N N P_{t_0}(N)$ is the mean value, the second cumulant $C_2 = \overline{(N-\overline{N})^2}$ the noise. Expressed by the current operator $\hat{I}(t)$ at time t, the first cumulant corresponds to

$$C_1 = \frac{1}{-e}\int_0^{t_0} dt \langle \hat{I}(t)\rangle$$

and the second cumulant to

$$C_2 = \frac{1}{2e^2}\int_0^{t_0}\int_0^{t_0} dt dt' \langle\{\Delta\hat{I}(t), \Delta\hat{I}(t')\}\rangle,$$

with $\Delta\hat{I}(t) = \hat{I}(t) - \langle\hat{I}(t)\rangle$, $\{\cdot,\cdot\}$ the anticommutator and e the elementary charge.

The CGF of a mesoscopic conductor corresponds to the Keldysh action (IV.3.16) introduced in chapter IV. A voltage drive $V(t)$ applied to one terminal induces a corresponding phase $\phi(t)$, defined by $\partial_t\phi(t) = eV(t)/\hbar$. The counting field χ and the classical drive $\phi(t)$ are combined into the time-dependent phases $\chi^{\pm}(t) = \phi(t) \pm \chi/2$, which differ between the forward $(+)$ and backward $(-)$ branches of the Keldysh contour. After performing the Keldysh rotation and tracing over the Keldysh structure, the CGF reduces to

$$\mathcal{S}(\chi) = 2\sum_n \mathrm{Tr}_E \ln\left(1 - \mathcal{T}_n(1-h\tilde{h})\sin^2(\chi/2) - i\mathcal{T}_n(h-\tilde{h})\sin(\chi/2)\cos(\chi/2)\right), \tag{IV.4.1}$$

where $\mathcal{T}_n$ are the transmission probabilities of the conductor, Tr_E denotes the trace over energy space. One terminal is assumed to be in equilibrium, leading to $h(E,E') = (1-2f(E))2\pi\hbar\delta(E-E')$, where $f(E) = [\exp(E/(k_\mathrm{B}T))+1]^{-1}$ is the Fermi distribution. In the other terminal, the time-dependent drive modifies the function h to $\tilde{h}(t,t') = [U * h * U^\dagger](t,t')$, where $U(t,t') = \exp(-i\phi(t))\delta(t-t')$ is a time-local gauge transformation, and $*$ denotes convolution in time. The function $\tilde{h}$ captures modified reservoir correlations and is connected to the corresponding Wigner function $W(\bar{t},\overline{E})$ through

$$\tilde{h}(E,E') = \delta(E-E') - \frac{1}{\hbar\pi}\int_{-\infty}^{\infty} d\bar{t} e^{-i(E-E')\bar{t}/\hbar} W(\bar{t},(E+E')/2) \tag{IV.4.2}$$

(see Chap. IV). The CGF does not decouple between different energies and remains a complex convolution sum. In the zero temperature limit, this can be solved for periodic voltages by a diagonalization procedure, described in detail in [43, 44]. The CGF $\mathcal{S}(\chi) = N_\mathrm{uni}\mathcal{S}_\mathrm{uni}(\chi) + N_\mathrm{bi1}\mathcal{S}_\mathrm{bi1}(\chi) + N_\mathrm{bi2}\mathcal{S}_\mathrm{bi2}(\chi)$ subdivides into a unidirectional part

$$\mathcal{S}_\mathrm{uni}(\chi) = \sum_n \ln[1 + \mathcal{T}_n(e^{-i\kappa\chi} - 1)]. \tag{IV.4.3}$$

and bidirectional parts

$$\mathcal{S}_\mathrm{bi1,2}(\chi) = \sum_n\sum_k \ln[1 + \mathcal{T}_n\mathcal{R}_n p_{k1,2}(e^{i\chi} + e^{-i\chi} - 2)]. \tag{IV.4.4}$$

The numbers of attempts in the measurement time are given by $N_{\text{uni}} = t_0|e\overline{V}|/\pi$, $N_{\text{bi1}} = t_0\Omega_1/\pi$, and $N_{\text{bi2}} = t_0(\Omega - \Omega_1)/\pi$, where $\Omega_1 = e\overline{V} - \lfloor e\overline{V}/\Omega \rfloor \Omega$, with $\lfloor x \rfloor$ the floor of the real number x. In the formulas, the repetition period $\tau = 2\pi/\Omega$ of the pulses, the average voltage $\overline{V} = (1/\tau)\int_{-\tau/2}^{\tau/2} V(t)dt$, the probabilities $p_{k1,2}$ of creating an electron-hole pair, and the reflection probabilities $\mathcal{R}_n = 1 - \mathcal{T}_n$ occur. The parameter $\kappa = 1$ ($\kappa = -1$) indicates the direction of charge transfer, determined by $e\overline{V} > 0$ ($e\overline{V} < 0$). We set $\hbar = 1$ in all expressions.

Unidirectional transport (IV.4.3) corresponds to a single electron transfer with probability $\mathcal{T}_n$, where each transport channel contributes independently. Within the measurement time t_0, there are $t_0|e\overline{V}|/\pi$ attempts of electrons to cross the conductor. Hence, unidirectional charge transfer only occurs at finite average voltages $\overline{V}$. The period τ and the characteristic correlation time of the current fluctuations are assumed to be much smaller than the measurement time. For a single transport channel, the CGF translates to a binomial distribution.

Bidirectional charge transport (IV.4.4) stems from two particle processes, namely the creation of electron-hole pairs in one terminal by the ac voltage $\Delta V(t) = V(t) - \overline{V}$. This pair contributes to the statistics if the electron traverses the conductor and the hole gets reflected, or vice versa. This process is captured by the probability $\mathcal{T}_n\mathcal{R}_n p_k$, which is composed of the transmission probability $\mathcal{T}_n$, the reflection probability $\mathcal{R}_n$, and the probability p_k of creating an electron-hole pair. The index k labels different electron-hole pair excitations of the Fermi sea [45]. We have to encounter two types of bidirectional processes. They differ by the number of attempts $N_{\text{bi1,2}}$ and electron-hole pair creation probability $p_{k1,2}$. In contrast to the unidirectional charge transport, the bidirectional parts only contribute to the noise and higher-order even cumulants.

The details of the time-dependent drive determine the probabilities of electron-hole pair creation. We obtain the probabilities p_k by diagonalizing the matrix

$$M_{nm}(E) = \operatorname{sgn}(E + n\Omega) \sum_{k=-\infty}^{\infty} a_{n+k} a^*_{m+k} \operatorname{sgn}(E - k\Omega - e\overline{V}), \tag{IV.4.5}$$

with the signum function $\operatorname{sgn}(\cdot)$, a^*_n the complex conjugate of a_n and the coefficients

$$a_n = \frac{(-1)^n}{\tau} \int_{-\tau/2}^{\tau/2} dt \exp\left(-i \int_{-\tau/2}^{t} dt' e\Delta V(t')\right) e^{in\Omega t}. \tag{IV.4.6}$$

This matrix represents $h * \tilde{h}$ and, upon diagonalization, decomposes the CGF (IV.4.1) into a sum of independent contributions [43]. The coefficients depend on the ac drive $\Delta V(t) = V(t) - \overline{V}$ and obey the properties

$$\sum_{k=-\infty}^{\infty} a_{n+k} a^*_{m+k} = \delta_{nm}, \quad \sum_{k=-\infty}^{\infty} k|a_k|^2 = 0.$$

In the relevant energy range $0 < E < \Omega$, the matrix is piecewise constant for energies $E \in (0, \Omega_1)$, $\Omega_1 = e\overline{V} - \lfloor e\overline{V}/\Omega \rfloor \Omega$ and $E \in (\Omega_1, \Omega)$. This leads to the two types of bidirectional processes denoted by an index of 1 for the first interval and an index of 2 for the second interval. The matrix M_{nm} is unitary, and therefore the eigenvalues assume the form $\exp(\pm i\alpha_{k1,2})$. If the unidirectional number $e\overline{V}/\Omega$ of attempts per cycle and per spin is an integer, then there is only one bidirectional CGF $\mathcal{S}_{\text{bi2}}(\chi)$. The phase $\alpha_{k1,2}$ of the eigenvalues enters directly into the electron-hole pair creation probability by $p_{k1,2} = \sin^2(\alpha_{k1,2}/2)$. The corresponding eigenvectors are related to the electron-hole quasiparticle amplitude and dictate the drive induced many-body wave function [45].

The bidirectional current-current noise is proportional to the sum of all probabilities p_k, which successively rise to one as the amplitude of the ac-drive is increased. In the following, we are concerned with time dependent voltages, which exhibit a vanishing average voltage $\overline{V} = 0$. Hence, the unidirectional noise vanishes and only type 2 bidirectional processes appear. The current-current noise per pulse and per spin has the form

$$S = 2e^2 \left(\sum_n \mathcal{T}_n \mathcal{R}_n \right) \sum_k p_k.$$

Based on the findings in [43, 44], we expect oscillatory behavior in the differential noise $\partial S/(\partial(eV_0))$, which fades out for large ac amplitudes. The oscillations come from the successive ramp up of the probabilities p_k with ac amplitude, where the slope determines the height and the turning point the position of the peak.

IV.4.2 Gaussian and Box-Shaped Pulses

The considered voltage pulses consist of an oscillating carrier modulated by an envelope. Their displacement against each other is described by the carrier-envelope phase (CEP). We are after the effect of the CEP on the noise. The voltage assumes the form

$$V(t) = E(t)V_0 \cos(\omega t + \varphi) - V_{\text{off}}, \tag{IV.4.7}$$

with the envelope $E(t)$, the ac amplitude V_0, the carrier frequency ω, the carrier-envelope phase φ, the offset $V_{\text{off}} = (1/\tau) \int_{-\tau/2}^{\tau/2} E(t)V_0 \cos(\omega t + \varphi)$, and the repetition rate $1/\tau$. The offset is subtracted to ensure a vanishing average voltage.

For the following results, we calculated the coefficients (IV.4.6) and diagonalized the matrix (IV.4.5) to get the electron-hole pair creation probabilities. The sum of the probabilities forms the noise. Numerically, we utilize a finite-dimensional matrix to obtain the eigenvalues. Cutoffs for n and m are chosen on a much larger scale than the one on which $|a_n|$ vanishes. An additional consistency check consists of controlling the unitary property and the deviation of the eigenvalues from an absolute value of 1.

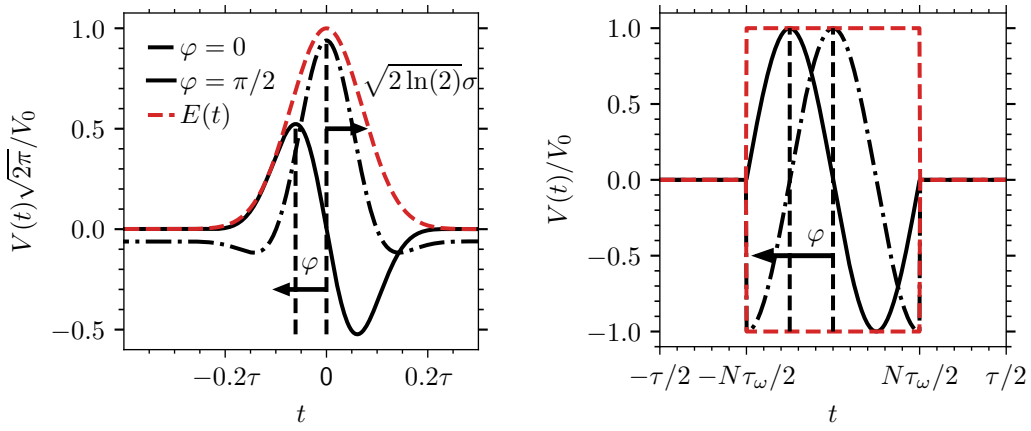

Figure IV.10: *Pulse shapes*. Left: Gauss pulse and its envelope for carrier-envelope phases $\varphi = 0, \pi/2$. The ratio between the variance σ and the pulse repetition time τ is chosen as $\tau/(\sqrt{2}\sigma) = 10$. Here, we set $\sigma\omega = 1$, which is a measure of the number of carrier cycles under the Gauss curve. Note the negative offset voltage for $\varphi = 0$ to keep the average voltage at zero. Right: Box pulse and its envelope for carrier-envelope phases $\varphi = 0, \pi/2$ (solid line, dashdotted line). The box counts $N = 1$ carrier cycles with a period of τ_ω and extends between $-N\tau_\omega/2$ and $N\tau_\omega/2$, which is assumed to be smaller than the pulse repetition time τ.

The first envelope is a Gauss curve of the contour

$$E(t) = \frac{1}{\sqrt{2\pi}} \exp\left(-\frac{t^2}{2\sigma^2}\right), \tag{IV.4.8}$$

where σ corresponds to the variance. An illustration of the Gaussian pulse is depicted in Fig. IV.10. The envelope shape is controlled by the ratio $\tau/(\sqrt{2}\sigma)$, which determines the relation between the width of the Gauss and the repetition rate. A measure for the number of carrier cycles under the envelope constitutes $\sigma\omega$. The offset voltage is given by

$$V_{\text{off}} = \cos\varphi \frac{\sigma}{\tau} V_0 e^{-(\sigma\omega)^2/2} \operatorname{Re}\left[\operatorname{erf}\left(\frac{\tau}{2\sqrt{2}\sigma} - \frac{i\sigma\omega}{\sqrt{2}}\right)\right],$$

with the error function $\operatorname{erf}(\cdot)$, and the real part $\operatorname{Re}[\cdot]$ of a complex number. A maximum is achieved for $\varphi = 0$ and a minimum for $\varphi = \pi/2$.

The CEP has an observable impact on the differential noise $\partial S/(\partial(eV_0))$, depicted in Fig. IV.10 for carrier-envelope phases between $\varphi = 0$ and $\varphi = \pi/2$. Successive ramp ups of the electron-hole pair creation probabilities p_k cause the oscillating character of the differential noise. The CEP has a noticeable influence on the onset and slope of these ramp ups. This is reflected in the differential noise by the position and height of the peaks. For example, $\varphi = \pi/2$ exhibits a larger period and smaller height compared to $\varphi = 0$.

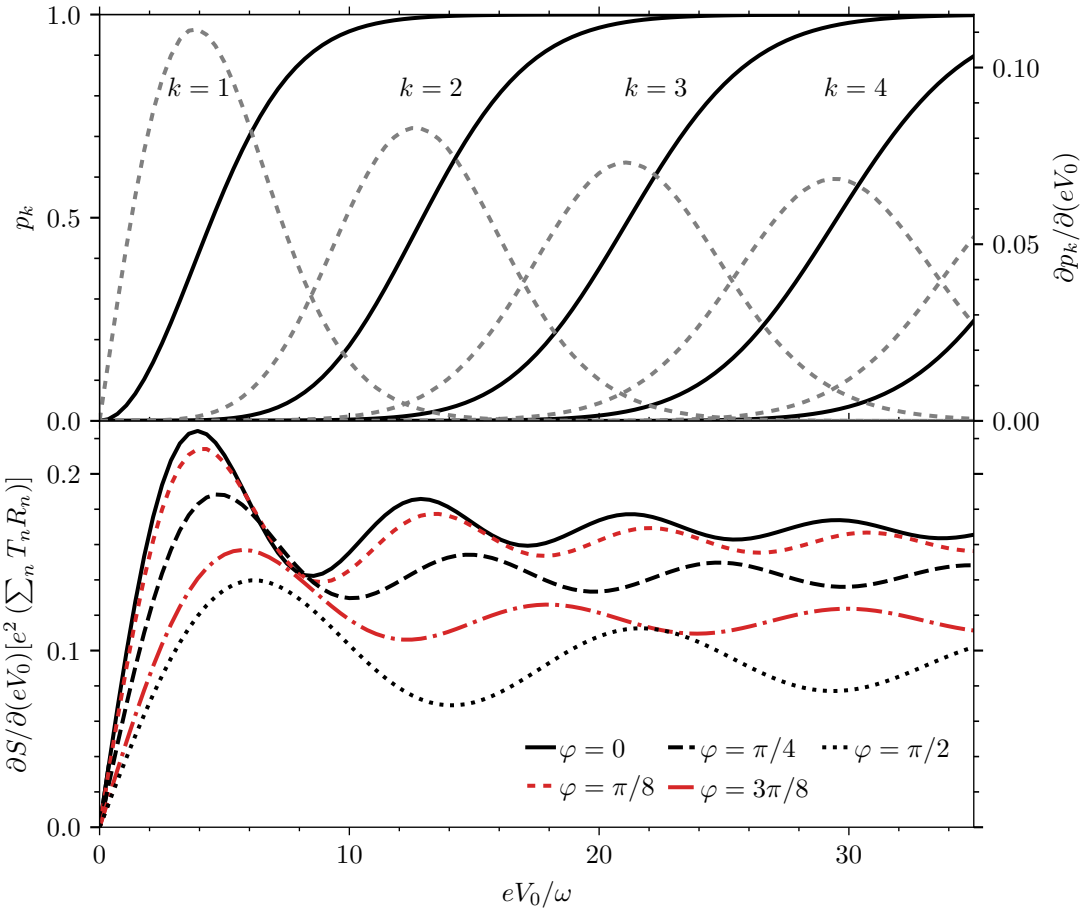

Figure IV.11: *The differential noise* $\partial S/(\partial(eV_0))$ of a Gaussian pulse is depicted over the ac amplitude V_0 for carrier-envelope phases between 0 and $\pi/2$. The variance σ in relation to the pulse repetition time τ was set to $\tau/(\sqrt{2}\sigma) = 10$ and in relation to the carrier angular frequency ω to $\sigma\omega = 1$.

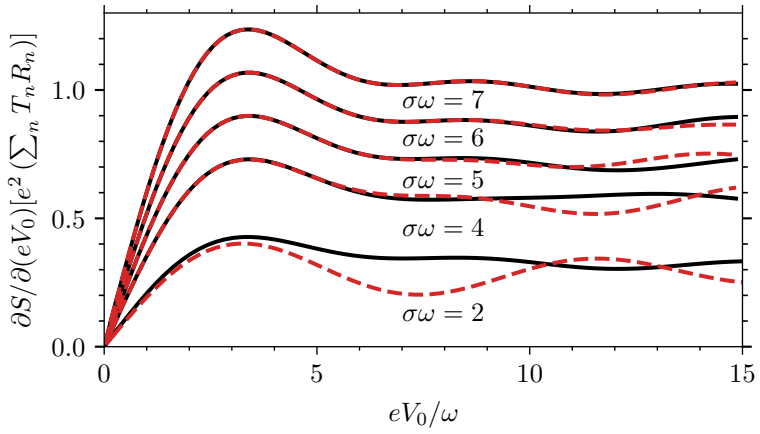

Figure IV.12: *Differential noise* $\partial S/(\partial(eV_0))$ of a Gaussian pulse for different numbers of carrier cycles under the Gaussian envelope. We compare the carrier-envelope phase 0 (black solid) to $\pi/2$ (red dashed) for $\sigma\omega = 2$ to $\sigma\omega = 7$. As the number of carrier cycles increases, the curves with CEP 0 and $\pi/2$ fall on top of each other. Additionally, more elementary processes p_k are contributing, and this leads to an increase in the differential noise. The ratio $\tau/(\sqrt{2}\sigma)$ was fixed at 10.

The influence of the CEP diminishes with the increasing number of carrier cycles in a pulse. Figure IV.12 outlines the dependence of the differential noise on the number of carrier cycles and their influence on the CEP dependence. For $\sigma\omega = 2$ the curves for $\varphi = 0$ and $\varphi = \pi/2$ are significantly different, while for rising $\sigma\omega$ they approach each other, and for $\sigma\omega = 7$ they almost overlap. An additional effect is that more probabilities ramp up at the same amplitude eV_0/ω, which shifts the oscillations upward. In comparison to $\sigma\omega = 1$ (see Fig. IV.11), the second peaks are shifted to lower amplitudes.

The pulses ought to be well separated, i.e., $\tau/(\sqrt{2}\sigma) \gg 1$. In this regime, the differential noise is ideally independent of this parameter. We chose $\tau/(\sqrt{2}\sigma) = 10$ as a trade-off between the computational costs and the already independent probabilities in the case of $\varphi = \pi/2$. For $\varphi = 0$, the probabilities slightly change with increasing $\tau/(\sqrt{2}\sigma) > 10$, presumably due to the non-negligible influence of the offset voltage. However, the differences in the oscillations are not exclusively attributable to the offset voltage, because we observe an even smaller period and higher peaks for values $\tau/(\sqrt{2}\sigma) > 10$.

As the second envelope, we study a box of the form

$$E(t) = \Theta(t + N\tau_\omega/2)(1 - \Theta(t - N\tau_\omega/2)), \tag{IV.4.9}$$

with $\Theta(\cdot)$ the Heaviside function, N the number of carrier cycles in the box and $\tau_\omega = 2\pi/\omega$ the period of one carrier cycle. The offset voltage vanishes for all carrier-envelope phases. Figure IV.10 depicts the box pulse for CEP $\varphi = 0, \pi/2$.

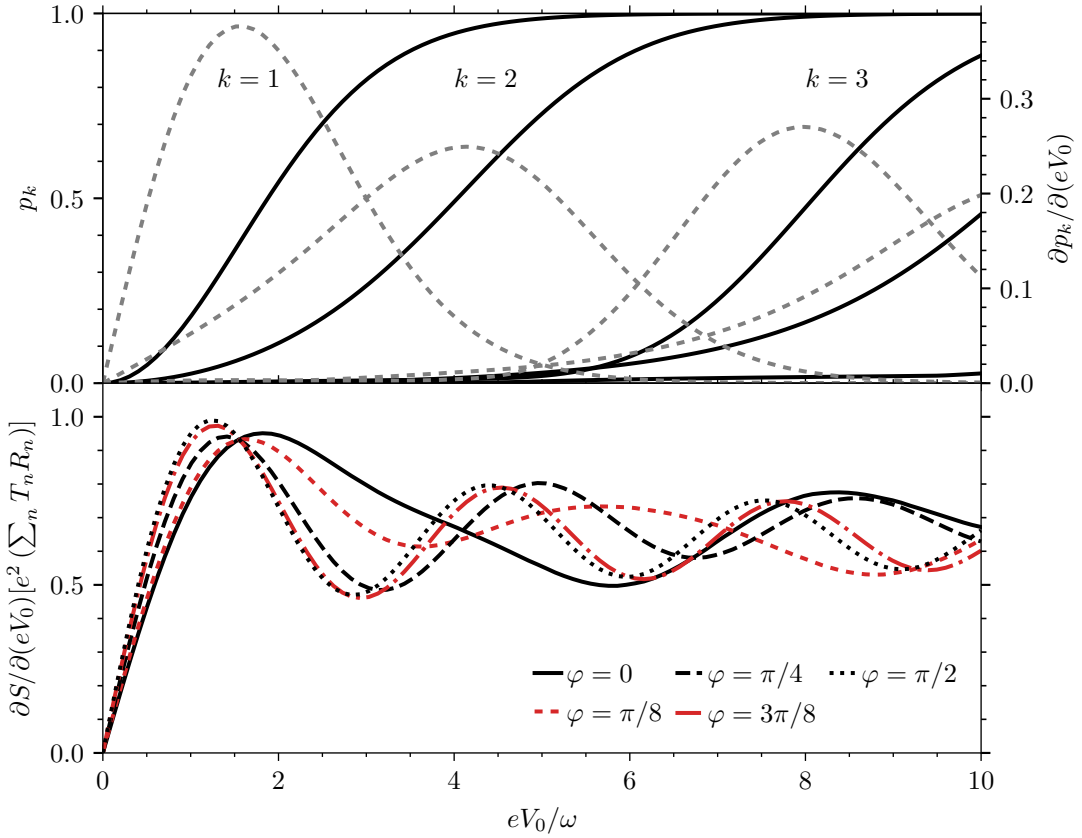

Figure IV.13: *Differential noise* $\partial S/(\partial(eV_0))$ of a box pulse drawn over the ac amplitude V_0 for carrier-envelope phases between 0 and $\pi/2$. The number of carrier cycles is $N = 1$. The width of the box in comparison to the pulse repetition rate was fixed to $\tau/(N\tau_\omega) = 2$, because the electron-hole pair creation probabilities are nearly independent of the box size. Oscillations are caused by elementary processes that are subsequently activated as the voltage amplitude increases.

Again, traces of the CEP are pronounced in the differential noise $\partial S/(\partial(eV_0))$. The dependence on different carrier-envelope phases is shown in Fig. IV.13. It impacts the position and slightly the height of the peaks. For example, for $\varphi = 0$, the second peak almost forms an excess wing of the first peak, while for $\varphi = \pi/2$ the second peak is clearly visible.

With increasing carrier cycles N in the box, more probabilities p_k ramp up at the same ac amplitude. Therefore, the differential noise experiences an upward shift, akin to the Gaussian envelope. In contrast to the Gaussian pulse, the peak positions remain unchanged for the first few N investigated. The differential noise for $\varphi = 0$ and $\varphi = \pi/2$ do not approach each other and stay distinct. We assume that the origin of this lies in the different behavior of the cosine and sine at the edges of the box. The cosine ($\varphi = 0$) jumps to zero, and the sine ($\varphi = \pi/2$) is zero

but exhibits a kink.

IV.4.3 Conclusion

We have addressed the influence of few-cycle voltage pulses on the noise at zero temperature in a mesoscopic conductor. Explicitly, we have studied a single-cycle pulse with a Gaussian envelope and with a box envelope. The noise is carried by bidirectional processes that lead to an oscillatory behavior of the differential noise. These oscillations change with the carrier-envelope phase, and the CEP is reflected in the peak height and position. For the Gaussian pulse, the impact of the CEP decreases with an increasing number of carrier cycles. To enable a meaningful comparison with the experiments reported in [220–222], the theoretical framework should be extended to account for energy-dependent transmission (see Chap. IV). Furthermore, pulse shapes that more closely resemble the experimental ones need to be employed, as the noise characteristics are highly sensitive to the exact pulse form.

Chapter V

Quantum Photon-Assisted Transport

In practice, mesoscopic transport does not occur under the idealized condition of a perfect voltage source, but is instead subject to quantum and thermal fluctuations of the electromagnetic field. However, it can be a useful approximation in the presence of a low-impedance environment. A more advanced description incorporates the electromagnetic environment, which enables energy exchange between the environment and the charge carriers. Rather than being merely a perturbation, the electromagnetic environment can also be deliberately engineered to control transport [47]. This motivates us to investigate tunnel junctions embedded in a quantum electromagnetic environment. Our analysis starts with the dynamical Coulomb blockade (DCB) theory, where a tunnel junction is placed in series with an impedance [46] (see Fig. V.1). The impedance is treated as a set of quantum-mechanical harmonic oscillators assumed to be in thermal equilibrium. By considering the limit of infinitely many oscillators, one can model an arbitrary frequency-dependent impedance $Z(\omega)$, capturing the full spectral response of the electromagnetic environment [253]. The Hamiltonian describing electron transport through the tunnel junction is given by

$$\hat{H} = \sum_{\alpha=1,2} \hat{H}_\alpha + \hat{H}_\mathrm{T} + \hat{H}_\mathrm{env}. \tag{V.0.1}$$

The Hamiltonian of terminal α takes the form

$$\hat{H}_\alpha = \sum_{k\sigma} \epsilon_{\alpha k} \hat{c}^\dagger_{\alpha k\sigma} \hat{c}_{\alpha k\sigma}, \tag{V.0.2}$$

where $\hat{c}_{\alpha k\sigma}$ annihilates a quasiparticle of energy $\epsilon_{\alpha k}$, momentum k and spin σ. Tunneling between the terminals is described by the Hamiltonian

$$\hat{H}_\mathrm{T} = \sum_{kq\sigma} t_{kq} \hat{c}^\dagger_{2q\sigma} \hat{c}_{1k\sigma} e^{-i\hat{\phi}} + t^*_{kq} \hat{c}^\dagger_{1k\sigma} \hat{c}_{2q\sigma} e^{i\hat{\phi}}, \tag{V.0.3}$$

in which t_{kq} denotes the hopping amplitudes between single-particle states in terminal 1 and 2 [254–256]. The charge shift operator $\exp(-i\hat{\phi})$ incorporates the effect of the electromagnetic environment through the phase operator $\hat{\phi}$, and shifts the charge $\hat{Q}$ on the junctions capacitor by one elementary charge, as expressed

by

$$e^{i\hat{\phi}}\hat{Q}e^{-i\hat{\phi}} = \hat{Q} - e, \tag{V.0.4}$$

which follows from the canonical commutation relations $[\hat{\phi}, \hat{Q}] = ie$. The dynamics of the phase is governed by the Hamiltonian of the environment $\hat{H}_{\text{env}}$, with its time derivative corresponding to the voltage drop across the conductor. The electromagnetic environment, modeled as a set of N harmonic oscillators with capacitances C_n and inductances L_n, is captured by the Hamiltonian

$$\hat{H}_{\text{env}} = \frac{(\hat{Q} - CV)^2}{2C} + \sum_{n=1}^{N}\left[\frac{\hat{q}_n^2}{2C_n} + \left(\frac{\hbar}{e}\right)^2 \frac{1}{2L_n}(\hat{\varphi} - \hat{\phi}_n)^2\right], \tag{V.0.5}$$

where $\hat{q}_n$ are the charge and phase $\hat{\phi}_n$ operators of the individual oscillators. The first term accounts for the charging energy stored in the junction capacitor of capacitance C, while the junction phase $\hat{\phi} = \hat{\varphi} + eVt/\hbar$ couples bilinearly to the environmental phase operators $\hat{\phi}_n$. In addition, the circuit is subject to an external dc bias V, as illustrated in Fig. V.1.

The tunneling rates are calculated by applying Fermi's golden rule, treating the tunneling Hamiltonian as a perturbation. The perturbative treatment is valid when the tunnel resistance R_{T} significantly exceeds the resistance quantum $R_{\text{Q}} = h/e^2$. The rate of tunneling from terminal 1 to terminal 2 is expressed by

$$\Gamma^+(V) = \frac{1}{e^2 R_{\text{T}}}\int_{-\infty}^{\infty} dE dE' f(E)[1 - f(E' + eV)]P(E - E'), \tag{V.0.6}$$

with the P-function

$$P(E) = \int_{-\infty}^{\infty}\frac{dt}{2\pi\hbar}\exp\left(iJ(t) + \frac{i}{\hbar}Et\right), \tag{V.0.7}$$

determined by the correlator

$$J(t) = \langle[\hat{\varphi}(t) - \hat{\varphi}(0)]\hat{\varphi}(0)\rangle_{\text{env}}. \tag{V.0.8}$$

Due to the symmetry of a biased junction, the rate in the opposite direction is given by $\Gamma^-(V) = \Gamma^+(-V)$. The phase $\hat{\varphi}(t)$ evolves under the Hamiltonian $\hat{H}_{\text{env}}$, and expectation values are taken with respect to an equilibrium state at temperature T. Wick's theorem is used to show that the P-function depends only on second-order correlation functions [46]. The fluctuation-dissipation theorem enables one to express the phase correlator $J(t)$ in terms of the environmental impedance and temperature,

$$J(t) = 2\int_0^{\infty}\frac{d\omega}{\omega}\frac{\text{Re}\, Z(\omega)}{R_{\text{Q}}}\left[\coth(\hbar\omega/(2k_{\text{B}}T))[\cos(\omega t) - 1] - i\sin(\omega t)\right]. \tag{V.0.9}$$

The P-function can be interpreted as the probability to exchange the energy E with the tunneling electron, as it satisfies $\int_{-\infty}^{\infty} dE P(E) = 1$. Moreover, the P-function obeys the detailed balance condition $P(-E) = \exp(E/(k_{\text{B}}T))P(E)$.

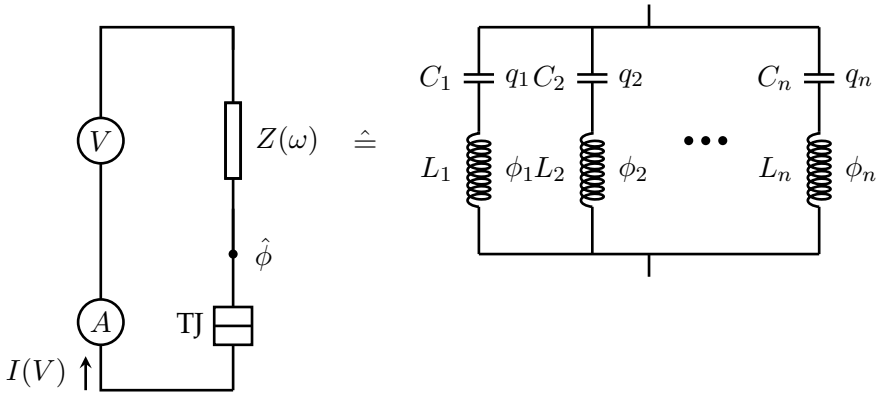

Figure V.1: *Circuit of DCB*. Left: Tunnel junction (TJ) in series with arbitrary impedance $Z(\omega)$, connected to a voltage source while measuring the current. Right: Equivalent representation of the impedance by harmonic oscillators.

For example, a high-impedance environment supports modes with frequencies close to zero, resulting in an effective impedance $Z(\omega) \approx (\pi/C)\delta(\omega)$, and a Gaussian P-function

$$P(E) = \frac{1}{\sqrt{4\pi E_c k_\mathrm{B} T}} \exp\left(-\frac{(E-E_c)^2}{4E_c k_\mathrm{B} T}\right), \tag{V.0.10}$$

with E_c denoting the charging energy. At low temperatures, $k_\mathrm{B}T \ll E_c$, the current

$$I(V) = \frac{eV - E_c}{eR_\mathrm{T}} \Theta(|eV| - E_c) \tag{V.0.11}$$

exhibits a Coulomb blockade, as the applied voltage must overcome the charging energy to initiate a current.

As another example, coupling to a single harmonic mode of frequency ω_0 with zero linewidth is modeled by the impedance $Z(\omega) = \pi/(2C)[\delta(\omega-\omega_0)+\delta(\omega+\omega_0)]$. The P-function reduces to

$$P(E) = \sum_{l=-\infty}^{\infty} p_l \delta(E - l\hbar\omega_0), \tag{V.0.12}$$

in which

$$p_l = \mathfrak{I}_l\left(\frac{g}{\sinh(\hbar\omega_0/(2k_\mathrm{B}T))}\right) \exp\left[l\hbar\omega_0/(2k_\mathrm{B}T) - g\coth(\hbar\omega_0/(2k_\mathrm{B}T))\right], \tag{V.0.13}$$

with $\mathfrak{I}_l(\cdot)$ denoting the modified Bessel functions and g characterizing the coupling strength. Analogous to the classical case in the previous section, the coefficients p_l quantify the probability for electrons to absorb or emit l energy quanta $\hbar\omega_0$ due to their interaction with the electromagnetic environment. At zero temperature, the probabilities reduce to a Poisson distribution $p_l^0 = e^{-g}g^l/l!$, and at finite temperature the P-function becomes a convolution of Poisson distributions [46].

V.1 Extension of DCB Theory to a Nonthermal Environment

Dynamical Coulomb blockade theory demonstrates that the state of the electromagnetic environment affects electron tunneling, as it enters the probability of energy exchange. In particular, a single mode drives the junction by a harmonic signal, similarly to the classical case in the previous section. However, here the average drive amplitude vanishes, and it is the fluctuations that yield a net driving effect. Quantum effects break the symmetry between emission and absorption, as indicated by $p_l \neq p_{-l}$, a feature not present with a harmonic classical drive. Novel ways of driving the junction emerge when the mode is prepared in nonclassical states, constituting the quantum analogue of classical photon-assisted transport. Souquet *et al.* [47] investigated transport though a normal-metal tunnel junction driven by a microwave cavity prepared in a nonequilibrium state, thereby extending DCB theory. They employed standard quantum linear response theory, treating the tunneling Hamiltonian (V.0.3) perturbatively, and obtained a modified tunnel current

$$I(t,V) = e\sum_{\nu=\pm}\nu\int_{-\infty}^{\infty} dE\Gamma(\nu eV - E)P^{\nu}(t,E), \tag{V.1.1}$$

where $\Gamma(E) = (e^2R_{\mathrm{T}})^{-1}E/(1-\exp(-E/(k_{\mathrm{B}}T)))$ is the bare tunneling rate, and

$$P^{\nu}(t,E) = -\frac{1}{\pi}\,\mathrm{Im}\int_{-\infty}^{\infty} d\tau e^{iE\tau/\hbar}G^{\nu}_{\mathrm{env}}(t,\tau) \tag{V.1.2}$$

are the generalized P-functions, depending on the environmental correlation functions

$$G^{\nu}_{\mathrm{env}}(t,\tau) = -(i/\hbar)\Theta(\tau)\langle e^{i\nu\hat{\varphi}(t)}e^{-i\nu\hat{\varphi}(t-\tau)}\rangle_{\mathrm{env}}. \tag{V.1.3}$$

The junction phase $\hat{\varphi}(t)$ evolves under the environmental Hamiltonian $\hat{H}_{\mathrm{env}}$, and expectation values are taken with respect to the (possibly nonthermal) environmental state. Specifically, they investigated a single mode with frequency ω_0 with a phase

$$\hat{\varphi}(t) = -i\sqrt{g}\left[\hat{a}(t) - \hat{a}^{\dagger}(t)\right], \tag{V.1.4}$$

where $\hat{a}(t)$ is the annihilation operator of the mode, and $g = \pi Z_{\mathrm{cav}}/R_Q$ characterizes the strength of the zero-point voltage fluctuations, determined by the cavity impedance Z_{cav}. The current oscillates at multiples of the mode frequency. In the following, we discuss the resulting dc component by averaging over time t, leading to $\overline{I}(V) = \lim_{\overline{T}\to\infty}(1/\overline{T})\int_{-\overline{T}/2}^{\overline{T}/2} dtI(t,V)$. The P-function reduces to

$$P^{\pm}(E) = P(E) = \sum_{l=-\infty}^{\infty} p_l\delta(E - l\hbar\omega_0) = \sum_{l,k=-\infty}^{\infty} p^0_k p^{\mathrm{occ}}_{l-k}\delta(E - l\hbar\omega_0), \tag{V.1.5}$$

where p^0_l is the energy exchange probability associated with the zero-point fluctuations of the cavity, and

$$p^{\mathrm{occ}}_l = \int d^2\alpha\mathscr{P}(\alpha)\left(J_l(2\sqrt{g}|\alpha|)\right)^2 \tag{V.1.6}$$

is the energy exchange quasiprobability arising from the (nonclassical) state of the mode, with $J_l(\cdot)$ the Bessel functions. Here, the cavity state is represented by its Glauber–Sudarshan P function $\mathscr{P}(\alpha)$, which expresses the cavity density matrix $\hat{\rho}$ as a quasidistribution over coherent states $|\alpha\rangle$, with $\alpha \in \mathbb{C}$ (see Eq. (V.2.3)). While the total p_l is a true probability, the contribution from the state, p_l^{occ}, is a quasiprobability that can take on negative values for nonclassical states. A nonclassical state is characterized by having a Glauber-Sudashan P-function which admits negative values or is more singular than the delta distribution. Nonclassicallity is carried over to the exchange probability, which can lead to distinct signatures in the current and differential conductance, respectively. Figure V.2 presents the differential conductance and the energy-exchange probability for three environmental states: vacuum-single-photon, coherent, and squeezed, as defined in Eqs. (V.2.6a), (V.2.8), and (V.2.13), respectively. The current–voltage characteristic is nonlinear, exhibiting piecewise-linear segments with kinks at multiples of the mode frequency. In contrast, the classical photon-assisted transport in Eq. (IV.1.22) shows a linear current-voltage characteristic. The differential conductance displays a sequence of plateaus, with jumps occurring at multiples of the mode frequency. The plateau height can serve as a signature of nonclassicality. One can derive general bounds on the differential conductance that must be satisfied if p_l^{occ} is positive definite; a violation of these bounds indicates a nonclassical cavity state [47]. By measuring the current and current noise, it is possible to extract the full energy exchange probability p_l. In conclusion, the normal-metal tunnel junction can serve as a device for probing the surrounding quantum environment.

V.2 Quantum Environment

The quantum electromagnetic environment can be engineered and controlled owing to innovations in circuit QED [108]. As discussed in the previous sections, tunneling charges exchange energy with the environment, whose energy spectrum is shaped by the surrounding circuit elements. For example, a two-level system, such as a superconducting qubit [108, 257], can undergo transitions between its two energy levels and exchange energy equal to the level spacing. Further, a single-mode resonator, as an example of a textbook quantum harmonic oscillator, features equally spaced energy levels determined by its mode frequency. The resonator is populated or depopulated by inducing transitions between the energy levels. Coupling a finite number of resonators results in a multimode environment that supports hybridized eigenmodes arising from interactions among individual resonances. An array of infinitely many coupled oscillators forms a distributed system known as a transmission line. An infinitely long transmission line supports a continuum of modes, while a line of finite length supports a discrete set of resonant modes determined by its boundary conditions. Furthermore, an arbitrary impedance can be represented as either a semi-infinite transmission line with mode filtering (see chapter III), or as a bath of oscillators with distinct resonance frequencies [258]. The Josephson junction itself is a nonlinear circuit element characterized by a cosine-shaped potential energy, resulting in a non-

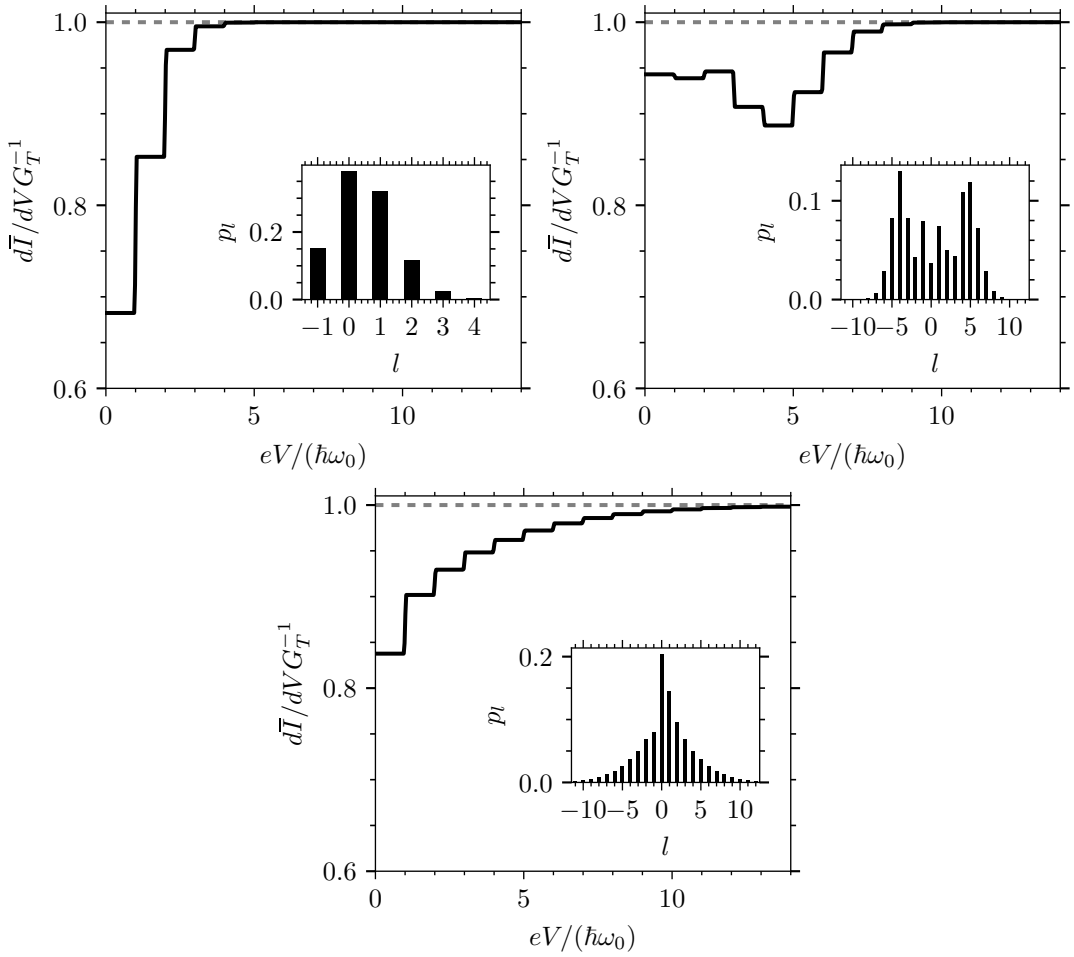

Figure V.2: *Differential conductance* $d\bar{I}/dV$ of a normal-metal tunnel junction coupled to a single electromagnetic mode with frequency ω_0. Panels: upper left, vacuum-single-photon state (V.2.6a); upper right, coherent state (V.2.8); lower, squeezed state (V.2.13). Inset: *energy-exchange probability* p_l that gives rise to the conductance steps. The gray dashed curves are the conductance in the absence of a quantum electromagnetic environment. Parameter: coupling constant $g = 1/2$.

equidistant (or anharmonic) energy spectrum [108]. Shunting with a capacitor introduces the charging energy E_C, and the ratio between the Josephson energy E_J and E_C distinguishes different types of qubits: the charge qubit ($E_C \gg E_J$), the quantronium ($E_C \sim E_J$), and the transmon ($E_C \ll E_J$) [108, 165]. Individual elements can be combined to engineer a more complex energy spectrum experienced by the junction.

Density matrix.— Beyond its energy spectrum, the behavior of the electromagnetic environment is determined by its quantum state, whether it is the vacuum, a thermal state, or a nonequilibrium state such as a coherent, Fock or squeezed state. The quantum state of the system is represented by the density matrix $\hat{\rho}$, a positive semi-definite, self-adjoint operator with unit trace acting on the system's Hilbert space [64]. There always exists an orthonormal basis $\{|\psi\rangle_j\}$ such that

$$\hat{\rho} = \sum_j \mathfrak{p}_j \left|\psi_j\right\rangle \left\langle\psi_j\right|, \tag{V.2.1}$$

where $\mathfrak{p}_j$ are the probabilities of finding the system in state $|\psi_j\rangle$. The unit trace condition of the density matrix implies that the probabilities obey the normalization condition $\sum_j \mathfrak{p}_j = 1$. In a continuous-variable Hilbert space, the summation over discrete quantum numbers is replaced by integration over continuous variables. A density matrix can be characterized by properties such as purity, entanglement, and nonclassicality. Their definitions are briefly summarized as follows:

Pure state.— The density matrix of a pure state has the form $\hat{\rho} = |\psi\rangle \langle\psi|$, representing a projection onto a single state. Such a state is not a statistical mixture, as indicated by its unit purity $\mathrm{Tr}\{\hat{\rho}^2\} = 1$.

Entangled state.— In a multipartite system of n subsystems, such as multiple environmental modes, a quantum state is said to be separable if it can be written as a convex combination of product states

$$\hat{\rho} = \sum_j \mathfrak{p}'_j \hat{\rho}_{1,j} \otimes \ldots \otimes \hat{\rho}_{n,j}, \tag{V.2.2}$$

where each $\hat{\rho}_{k,j}$, with $k = 1, \ldots, n$, is a density matrix acting on subsystem k, and $\mathfrak{p}'_j$ are probabilities satisfying $\sum_j \mathfrak{p}'_j = 1$. A quantum state is considered entangled when its density matrix cannot be written in this separable form [259].

Nonclassical state.— In quantum optics, nonclassicality is characterized by the behavior of quasiprobability distributions, such as the Glauber-Sudarshan P-function and the Wigner function, associated with the electromagnetic field mode [260]. In the coherent state representation, the density matrix takes the form

$$\hat{\rho} = \iint_{-\infty}^{\infty} d^2\alpha \mathscr{P}(\alpha) \left|\alpha\right\rangle \left\langle\alpha\right|, \tag{V.2.3}$$

where $\mathscr{P}(\alpha)$ is the Glauber-Sudashan P-function, representing the state as a quasidistribution over coherent states $|\alpha\rangle$ (see Eq. (V.2.8)). The complex plane spanned by the coherent-state parameter α defines the phase space of the mode. A quantum state is defined as nonclassical when its Glauber-Sudashan P-function is not a well-behaved probability distribution, that is, when it assumes negative values or becomes more singular than a Dirac delta distribution, as in the case of Fock or squeezed states. The Wigner function is another quasiprobability distribution defined in phase space, and it is related to the Glauber–Sudarshan P-function via an integral transformation. When the Wigner function takes on negative values in phase space, the state is considered nonclassical. The Wigner function can be experimentally reconstructed, as, for example, demonstrated by [261].

When expressed in a different basis the density matrix typically includes off-diagonal elements, which represent quantum coherences between basis states. Thus, the density matrix in the eigenbasis of the Hamiltonian $\{|E_j\rangle\}$ is given by

$$\hat{\rho} = \sum_{jk} \rho_{jk} \left|E_j\right\rangle \left\langle E_k\right| , \tag{V.2.4}$$

where ρ_{jk} are the matrix elements of $\hat{\rho}$ in the energy basis. Under unitary evolution governed by the von Neumann equation, the density matrix evolves as

$$\hat{\rho}(t) = e^{-i\hat{H}t/\hbar}\hat{\rho}(0)e^{i\hat{H}t/\hbar} = \sum_{jk} e^{-i(E_j-E_k)t/\hbar}\rho_{jk} \left|E_j\right\rangle \left\langle E_k\right| , \tag{V.2.5}$$

with $\hat{H}$ denoting the systems Hamiltonian and ρ_{jk} the matrix elements of the density matrix at initial time $t = 0$. This decomposition illustrates that the populations (diagonal elements) remain stationary, since $E_j - E_k = 0$ when $j = k$, whereas the coherences (off-diagonal elements) oscillate with frequencies determined by the energy differences between states. In the next chapter, we show that the Josephson oscillations of a superconducting tunnel junction phase-lock to the coherence oscillations, resulting in the emergence of generalized Shapiro steps. Especially, this thesis investigates how a single mode, prepared in Fock-state superpositions, a coherent state, or a squeezed vacuum state, affects a superconducting tunnel junction. We therefore begin by briefly introducing these states, because charge transport depends on these states through their density matrix elements $\rho_{n+jn} = \langle n+j|\,\hat{\rho}\,|n\rangle$, $n+j, n \in \mathbb{N}$; see Eqs. (V.4.14).

Fock superposition.— In recent years, various approaches have been developed to prepare and stabilize numerous (nonthermal) quantum states [108, 260, 262–267]. The Hamiltonian (III.4.3) for a single mode is introduced in Sec. III.4, where the number states $|n\rangle$, $n \in \mathbb{N}$, are the energy eigenstates, known as Fock states. Here, ω_0 is the mode frequency, and $\hat{a}$ and $\hat{a}^\dagger$ are the mode annihilation and creation operators, respectively. A coherent superposition of Fock states has the form $|\psi\rangle = \sum_{n=0}^{\infty} c_n |n\rangle$, with complex amplitudes $c_n \in \mathbb{C}$ normalized such that

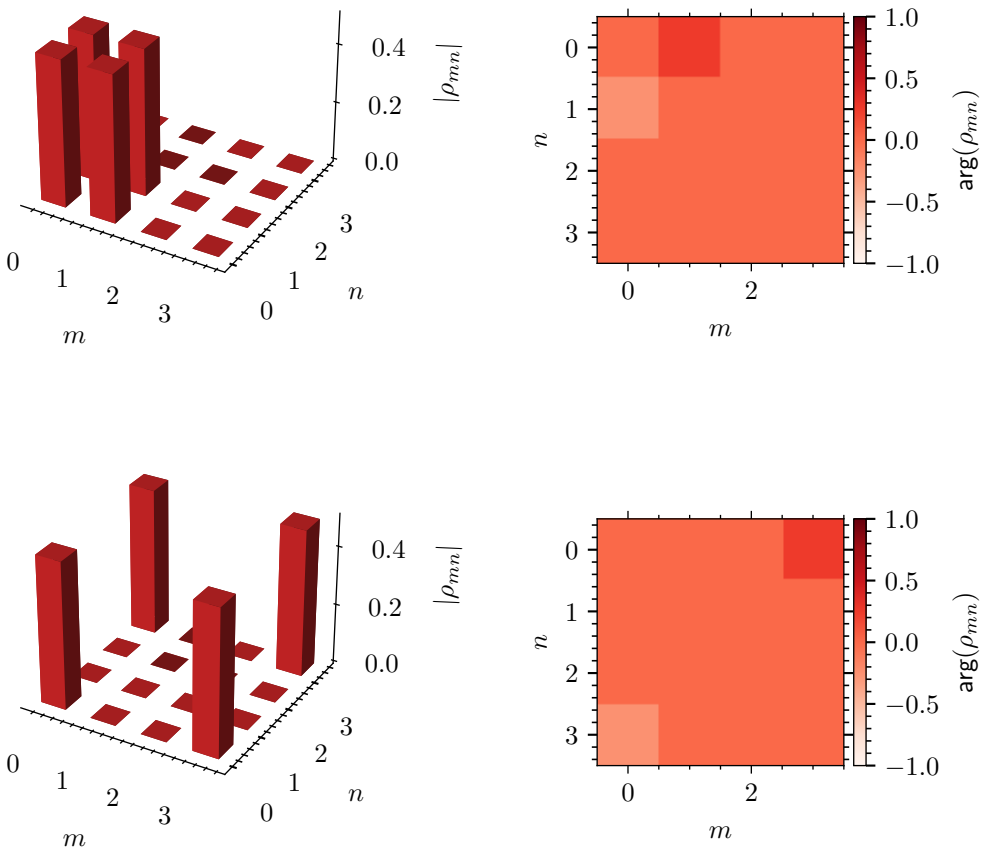

Figure V.3: *Density matrix elements* for the vacuum–single-photon (upper row) and vacuum-three-photon (lower row) superposition (Eq. (V.2.6b)) , with coherence phases $\theta_1, \theta_2 = \pi/4$.

$\sum_{n=0}^{\infty} |c_n|^2 = 1$. In particular, we consider the superpositions

$$|\psi_{01}\rangle = \frac{1}{2}\left(|0\rangle + e^{i\theta_1}|1\rangle\right), \quad |\psi_{03}\rangle = \frac{1}{2}\left(|0\rangle + e^{i\theta_2}|3\rangle\right), \tag{V.2.6a}$$

whose density matrix elements are

$$\rho_{n+jn} = \frac{1}{2}\begin{cases} 1 & n \leq 1 \text{ and } j = 0 \\ e^{i\theta_1} & n = 0 \text{ and } j = 1 \\ e^{-i\theta_1} & n = 1 \text{ and } j = -1 \end{cases}, \quad \rho_{n+jn} = \frac{1}{2}\begin{cases} 1 & n = 0, 3 \text{ and } j = 0 \\ e^{i\theta_2} & n = 0 \text{ and } j = 3 \\ e^{-i\theta_2} & n = 3 \text{ and } j = -3 \end{cases}, \tag{V.2.6b}$$

reflecting vacuum–single-photon and vacuum-three-photon coherence, respectively. The density matrix elements of these vacuum-single-photon and vacuum-three-photon superpositions is depicted in Fig. V.3.
The deterministic generation of Fock states in circuit QED was experimentally

shown by Hofheinz et al. [262] using a superconducting phase-qubit coupled to a microwave resonator. The experiment exploits the ability to prepare a two-level system in an arbitrary state via a classical drive, creating an excitation in the qubit that is transferred to the resonator. Fock states with up to six [262] and later up to 9 [263] photons were generated in the resonator, limited mainly by coherence times and the photon transfer rate to the resonator. This experimental platform also enables the generation of arbitrary quantum states in the resonator [263]. Depending on the target state, the protocol prepares the qubit in the required ground–excited superposition, followed by a partial photon transfer to the resonator [264]. Fock-state superpositions with controlled amplitudes and phases, including an approximate „Voodoo cat" state, were generated and measured via Wigner tomography. Another method of creating single-photon Fock states and photon-blockade states was proposed by [265], employing weak Kerr-type nonlinearities combined with coherent and parametric driving. A photon-blockade state exhibits an abrupt cutoff in its photon-number distribution, containing only Fock states with photon numbers below a certain threshold.

Thermal state.— The thermal state is an incoherent superposition of Fock states,

$$\rho_{n+jn} = \begin{cases} \frac{\overline{n}_{\text{th}}^n}{(\overline{n}_{\text{th}}+1)^{n+1}} & j=0 \\ 0 & \text{else} \end{cases}, \tag{V.2.7}$$

where $\overline{n}_{\text{th}} = [\exp(\beta\hbar\omega_0) - 1]^{-1}$ is the average thermal photon number, and $\beta = (k_{\text{B}}T)^{-1}$ the inverse thermal energy, which is determined by the temperature T. The thermal state is attained through thermalization with the environment, taking on the temperature T of the environment.

Coherent state.— A coherent state $|\alpha\rangle$ is an eigenstate of the annihilation operator $\hat{a}$ with eigenvalue α, i.e., $\hat{a}\,|\alpha\rangle = \alpha\,|\alpha\rangle$, and saturates the Heisenberg uncertainty relation. It can be expressed in the Fock basis as

$$|\alpha\rangle = \exp\left(-\frac{|\alpha|^2}{2}\right)\sum_{n=0}^{\infty}\frac{\alpha^n}{\sqrt{n!}}\,|n\rangle\,, \tag{V.2.8}$$

or equivalently generated from the vacuum $|0\rangle$ by the displacement operator

$$\hat{\mathcal{D}}[\alpha] \equiv \exp(\alpha\hat{a}^\dagger - \alpha^*\hat{a}). \tag{V.2.9}$$

The coherent state $|\alpha\rangle$ yields a density matrix element, shown in Fig. V.4,

$$\rho_{n+jn} = \frac{|\alpha|^{2n}\alpha^{*j}}{\sqrt{n!(n+j)!}}e^{-|\alpha|^2}, \tag{V.2.10}$$

with $\alpha = |\alpha|e^{i\theta_3} \in \mathbb{C}$ the coherent parameter.
A coherent state is nearly classical, with α specifying the oscillations amplitude and phase, and containing only the minimum vacuum noise allowed by quantum mechanics. The coherent state is generated by applying a classical drive that

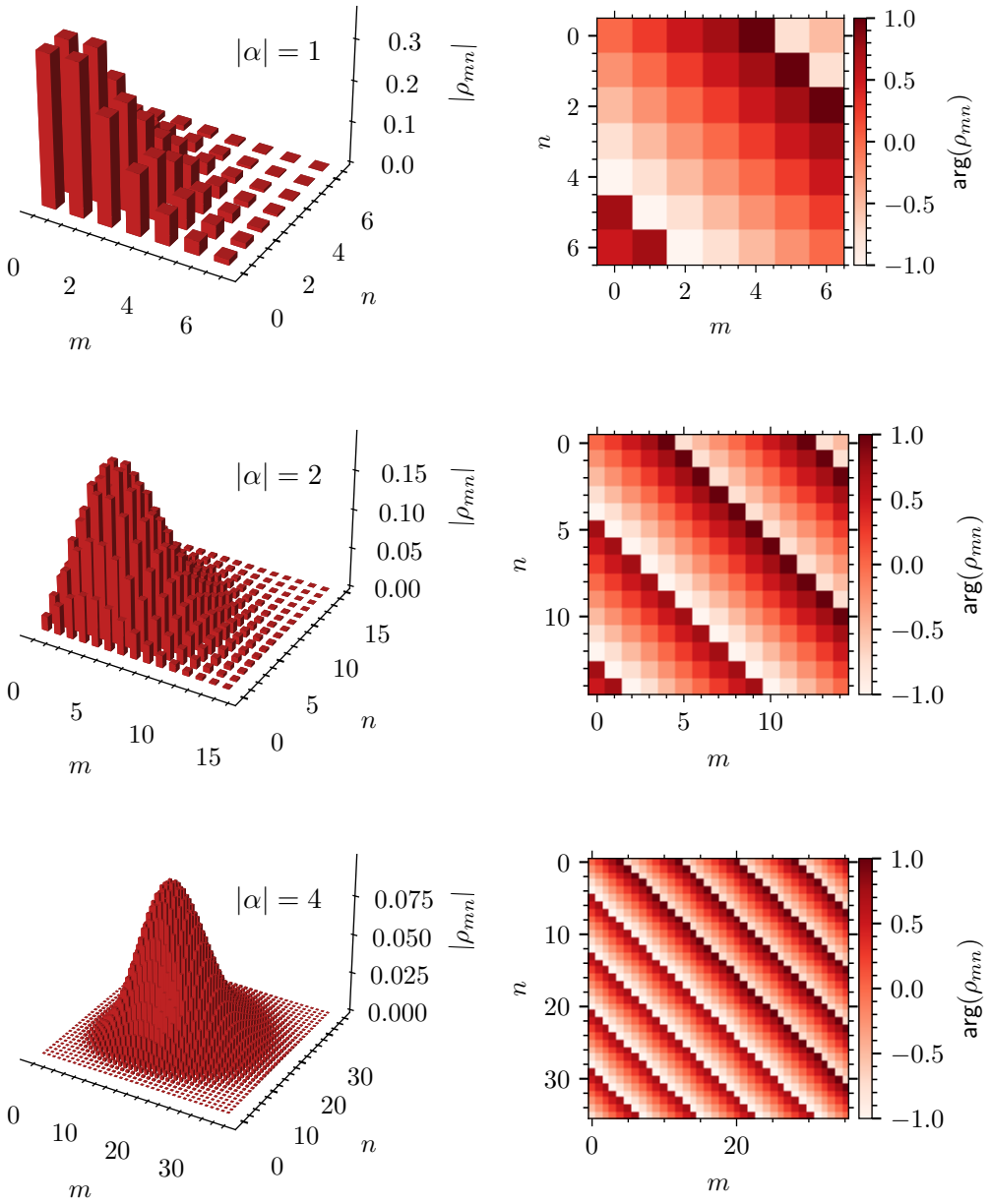

Figure V.4: *Density matrix elements* corresponding to coherent state defined in Eq. (V.2.10), for amplitudes $|\alpha| = 1, 2, 4$ and phase $\theta_3 = \pi/4$.

couples to its field quadratures. In the rotating-wave approximation, this yields the drive Hamiltonian

$$\hat{H}(t) = \hbar\omega_0 \left(\hat{a}^\dagger \hat{a} + \frac{1}{2}\right) + \hbar\epsilon(t)\hat{a}^\dagger + \hbar\epsilon^*(t)\hat{a}, \tag{V.2.11}$$

where $\epsilon(t)$ is the time-dependent drive. For example, a harmonic drive $\epsilon(t) = \epsilon \exp(-i\omega_\mathrm{d} t)$ is specified by its complex amplitude $\epsilon \in \mathbb{C}$ and frequency ω_d. The temporal evolution reduces to a displacement operation $\hat{\mathcal{D}}[\alpha(t)]$ modulo a global phase, thereby resulting in $|0\rangle \mapsto |\alpha(t)\rangle$ [258]. On resonance ($\omega_0 = \omega_\mathrm{d}$), the coherent amplitude $\alpha(t) = -i\epsilon \exp(-i\omega_0 t)t$ describes an outward spiral in phase space, its magnitude increasing linearly from the switch-on time $t = 0$. In the absence of dissipation, the harmonic drive continuously pumps energy into the resonator, causing the displacement parameter $\alpha(t)$, and thus the photon number, to increase over time. A coherent steady state emerges in the presence of dissipation, which is typically described using the input–output formalism [108, 258]. Applying a classical drive pulse can also prepare a coherent state of the resonator field, as demonstrated with a Gaussian-shaped pulse in Ref. [262].

Squeezed state.— Fluctuations in one field quadrature can be reduced below the vacuum level at the expense of increased fluctuations in the conjugate quadrature, thus satisfying the Heisenberg uncertainty relation. This effect is known as squeezing, and a squeezed state is generated by the squeezing operator [260]

$$\hat{\mathcal{S}}[\xi] \equiv \exp\left(-\frac{1}{2}[\xi \hat{a}^{\dagger 2} - \xi^* \hat{a}^2]\right), \tag{V.2.12}$$

acting on an initial state, where $\xi = re^{i\theta_4}$ is the complex squeezing parameter. When applied to the vacuum state, the squeezing operator generates the squeezed vacuum state [260]

$$|\xi\rangle = \frac{1}{\sqrt{\cosh(r)}} \sum_{m=0}^{\infty} (-1)^m \frac{\sqrt{(2m!)}}{2^m m!} e^{im\theta_4} (\tanh(r))^m |2m\rangle, \tag{V.2.13}$$

which has the matrix element

$$\varrho_{n+jn} = \begin{cases} B_{nj} e^{ij\theta_4/2} \frac{[\tanh(r)]^{n+j/2}}{\cosh(r)} & n, j \text{ even} \\ 0 & \text{else} \end{cases}, \tag{V.2.14}$$

with $B_{nj} = (-1)^{j/2}\sqrt{(n+j)!n!}/(2^{n+j/2}((n+j)/2)!(n/2)!)$. Figure V.5 depicts the density matrix elements of the squeezed vacuum for different squeezing parameter. The charge and flux quadratures, $\hat{Q}$ and $\hat{\Phi}$, are squeezed such that for $\theta_4 = 0$ (squeezing along the charge quadrature) the charge variance is reduced to

$$\langle(\Delta\hat{Q})^2\rangle = \frac{Q_\mathrm{zpf}^2}{4} e^{-2r}, \tag{V.2.15}$$

while the flux variance is increased to

$$\langle(\Delta\hat{\Phi})^2\rangle = \frac{\Phi_\mathrm{zpf}^2}{4} e^{2r}, \tag{V.2.16}$$

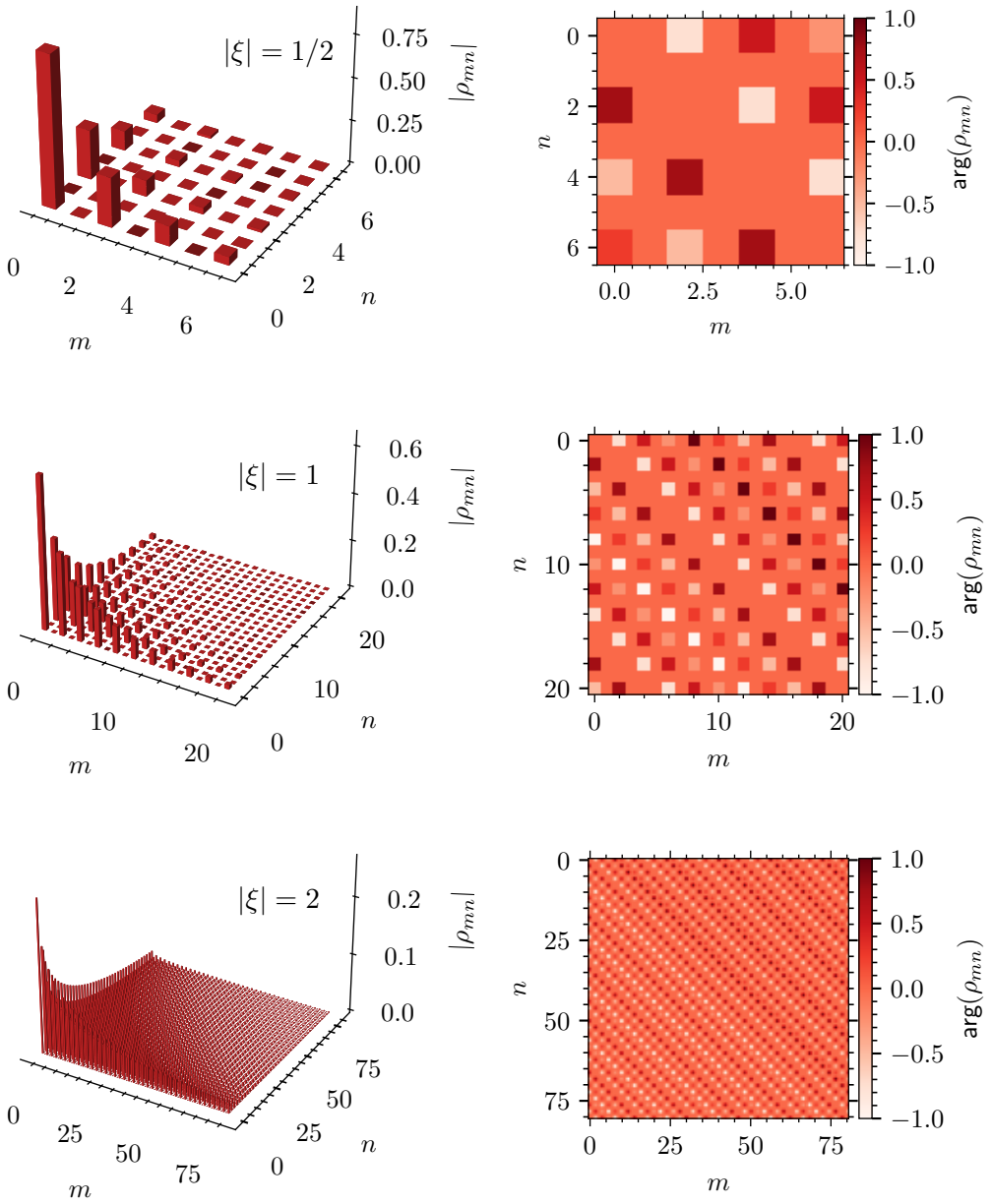

Figure V.5: *Density matrix elements* corresponding to squeezed state defined in Eq. (V.2.14), for squeezing amplitudes $|\xi| = 1, 1.5, 2$ and squeezing phase $\theta_4 = \pi/4$.

where $\Delta\hat{Q} \equiv \hat{Q} - \langle\hat{Q}\rangle$ and $\Delta\hat{\Phi} \equiv \hat{\Phi} - \langle\hat{\Phi}\rangle$, and Q_{zpf} and Φ_{zpf} denote the zero point fluctuations of charge and flux, respectively. Squeezing can be generated by the Hamiltonian of a degenerate parametric amplifier,

$$\hat{H}(t) = \hbar\omega_0 \left(\hat{a}^\dagger\hat{a} + \frac{1}{2}\right) + \hbar\epsilon(t)\hat{a}^{\dagger 2} + \hbar\epsilon^*(t)\hat{a}^2, \tag{V.2.17}$$

where $\epsilon(t) = \epsilon \exp(-i\omega_{\text{d}}t)$ is the parametric drive with amplitude ϵ and frequency $\omega_{\text{d}} \approx 2\omega_0$. Analogously to the coherent-state case, working in the interaction picture shows that the time-evolution operator is equivalent to the squeezing operator $\hat{\mathcal{S}}[\xi(t)]$, up to a physically irrelevant time-dependent global phase. At zero detuning, $2\omega_0 - \omega_{\text{d}} = 0$, the squeezing parameter is $\xi(t) = 2i\epsilon \exp(-2i\omega_0 t)t$ showing a linear growth in magnitude and a phase rotation at the frequency $2\omega_0$. As before, without dissipation no steady state is attained, and the squeezing of the quadratures grows without bound.Therefore, a continuously driven system requires dissipation to stabilize the squeezed state. For an optical mode, the degenerate parametric amplifier Hamiltonian arises from pumping a Kerr medium inside a cavity at twice the cavity's resonance frequency [258, 268–270]. In superconducting platforms, squeezing is achieved with a Josephson parametric amplifier, in which the Josephson junction serves as the nonlinear inductance responsible for the Kerr nonlinearity [108, 267]. In the presence of this weak Kerr nonlinearity, combined with coherent driving and dissipation, the system exhibits squeezed fluctuations around the driven coherent state, resulting in a displaced, weakly non-Gaussian steady state. Squeezing can also be generated using a Josephson parametric amplifier based on a radio-frequency SQUID, rather than by coherently driving the Josephson junction, as demonstrated experimentally by [270, 271]. In this setup, the Josephson junction is parametrically driven via modulation of its nonlinear inductance using a time-dependent flux through the superconducting loop [108, 266, 267]. An alternative route to squeezing is dissipation-driven quantum state engineering, which prepares a desired steady state by controlling the coupling to the environment while retaining quantum coherence. Didier [272] proposed modulating the environment–resonator coupling at twice the resonator frequency to realize ideal squeezing. Control over the coupling between a superconducting resonator and a transmission line was experimentally demonstrated in [273]. Recently, steady-state intraresonator squeezing was observed in the experiment via dissipation engineering in [274]. Furthermore, Xie et al. [275] discuss the dissipative stabilization of superpositions of squeezed coherent states in a single resonator mode, as well as in two superconducting resonator modes, the latter including entangled two-mode cat states. A general multimode state-generation scheme is presented in [276], illustrated with examples such as uncorrelated photon pairs, Bell states, and W states.

V.3 Josephson Effect and Shapiro Steps

The Josephson effect refers to the coherent tunneling of Cooper pairs between two superconductors connected via a weak link, such as a thin insulating barrier or a constriction [17]. In 1962, Brian Josephson [16] predicted two hallmark effects

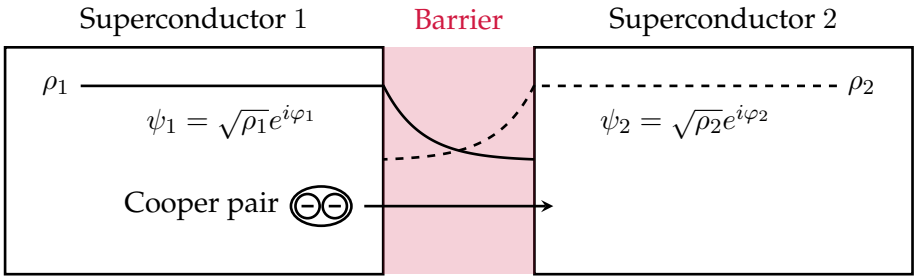

Figure V.6: *Schematic of the Josephson effect*. Minimal model: The macroscopic wavefunctions ψ_j of the superconductors ($j = 1, 2$) are weakly coupled in the barrier region, giving rise to transitions between quantum states and thus to Cooper-pair tunneling.

in superconducting systems: the dc Josephson effect, in which a supercurrent can flow across a weak link without any applied voltage, and the ac Josephson effect, where a static voltage across the junction induces an alternating current. The fundamental physics emerges from a minimal model that treats the superconducting junction as a coherent two-level quantum system [277], as illustrated in Fig. V.6. Each superconductor is in a macroscopic quantum state represented by a wavefunction of the form $\psi_j = \sqrt{\rho_j}e^{i\varphi_j}$, with $j = 1, 2$, where ρ_j denotes the Cooper pair density and φ_j the corresponding superconducting phase. In the presence of weak coupling, transitions between the superconducting states occur via quantum tunneling, characterized by a tunneling Hamiltonian with amplitude K. The time-dependent Schrödinger equation, under the assumption $\rho_1 \approx \rho_2$, yields the Josephson relations

$$I_{\mathrm{cp}}(t) = I_{\mathrm{c}} \sin \phi(t) \tag{V.3.1a}$$

$$\frac{d\phi(t)}{dt} = \frac{2eV}{\hbar}, \tag{V.3.1b}$$

where $I_{\mathrm{cp}}(t)$ is the Cooper pair current, $I_{\mathrm{c}} = 2K\sqrt{\rho_1\rho_2}/\hbar$ the critical current, and $\phi(t) = \phi_1(t) - \phi_2(t)$ is the phase difference between the superconductors. Therefore, in the absence of an applied voltage, a nonzero phase difference can sustain a steady supercurrent. The first experimental verification of the dc Josephson effect was carried out by Anderson and Rowell in 1963 [278]. When a voltage V is applied across the junction, the phase difference evolves linearly with time, giving rise to a supercurrent oscillating at the Josephson frequency $\omega_{\mathrm{J}} = 2eV/\hbar$. The Josephson frequency-to-voltage ratio is given by $\omega_{\mathrm{J}}/V = 3.038\,\mathrm{GHz/\mu V}$, and the resulting oscillations are too fast to be directly detected using present-day electronics.

A method to detect the ac Josephson effect was proposed by Shapiro [279], who observed quantized voltage steps in the current–voltage characteristic when the junction was irradiated with a microwave field. The model used to describe the Shapiro effect depends on what is controlled, current or voltage, and on the impedance and dynamical response of the surrounding circuit [280, 281]. To capture the fundamental physical behavior of a Josephson junction under microwave irradiation, a common approach is to model the external field as an imposed al-

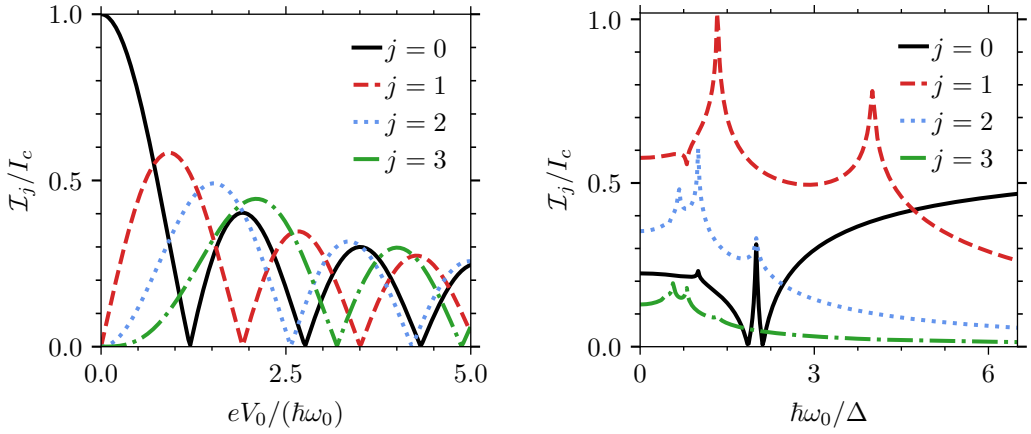

Figure V.7: *Amplitude* $\mathcal{I}_j$ of the jth *current spike* (Eq. (V.3.8)) as a function of the ac amplitude V_0 (left) and the frequency ω_0 (right). By symmetry of the Bessel functions, $\mathcal{I}_{-j} = \mathcal{I}_j$. Here, the current amplitude $I_{c,1}$ is evaluated at zero temperature with a broadening parameter $\eta = 5 \times 10^{-3}$, while the drive frequency is $\hbar\omega_0 = 0.2\Delta$ (left) and $a = 2$ is fixed (right).

ternating voltage, referred to as the voltage source model [17]. The junction experiences a voltage $V(t) = V + V_0 \cos(\omega_0 t)$, where V is the constant dc bias, V_0 the amplitude and ω_0 the frequency of the microwave radiation. Using the Josephson relations, the phase evolves as

$$\phi(t) = \omega_J t + \frac{\omega_J}{\omega_0}\frac{V_0}{V}\sin(\omega_0 t) + \phi_0, \tag{V.3.2}$$

which leads to a supercurrent of the form

$$I_{cp}(t) = I_c \sin\left(\omega_J t + \frac{\omega_J}{\omega_0}\frac{V_0}{V}\sin(\omega_0 t) + \phi_0\right), \tag{V.3.3}$$

where ϕ_0 is the initial static phase difference between the superconductors. Expanding the current using Bessel functions of the first kind $J_l(\cdot)$ (Jacobi-Anger expansion), one obtains

$$\begin{aligned} I_{cp}(t) = I_c\Bigg(J_0(a)\sin(\omega_J t + \phi_0) + \sum_{l=1}^{\infty} J_l(a)\Bigg(\sin[(l\omega_0 + \omega_J)t + \phi_0] \\ - (-1)^l \sin[(l\omega_0 - \omega_J)t + \phi_0]\Bigg)\Bigg), \end{aligned} \tag{V.3.4}$$

with $a = \omega_J V_0/(\omega_0 V)$. The oscillating Cooper pair current acquires a dc component whenever the Josephson frequency is commensurate with the external drive frequency, i.e., when

$$\omega_J = \frac{2e}{\hbar}V = l\omega_0, \quad l \in \mathbb{Z}, \tag{V.3.5}$$

in which case the time-averaged current contains a contribution

$$\overline{I}_l^{\mathrm{cp}} = I_c J_l\left(\frac{lV_0}{V}\right)\sin\phi_0. \tag{V.3.6}$$

The dc supercurrent is superimposed on the background quasiparticle current present at finite bias. In this voltage source model, Shapiro steps manifest as peaks in the current at voltages $l\hbar\omega_0/(2e)$, where $l \in \mathbb{Z}$. However, current-biased experiments reveal Shapiro steps as plateaus in the voltage, occurring when the Josephson frequency synchronizes with the external drive [17]. In this simplified model, the voltage dependence of the critical current is neglected, making a microscopic description necessary to capture the relevant physics. Barone [17] uses a tunneling Hamiltonian formalism to derive both the quasiparticle and Cooper pair currents, treating the superconductors as macroscopic reservoirs within the BCS framework and modeling interaction via tunneling between them. In the presence of the applied microwave field, the Cooper pair current through the junction is given by

$$\begin{aligned} I_{\mathrm{cp}}(t) = \sum_{n,l=-\infty}^{\infty} J_n(a/2)J_l(a/2)\Big(&I_{\mathrm{c},1}(\omega_{\mathrm{J}}/2 + l\omega_0)\sin([(n+l)\hbar\omega_0 + \hbar\omega_{\mathrm{J}}]t + \phi_0) \\ &+ I_{\mathrm{c},2}(\omega_{\mathrm{J}}/2 + l\omega_0)\cos([(n+l)\omega_0 + \omega_{\mathrm{J}}]t + \phi_0)\Big), \end{aligned} \tag{V.3.7}$$

where the critical currents $I_{\mathrm{c},1}(V)$, $I_{\mathrm{c},2}(V)$ are defined in Eqs. (V.5.27b) and Eq. (V.5.27c), respectively. Pronounced singularities in the critical current $I_{\mathrm{c},1}(V)$ appear at $|eV| = 2\Delta$, known as the Riedel peaks, as illustrated in Fig. V.21.
The time-average ($\overline{I}^{\mathrm{cp}} = \lim_{\overline{T}\to\infty}(1/\overline{T})\int_{-\overline{T}/2}^{\overline{T}/2} dt I_{\mathrm{cp}}(t)$) of the Cooper pair current leads to the current spikes at positions $eV = j\hbar\omega_0/2, j \in \mathbb{Z}$, which have peak heights

$$\overline{I}_j^{\mathrm{cp}} = \sum_{l=-\infty}^{\infty} J_l(a/2)J_{j-l}(a/2)I_{c,1}([l - j/2]\hbar\omega_0)\sin(\phi_0) \tag{V.3.8}$$

Here, we neglected the contribution of the cosine term in Eq. (V.3.7). Figure V.7 depicts the amplitude $\mathcal{I}_j = |\overline{I}_j^{\mathrm{cp}}|$ versus the amplitude V_0 and frequency ω_0 of the applied radiation field. The dependence on amplitude reveals Bessel-function oscillations, whereas the frequency dependence at fixed a shows replicas of the Riedel-peak. In Section V.5.7, we present an alternative derivation of Shapiro physics based on the Keldysh action formalism.

V.4 Nonclassical Photon-Assisted Transport in Superconducting Tunnel Junctions

The first investigations of microwave-irradiated Josephson tunnel junctions date back to the early 1960's [17], which in particular revealed two textbook phenomena. First, the appearance of microwave-induced steps in the current-voltage characteristics [282], which were interpreted as *photon-assisted tunneling* of single quasiparticles [199]. Second, the occurrence of *Shapiro steps*, which consists of additional contributions to the dc current at very specific bias voltages that stem from the phase locking between the ac Josephson current components and the microwave field [279]. These two phenomena illustrated the duality that Josephson junctions can be used as microwave detectors and microwaves can be used to learn about the Josephson effect. With the advent of circuit quantum electrodynamics (circuit QED) in recent years [108, 283], and the ability to create nonclassical microwave states almost at will [263], a natural question arises: what novel physical phenomena may result when Josephson tunnel junctions are subjected to nonclassical microwaves?
In fact, the nonclassical microwaves generated by superconducting resonators have already provided novel insight into the physics of Josephson junctions via microwave spectroscopy of Andreev bound states, see e.g. [284, 285]. It has also been shown that the coupling of a high impedance microwave resonator to a Josephson tunnel junction can be used for quantum bath engineering [286].
In this work, we address the question above and present a theoretical study of the current-voltage characteristics of Josephson tunnel junctions interacting with nonclassical microwave states. Our main goal is to show that superconducting tunnel junctions can be used as detectors to reveal the nature of nonclassical microwave states beyond the capabilities of normal (nonsuperconducting) tunnel junctions [47]. To be precise, we show how the analysis of the supercurrent and the quasiparticle current flowing through the Josephson junction enables the complete reconstruction of the density matrix of quantum states fabricated with circuit QED setups.

General environment.— We investigate how a general electromagnetic environment modifies quantum transport in a superconducting tunnel junction (see Fig. V.8(a) for the setup). The environment imposes a voltage, and thereby a dynamical phase $\hat{\phi}(t)$, across the junction. This phase couples to the tunneling current $\hat{I}$ via the interaction term $\hat{H}_{\text{int}}(t) = (\hbar/e)\,\hat{\phi}(t)\hat{I}$, where $\hbar$ is the reduced Planck constant, and e is the elementary charge. For example, a constant voltage bias V induces the phase $\hat{\phi}(t) = \varphi_{\text{dc}}(t) = eV(t-t_s)/\hbar + \phi_0/2$, with $\phi_0/2$ the phase at the initial time t_s. Photon-assisted tunneling is described by an additional phase $\varphi(t) = \alpha\sin(\omega_0(t-t_s))$, with α the strength of the classical drive, and ω_0 the driving frequency [17, 199]. A quantum environment introduces a phase operator $\hat{\varphi}$, whose dynamics is governed by an environmental Hamiltonian $\hat{H}_{\text{env}}$. In the interaction picture, this phase evolves as $\hat{\varphi}(t) = \exp(i\hat{H}_{\text{env}}(t-t_s))\hat{\varphi}\exp(-i\hat{H}_{\text{env}}(t-t_s))$ leading to a total phase across the junction given by $\hat{\phi}(t) = \hat{\varphi}(t) + \varphi_{\text{dc}}(t)$ (see Appendix).

Our goal is the analysis of the tunnel current in a superconducting junction arising from both a voltage bias and an arbitrary quantum electromagnetic environment (see Fig. V.8(a)). We employ the Keldysh formalism [244] to compute the cumulant-generating functional of the hybrid system to the lowest order in the tunnel conductance G_{T} (see Appendix for details). In principle, the current, noise, and higher-order cumulants can be obtained from the cumulant-generating function. We focus here on the tunnel current, as it already captures a broad range of physical effects.

The tunnel current comprises quasiparticle (qp) and Cooper pair (cp) transport, and takes the form:

$$\begin{aligned} I(t) =& I_{\mathrm{qp}}(t) + I_{\mathrm{cp}}(t) \\ =& \sum_{\nu=\pm} \nu \int_{-\infty}^{\infty} dE\, P^{\nu}(t,E)\Gamma_{\mathrm{qp}}(E) && \text{(V.4.1a)} \\ &+ \sum_{\nu=\pm} \nu \int_{-\infty}^{\infty} dE\, C^{\nu}(t,E)\Gamma_{\mathrm{cp}}(E). && \text{(V.4.1b)} \end{aligned}$$

Both contributions depend on the tunneling rate of the isolated junction, which are given by

$$\Gamma_{\mathrm{qp}}(E) = \frac{G_T}{e}\int_{-\infty}^{\infty} d\epsilon \varrho_1(\epsilon - E)\varrho_2(\epsilon)[1 - f(\epsilon - E)]f(\epsilon) \qquad \text{(V.4.2a)}$$

$$\Gamma_{\mathrm{cp}}(E) = \frac{G_T}{e}\int_{-\infty}^{\infty} d\epsilon \varsigma_1(\epsilon - E)\varsigma_2(\epsilon)[1 - f(\epsilon - E)]f(\epsilon), \qquad \text{(V.4.2b)}$$

where

$$\varrho_p(\epsilon) = \mathrm{Re}\left(\frac{-i(E+i\eta)}{\sqrt{\Delta_j^2 - (E+i\eta)^2}}\right) \qquad \text{(V.4.2c)}$$

is the normalized quasiparticle density of states,

$$\varsigma_p(E) = \mathrm{Re}\left(\frac{i\Delta_j}{\sqrt{\Delta_j^2 - (E+i\eta)^2}}\right) \qquad \text{(V.4.2d)}$$

is the normalized pair density with $\eta \ll 1$ the broadening parameter, $\Delta_p \equiv \Delta$ is the superconducting gap of terminal $p = 1, 2$, and $f(\epsilon) = [1 + \exp(\epsilon/(k_{\mathrm{B}}T))]^{-1}$ is the Fermi-distribution at thermal energy $k_{\mathrm{B}}T$. Here, the terminals are assumed to be s-wave superconductors. The $\nu = +$ terms in Eqs. (V.4.1a) and (V.4.1b) describe transport from terminal 2 to terminal 1, while the $\nu = -$ terms describe transport in the opposite direction. The environment influences the transport via the generalized P-functions [47]

$$P^{\nu}(t,E) = \int_{-\infty}^{\infty} d\tau\, \mathrm{Im}\left(e^{iE\tau/\hbar}G^{\nu+}_{\mathrm{env}}(t,\tau)\right) \qquad \text{(V.4.3a)}$$

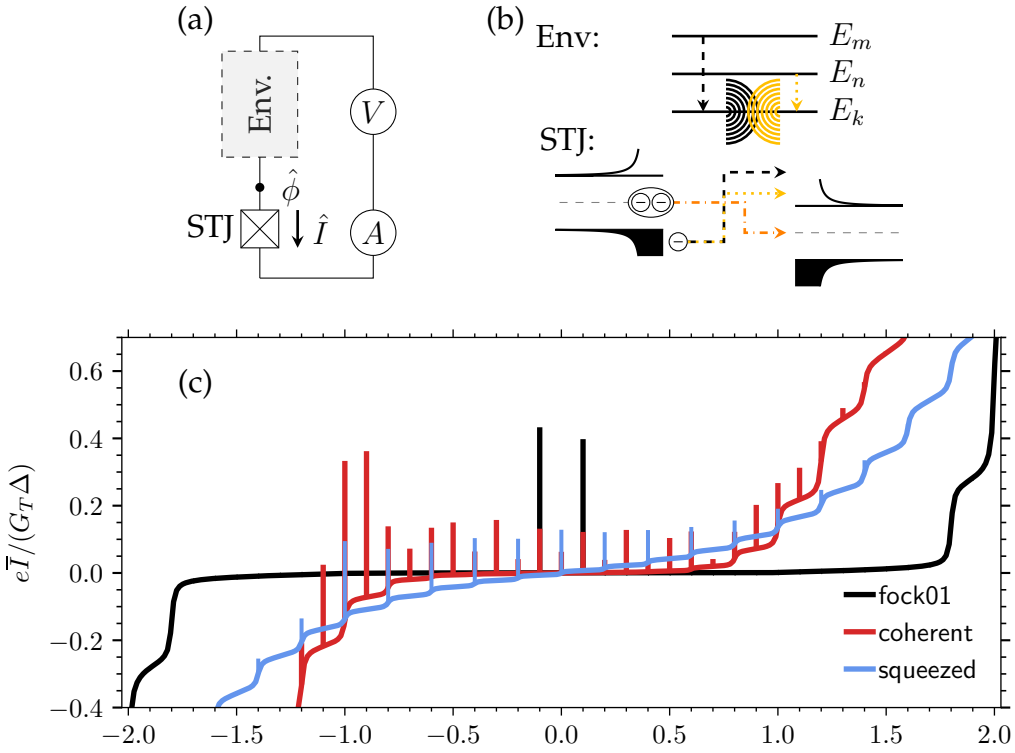

Figure V.8: (a) *Superconducting tunnel junction* (STJ) interacting with an electromagnetic environment (Env.) that imposes a quantum phase $\hat{\phi}$ on the junction. A dc voltage V is applied, and the current-voltage characteristic is investigated. (b) *Transitions* $E_m \to E_k$ or $E_n \to E_k, \ldots$ between the discrete energy levels of the electromagnetic environment induce quasiparticle transport in the STJ. Interference between a pair of transitions leads to inelastic Cooper pair transport, which manifests as current spikes at $eV = (E_m - E_n)/2$ in the dc current. (c) *dc current* as a function of the voltage for an STJ at zero temperature, coupled to an LC-resonator with frequency $\hbar\omega_0 = 0.2\Delta$ and coupling strength $g = 1/2$. The oscillator is in the states defined in Eqs. (V.4.14), where $|\alpha| = 4$, $|\xi| = 2$, and the phases are arbitrary. The spikes represent the amplitude of the Cooper pair current-phase relation (V.4.16c), while the background corresponds to the quasiparticle current (V.4.15a). Spikes appear at $eV = j\hbar\omega_0/2$, whereas steps occur at $eV = 2\Delta + l\hbar\omega_0$, with $j, l \in \mathbb{Z}$.

and C-functions

$$C^{\nu}(t,E) = \int_{-\infty}^{\infty} d\tau \, \mathrm{Im}\left(e^{iE\tau/\hbar} G^{\nu-}_{\mathrm{env}}(t,\tau)\right), \tag{V.4.3b}$$

which depend on the environmental correlator

$$G^{\nu\mu}_{\mathrm{env}}(t,\tau) = \frac{i}{\pi\hbar}\Theta(\tau)\left\langle e^{i\mu\nu\hat{\phi}(t)} e^{-i\nu\hat{\phi}(t-\tau)}\right\rangle. \tag{V.4.3c}$$

The structure of the quasiparticle current $I_{\mathrm{qp}}(t)$ is identical to that found in a normal-metal tunnel junction coupled to an arbitrary electromagnetic environment [47]. The only difference is that the quasiparticle rates involve the superconducting rather than the normal-metal density of states. The P-functions in Eq. (V.4.3a) coincide with that of the normal-metal case [47] and reduce to the known result from dynamical Coulomb blockade theory for an environment in equilibrium [46, 287, 288]. The key difference between a quantum and a classical environment is that phase operators at different times do not commute, leading to distinct P-functions ($\nu = \pm$) for charge transport from terminal 1 to 2 versus from 2 to 1. If the phase operator commutes at all times, the symmetry $P^{-}(t,E) = P^{+}(t,-E)$ is recovered. This symmetry ensures that the current depends directly on the bare current,

$$I^{0}_{\mathrm{qp}}(E) = \Gamma_{\mathrm{qp}}(-E) - \Gamma_{\mathrm{qp}}(E) = \frac{G_{\mathrm{T}}}{e}\int_{-\infty}^{\infty} d\epsilon \varrho(\epsilon - E)\varrho(\epsilon)[f(\epsilon - E) - f(\epsilon)], \tag{V.4.4}$$

as is the case in photon-assisted tunneling [17, 199, 279]. In a normal-metal junction, this non-commutativity leads to a nonlinear I-V characteristic, as opposed to the linear behavior predicted by photon-assisted tunneling, which is attributed to the zero-point fluctuations of the field [47].
The Cooper pair current $I_{\mathrm{cp}}(t)$ has a similar structure, with the density of states replaced by the pair density, and with the exponents in the environmental correlator carrying the same sign. This sign difference profoundly affects the system's behavior and is responsible for both the dc and ac Josephson effects. The standard dc Josephson effect is recovered when the phase is constant, resulting in a sinusoidal current-phase relation. A dc bias induces a linear time-dependence of the phase, leading to an oscillating Cooper pair current at the Josephson frequency, as can be derived from Eqs. (V.4.3) (see Appendix).

V.4.1 Discrete Environmental Spectrum

We focus now on a broad class of environments composed of discrete modes. This class is encountered in circuit QED systems [108], where the environment may consist of an LC-resonator, an artificial atom, a superconducting qubit, etc. The environmental Hamiltonian $\hat{H}_{\mathrm{env}}$ has a discrete spectrum, with eigenenergies E_n and eigenstates $|E_n\rangle$. The phase $\hat{\varphi}(t)$ evolves according to the unitary operator $\hat{U}(t,t_s)$, which takes the spectral form $\hat{U}(t,t_s) = \sum_n \exp(-iE_n(t-t_s))\,|E_n\rangle\langle E_n|$,

where the sum runs over all eigenstates. We consider the electromagnetic environment to be initialized in a general quantum state, described by the density matrix $\hat{\rho}$. The environmental correlator reduces to

$$\langle e^{-i\nu\hat{\varphi}(t)} e^{-i\nu'\hat{\varphi}(t-\tau)} \rangle = \sum_{n,m,k} \langle \hat{L}_{mk} \hat{L}_{kn} \rangle A^{\nu}_{mk} A^{\nu'}_{kn} e^{-i(E_k - E_n)\tau/\hbar - i(E_n - E_m)t/\hbar}, \tag{V.4.5}$$

with the ladder operator $\hat{L}_{kn} = |E_k\rangle \langle E_n|$ corresponding to the transition $E_n \to E_k$, and the transition amplitude $A^{\nu}_{kn} = \langle E_k | \exp(-i\nu\hat{\varphi}) | E_n \rangle$. The operator $e^{-i\nu\hat{\varphi}}$ acts as a translation operator for the charge operator $\hat{Q}$, which is canonically conjugate to the phase $\hat{\varphi}$, shifting the charge in the environment by one elementary unit [46].

The current $I(t)$ oscillates in time, and we focus on its dc component, given by the long-time average $\overline{I} = \lim_{\overline{T}\to\infty} (1/\overline{T}) \int_{-\overline{T}/2}^{\overline{T}/2} I(t) dt$. The quasiparticle current is a superposition of oscillations at transition frequencies between the states, and the time-averaged current is given by

$$\overline{I}_{\mathrm{qp}} = \sum_{\nu=\pm} \nu \sum_{n,k} \gamma^{\nu}[k,n] \Gamma_{\mathrm{qp}}(E_k - E_n - \nu eV), \tag{V.4.6a}$$

where

$$\gamma^{\nu}[k,n] = |A^{\nu}_{kn}|^2 \, \mathrm{Tr}\{\hat{L}_{kn} \hat{\rho} \hat{L}^{\dagger}_{kn}\} = |A^{\nu}_{kn}|^2 \rho_{nn}. \tag{V.4.6b}$$

Here, ρ_{nn} are the diagonal entries of the density matrix in the energy basis and $\mathrm{Tr}\{\cdot\}$ represents the trace. The transition rate $\gamma^{\nu}[k,n]$ from state E_n to state E_k involves the transition probability $|A^{\nu}_{kn}|^2$ induced by the charge transport and the occupation probability of the initial state ρ_{nn}. The transition rates satisfy the normalization condition $\sum_{k,n} \gamma^{\nu}[k,n] = 1$, reflecting the conservation of probability. Figure V.8(b) illustrates quasiparticle transport processes.
Due to the ac Josephson effect, the oscillations in the Cooper pair current are shifted by the Josephson frequency $\omega_{\mathrm{J}} = 2eV/\hbar$, such that the current becomes a superposition of oscillatory components at frequencies $\omega_{\mathrm{J}} + (E_n - E_m)/\hbar$. The time-averaged Cooper pair current is given by

$$\overline{I}_{\mathrm{cp}} = \sum_{m,n} \delta_{eV,(E_m - E_n)/2} \, \overline{I}^{\mathrm{cp}}_{mn}, \tag{V.4.7a}$$

where $\delta_{x,y}$ equals one for $x = y$, and zero otherwise. Therefore, the transport of Cooper pairs results in spikes in the dc I-V characteristics, occurring when the applied voltage satisfies the resonance condition $eV = (E_m - E_n)/2$. For an overview, Fig. V.8(c) shows the spike structure due to Cooper pair transport, along with the step-like quasiparticle current resulting from an LC-resonator used as the environment. Each pair of states $|E_m\rangle$, $|E_n\rangle$ contributes

$$\overline{I}^{\mathrm{cp}}_{mn} = \sum_{k} \Gamma_{\mathrm{S}}(E_k - (E_m + E_n)/2) \, \mathrm{Im}\left(e^{i\phi_0} C_{nkm} \right), \tag{V.4.7b}$$

with

$$\Gamma_{\mathrm{S}}(E) = 2\,\mathrm{P.V.}\int_{-\infty}^{\infty} d\epsilon \frac{\Gamma_{\mathrm{cp}}(\epsilon)}{\pi(\epsilon - E)} \tag{V.4.7c}$$

$$C_{nkm} = (A^{+}_{kn})^{*} A^{-}_{km}\,\mathrm{Tr}\{\hat{L}_{km}\hat{\rho}\hat{L}^{\dagger}_{kn}\} = (A^{+}_{kn})^{*} A^{-}_{km}\rho_{mn}, \tag{V.4.7d}$$

where P.V. denotes principal value. The rate $\Gamma_{\mathrm{S}}(eV)$ is related to the ac Josephson current $I_{c,1}(V)\sin(\phi_0 + \omega_f t)$ by [17]

$$I_{c,1}(V) = [\Gamma_{\mathrm{S}}(eV) + \Gamma_{\mathrm{S}}(-eV)]/2. \tag{V.4.8}$$

The factor C_{nkm} incorporates the effect of the environment, and contains the transition amplitudes A^{+}_{kn} and A^{-}_{km}. We interpret this factor as an interference contribution between the transitions E_m to E_k and E_n to E_k, with an initial coherence ρ_{mn} being necessary to generate interference between the transitions, see Fig. V.8(b). Degenerate energy splittings among multiple levels lead to their collective contribution to a single spike in the I-V characteristics. If all transition energies are distinct, the spike height is directly proportional to the coherences ϱ_{mn} of the environmental density matrix, enabling their direct extraction.
The physics at play here is closely related to the Shapiro effect that occurs under a harmonic current drive [17, 279]. There, voltage plateaus emerge at multiples of half the driving frequency, manifesting as current spikes in the voltage-source model [17]. Here, the spikes occur at the transition energies of the environment and need not be regularly spaced.
Note that a system in equilibrium, or in an incoherent superposition of energy eigenstates, does not exhibit spikes at finite voltage. Interestingly, a modified supercurrent $\overline{I}^{\mathrm{cp}} = \sum_{n,k}\Gamma_{\mathrm{S}}(E_k - E_n)\,\mathrm{Im}(e^{i\phi_0}C_{nkn})$ arises even in equilibrium. This is in contrast to predictions from standard dynamical Coulomb blockade theory [46], where the supercurrent vanishes and the first nonzero contribution to the Cooper pair current is second order in the tunnel conductance. In Ref. [46], the Cooper pair condensate was modeled using the Josephson Hamiltonian. The microscopic analysis [287] shows that the supercurrent survives for environments in which the real part of the impedance vanishes as $\mathcal{O}(\omega^2)$ or faster as $\omega \to 0$. A set of discrete modes satisfies this scaling behavior, and the supercurrent remains finite.

V.4.2 Example 1: Qubit

To illustrate the physics, we consider a superconducting qubit (e.g., a charge qubit or a transmon [108]) acting as the electromagnetic environment. Working within a two-level truncation, the environmental Hamiltonian is $\hat{H}_{\mathrm{env}} = -\hbar\omega_q\hat{\sigma}_3/2$, where $\hbar\omega_q$ is the level spacing, depending on the qubit frequency ω_q and $\hat{\sigma}_3$ the third Pauli matrix. Accordingly, the superconducting tunnel junction couples to the phase operator $\hat{\varphi} = \varphi_{\mathrm{zpf}}\hat{\sigma}_1$, where $\varphi_{\mathrm{zpf}} = (2E_{\mathrm{c}}/E_{\mathrm{J}})^{1/4}$ denotes the zero-point phase fluctuations, E_{C} and E_{J} are the charging and Josephson energies, and $\hat{\sigma}_1$ the first Pauli matrix [108]. The state of the qubit is encoded in the density matrix

$$\hat{\rho} = \begin{pmatrix} \rho_{00} & \rho_{01} \\ \rho_{10} & \rho_{11} \end{pmatrix}, \tag{V.4.9}$$

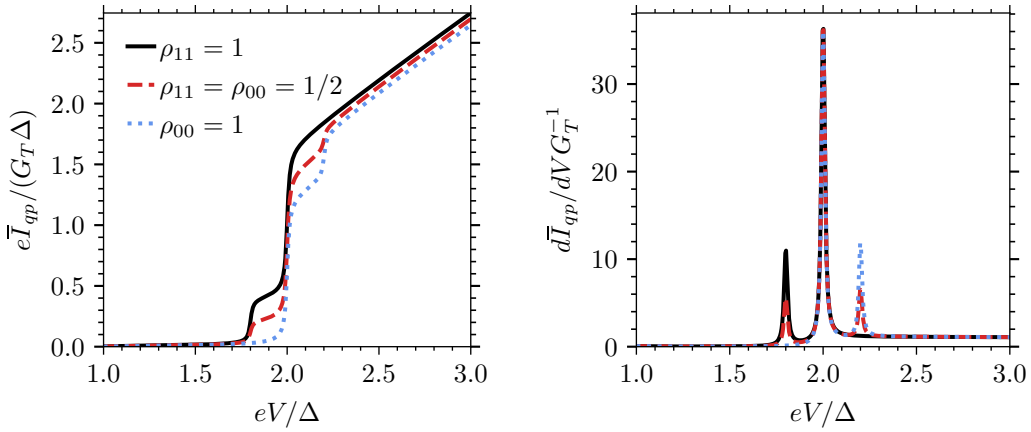

Figure V.9: *Quasiparticle current* $\bar{I}_{\rm qp}$ (left) and *differential conductance* $d\bar{I}_{\rm qp}/dV$ (right) for an environmental qubit prepared in the ground state ($\rho_{00} = 1$),the excited state ($\rho_{11} = 1$), and an equal mixture ($\rho_{00} = \rho_{11} = 1/2$). The zero-point fluctuations are $\varphi_{\rm zpf} = 1/2$, the qubit frequency is $\hbar\omega_q = 0.2\Delta$, and the tunnel rate (V.4.2a) is evaluated at zero temperature with a broadening parameter $\eta = 5 \times 10^{-3}$.

with elements ρ_{jk} ($j, k \in \{0, 1\}$) satisfying $\rho_{00} + \rho_{11} = 1$ and $\rho_{10} = \rho_{01}^*$.
The dc quasiparticle current through the superconducting junction is given by Eq. (V.4.6a) and reduces to

$$\begin{aligned}\bar{I}_{\rm qp} = &\cos^2(\varphi_{\rm zpf})\bar{I}^0_{\rm qp}(eV) + \rho_{00}\sin^2(\varphi_{\rm zpf})\sum_{\nu=\pm}\nu\Gamma_{\rm qp}(\hbar\omega_q - \nu eV)\\ &+ \rho_{11}\sin^2(\varphi_{\rm zpf})\sum_{\nu=\pm}\nu\Gamma_{\rm qp}(-\hbar\omega_q - \nu eV),\end{aligned} \tag{V.4.10}$$

with $\bar{I}^0_{\rm qp}(eV)$ refers to bare current-voltage characteristic (V.4.4), which exhibits an onset of quasiparticle current at $|eV| = 2\Delta$. Transitions from the excited state $|1\rangle$ to the ground state $|0\rangle$ give rise to subgap transport that sets in at $eV = 2\Delta - \hbar\omega_q, -2\Delta + \hbar\omega_q$. Conversely, transitions $|0\rangle \to |1\rangle$ appear at $eV = 2\Delta + \hbar\omega_q, -2\Delta - \hbar\omega_q$. Therefore, the quasiparticle current features at most three step-like onsets: a subgap step that occurs when the excited state is populated ($\rho_{11} \neq 0$), and a above-gap step that occurs when the ground state is populated ($\rho_{00} \neq 0$). Figure V.9 shows the quasiparticle current and the corresponding differential conductance for different qubit states. Therefore, measurement of the quasiparticle current enables extraction of the diagonal elements of the qubit density matrix.
Cooper pair transport leads to current spikes at $eV = 0$ ($\bar{I}^{cp}_0$), $eV = \hbar\omega_q/2$ ($\bar{I}^{cp}_+$), and $eV = -\hbar\omega_q/2$ ($\bar{I}^{cp}_-$). The zero-bias current corresponds to a modified supercurrent and takes the form

$$\bar{I}^{\rm cp}_0 = \tilde{I}_c \sin(\phi_0), \tag{V.4.11}$$

with an effective critical current

$$\tilde{I}_c = \cos^2(\varphi_{\rm zpf})I_c - \sin^2(\varphi_{\rm zpf})\left[\rho_{00}\Gamma_{\rm S}(\hbar\omega_q/2) + \rho_{11}\Gamma_{\rm S}(-\hbar\omega_q/2)\right], \tag{V.4.12}$$

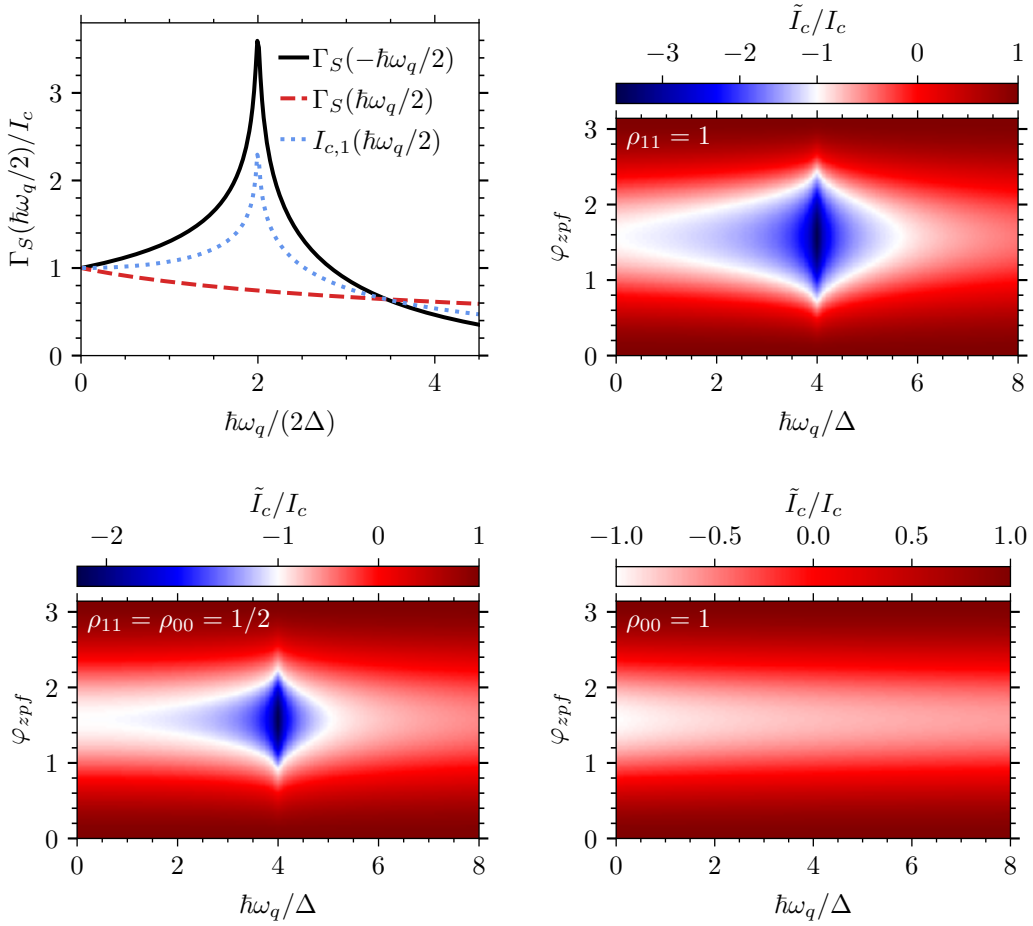

Figure V.10: *Rate* Γ_S and *amplitude of the AC Josephson current* $I_{c,1}$ that enter the Cooper-pair transport. *Effective critical current* $\tilde{I}_c$ for an environmental qubit prepared in the ground state ($\rho_{00} = 1$),the excited state ($\rho_{11} = 1$), and an equal mixture ($\rho_{00} = \rho_{11} = 1/2$). The effective critical current can become negative and, in magnitude, exceed the (no-environment) critical current due to the Riedel peak. Parameter: zero temperature; broadening parameter $\eta = 5 \times 10^{-3}$.

where I_c is the critical current without environment. In the limit $\hbar\omega_q \ll \Delta$, the effective critical current reduces to $\tilde{I}_c \approx \cos(2\varphi_{\text{zpf}})I_c \in [-I_c, I_c]$ and is therefore independent of the qubit state, depending only on φ_{zpf}. The frequency dependence is governed by the rate Γ_{S} in Eq. (V.4.7c), which exhibits the Riedel singularity shown in Fig. V.10. Transitions between the qubit levels ($|0\rangle \leftrightarrow |1\rangle$) reduce the effective critical current. It can become negative, reflecting a phase shift of π and, due to the Riedel peak, can even be smaller than $-I_c$. Figure V.10 depicts the effective critical current $\tilde{I}_c$ for different zero-point fluctuations and qubit frequencies. The global minimum $\min_{\varphi_{\text{zpf}},\omega_q,\hat{\rho}} \tilde{I}_c$ is attained for $\rho_{11} = 1, \varphi_{\text{zpf}} = \pi/2, \hbar\omega_q = 4\Delta$. For the ground state $\rho_{00} = 1$, the minimum equals $-I_c$ at $\varphi_{\text{zpf}} = \pi/2$ and $\hbar\omega_q = 0$. The finite-bias spikes have peak heights

$$\overline{I}_{\pm}^{\text{cp}} = \sin(2\varphi_{\text{zpf}})|\rho_{10}|I_{c,1}(\hbar\omega_q/2)\cos(\phi_0 \pm \vartheta_{10}), \tag{V.4.13}$$

where $\rho_{10} = |\rho_{10}|e^{i\vartheta_{10}}$. Here $I_{c,1}(\hbar\omega_q/2)$ is the voltage-dependent current amplitude known from the Shapiro effect (see Eq. (V.5.27b) and Ref. [17]). Figure V.10 displays the current amplitude $I_{c,1}$, which sets the frequency dependence of the spikes. Overall, the two finite-bias current spikes provide information about the qubit coherence $|\rho_{10}|$.

V.4.3 Example 2: Quantum harmonic oscillator

Let us turn now to the case of a single electromagnetic mode modeled as a quantized LC circuit. The flux $\hat{\Phi} = \hbar\hat{\varphi}/e$ through the inductor is related to the phase operator $\hat{\varphi} = -i\sqrt{g}(\hat{a} - \hat{a}^\dagger)$, with $g = \pi Z_{LC}/R_K$ the strength of the zero-point voltage fluctuations, determined by the impedance of the resonator $Z_{LC} = \sqrt{L/C}$ and the resistance quantum $R_{\text{K}} = 2\pi\hbar/e^2$, and $\hat{a}/\hat{a}^\dagger$ the annihilation/creation operator of the mode. The oscillator has eigenenergies $E_n = \hbar\omega_0(n + 1/2)$ and Fock states $|n\rangle$, with transition energies $E_{n+l} - E_n = l\hbar\omega_0, l \in \mathbb{Z}$ between the states, where $\omega_0 = 1/\sqrt{LC}$ is the resonance frequency. To explore how different quantum states influence the transport, we prepare the oscillator in Fock superpositions

$$|\Psi_{01}\rangle = \frac{|0\rangle + \exp(i\theta_1)\,|1\rangle}{\sqrt{2}}, \quad |\Psi_{03}\rangle = \frac{|0\rangle + \exp(i\theta_2)\,|3\rangle}{\sqrt{2}} \tag{V.4.14a}$$

a squeezed vacuum state

$$|\xi\rangle = \sum_{n=0}^{\infty}(-1)^n \frac{\sqrt{(2n!)}}{2^n n!}\exp(in\theta_3)\frac{(\tanh(|\xi|))^n}{\sqrt{\cosh(|\xi|)}}\,|2n\rangle\,, \tag{V.4.14b}$$

or a coherent state

$$|\alpha\rangle = \exp\left(-\frac{|\alpha|^2}{2}\right)\sum_{n=0}^{\infty}\frac{|\alpha|^n e^{in\theta_4}}{\sqrt{n!}}\,|n\rangle\,. \tag{V.4.14c}$$

The squeezed state is controlled by the squeezing amplitude $|\xi|$, which characterizes the degree of squeezing, while the coherent state depends on $|\alpha|$, which determines the amplitude of the oscillations. All states can carry an associated phase

θ_s ($s = 1, 2, 3, 4$). By simple inspection, we can infer from Eq. (V.4.7d) and the properties of the states which Cooper pair current spikes may appear in the I-V characteristics. Since $|\psi_{01}\rangle$ ($|\psi_{03}\rangle$) only has nonzero coherences on the first (third) off-diagonals of the density matrix, spikes only appear at $eV = -\hbar\omega_0/2, 0, \hbar\omega_0/2$ ($eV = -3\hbar\omega_0/2, 0, 3\hbar\omega_0/2$). A squeezed vacuum state possesses nonzero entries only for even occupation numbers, so no peaks appear at $eV = j\hbar\omega_0/2$, with j odd. In contrast, a coherent state can have spikes at all $j \in \mathbb{Z}$ due to its nonzero coherences across all Fock states. The distinct coherence structures of these states are directly reflected in the Cooper pair transport (see Fig. V.8(c)).
The background current in Fig. V.8(c) arises from quasiparticle transport and is described by

$$\overline{I}_{\mathrm{qp}} = \sum_{l=-\infty}^{\infty} p_l \sum_{\nu=\pm} \nu\Gamma_{\mathrm{qp}}(l\hbar\omega_0 - \nu eV), \tag{V.4.15a}$$

where the quasiparticles exchange l energy quanta with the environment, with probability

$$p_l = \sum_{n=0}^{\infty} \Theta(n+l)|A^{-}_{n+ln}|^2 \rho_{nn}, \tag{V.4.15b}$$

determined by the transition amplitudes

$$A^{\nu}_{n+ln} = e^{-g/2} \begin{cases} \sqrt{\frac{n!}{(n+l)!}}(\nu g)^{l/2} L^l_n(g) & l \geq 0 \\ \sqrt{\frac{(n+l)!}{n!}}(-\nu g)^{-l/2} L^{-l}_{n+l}(g) & l < 0 \end{cases}. \tag{V.4.15c}$$

Here, $L^l_n(x)$ are generalized Laguerre polynomials.
Figures V.11 and V.12 show the quasiparticle current and the differential conductance for the four environmental states in Eqs. (V.4.14). Due to the superconducting energy gap, the quasiparticle rate $\Gamma_{\mathrm{qp}}(E)$ becomes nonzero only for $E \leq -2\Delta$. Therefore, the processes involving the exchange of l energy quanta with the resonator set in successively at $2\Delta + l\hbar\omega_0$, where the exchange probability p_l determines the height of the step. For example, the Fock superpositions $|\Psi_{01}\rangle$ and $|\Psi_{03}\rangle$ can emit at most one and three excitations, respectively, which implies $p_l = 0$ for $l < -1$ and $l < -3$. As a result, the first step appears at $eV = 2\Delta - \hbar\omega_0$ and $eV = 2\Delta - 3\hbar\omega_0$, respectively, whereas for the squeezed state, the first step occurs around $2\Delta - 11\hbar\omega_0$. The successive appearance of the steps enables direct extraction of the exchange probability p_l from the quasiparticle current. In contrast, for normal-conducting junctions, determining the exchange probability requires both the average current and current noise (compare to Fig. V.2 and Ref. [47]). As proposed by Souquet *et al.* [47], the exchange probability can serve as a diagnostic tool to distinguish classical from nonclassical states.
Cooper pair transport occurs at $eV = j\hbar\omega_0/2$, $j \in \mathbb{Z}$, and the height of the resulting current spike is given by

$$\overline{I}^{\mathrm{cp}}_j = \sum_{l=-\infty}^{\infty} \Gamma_{\mathrm{S}}([l - j/2]\hbar\omega_0)\, \mathrm{Im}\left(e^{i\phi_0}\mathcal{C}_{lj}\right), \tag{V.4.16a}$$

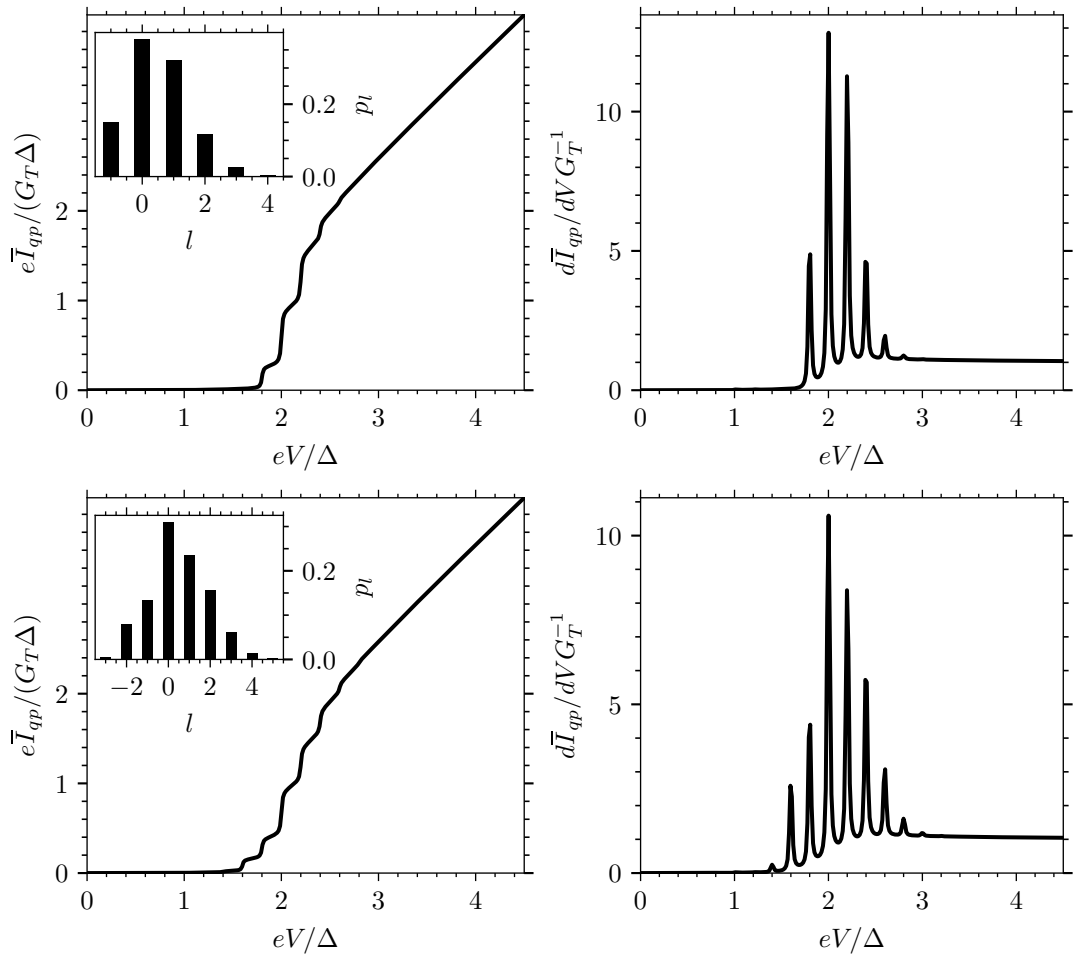

Figure V.11: *Quasiparticle current* $\overline{I}_{\mathrm{qp}}$ (left) and *differential conductance* $d\overline{I}_{\mathrm{qp}}/dV$ (right) when the environment was prepared in a vacuum-single-photon Fock state $|\Psi_{01}\rangle$ (upper row) and vacuum-three-photon Fock state $|\Psi_{03}\rangle$ (lower row). Insets show the corresponding probability p_l to exchange l energy quanta with the environment. The peaks in the differential conductance mark the positions $2\Delta+l\hbar\omega_0$, where the l-th energy exchange begins to contribute to the current. The parameters are $\hbar\omega_0 = 0.2\Delta$, $g = 1/2$, coherence phases $\theta_{1,2}$ arbitrary, and the tunnel rate (V.4.2a) is evaluated at zero temperature with a broadening parameter $\eta = 5 \times 10^{-3}$.

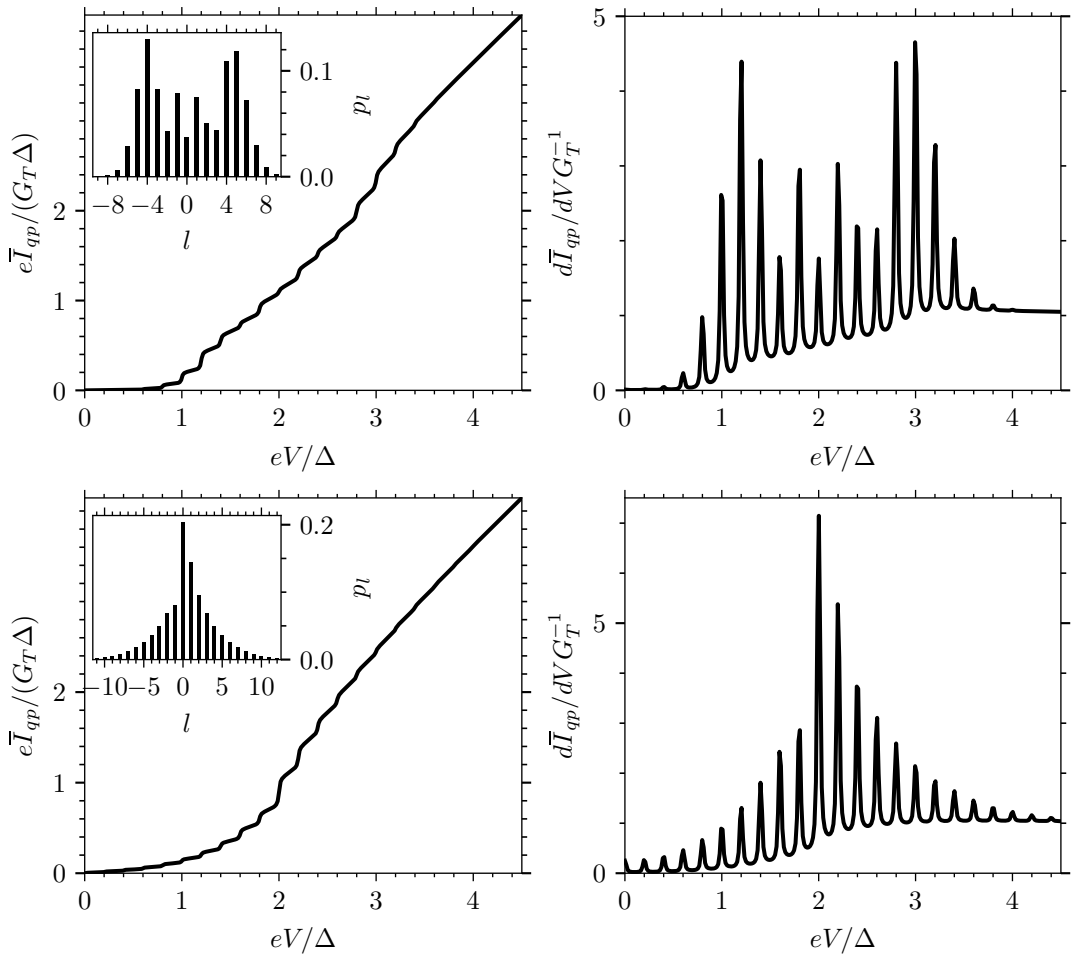

Figure V.12: *Quasiparticle current* $\overline{I}_{\mathrm{qp}}$ (left) and *differential conductance* $d\overline{I}_{\mathrm{qp}}/dV$ (right) for environments prepared in coherent ($|\alpha| = 4$,$\theta_3 \in \mathbb{R}$) and squeezed ($|\xi| = 2, \theta_4 \in \mathbb{R}$) state (upper and lower rows, respectively). Insets display the probability p_l of exchanging l energy quanta with the environment, while peaks in the conductance appear at $2\Delta + l\hbar\omega_0$, signaling the onset of the l-th exchange process. Parameters: $\hbar\omega_0 = 0.2\Delta$, $g = 1/2$, zero temperature, and broadening $\eta = 5 \times 10^{-3}$.

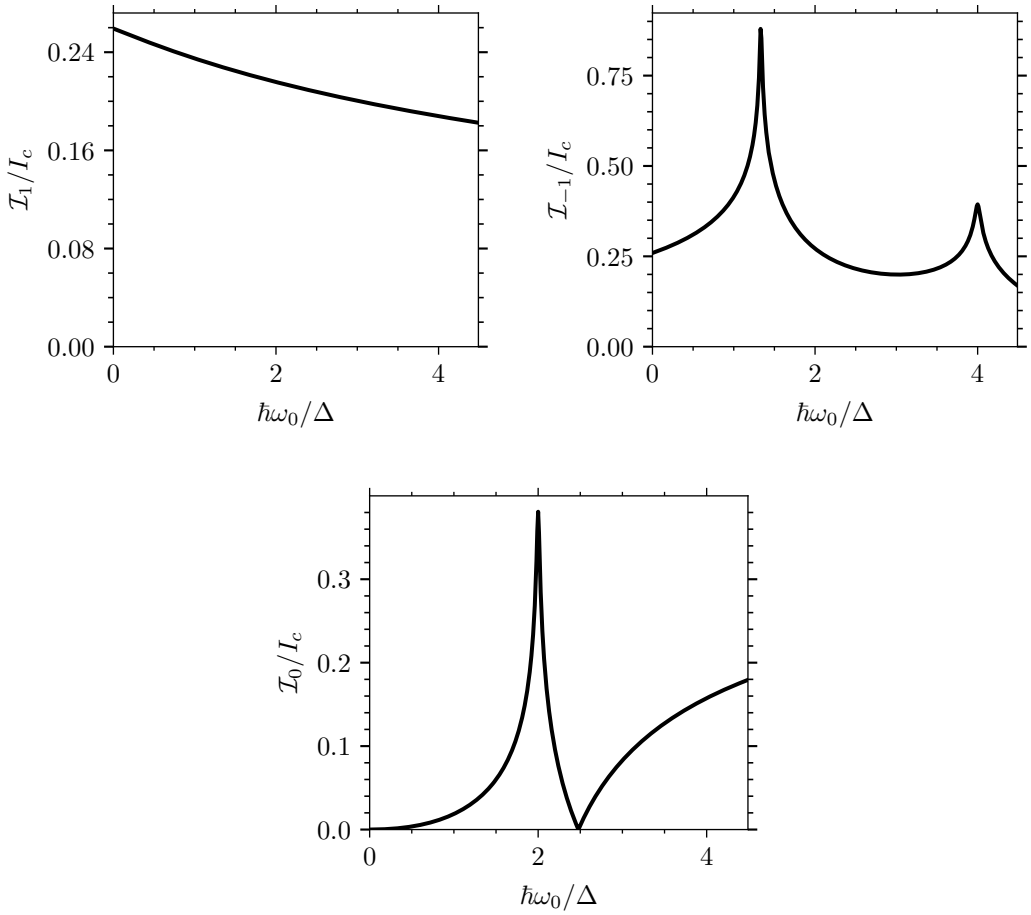

Figure V.13: *Cooper pair current amplitudes* $\mathcal{I}_j$ as a function of the frequency for a vacuum-single-photon Fock state. The amplitudes are normalized to the junction's critical current I_c in the absence of environmental coupling. The remaining amplitudes $\mathcal{I}_j$ with $j \neq -1, 0, 1$ vanish. The tunnel rate (Eq. (V.4.2b)) is evaluated at zero temperature with broadening $\eta = 5 \times 10^{-3}$. Parameters: $\theta_1 \in \mathbb{R}$, $g = 1/2$.

where

$$\mathcal{C}_{lj} = \sum_{n=0}^{\infty} \Theta(n+l)\Theta(n+j) A^{-}_{nn+l} A^{-}_{nn+j} \rho_{n+jn}. \tag{V.4.16b}$$

This expression reduces to a current-phase relation

$$\overline{I}_j^{\mathrm{cp}} = \mathcal{I}_j \sin(\phi_0 - \vartheta_j), \tag{V.4.16c}$$

with the amplitude $\mathcal{I}_j$ and phase shift ϑ_j depending on the environmental state, the coupling strength $\sqrt{g}$, and the resonator frequency ω_0. The j-th spike is sensitive to the j-th diagonal of the density matrix ρ_{n+jn}. A φ_0-junction cannot be realized in this case, as the modified supercurrent $\overline{I}_0^{\mathrm{cp}}$ depends only on the diagonal elements of the density matrix, which are real. This leads to $\vartheta_0 = 0$, implying a purely sinusoidal current-phase relation.
Figures V.13, V.14, V.15, and V.16 show the frequency dependence of the Cooper

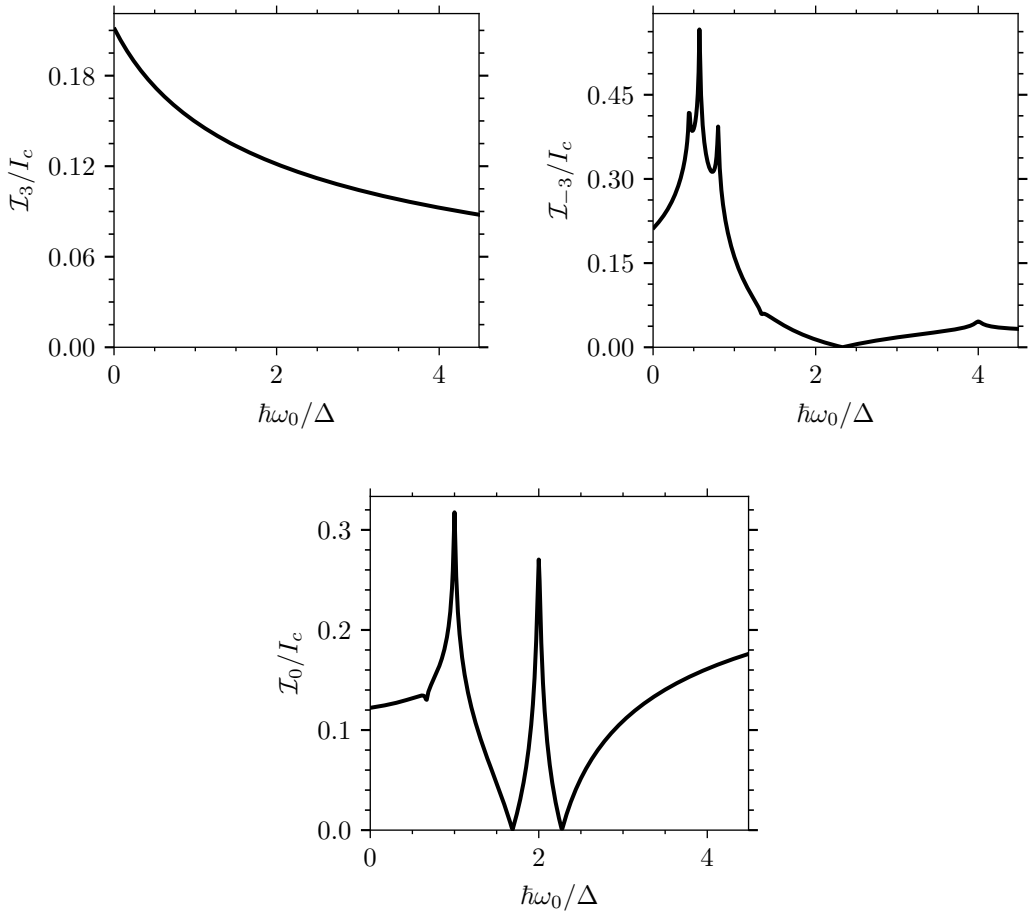

Figure V.14: *Cooper pair current amplitudes* $\mathcal{I}_j$ as a function of the frequency for a vacuum-three-photon Fock state. The remaining amplitudes $\mathcal{I}_j$ with $j \neq -3, 0, 3$ vanish. The amplitudes are normalized to the junction's critical current I_c in the absence of environmental coupling. The tunnel rate (Eq. (V.4.2b)) is evaluated at zero temperature with broadening $\eta = 5 \times 10^{-3}$. Parameters: $\theta_2 \in \mathbb{R}$, $g = 1/2$.

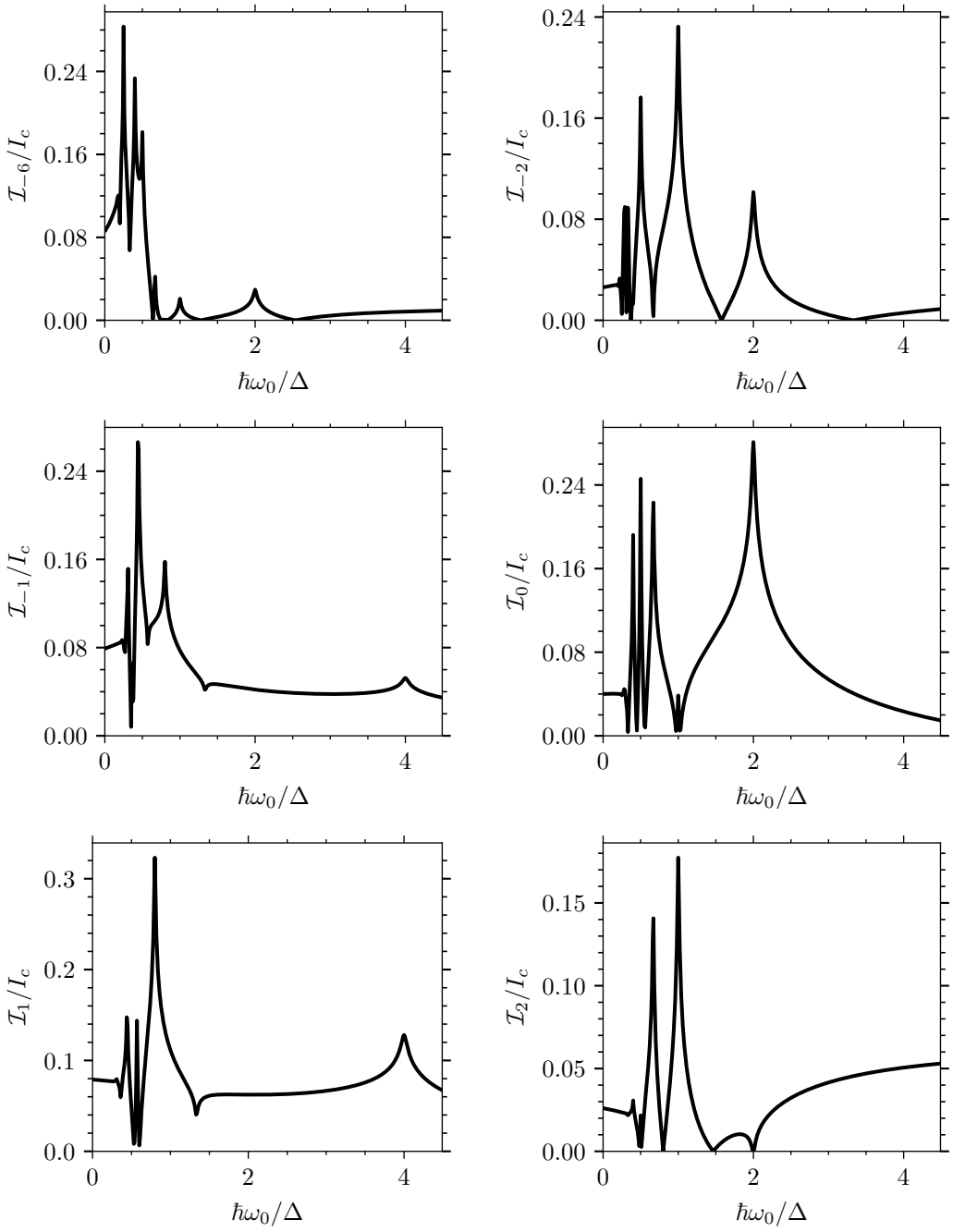

Figure V.15: *Selection of Cooper pair current amplitudes* $\mathcal{I}_j$ as a function of the frequency for a coherent state with $|\alpha| = 4$. The amplitudes are normalized to the junction's critical current I_c in the absence of environmental coupling. The tunnel rate (Eq. (V.4.2b)) is evaluated at zero temperature with broadening $\eta = 5\times10^{-3}$. Parameters: $\theta_3 \in \mathbb{R}$, $g = 1/2$.

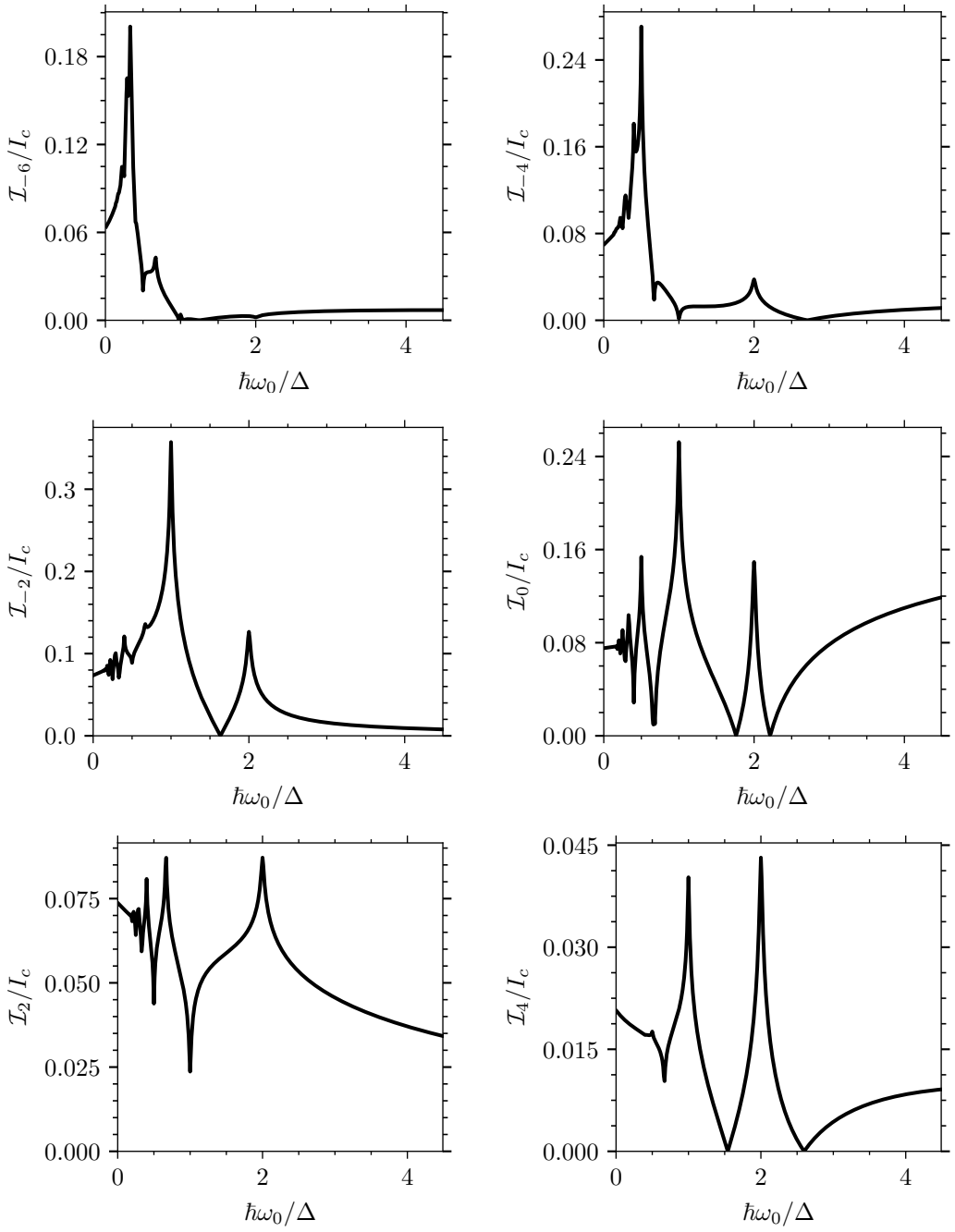

Figure V.16: *Selection of Cooper pair current amplitudes* $\mathcal{I}_j$ as a function of the frequency for a squeezed state with $|\xi| = 2$. The amplitudes are normalized to the junction's critical current I_c in the absence of environmental coupling. The tunnel rate (Eq. (V.4.2b)) is evaluated at zero temperature with broadening $\eta = 5\times10^{-3}$. Parameters: $\theta_3 \in \mathbb{R}$, $g = 1/2$.

pair current amplitudes. The frequency dependence exhibits sharp features at specific frequencies, which are related to Riedel peaks, which are singularities at $|eV| = 2\Delta$ in the ac Josephson current amplitude [17]. Here, the superconducting rate is related to the ac Josephson current amplitude through Eq. (V.4.8). In contrast, the rate is asymmetric in energy and exhibits a Riedel peak only at $E = -2\Delta$ (see Fig. V.21). Hence, the frequency dependence of the amplitude $\mathcal{I}_j$ consists of replicas of the Riedel peak at $\hbar\omega_0 = -4\Delta/(2l - j)$, weighted by the interference factors $\mathcal{C}_{lj}$. Kinks at $\mathcal{I}_j = 0$ indicate a sign change of the spike and arise from taking the absolute value, $\mathcal{I}_j = |\overline{I}_j^{cp}|$.
Figures V.17, V.18, V.15, and V.20 show the coupling dependence of the amplitudes $\mathcal{I}_j$ for $\hbar\omega_0 = 2 \times 10^{-2}\Delta$, and compares it to frequencies much smaller than the superconducting gap (gray dashed lines). Varying the coupling strength modifies the transition amplitudes and, consequently, the interference factor (V.4.16b). The interference factor satisfies the identity $\sum_{l,j} \mathcal{C}_{lj} = \langle e^{2\sqrt{g}(\hat{a}-\hat{a}^\dagger)} \rangle \equiv M[2\sqrt{g}]$, which corresponds to the moment-generating function of the quadrature $\hat{a} - \hat{a}^\dagger$ evaluated at $2\sqrt{g}$. As $\hbar\omega_0/\Delta \ll 1$, the total Cooper pair current reduces to an expression involving the moment-generating function, $\sum_j \overline{I}_j^{\mathrm{cp}} = I_c \,\mathrm{Im}(e^{i\phi_0} M[2\sqrt{g}])$, where $I_c = \Gamma_{\mathrm{S}}(0)$ is the critical current of the uncoupled junction. The individual amplitudes take the form $\lim_{\omega_0 \to 0} \mathcal{I}_j = I_c |\sum_n \Theta(n+j) \tilde{A}^-_{nn+j} \rho_{n+jn}|$, with a rescaled transition amplitude $\tilde{A}^-_{nn+j} = \langle n| \exp(2i\hat{\varphi}) |n+j\rangle$. Thus, the coupling dependence serves as a sensitive indicator of the environmental state.

V.4.4 Conclusion

We have shown that the coupling between a nonclassical electromagnetic environment and a Josephson tunnel junction gives rise to a very rich phenomenology in the current-voltage characteristics. In particular, we have illustrated how a superconducting tunnel junction can be used to completely characterize the nature of quantum states generated with circuit-QED setups, something that is not possible with normal tunnel junctions. Moreover, with the theoretical framework used here, the analysis of the transport characteristics can be straightforwardly extended to the study of higher-order cumulants like shot noise.

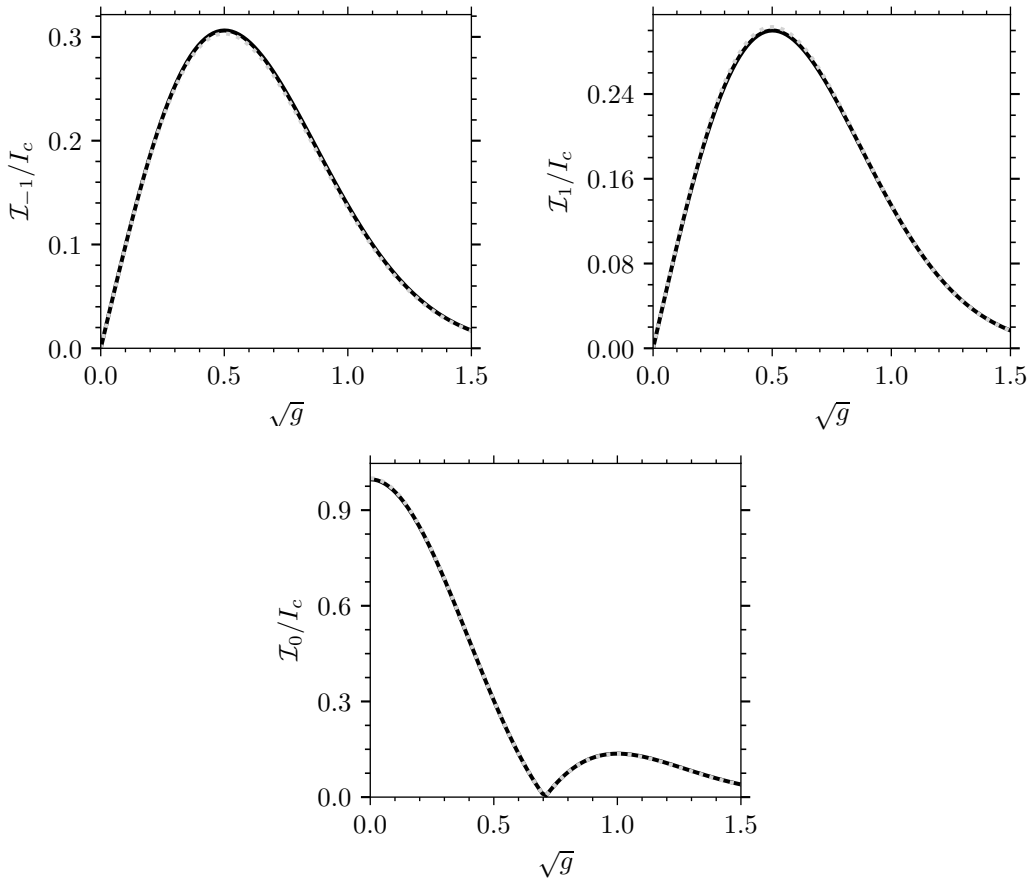

Figure V.17: *Cooper pair current amplitudes* $\mathcal{I}_j$ as a function of the frequency for a vacuum-single-photon Fock state. Each amplitude probes the j-th diagonal of the corresponding density matrix such that in this case the remaining amplitudes $\mathcal{I}_j$ with $j \neq -1, 0, 1$ vanish. The gray dashed lines indicate the low-frequency limit, which depends solely on the transition amplitudes $\tilde{A}^{-}_{nn+j}$ and the density matrix elements ρ_{n+jn}. The amplitudes are normalized to the junction's critical current I_c in the absence of environmental coupling. The tunnel rate (Eq. (V.4.2b)) is evaluated at zero temperature with broadening $\eta = 5 \times 10^{-3}$. Parameters: $\theta_1 \in \mathbb{R}$, $\hbar\omega_0 = 5 \times 10^{-2}\Delta$.

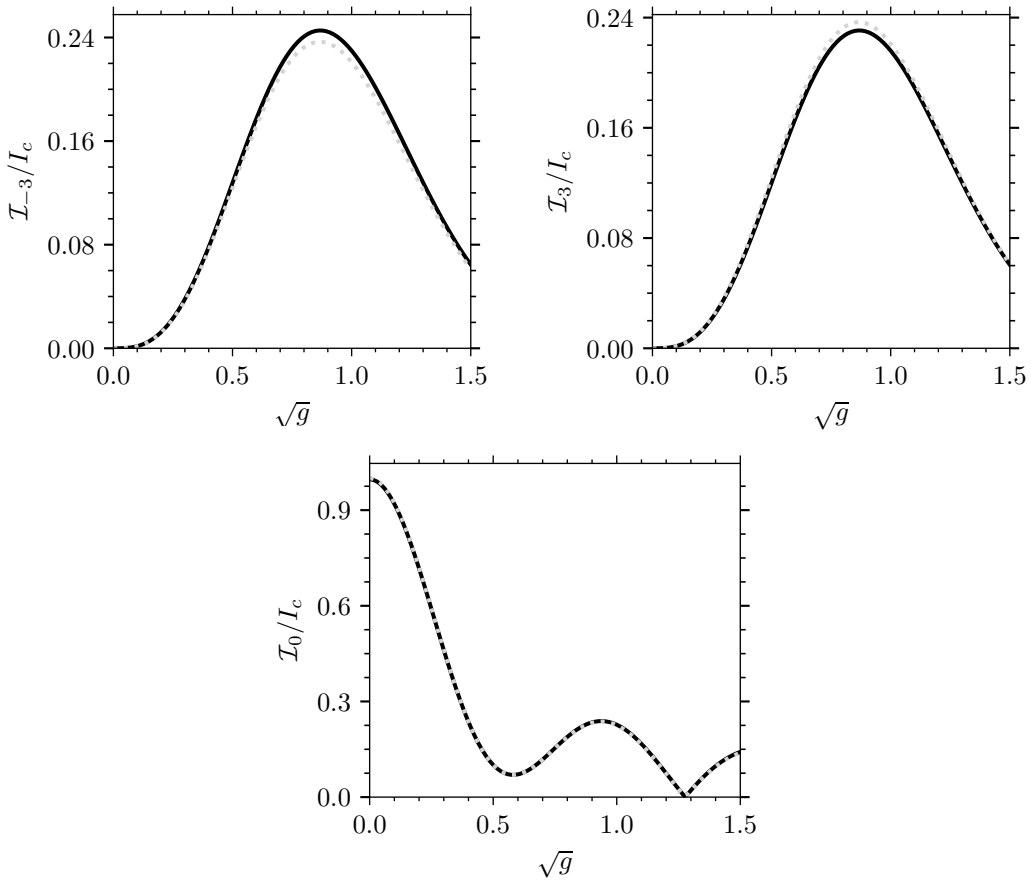

Figure V.18: *Cooper pair current amplitudes* $\mathcal{I}_j$ as a function of the frequency for a vacuum-three-photon Fock state. Each amplitude probes the j-th diagonal of the corresponding density matrix such that in this case the remaining amplitudes $\mathcal{I}_j$ with $j \neq -3, 0, 3$ vanish. Gray dashed lines mark the zero-frequency limit, which depends solely on the transition amplitudes $\tilde{A}^-_{nn+j}$ and the density matrix elements ρ_{n+jn}. The amplitudes are normalized to the junction's critical current I_c in the absence of environmental coupling. The tunnel rate (Eq. (V.4.2b)) is evaluated at zero temperature with broadening $\eta = 5 \times 10^{-3}$. Parameters: $\theta_2 \in \mathbb{R}$, $\hbar\omega_0 = 5 \times 10^{-2}\Delta$.

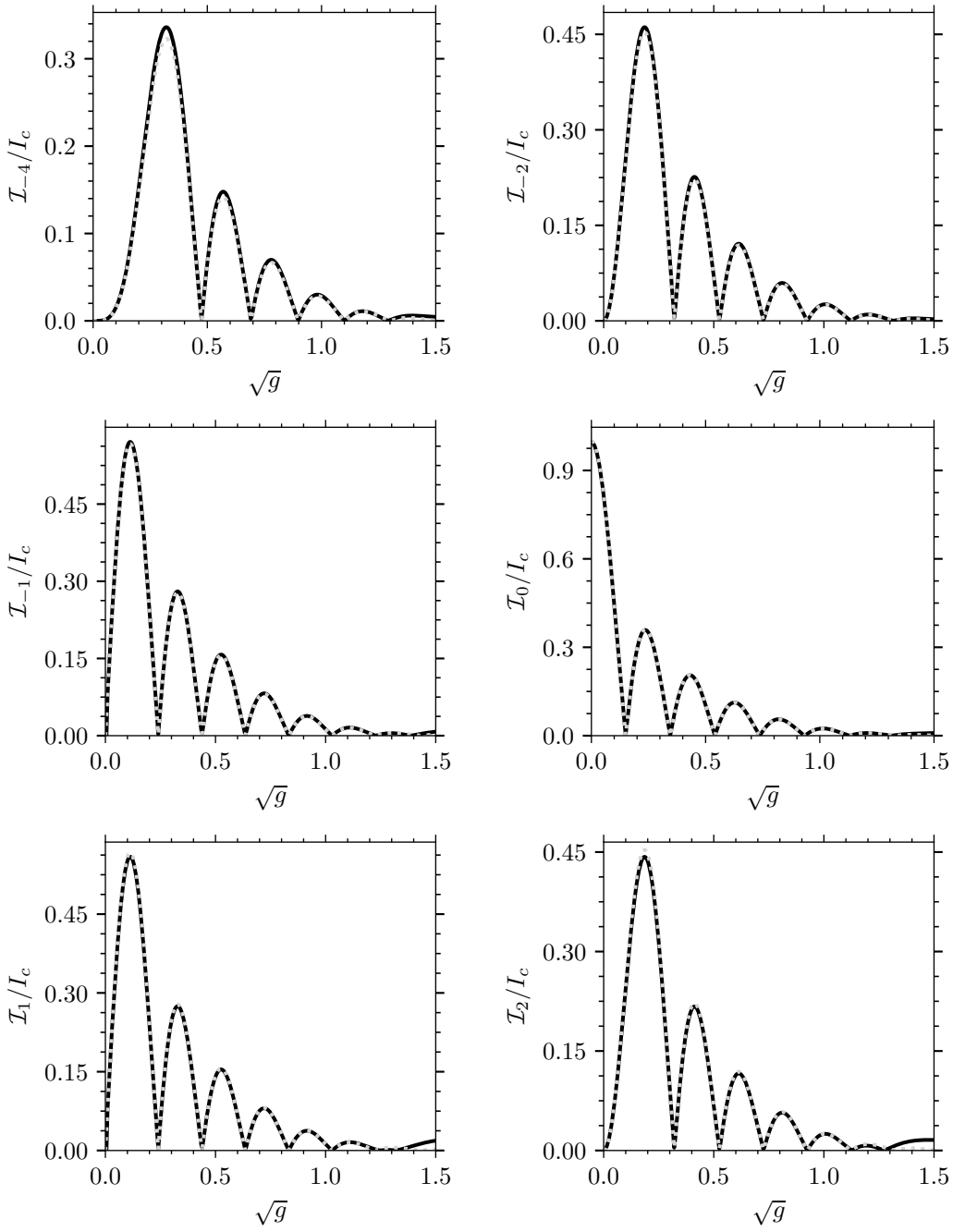

Figure V.19: *Selection of Cooper pair current amplitudes* $\mathcal{I}_j$ as a function of the frequency for a coherent state with $|\alpha| = 4$. Gray dashed lines mark the low-frequency limit, which depends solely on the transition amplitudes $\tilde{A}^-_{nn+j}$ and the density matrix elements ρ_{n+jn}. The amplitudes are normalized to the junction's critical current I_c in the absence of environmental coupling. The tunnel rate (Eq. (V.4.2b)) is evaluated at zero temperature with broadening $\eta = 5 \times 10^{-3}$. Parameters: $\theta_3 \in \mathbb{R}$, $\hbar\omega_0 = 5 \times 10^{-2}\Delta$.

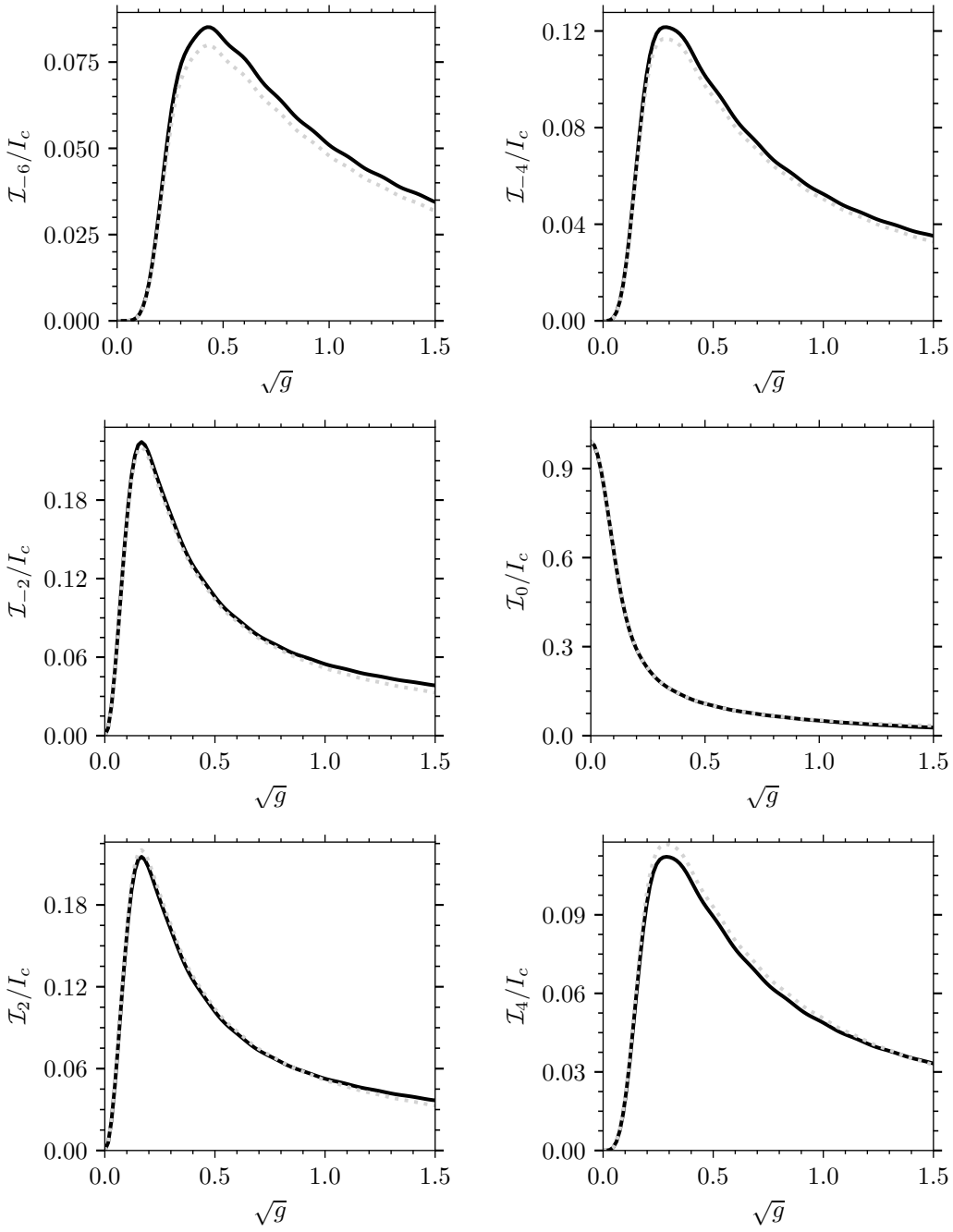

Figure V.20: *Selection of Cooper pair current amplitudes* $\mathcal{I}_j$ as a function of the frequency for a squeezed state with $|\xi| = 2$. Gray dashed lines mark the low-frequency limit, which depends solely on the transition amplitudes $\tilde{A}^-_{nn+j}$ and the density matrix elements ρ_{n+jn}. The amplitudes are normalized to the junction's critical current I_c in the absence of environmental coupling. The tunnel rate (Eq. (V.4.2b)) is evaluated at zero temperature with broadening $\eta = 5 \times 10^{-3}$. Parameters: $\theta_4 \in \mathbb{R}$, $\hbar\omega_0 = 5 \times 10^{-2}\Delta$.

V.5 Appendix

V.5.1 Hamiltonian

Our objective is to analyze the impact of an arbitrary electromagnetic environment on the current through a superconducting tunnel junction. In the absence of an environment, quantum transport in the mesoscopic conductor is governed by the Hamiltonian $\hat{H}_{\text{cond}}$ [46, 219, 232, 246]. We model the coupling between the junction and the environment via the interaction Hamiltonian

$$\hat{H}_{\text{int}} = \frac{\hbar}{e}\hat{\phi}(t)\hat{I}, \tag{V.5.1a}$$

where $\hat{I}$ denotes the junction's current operator, $\hat{\phi}(t)$ represents the phase operator associated with the electromagnetic environment, and e corresponds to the elementary charge. As a specific example, a constant phase operator corresponds to a static phase bias, which gives rise to the standard supercurrent. A classical, time-dependent voltage bias $V(t)$ induces a dynamic phase $\hat{\phi}(t) = \int_{t_s}^{t} dt' eV(t')/\hbar$, which describes the AC Josephson effect in the case of a constant voltage (see Eq. (V.5.27a)), and gives rise to Shapiro steps when the drive is harmonic. In general, the dynamics of the phase operator is captured by a Hamiltonian $\hat{H}_{\text{env}}$. Then, the total Hamiltonian is given by [244]

$$\hat{H} = \hat{H}_{\text{cond}} + \hat{H}_{\text{env}} + \hat{H}_{\text{int}}. \tag{V.5.1b}$$

V.5.2 Cumulant-Generating Functional

The statistics of the current $\hat{I}_{\text{H}}(t)$ is fully encoded in the partition functional [219, 232, 234, 246, 289]

$$\mathcal{Z}[\chi] = \left\langle \tilde{\mathcal{T}}[e^{\frac{i}{e}\int_{t_s}^{\infty} dt \chi^{-}(t)\hat{I}_{\text{H}}(t)}]\mathcal{T}[e^{-\frac{i}{e}\int_{t_s}^{\infty} dt \chi^{+}(t)\hat{I}_{\text{H}}(t)}]\right\rangle, \tag{V.5.2}$$

where $\mathcal{T}$ and $\tilde{\mathcal{T}}$ denote the time-ordering and anti-time-ordering operators, respectively. The functions $\chi^{+}(t)$ and $\chi^{-}(t)$ are the forward and backward components of the counting field defined on the Keldysh contour $C = C^{+} + C^{-}$, which runs from t_s to infinity and back to t_s. The subscript H indicates that the operator evolves in the Heisenberg picture, i.e., according to the Hamiltonian given in Eq. (V.5.1b). The average $\langle\cdot\rangle$ is taken with respect to the initial density matrix $\hat{\varrho} = \hat{\varrho}_{\text{cond}} \otimes \hat{\varrho}_{\text{env}}$, which is assumed to be separable. Taking the logarithm of the partition functional results in the cumulant-generating functional $\mathcal{S}[\chi] = \log(\mathcal{Z}[\chi])$. Time-ordered current correlations can be obtained by functionally differentiating the moment-generating functional with respect to the counting field (see Eqs.(IV.3.3)). The average current and the noise are obtained by

$$\langle \hat{I}_{\text{H}}(t)\rangle = ie\frac{\delta \mathcal{S}[\chi]}{\delta \chi^{q}(t)}\bigg|_{\chi=0} \tag{V.5.3a}$$

$$\langle\{\Delta\hat{I}_{\text{H}}(t), \Delta\hat{I}_{\text{H}}(t')\}\rangle = -e^2\frac{\delta^2 \mathcal{S}[\chi]}{\delta\chi^{q}(t)\delta\chi^{q}(t')}\bigg|_{\chi=0}, \tag{V.5.3b}$$

with the quantum field $\chi^q(t) = \chi^+(t) - \chi^-(t)$, $\{\cdot,\cdot\}$ the anti-commutator and $\Delta\hat{I}_{\mathrm{H}}(t) = \hat{I}_{\mathrm{H}}(t) - \langle\hat{I}_{\mathrm{H}}(t)\rangle$ the difference to the mean [15, 233].

The central idea is to express the partition functional (V.5.2) in terms of the known partition functional for an isolated tunnel junction [246, 289]. Accordingly, we transition to the interaction picture to decouple the dynamics of the junction and the environment. An operator $\hat{O}_{\mathrm{H}}(t)$ in the Heisenberg picture is related to the operator in the interaction picture $\hat{O}_{\mathrm{I}}(t)$ by

$$\hat{O}_{\mathrm{H}}(t) = \hat{U}^{\dagger}_{\mathrm{int}}(t,t_{\mathrm{s}})\hat{O}_{\mathrm{I}}(t)\hat{U}_{\mathrm{int}}(t,t_{\mathrm{s}}), \tag{V.5.4a}$$

where

$$\hat{U}_{\mathrm{int}}(t,t_{\mathrm{s}}) = \mathscr{T}\exp\left(-\frac{i}{\hbar}\int_{t_{\mathrm{s}}}^{t}\hat{H}^{\mathrm{I}}_{\mathrm{int}}(t')dt'\right), \tag{V.5.4b}$$

is the interaction-picture evolution operator, and

$$\hat{H}^{\mathrm{I}}_{\mathrm{int}}(t) = \frac{\hbar}{e}\hat{\phi}_I(t)\hat{I}_I(t), \tag{V.5.4c}$$

with the subscript I indicating operators in the interaction picture. The operator $\hat{\phi}_{\mathrm{I}}(t)$ evolves under the Hamiltonian $\hat{H}_{\mathrm{env}}$, while $\hat{I}_{\mathrm{I}}(t)$ evolves under $\hat{H}_{\mathrm{cond}}$. To simplify the notation, we promote the time variable to the full Keldysh contour C, and introduce the contour-ordering operator $\mathscr{T}_{\mathrm{C}}$, the contour evolution operator $\hat{U}^{\mathrm{C}}_{\mathrm{int}} = \mathscr{T}_{\mathrm{C}}\exp(-\frac{i}{\hbar}\int_{\mathrm{C}}dt\hat{H}^{\mathrm{I}}_{\mathrm{int}}(t))$, and a unified counting field $\chi(t)$, which equals $\chi^+(t)$ on the forward branch and $\chi^-(t)$ on the backward branch of the contour. The partition functional transforms to

$$\begin{aligned}
\mathcal{Z}[\chi] =& \sum_{n=0}^{\infty}\frac{(-i)^n}{n!}\int_{\mathrm{C}}dt_1\ldots\int_{\mathrm{C}}dt_n\langle\mathscr{T}_{\mathrm{C}}[\chi(t_1)\hat{I}_{\mathrm{H}}(t_1)\ldots\chi(t_n)\hat{I}_{\mathrm{H}}(t_n)]\rangle\\
=&1+\sum_{n=1}^{\infty}\frac{(-i)^n}{n!}\int_{\mathrm{C}}dt_1\ldots\int_{\mathrm{C}}dt_n\langle\mathscr{T}_{\mathrm{C}}[\hat{U}_{\mathrm{int}}(t_{\mathrm{s}},t_1)\chi(t_1)\hat{I}_{\mathrm{I}}(t_1)\hat{U}_{\mathrm{int}}(t_1,t_2)\ldots\\
&\times\hat{U}_{\mathrm{int}}(t_{n-1},t_n)\chi(t_n)\hat{I}_{\mathrm{I}}(t_n)\hat{U}_{\mathrm{int}}(t_n,t_{\mathrm{s}})]\rangle\\
=&1+\sum_{n=1}^{\infty}\frac{(-i)^n}{n!}\int_{\mathrm{C}}dt_1\ldots\int_{\mathrm{C}}dt_n\langle\mathscr{T}_{\mathrm{C}}[\hat{U}^{\mathrm{C}}_{\mathrm{int}}\chi(t_1)\hat{I}_{\mathrm{I}}(t_1)\ldots\chi(t_n)\hat{I}_{\mathrm{I}}(t_n)]\rangle+\langle\mathscr{T}_{\mathrm{C}}\hat{U}^{\mathrm{C}}_{\mathrm{int}}\rangle\\
&-\langle\mathscr{T}_{\mathrm{C}}\hat{U}^{\mathrm{C}}_{\mathrm{int}}\rangle\\
=&1+\left\langle\mathscr{T}_{\mathrm{C}}\exp\left(-\frac{i}{e}\int_{\mathrm{C}}[\chi(t)+\hat{\phi}_{\mathrm{I}}(t)]\hat{I}_{\mathrm{I}}(t)dt\right)\right\rangle-\langle\mathscr{T}_{\mathrm{C}}\hat{U}^{\mathrm{C}}_{\mathrm{int}}\rangle\\
=&1+\sum_{m=0}^{\infty}\frac{g^m}{m!}\int_{\mathrm{C}}dt_1\ldots\int_{\mathrm{C}}dt_m\left[\frac{\delta^m\mathcal{Z}_0[\chi]}{\delta\chi(t_1)\ldots\delta\chi(t_m)}-\frac{\delta^m\mathcal{Z}_0[\chi]}{\delta\chi(t_1)\ldots\delta\chi(t_m)}\bigg|_{\chi=0}\right]\\
&\times\left\langle\mathscr{T}_{\mathrm{C}}[\hat{\phi}_{\mathrm{I}}(t_1)\ldots\hat{\phi}_{\mathrm{I}}(t_m)]\right\rangle_{\mathrm{env}},
\end{aligned} \tag{V.5.5}$$

with the partition functional $\mathcal{Z}_0[\chi]$ of the isolated tunnel junction, and $\langle\cdot\rangle_{\text{env}}$ the average with respect to $\hat{\rho}_{\text{env}}$. The final line is obtained by expanding $\hat{U}^{\text{C}}_{\text{int}}$ and exploitation of the defining property of the partition functional. The term $\langle\mathscr{T}_{\text{C}}\hat{U}^{\text{C}}_{\text{int}}\rangle$ ensures proper normalization of the partition functional, such that $\mathcal{Z}[0] = 1$. The partition functional formally resembles a functional Taylor expansion of $1 + \langle\mathscr{T}_{\text{C}}[\mathcal{Z}_0[\chi+\delta\chi] - \mathcal{Z}_0[\delta\chi]]\rangle_{\text{env}}$, with a displacement $\delta\chi(t) = \hat{\phi}_{\text{I}}(t)$.

The cumulant-generating functional (or Keldysh action) for a general multiterminal and time-dependent scatterer was derived by Snyman and Nazarov [246, 248]. In a two-terminal device with an energy-independent scattering matrix, the cumulant-generating functional is given by (see Eq. (IV.3.16))

$$\mathcal{S}[\chi] = \frac{1}{4}\sum_n \operatorname{Tr}\ln\left[1 + \frac{\mathcal{T}_n}{4}\left(\{\check{G}_1(\chi)\overset{\otimes}{,}\check{G}_2\} - 2\right)\right], \tag{V.5.6}$$

where $\check{G}_1(\chi)$ is the counting-field-dependent Green's function of terminal 1, and $\check{G}_2$ the corresponding Green's function of terminal 2, and $\mathcal{T}_n$ are transmission eigenvalues [231, 246, 248, 289]. The Green's functions are treated as operators in time, Keldysh, Nambu, spin, and channel space, where $\log()$ denotes the operator logarithm, and Tr represents the trace over all these degrees of freedom. Operator multiplication involves integration over time variable, while the remaining spaces (Keldysh, Nambu, spin, and channel) entail summation over discrete indices. For example, $[\check{G}_1\check{G}_2](t,t'') \equiv \int_{\text{C}} dt' \check{G}_1(t,t')\check{G}_2(t',t'')$. Note that the the Green's functions $\check{G}_{1,2}$ are defined with a third Pauli matrix in Keldysh space to ensure normalization $\check{G}_{1,2}\check{G}_{1,2} = \check{1}$, but therefore the Keldysh $-+/--$ components correspond to the negative of the greater/anti-time ordered Green's function. The counting-field is incorporated in terminal 1 by [232, 234, 289]

$$\check{G}_1(\chi,t,t') = e^{-i\chi(t)\hat{\sigma}_3}\check{G}_1(t,t')e^{i\chi(t')\hat{\sigma}_3}, \tag{V.5.7}$$

with $\hat{\sigma}_3$ the third Pauli-matrix in Nambu space.

We calculate the CGF $\mathcal{S}[\chi]$ in the tunnel limit and therefore retain only terms that are first-order in the tunnel conductance $G_T = e^2\sum_n \mathcal{T}_n/(\pi\hbar)$. In principle, higher-order terms can be obtained by expanding the CGF to the desired order in the tunnel conductance G_T, although the expressions become increasingly cumbersome. After tracing out the Keldysh and Nambu structure, we obtain

$$\begin{aligned}\mathcal{S}[\chi] =& \frac{G_T\pi\hbar}{8e^2}\iint_{t_{\text{s}}}^{\infty} dtdt' \sum_{\substack{\nu,\nu'=\pm\\ \mu,\mu'=\pm}} (e^{-i\mu\chi^{\nu}(t)+i\mu'\chi^{\nu'}(t')} - 1)\\ &\times G^{\nu\nu'\mu\mu'}_{\text{env}}(t,t')\operatorname{Tr}\{\tilde{G}_1^{\nu\nu'\mu\mu'}(t,t')\tilde{G}_2^{\nu'\nu\mu'\mu}(t',t)\},\end{aligned} \tag{V.5.8a}$$

with $\tilde{G}_j^{\nu\nu'\mu\mu'}, j = 1,2$ a matrix in spin space, and $\operatorname{Tr}\{\cdot\}$ the trace in spin space. The indices ν,ν' refer to the Keldysh structure, with $\nu = +$ labeling the forward contour and $\nu = -$ the backward contour. The indices μ,μ' correspond to the Nambu

structure, where $\mu = +$ denotes the particle component and $\mu = -$ the hole component. The Green's functions $\check{G}_j$ are assumed to have a trivial spin structure, corresponding to the identity matrix. The environmental Green's functions are

$$G_{\text{env}}^{++\mu\mu'}(t,t') = \langle \mathscr{T} e^{-i\mu\hat{\phi}_{\text{I}}(t)} e^{i\mu'\hat{\phi}_{\text{I}}(t')} \rangle_{\text{env}} \tag{V.5.8b}$$

$$G_{\text{env}}^{--\mu\mu'}(t,t') = \langle \tilde{\mathscr{T}} e^{-i\mu\hat{\phi}_{\text{I}}(t)} e^{i\mu'\hat{\phi}_{\text{I}}(t')} \rangle_{\text{env}} \tag{V.5.8c}$$

$$G_{\text{env}}^{+-\mu\mu'}(t,t') = \langle e^{i\mu'\hat{\phi}_{\text{I}}(t')} e^{-i\mu\hat{\phi}_{\text{I}}(t)} \rangle_{\text{env}} \tag{V.5.8d}$$

$$G_{\text{env}}^{-+\mu\mu'}(t,t') = \langle e^{-i\mu\hat{\phi}_{\text{I}}(t)} e^{i\mu'\hat{\phi}_{\text{I}}(t')} \rangle_{\text{env}}. \tag{V.5.8e}$$

V.5.3 Full Counting Statistics

The full counting statistics (FCS) is obtained using the fields $\chi^{\pm}(t) = \pm(1 - \Theta(t - t_{\text{e}}))\chi/2$, where χ is the counting variable and the measurement interval runs from t_{s} to t_{e}. The cumulant generating function, derived from Eq. (V.5.8a), is given by

$$\mathcal{S}(\chi) = (e^{-i\chi} - 1)N_{21} + (e^{i\chi} - 1)N_{12}. \tag{V.5.9}$$

For a normal-metal junction, N_{21} and N_{12} represent the number of charges transferred from terminal 1 to terminal 2, and from terminal 2 to terminal 1, respectively. The charge transfer statistics follow a generalized Poisson distribution, as expected for transport through a tunnel junction [232]. Accounting for higher-order terms in the conductance G_T causes deviations from Poissonian statistics, whereas in the absence of a quantum environment, the resulting full counting statistics is multinomial [43, 44, 231, 233, 235, 290, 291]. A superconducting tunnel junction can exhibit negative values for N_{21} and N_{12}, thereby undermining the interpretation of the FCS as a probability distribution. However, the FCS is observable when the dynamics of an idealized measurement device is taken into account [231]. Quasiparticles and Cooper pairs contribute to charge transfer such that

$$N_{jk} = N_{jk}^{\text{qp}} + N_{jk}^{\text{cp}}, \tag{V.5.10a}$$

with the individual contributions

$$N_{21}^{\text{qp}} = \frac{1}{e}\int_{-\infty}^{\infty} dE \sum_{\substack{\nu,\nu'=\pm \\ \nu\neq\nu'}} \overline{G}_{\text{env}}^{\nu\nu'\nu\nu}(E)\Gamma^{\nu\nu'\nu\nu}(E) \tag{V.5.10b}$$

$$N_{21}^{\text{cp}} = \frac{1}{e}\int_{-\infty}^{\infty} dE \sum_{\substack{\nu,\nu'=\pm \\ \nu\neq\nu'}} \overline{G}_{\text{env}}^{\nu\nu\nu\nu'}(E)\Gamma^{\nu\nu\nu\nu'}(E) \tag{V.5.10c}$$

$$N_{12}^{\text{qp}} = \frac{1}{e}\int_{-\infty}^{\infty} dE \sum_{\substack{\nu,\nu'=\pm \\ \nu\neq\nu'}} \overline{G}_{\text{env}}^{\nu'\nu\nu\nu}(E)\Gamma^{\nu'\nu\nu\nu}(E) \tag{V.5.10d}$$

$$N_{12}^{\text{cp}} = \frac{1}{e}\int_{-\infty}^{\infty} dE \sum_{\substack{\nu,\nu'=\pm \\ \nu\neq\nu'}} \overline{G}_{\text{env}}^{\nu\nu\nu'\nu}(E)\Gamma^{\nu\nu\nu'\nu}(E), \tag{V.5.10e}$$

where

$$\overline{G}_{\text{env}}^{\nu\nu'\mu\mu'}(E) = \iint_{t_\text{s}}^{t_\text{e}} \frac{dtdt'}{4\pi\hbar} e^{iE(t-t')/\hbar} G_{\text{env}}^{\nu\nu'\mu\mu'}(t,t') \tag{V.5.10f}$$

is the time-averaged environmental Green's function. In the absence of an electromagnetic environment, the tunneling rates are

$$\Gamma^{\nu\nu'\mu\mu'}(E) = \frac{G_T}{8e} \int_{-\infty}^{\infty} d\epsilon \, \text{Tr}\{\tilde{G}_1^{\nu\nu'\mu\mu'}(\epsilon - E)\tilde{G}_2^{\nu'\nu\mu'\mu}(\epsilon)\}, \tag{V.5.10g}$$

with the energy domain representation $G_j^{\nu\nu'\mu\mu'}(E) = \int_{-\infty}^{\infty} e^{iE\tau/\hbar} d\tau G_j^{\nu\nu'\mu\mu'}(\tau)$, where $\tau = t - t'$. Here, the terminals are assumed to be in thermal equilibrium, which implies time-translation invariance of the Green's functions, i.e., $G_j^{\nu\nu'\mu\mu'}(t,t') = G_j^{\nu\nu'\mu\mu'}(t-t')$. The Green's function in Keldysh space takes the form:

$$\check{G}_j = \begin{pmatrix} \hat{G}_j^{++} & \hat{G}_j^{+-} \\ \hat{G}_j^{-+} & \hat{G}_j^{--} \end{pmatrix} = \frac{1}{2} \begin{pmatrix} \hat{G}_j^a + \hat{G}_j^r + \hat{G}_j^k & \hat{G}_j^a - \hat{G}_j^r + \hat{G}_j^k \\ \hat{G}_j^a - \hat{G}_j^r - \hat{G}_j^k & \hat{G}_j^a + \hat{G}_j^r - \hat{G}_j^k \end{pmatrix}, \tag{V.5.11}$$

with the retarded/advanced $\hat{G}_j^{r/a}(E)$ component, and the Keldysh component $\hat{G}_j^k = (\hat{G}_j^r(E) - \hat{G}_j^a(E))(1 - 2f_j(E))$, where $f_j(E) = (1 + e^{(E-\tilde{\mu}_j)/(k_\text{B}T_j)})^{-1}$ is the Fermi-Dirac distribution. The Fermi-Dirac distribution is determined by the temperature T_j, and the chemical potential $\tilde{\mu}_j$ of the corresponding terminal.
A pure voltage bias V results in the environmental Green's functions

$$\overline{G}_{\text{env}}^{\nu\nu'\mu\mu'}(E) = \frac{t_0 \delta(E - \mu' eV) e^{i\phi_0(\mu'-\mu)/2}}{2} \cdot \begin{cases} 1 & \mu = \mu' \\ \frac{\exp(i\mu'\omega_J t_0) - 1}{i\mu'\omega_J t_0} & \mu \neq \mu' \end{cases}, \tag{V.5.12}$$

with Josephson frequency $\omega_J = 2eV/\hbar$, the superconducting phase difference ϕ_0, and the length of the measurement interval $t_0 = t_\text{e} - t_\text{s}$. Here, we assume that the measurement interval is large, such that $\omega_J t_0 \gg 1$. The components N_{jk}^{cp} oscillate at ω_J, reflecting the ac Josephson effect. As expected for transport under voltage bias [232], the number of transferred quasiparticles is given by the tunneling rates times the measurement interval.

V.5.4 Tunnel Current

The tunnel current $I(t) = \langle \hat{I}_\text{H}(t) \rangle$ is obtained by functionally differentiating the CGF with respect to the counting field (see Eq. (V.5.3a)). This yields the expression

$$I(t) = \sum_{\substack{\nu \neq \nu' = \pm \\ \mu\mu' = \pm}} \int_{-\infty}^{\infty} dE P^{\nu\nu'\mu\mu'}(t,E) \Gamma^{\nu\nu'\mu\mu'}(E), \tag{V.5.13}$$

with the generalized P-function

$$P^{\nu\nu'\mu\mu'}(t,E) = \int_0^{t-t_\text{s}} \frac{d\tau}{2\pi\hbar} \left(\mu\nu e^{iE\tau/\hbar} G_{\text{env}}^{\nu\nu'\mu\mu'}(t, t-\tau) - \mu'\nu' e^{-iE\tau/\hbar} G_{\text{env}}^{\nu\nu'\mu\mu'}(t-\tau, t) \right). \tag{V.5.14}$$

We employed the identities relating time-ordered and anti-time-ordered Green's functions to the lesser and greater components in order to eliminate the $++/--$ contributions.

V.5.5 Normal Conducting Tunnel Junction

In this section, we examine a tunnel junction between two normal conductors interacting with an environment. The retarded/advanced Green's function of a normal lead is

$$\hat{G}^{r/a}(E) = \pm\hat{\tau}_0 \otimes \hat{\sigma}_3, \tag{V.5.15}$$

with with $\hat{\tau}_0$ the zeroth Pauli matrix in spin space, and $\hat{\sigma}_3$ the third Pauli matrix in Nambu space. The rates $\Gamma^{\nu\nu'\mu\mu'}$ with $\mu \neq \mu'$ vanish. The remaining nonzero rates simplify to $\Gamma^{\nu\nu'\mu\mu}(E) = \Gamma(\nu' E)$, for $\nu \neq \nu'$, and $\Gamma(E)$ represents the tunneling rate of the uncoupled junction:

$$\Gamma(E) = \frac{G_T}{e}\int_{-\infty}^{\infty} d\epsilon[1 - f(\epsilon - E)]f(\epsilon) = \frac{G_T}{e}\frac{E}{1 - e^{-E/(k_B T)}}, \tag{V.5.16}$$

assuming equal temperatures $T_1 = T_2 = T$. $f(E)$ denotes the Fermi function evaluated at zero chemical potential. The average current reduces to

$$I(t) = \sum_{\nu=\pm} \nu \int_{-\infty}^{\infty} dE P^{\nu}(t, E)\Gamma(E), \tag{V.5.17}$$

with the P-functions

$$P^{\nu}(t, E) = \int_0^{\infty} \frac{d\tau}{\pi\hbar} \mathrm{Re}\left(e^{iE\tau/\hbar}\langle e^{i\nu\hat{\phi}_{\mathrm{I}}(t)} e^{-i\nu\hat{\phi}_{\mathrm{I}}(t-\tau)}\rangle\right), \tag{V.5.18}$$

where, for brevity, $\langle\cdot\rangle \equiv \langle\cdot\rangle_{\mathrm{env}}$. We consider the perturbation to have been switched on in the distant past, and took the limit $t_s \to -\infty$. Therefore, we recover the standard expressions of dynamical Coulomb blockade physics (DCB) [46, 287], and the formula derived in [47] for a non-equilibrium environment.

V.5.6 Superconducting Tunnel Junction

We turn to the case of a superconducting tunnel junction coupled to an environment, examining how the environment impacts both the quasi-particle and Cooper pair tunneling currents. The superconducting Green's function acquires a nontrivial matrix structure in Nambu space, reflecting the intrinsic particle–hole coherence characteristic of the superconducting state. The retarded and advanced Green's functions are given by

$$\hat{G}_j^{r/a} = \tilde{\mathbb{1}} \otimes \frac{-i}{\sqrt{\Delta_j^2 - (E \pm i\eta)^2}} \begin{pmatrix} (E \pm i\eta) & \Delta_j e^{i\phi_j} \\ -\Delta_j e^{-i\phi_j} & -(E \pm i\eta) \end{pmatrix}, \tag{V.5.19}$$

with $\tilde{\mathbb{1}}$ the identity in spin space, Δ_j the superconducting gap, ϕ_j the superconducting phase, and the regularisation parameter η, which tends to zero, but can

be kept finite to describe inelastic processes, which broaden the electronic states. The superconducting phases ϕ_j are set to zero in the following, as they are already accounted for in $\hat{\phi}_{\mathrm{I}}(t)$. The normalization condition requires $\hat{G}^{r/a}\hat{G}^{r/a} = \hat{\mathbb{1}}$, where $\hat{\mathbb{1}}$ is the identity in spin-Nambu space.
The quasi-particle current is associated with the diagonal components in Nambu space, corresponding to terms with $\mu = \mu'$. The corresponding rates are $\Gamma^{\nu\nu'\mu\mu}(E)$- $= \Gamma_{\mathrm{qp}}(\nu' E)$, $\nu \neq \nu'$, with

$$\Gamma_{\mathrm{qp}}(E) = \frac{G_T}{e}\int_{-\infty}^{\infty} d\epsilon \varrho_1(\epsilon - E)\varrho_2(\epsilon)[1 - f(\epsilon - E)]f(\epsilon), \tag{V.5.20a}$$

and the superconducting density of states

$$\varrho_j(E) = \mathrm{Re}\left(\frac{-i(E + i\eta)}{\sqrt{\Delta_j^2 - (E + i\eta)^2}}\right). \tag{V.5.20b}$$

The resulting quasi-particle current,

$$I(t) = \sum_{\nu=\pm} \nu \int_{-\infty}^{\infty} dE P^{\nu}(t, E)\Gamma_{\mathrm{qp}}(E), \tag{V.5.21}$$

exhibits the same structure as the electron current discussed in the previously and involves the same P-function defined in Eq. (V.4.3a). The only difference lies in the bare quasi-particle tunneling rate, which additionally incorporates the superconducting densities of states.
The Cooper pair current originates from the anomalous (off-diagonal) components of the Green's functions, corresponding to $\mu \neq \mu'$, and gives rise to transition rates of the form $\Gamma^{\nu\nu'\mu\mu'}(E) = -\Gamma_{\mathrm{cp}}(\nu' E)$, for $\nu \neq \nu'$ and $\mu \neq \mu'$. The Cooper pair tunneling rate $\Gamma_{\mathrm{cp}}(E)$ is given by

$$\Gamma_{\mathrm{cp}}(E) = \frac{G_T}{e}\int_{-\infty}^{\infty} d\epsilon \varsigma_1(\epsilon - E)\varsigma_2(\epsilon)(1 - f(\epsilon - E))f(\epsilon), \tag{V.5.22a}$$

with the pair densities

$$\varsigma_j(E) = \mathrm{Re}\left(\frac{i\Delta_j}{\sqrt{\Delta_j^2 - (E + i\eta)^2}}\right). \tag{V.5.22b}$$

Cooper pair tunneling leads to the contribution

$$I_{\mathrm{cp}}(t) = \sum_{\nu=\pm} \nu \int_{-\infty}^{\infty} dE C^{\nu}(t, E)\Gamma_{\mathrm{cp}}(E), \tag{V.5.23}$$

with a correlation function

$$C^{\nu}(t, E) = \int_0^{\infty} \frac{d\tau}{\pi\hbar}\,\mathrm{Re}\left(e^{iE\tau/\hbar}\langle e^{-i\nu\hat{\phi}_{\mathrm{I}}(t)}e^{-i\nu\hat{\phi}_{\mathrm{I}}(t-\tau)}\rangle\right). \tag{V.5.24}$$

A dc voltage V and a superconducting phase shift applied additionally to the tunnel junction leads to a dynamical phase $\varphi_{dc}(t) = eVt/\hbar + \phi_0/2$, and can be incorporated by $\hat{\phi}_{\mathrm{I}}(t) = \hat{\varphi}_{\mathrm{I}}(t) + \varphi_{dc}(t)$, where $\hat{\varphi}$ is the phase operator of the environment. Thus, the P- and C-function are

$$P^{\nu}(t,E) = \int_0^{\infty} \frac{d\tau}{\pi\hbar} \mathrm{Re}\left(e^{i(E+\nu eV)\tau/\hbar} \langle e^{i\nu\hat{\varphi}_{\mathrm{I}}(t)} e^{-i\nu\hat{\varphi}_{\mathrm{I}}(t-\tau)} \rangle \right) \tag{V.5.25a}$$

$$C^{\nu}(t,E) = \int_0^{\infty} \frac{d\tau}{\pi\hbar} \mathrm{Re}\left(e^{i(E+\nu eV)\tau/\hbar} e^{-i\nu\phi_0 - 2i\nu eVt/\hbar} \langle e^{-i\nu\hat{\varphi}_{\mathrm{I}}(t)} e^{-i\nu\hat{\varphi}_{\mathrm{I}}(t-\tau)} \rangle \right). \tag{V.5.25b}$$

To the best of our knowledge, the C-function has not been discussed in the literature in this level of generality and constitutes the novel part of our work.

V.5.7 AC-Josephson Effect and Shapiro Steps

A constant voltage bias represents the most basic example of an electromagnetic environment. The C-function reduces to

$$C^{\nu}(t,E) = \cos(\phi_0 + 2eVt/\hbar)\delta(E+\nu eV) + \nu \sin(\phi_0 + 2eVt/\hbar)\frac{1}{\pi}\mathrm{P.V.}\left[\frac{1}{E+\nu eV}\right], \tag{V.5.26}$$

with P.V. the principal value. The Cooper pair current is given by

$$I_{\mathrm{cp}}(t) = I_{\mathrm{c},1}(V)\sin(\phi_0 + 2eVt/\hbar) + I_{\mathrm{c},2}(V)\cos(\phi_0 + 2eVt/\hbar), \tag{V.5.27a}$$

with the critical currents

$$I_{\mathrm{c},1}(V) = \frac{G_T}{\pi e}\mathrm{P.V.}\iint_{-\infty}^{\infty} dE d\epsilon \frac{\varsigma_1(E)\varsigma_2(\epsilon)}{E-\epsilon-eV}[f(E) - f(\epsilon)] \tag{V.5.27b}$$

$$I_{\mathrm{c},2}(V) = \frac{G_T}{e}\int_{-\infty}^{\infty} d\epsilon \varsigma_1(\epsilon - eV)\varsigma_2(\epsilon)[f(\epsilon - eV) - f(\epsilon)]. \tag{V.5.27c}$$

We recover the well-known ac Josephson effect [16, 17]. The rate $\Gamma_{\mathrm{S}}(E)$, as defined in the main text, is related to the critical current amplitude $I_{\mathrm{c},1}(V)$ via the relation $I_{\mathrm{c},1}(V) = [\Gamma_{\mathrm{S}}(eV) + \Gamma_{\mathrm{S}}(-eV)]/2$, as shown in Fig. V.21.
An external microwave field incident at the tunnel junction is modeled by a voltage $V(t) = V_0\cos(\omega_0 t)$, where V_0 and ω_0 are the amplitude and angular frequency of the microwave drive, respectively. The time-dependent voltage induces a dynamical phase

$$\phi(t) = \frac{eV}{\hbar}t + \frac{a}{2}\sin(\omega_0 t), \tag{V.5.28}$$

where V corresponds to the applied dc voltage, and $a = \omega_{\mathrm{J}}V_0/(\hbar\omega_0 V)$ to the strength of the drive. Therefore, the environmental phase $\hat{\phi}(t) = \phi(t)$ results in

$$C^{\nu}(t,E) = \sum_{n,l=-\infty}^{\infty} J_n(a/2)\, J_l(a/2)\left(\cos(\phi_0 + \Omega_{nl}t)\delta(E+\nu eV+\nu l\hbar\omega_0) + \nu\sin(\phi_0+\Omega_{nl}t)\frac{1}{\pi}\mathrm{P.V.}\left[\frac{1}{E+\nu eV+\nu l\hbar\omega_0}\right]\right), \tag{V.5.29}$$

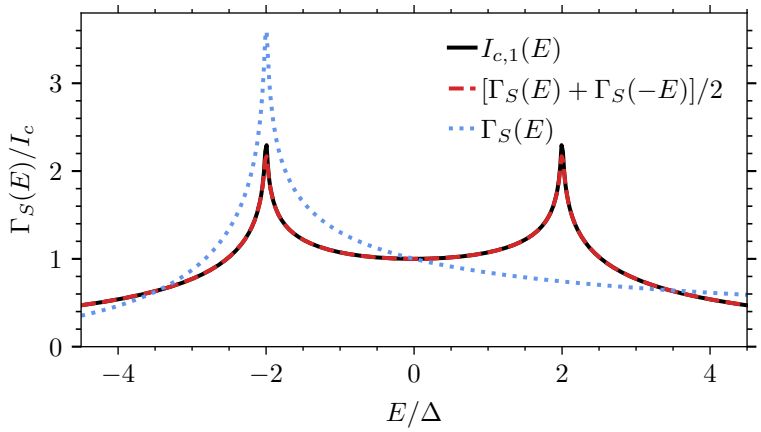

Figure V.21: Comparison between the *rate* Γ_S from Eq. (V.4.7c) and the *current amplitude* $I_{c,1}$. The plot illustrates that the critical current is given by the symmetrized rate evaluated at $\pm eV$.

with $\Omega_{nl} = 2eV/\hbar + (n+l)\omega_0$. We utilized the identity $\exp(iz\sin(\Theta)) = \sum_{l=-\infty}^{\infty} J_l(z)\exp(il\Theta)$, where $J_l(z)$ denotes the Bessel function of the first kind of order l. The resulting Cooper pair current

$$I_{\rm cp}(t) = \sum_{n,l=-\infty}^{\infty} J_n\left(a/2\right) J_l\left(a/2\right) \left[I_{\rm c,2}(eV + l\hbar\omega_0)\cos(\phi_0 + \Omega_{nl}t) + I_{\rm c,1}(eV + l\hbar\omega_0)\sin(\phi_0 + \Omega_{nl}t)\right] \tag{V.5.30}$$

oscillates at harmonics of the driving frequency and is consistent with the results reported in [17]. The time averaged Cooper pair current

$$\begin{aligned}\overline{I}_{\rm cp} &= \lim_{\overline{T}\to\infty} \frac{1}{\overline{T}} \int_{-\overline{T}/2}^{\overline{T}/2} I_{\rm cp}(t)dt \\ &= \sum_{m=-\infty}^{\infty} \delta_{eV,m\hbar\omega_0/2} \sum_{l=-\infty}^{\infty} J_{m-l}\left(\alpha\right) J_l\left(\alpha\right) \\ &\quad \times \left[I_{\rm c,1}(eV + l\hbar\omega_0)\sin(\phi_0) - I_{\rm c,2}(eV + l\hbar\omega_0)\cos(\phi_0)\right]\end{aligned} \tag{V.5.31}$$

exhibits spikes at $eV = m\hbar\omega_0/2$ in the $I-V$ curve, with $\delta_{eV,m\hbar\omega_0/2} = 1$ for $eV = m\hbar\omega_0/2$, and $\delta_{eV,m\hbar\omega_0/2} = 0$ for $eV \neq m\hbar\omega_0/2$. These spikes correspond to Shapiro steps in a current-biased tunnel junction [17, 279].

V.5.8 State Preparation

We envisage a finite-time state preparation protocol that initializes the environment in a desired state [263], after which the average tunnel current is measured over a substantially longer time interval. The time-averaged current of interest is

$$\overline{I} \equiv \frac{1}{t_{\rm e} - t_{\rm m}} \int_{t_{\rm m}}^{t_{\rm e}} dt I(t) = \overline{I}_{in} + \overline{I}_{prep}, \tag{V.5.32}$$

where the preparation takes place from time t_s up to t_m, at which point the measurement begins and continues until t_e. The current $\overline{I}_{in}$ depends solely on the prepared state, while $\overline{I}_{prep}$ depends on the preparation protocol. The integrals in $\overline{I}_{in}$ run over times later than t_m such that the environmental correlator can be reformulated as

$$\begin{aligned}\langle e^{i\nu\hat{\varphi}_\mathrm{I}(t)}e^{-i\nu'\hat{\varphi}_\mathrm{I}(t')}\rangle &= \mathrm{Tr}\{U^\dagger(t,t_\mathrm{s})e^{i\nu\hat{\varphi}}U(t,t_\mathrm{s})U^\dagger(t',t_\mathrm{s})e^{-i\nu'\hat{\varphi}}U(t',t_\mathrm{s})\hat{\rho}_\mathrm{env}\}\\ &= \mathrm{Tr}\{U^\dagger(t,t_\mathrm{m})e^{i\nu\hat{\varphi}}U(t,t_\mathrm{m})U^\dagger(t',t_\mathrm{m})e^{-i\nu'\hat{\varphi}}U(t',t_\mathrm{m})\\ &\quad\times U(t_\mathrm{m},t_\mathrm{s})\hat{\rho}_\mathrm{env}U^\dagger(t_\mathrm{m},t_\mathrm{s})\}\\ &= \mathrm{Tr}\{e^{i\nu\hat{\varphi}_\mathrm{m}(t)}e^{-i\nu'\hat{\varphi}_\mathrm{m}(t')}\hat{\rho}_{in}\},\end{aligned} \tag{V.5.33}$$

with $\hat{\rho}_\mathrm{env}$ is the initial density matrix at t_s, $\hat{\rho}_{in}$ the initialized density matrix at t_m, and $U(t,t_\mathrm{s})$ the time-evolution operator of the environment. The average current $\overline{I}_{prep}$ involves correlators of the form

$$\frac{1}{t_\mathrm{e}-t_\mathrm{m}}\int_0^{t_\mathrm{e}-t_\mathrm{m}}dt\int_0^{t_\mathrm{m}-t_\mathrm{s}}\frac{d\tau}{\pi\hbar}\,\mathrm{Re}\left(e^{iE(t+\tau)/\hbar}\langle e^{i\nu\hat{\varphi}_\mathrm{I}(t+t_\mathrm{m})}e^{-i\nu'\hat{\varphi}_\mathrm{I}(t_\mathrm{m}-\tau)}\rangle\right), \tag{V.5.34}$$

and is sensitive to the time evolution of the environmental operator during the state preparation period. If, $\hat{H}\,|E_n\rangle = E_n\,|E_n\rangle$, with a discrete set of eigenvalues E_n and orthonormal eigenstates $|E_n\rangle$, then

$$\begin{aligned}\frac{1}{t_\mathrm{e}-t_\mathrm{m}}\int_0^{t_\mathrm{e}-t_\mathrm{m}}dte^{iEt/\hbar}e^{i\nu\hat{\varphi}_\mathrm{m}(t)} &= \sum_{n,m}\langle n|\,e^{i\nu\hat{\varphi}}\,|m\rangle\,|n\rangle\,\langle m|\\ &\quad\times\frac{1}{t_\mathrm{e}-t_\mathrm{m}}\int_0^{t_\mathrm{e}-t_\mathrm{m}}dte^{i(E+E_n-E_m)t/\hbar}.\end{aligned} \tag{V.5.35}$$

The time average leads to a factor

$$\begin{aligned}\frac{1}{t_\mathrm{e}-t_\mathrm{m}}\int_0^{t_\mathrm{e}-t_\mathrm{m}}dte^{i(E+E_n-E_m)t/\hbar} &= \frac{\cos(\Omega(t_\mathrm{e}-t_\mathrm{m}))}{i\Omega(t_\mathrm{e}-t_\mathrm{m})}+\frac{\sin(\Omega(t_\mathrm{e}-t_\mathrm{m}))}{\Omega(t_\mathrm{e}-t_\mathrm{m})}-\frac{1}{i\Omega(t_\mathrm{e}-t_\mathrm{m})}\\ &\xrightarrow[t_\mathrm{e}-t_\mathrm{m}\to\infty]{}\delta_{\Omega,0},\end{aligned} \tag{V.5.36}$$

with $\Omega = (E+E_n-E_m)/\hbar$. In the limit of a large measurement window, this factor becomes non-zero only when $E+E_n-E_m=0$. Therefore, the integrand in the energy integral over E is non-zero only on a set of measure zero, implying that $\overline{I}_{prep}\to 0$ in the limit $t_\mathrm{e}-t_\mathrm{m}\to\infty$. Including a finite voltage bias merely shifts Ω, while the underlying reasoning remains unchanged. This demonstrates that the average current $\overline{I}=\overline{I}_{in}$ depends on the initialized state as well as on the system's evolution during the measurement interval, and not on the preparation protocol.

Chapter VI

Conclusion

This thesis has examined fluctuation phenomena in mesoscopic transport, with a focus on electric and energy current fluctuations. The projects addressed various physical systems, including electronic, Cooper-pair, and radiative transport, all of which can be described within a scattering-theory framework. Transport processes were driven by different mechanisms, namely thermal, classical time-dependent, and quantum driving.

The first project in Chap. II analyzed light emission of a mesoscopic conductor under thermal bias and is published in [292]. The emission is linked to the non-symmetrized noise spectrum, with negative frequencies corresponding to emission and positive frequencies to the absorption spectrum. In voltage-biased conductors, the noise consists of equilibrium Nyquist–Johnson noise and nonequilibrium shot noise. The two contributions originate from distinct microscopic mechanisms: thermal occupation of electronic states in the reservoirs, and stochastic partitioning of charge carriers in the scattering region. In thermally biased conductors, we identified a thermallike noise spectrum, and the nonequilibrium spectrum, referred to as the delta-T noise spectrum. Unlike in voltage-biased conductors, the delta-T noise spectrum can exhibit negative values, reflecting the different driving mechanism. For conductors with an energy-independent scattering matrix, the delta-T noise spectrum is associated with processes in which an electron and a hole originating from reservoirs at different temperatures (hot and cold) recombine, resulting in the emission or absorption of energy. Accordingly, the thermal-like noise spectrum is associated with recombination processes of electron–hole pairs from reservoirs with equal temperature. In the presence of asymmetric scattering the delta-T noise acquires an additional contribution originating from the difference between the number of hot and cold recombination events. We illustrated this asymmetric contribution using resonant scattering.

The second project in Sec. III.6 developed a scattering formalism to near-field radiative heat transfer, currently available on arXiv [293]. Near-field radiative heat transfer exhibits a Landauer-type expression for the average heat current, whereas the noise spectrum deviates from a Landauer-Büttiker expression, as was demonstrated [33]. We first focused on the circuit version of near-field radiative heat transfer, in which the thermal bodies are represented by arbitrary

impedances and the coupling is mediated by circuit elements. Quantum mechanically, the impedance is modeled by a transmission line that accounts for thermal fluctuations and dissipation, while reactive elements attached to the line capture the frequency dependence. This made it possible to construct the scattering states and to identify the full scattering matrix. We obtained the energy current, thus extending the Landauer–Büttiker theory to near-field radiative heat transfer, and calculated both the average dissipated energy and the energy current fluctuations. Reactive components within the thermal body can dominate the energy fluctuation spectrum and are beyond the prediction of the Landauer–Büttiker theory. The results are illustrated using two coupled surface phonon-polariton modes as well as simple circuit examples. Further, the scattering approach is extended to radiative heat transfer between macroscopic bodies, using the same scattering-state structure as in the circuit model.

The third project in Chap. IV investigated the full counting statistics of a mesoscopic conductor subject to voltage pulses, and is published in [294]. The full counting statistics reveal the underlying elementary processes, demonstrating that a voltage drive produces single-electron excitations and electron–hole pairs, which then scatter in the conductor. Motivated by the experiments [220–222], we studied voltage pulses with an oscillating carrier and either a Gaussian or box-shaped envelope. We calculated the probabilities to create an electron-hole pairs, which determines the cumulant generating function and, in turn, the noise. We showed that the noise depends sensitively on the carrier–envelope phase, i.e. the relative phase between the oscillating carrier and the envelope. The statistics depend on the shape of the drive, and comparison with experiments requires knowledge of the actual drive shape. Further shortcomings are that the full counting statistics framework used here was limited to energy-independent scattering, periodic driving, a spatially uniform reservoir field, and noninteracting electrons. For meaningful comparison with experiments, it is essential to include energy-dependent scattering, as the measurements [220–222] exhibit nonlinear current–voltage characteristics. As a first step, we discussed the current and noise for an energy-dependent scattering matrix and non-periodic drives. Transport properties are determined by the quasidistribution of the electron reservoir, namely the Wigner function, which we calculated for Gaussian and box-shaped pulses.

The fourth project in Sec. V.4 studied how a nonclassical electromagnetic environment influences transport through a superconducting tunnel junction, and extended classical transport phenomena such as photon-assisted tunneling and Shapiro steps into the quantum regime. The work is currently available on arXiv [295]. Advances in circuit quantum electrodynamics allow the preparation and control of quantum states of the electromagnetic field. By focusing on a multimode electromagnetic environment, we demonstrated that the superconducting tunnel junction can serve as a detector of the prepared quantum state, allowing the complete reconstruction of the environmental state. The quasiparticle current provides direct access to the probability of energy exchange between the quasiparticle and the environment. Further, the Cooper pair current is sensitive

to the coherences of the environmental state, so that Shapiro steps encode information about the coherence. By contrast, in normal-metal junctions extracting the probability of energy exchange requires combined current and noise measurements, while coherence information remains inaccessible. In particular, we considered the quasiparticle and Cooper pair currents when the environment was a superconducting qubit or a single-mode environment prepared in vacuum-single-photon, vacuum-three-photon, coherent, and squeezed states. The different states leave distinct signatures in the quasiparticle and Cooper pair currents. As our calculation already contains the necessary ingredients, it is a direct next step to investigate the noise properties of the junction and to examine whether they offer advantageous access to information about the environmental state. Furthermore, it would be intriguing to derive a criterion for the current or noise that enables one to distinguish different properties of the environmental state, such as purity, entanglement, or nonclassicality. Our framework also permits a perturbative treatment beyond the lowest order in transmission, thereby incorporating multiple-electron transfer processes. Although our analysis concentrated on the current statistics of the superconducting tunnel junction, an important extension would be to study how the junction influences the environmental state.

Overall, the thesis provides a set of theoretical results on fluctuation phenomena in quantum transport. The findings illustrate how the average current and its fluctuations encode information about scattering properties, driving protocols, and environmental quantum states.

Bibliography

[1] R. Landauer, "Spatial Variation of Currents and Fields Due to Localized Scatterers in Metallic Conduction", IBM J. Res. Dev. **1**, 223–231 (1957).

[2] B. J. van Wees, H. van Houten, C. W. J. Beenakker, J. G. Williamson, L. P. Kouwenhoven, D. van der Marel, and C. T. Foxon, "Quantized conductance of point contacts in a two-dimensional electron gas", Phys. Rev. Lett. **60**, 848–850 (1988).

[3] S. Datta, *Electronic Transport in Mesoscopic Systems* (Cambridge University Press, 1997).

[4] Y. Imry, *Introduction to mesoscopic physics* (Oxford University Press, 2002).

[5] N. Agraı̈t, A. L. Yeyati, and J. M. van Ruitenbeek, "Quantum properties of atomic-sized conductors", Phys. Rep. **377**, 81–279 (2003).

[6] Y. V. Nazarov and Y. M. Blanter, *Quantum Transport: Introduction to Nanoscience* (Cambridge University Press, 2009).

[7] J. C. Cuevas and E. Scheer, *Molecular Electronics: An Introduction to Theory and Experiment* (World Scientific, 2010).

[8] C. Zhou, C. J. Muller, M. R. Deshpande, J. W. Sleight, and M. A. Reed, "Microfabrication of a mechanically controllable break junction in silicon", Appl.Phys. Lett. **67**, 1160–1162 (1995).

[9] D. Rondoni and J. Hoekstra, "Quantum effects: from physics to electronics", in Annual workshop on circuits, systems and signal processing 2006 (STW, 2006), pp. 75–79.

[10] S. J. Tans, M. H. Devoret, H. Dai, A. Thess, R. E. Smalley, L. J. Geerligs, and C. Dekker, "Individual single-wall carbon nanotubes as quantum wires", Nature **386**, 474–477 (1997).

[11] S. Washburn, "Resistance Fluctuations in Small Samples: Be Careful When Playing with Ohm's Law", in *Quantum coherence in mesoscopic systems* (Springer, 1991), pp. 341–367.

[12] D. A. Wharam, T. J. Thornton, R. Newbury, M. Pepper, H. Ahmed, J. E. F. Frost, D. G. Hasko, D. C. Peacock, D. A. Ritchie, and G. A. C. Jones, "One-dimensional transport and the quantisation of the ballistic resistance", Journal of Physics C: Solid State Physics **21**, L209 (1988).

[13] M. Brandbyge, J. Schio/tz, M. R. So/rensen, P. Stoltze, K. W. Jacobsen, J. K. No/rskov, L. Olesen, E. Laegsgaard, I. Stensgaard, and F. Besenbacher, "Quantized conductance in atom-sized wires between two metals", Phys. Rev. B **52**, 8499–8514 (1995).

[14] M. Büttiker, "Scattering theory of current and intensity noise correlations in conductors and wave guides", Phys. Rev. B **46**, 12485–12507 (1992).

[15] Y. Blanter and M. Büttiker, "Shot noise in mesoscopic conductors", Phys. Rep. **336**, 1–166 (2000).

[16] B. D. Josephson, "Possible new effects in superconductive tunnelling", Phys Lett. **1**, 251–253 (1962).

[17] A. Barone and G. Paterno, *Physics and Applications of the Josephson Effect* (John Wiley & Sons, New York, 1982).

[18] A. Chang, "A unified transport theory for the integral and fractional quantum hall effects: Phase boundaries, edge currents, and transmission/reflection probabilities", Solid State Commun. **74**, 871–876 (1990).

[19] C. W. J. Beenakker, "Edge channels for the fractional quantum hall effect", Phys. Rev. Lett. **64**, 216–219 (1990).

[20] H. Saleur, "Edge states tunneling in the fractional quantum hall effect: integrability and transport", C. R. Phys. **3**, 685–695 (2002).

[21] S.-A. Biehs, R. Messina, P. S. Venkataram, A. W. Rodriguez, J. C. Cuevas, and P. Ben-Abdallah, "Near-field radiative heat transfer in many-body systems", Rev. Mod. Phys. **93**, 025009 (2021).

[22] J. P. Pekola and B. Karimi, "Colloquium: Quantum heat transport in condensed matter systems", Rev. Mod. Phys. **93**, 041001 (2021).

[23] T. S. Tighe, J. M. Worlock, and M. L. Roukes, "Direct thermal conductance measurements on suspended monocrystalline nanostructures", Appl. Phys. Lett. **70**, 2687–2689 (1997).

[24] D. Angelescu, M. Cross, and M. Roukes, "Heat transport in mesoscopic systems", Superlatt. Microstruct. **23**, 673–689 (1998).

[25] L. G. C. Rego and G. Kirczenow, "Quantized Thermal Conductance of Dielectric Quantum Wires", Phys. Rev. Lett. **81**, 232–235 (1998).

[26] S. G. Das and A. Dhar, "Landauer formula for phonon heat conduction: relation between energy transmittance and transmission coefficient", Eur. Phys. J. B **85**, 372 (2012).

[27] B. Wang, J. Wang, J. Wang, and D. Y. Xing, "Spin current carried by magnons", Phys. Rev. B **69**, 174403 (2004).

[28] J. Zheng, S. Bender, J. Armaitis, R. E. Troncoso, and R. A. Duine, "Green's function formalism for spin transport in metal-insulator-metal heterostructures", Phys. Rev. B **96**, 174422 (2017).

[29] C.-C. Chien, M. Di Ventra, and M. Zwolak, "Landauer, Kubo, and microcanonical approaches to quantum transport and noise: A comparison and implications for cold-atom dynamics", Phys. Rev. A **90**, 023624 (2014).

[30] C.-C. Chien, S. Peotta, and M. Di Ventra, "Quantum transport in ultracold atoms", Nat. Phys. **11**, 998–1004 (2015).

[31] J. Eriksson, M. Acciai, L. Tesser, and J. Splettstoesser, "General Bounds on Electronic Shot Noise in the Absence of Currents", Phys. Rev. Lett. **127**, 136801 (2021).

[32] M. Meschke, W. Guichard, and J. P. Pekola, "Single-mode heat conduction by photons", Nature **444**, 187–190 (2006).

[33] J. L. Wise, N. Roubinowitz, W. Belzig, and D. M. Basko, "Signature of resonant modes in radiative heat current noise spectrum", Phys. Rev. B **106**, 165407 (2022).

[34] R. Landauer, "The noise is the signal", Nature **392**, 658–659 (1998).

[35] W. Schottky, "Über spontane Stromschwankungen in verschiedenen Elektrizitätsleitern", Ann. Phys. (Leipzig) **362**, 541–567 (1918).

[36] R. A. Millikan., "On the Elementary Electrical Charge and the Avogadro Constant", Phys. Rev. **2**, 109–143 (1913).

[37] L. Saminadayar, D. C. Glattli, Y. Jin, and B. Etienne, "Observation of the $e/3$ Fractionally Charged Laughlin Quasiparticle", Phys. Rev. Lett. **79**, 2526–2529 (1997).

[38] R. de-Picciotto, M. Reznikov, M. Heiblum, V. Umansky, G. Bunin, and D. Mahalu, "Direct observation of a fractional charge", Physica B: Condens. Matter **249-251**, 395–400 (1998).

[39] M. Reznikov, R. de Picciotto, T. G. Griffiths, M. Heiblum, and V. Umansky, "Observation of quasiparticles with one-fifth of an electron's charge", Nature **399**, 238–241 (1999).

[40] C. W. J. Beenakker and C. Schönenberger, "Quantum Shot Noise", Phys. Today **56**, 37–42 (2003).

[41] U. Gavish, Y. Levinson, and Y. Imry, "Detection of quantum noise", Phys. Rev. B **62**, R10637–R10640 (2000).

[42] L. Lesovik, "On the detection of finite-frequency current fluctuations", JETP Lett. **65**, 280–284 (1997).

[43] M. Vanevic, Y. V. Nazarov, and W. Belzig, "Elementary Events of Electron Transfer in a Voltage-Driven Quantum Point Contact", Phys. Rev. Lett. **99**, 225 (2007).

[44] M. Vanevic, Y. V. Nazarov, and W. Belzig, "Elementary charge-transfer processes in mesoscopic conductors", Phys. Rev. B **78**, 225 (2008).

[45] M. Vanević, J. Gabelli, W. Belzig, and B. Reulet, "Electron and electron-hole quasiparticle states in a driven quantum contact", Phys. Rev. B **93**, 041416 (2016).

[46] G.-L. Ingold and Y. V. Nazarov, "Charge Tunneling Rates in Ultrasmall Junctions", in *Single Charge Tunneling: Coulomb Blockade Phenomena In Nanostructures*, edited by H. Grabert and M. H. Devoret (Springer US, Boston, MA, 1992), pp. 21–107.

[47] J.-R. Souquet, M. J. Woolley, J. Gabelli, P. Simon, and A. A. Clerk, "Photon-assisted tunnelling with nonclassical light", Nat. Commun. **5**, 5562 (2014).

[48] M. Tinkham, *Introduction to Superconductivity* (Courier Corporation, 2004).

[49] Y. Asano, *Andreev reflection in superconducting junctions*, Vol. 278 (Springer, Singapore, 2021).

[50] L. D. Landau and E. M. Lifshitz, *Statistical physics, part 2*, 2nd ed., Vol. 9, Course of Theoretical Physics (Pergamon Press, Oxford, 1981).

[51] J.-X. Zhu, *Bogoliubov-de gennes method and its applications*, Vol. 924, Lecture Notes in Physics (Springer, Cham, Switzerland, 2016).

[52] J. Bardeen, L. N. Cooper, and J. R. Schrieffer, "Microscopic Theory of Superconductivity", Phys. Rev. **106**, 162–164 (1957).

[53] J. Bardeen, L. N. Cooper, and J. R. Schrieffer, "Theory of Superconductivity", Phys. Rev. **108**, 1175–1204 (1957).

[54] V. B. Berestetskii, E. M. Lifshitz, and L. P. Pitaevskii, *Quantum Electrodynamics*, Vol. 4, Course of Theoretical Physics (Butterworth-Heinemann, 1982).

[55] L. Gor'kov, L. Dzyaloshinskii, and I. Abrikosov, *Quantum Field Theoretical Methods in Statistical Physics* (Pergamon Press Oxford, 1965).

[56] G. Rickayzen, *Green's Functions and Condensed Matter* (Academic Press, London, 1980).

[57] E. M. Lifshitz and L. P. Pitaevskii, *Statistical Physics (Part 2)* (Pergamon Press, Oxford, 1980).

[58] L. P. Pitaevskii and E. Lifshitz, *Physical Kinetics*, Vol. 10 (Butterworth-Heinemann, 2012).

[59] J. Rammer and H. Smith, "Quantum field-theoretical methods in transport theory of metals", Rev. Mod. Phys. **58**, 323–359 (1986).

[60] N. B. Kopnin, *Theory of Nonequilibrium Superconductivity*, Vol. 110 (Clarendon Press, Oxford, 2001).

[61] A. L. Fetter and J. D. Walecka, *Quantum Theory of Many-Particle Systems* (Dover Publications, New York, 2003).

[62] H. Bruus and K. Flensberg, *Many-Body Quantum Theory in Condensed Matter Physics: An Introduction* (Oxford University Press, New York, 2004).

[63] A. Kamenev, *Field Theory of Non-Equilibrium Systems* (Cambridge University Press, 2011).

[64] J. von Neumann, *Mathematische Grundlagen der Quantenmechanik* (Springer, Berlin, 1932).

[65] F. J. Dyson, "The S Matrix in Quantum Electrodynamics", Phys. Rev. **75**, 1736–1755 (1949).

[66] G. C. Wick, "The Evaluation of the Collision Matrix", Phys. Rev. **80**, 268–272 (1950).

[67] J. B. Johnson, "Thermal Agitation of Electricity in Conductors", Phys. Rev. **32**, 97–109 (1928).

[68] H. Nyquist, "Thermal Agitation of Electric Charge in Conductors", Phys. Rev. **32**, 110–113 (1928).

[69] L. Spietz, K. W. Lehnert, I. Siddiqi, and R. J. Schoelkopf, "Primary electronic thermometry using the shot noise of a tunnel junction", Science **300**, 1929–1932 (2003).

[70] O. Lumbroso, L. Simine, A. Nitzan, D. Segal, and O. Tal, "Electronic noise due to temperature differences in atomic-scale junctions", Nature **562**, 240–244 (2018).

[71] E. Sivre, H. Duprez, A. Anthore, A. Aassime, F. Parmentier, A. Cavanna, A. Ouerghi, U. Gennser, and F. Pierre, "Electronic heat flow and thermal shot noise in quantum circuits", Nat. Commun. **10**, 5638 (2019).

[72] S. Larocque, E. Pinsolle, C. Lupien, and B. Reulet, "Shot Noise of a Temperature-Biased Tunnel Junction", Phys. Rev. Lett. **125**, 106801 (2020).

[73] K. Iyer, J. Rech, T. Jonckheere, L. Raymond, B. Grémaud, and T. Martin, "Colored delta-T noise in fractional quantum Hall liquids", Phys. Rev. B **108**, 245427 (2023).

[74] E. Zhitlukhina, M. Belogolovskii, and P. Seidel, "Low-Temperature Thermally Induced Noise in the Presence of an AC Voltage Bias", J. Low Temp. Phys. **212**, 79–88 (2023).

[75] L. Tesser, M. Acciai, C. Spånslätt, J. Monsel, and J. Splettstoesser, "Charge, spin, and heat shot noises in the absence of average currents: Conditions on bounds at zero and finite frequencies", Phys. Rev. B **107**, 075409 (2023).

[76] A. Crépieux, T. Q. Duong, and M. Lavagna, "Finite-frequency noise, Fano factor, ΔT-noise and cross-correlations in double quantum dots", J. Phys.: Condens. Matter **37**, 075302 (2024).

[77] M. Acciai, G. Zhang, and C. Spånslätt, "Role of scaling dimensions in generalized noises in fractional quantum Hall tunneling due to a temperature bias", SciPost Phys. **18**, 058 (2025).

[78] M. Gerry, J. J. Wang, J. Li, O. Shein-Lumbroso, O. Tal, and D. Segal, "Machine learning delta-T noise for temperature bias estimation", J. Chem. Phys. **162**, 084108 (2025).

[79] L. Pierattelli, F. Taddei, and A. Braggio, "ΔT-noise in multiterminal hybrid systems", Phys. Rev. Res. **7**, 023321 (2025).

[80] E. V. Sukhorukov and D. Loss, "Noise in multiterminal diffusive conductors: universality, nonlocality, and exchange effects", Phys. Rev. B **59**, 13054–13066 (1999).

[81] J. Rech, T. Jonckheere, B. Grémaud, and T. Martin, "Negative Delta-T Noise in the Fractional Quantum Hall Effect", Phys. Rev. Lett. **125**, 086801 (2020).

[82] G. Rebora, J. Rech, D. Ferraro, T. Jonckheere, T. Martin, and M. Sassetti, "Delta-T noise for fractional quantum hall states at different filling factor", Phys. Rev. Res. **4**, 043191 (2022).

[83] Y. He, D. M. Kennes, and V. Meden, "Conductance of correlated many-fermion systems from charge fluctuations", Phys. Rev. B **105**, 165120 (2022).

[84] G. Zhang, I. V. Gornyi, and C. Spånslätt, "Delta-T noise for weak tunneling in one-dimensional systems: interactions versus quantum statistics", Phys. Rev. B **105**, 195423 (2022).

[85] M. Hasegawa and K. Saito, "Delta-T noise in the kondo regime", Phys. Rev. B **103**, 045409 (2021).

[86] R. A. Melcer, B. Dutta, C. Spånslätt, J. Park, A. D. Mirlin, and V. Umansky, "Absent thermal equilibration on fractional quantum hall edges over macroscopic scale", Nat. Commun. **13**, 1–7 (2022).

[87] G. B. Lesovik, T. Martin, and J. Torrès, "Josephson frequency singularity in the noise of normal-metal–superconductor junctions", Phys. Rev. B **60**, 11935–11938 (1999).

[88] A. Cottet, B. Douçot, and W. Belzig, "Finite frequency noise of a superconductor-ferromagnet quantum point contact", Phys. Rev. Lett. **101**, 257001 (2008).

[89] M. Büttiker, "Coherent and sequential tunneling in series barriers", IBM J. Res. Dev. **32**, 63–75 (1988).

[90] A. Prêtre, H. Thomas, and M. Büttiker, "Dynamic admittance of mesoscopic conductors: discrete-potential model", Phys.l Rev. B **54**, 8130–8143 (1996).

[91] M. H. Pedersen and M. Büttiker, "Scattering theory of photon-assisted electron transport", Phys. Rev.B **58**, 12993–13006 (1998).

[92] M. Filipović and W. Belzig, "Photon-assisted electronic and spin transport in a junction containing precessing molecular spin", Phys. Rev. B **93**, 075402 (2016).

[93] U. Gavish, Y. Levinson, and Y. Imry, "Shot-Noise in Transport and Beam Experiments", Phys. Rev. Lett. **87**, 216807 (2001).

[94] G. Baym, *Lectures On Quantum Mechanics* (W. A. BENJAMIN, INC., 1969).

[95] R. Zamoum, M. Lavagna, and A. Crépieux, "Nonsymmetrized noise in a quantum dot: interpretation in terms of energy transfer and coherent superposition of scattering paths", Phys. Rev. B **93**, 235449 (2016).

[96] G. Breit and E. Wigner, "Capture of slow neutrons", Phys. Rev. **49**, 519–531 (1936).

[97] A. Bejan, *Convection Heat Transfer* (John Wiley & Sons, 2013).

[98] D. W. Hahn and M. N. Özisik, *Heat Conduction* (John Wiley & Sons, 2012).

[99] M. F. Modest and S. Mazumder, *Radiative Heat Transfer* (Academic Press, 2021).

[100] M. Meftah, L. Damé, D. Bolsée, A. Hauchecorne, N. Pereira, D. Sluse, G. Cessateur, A. Irbah, J. Bureau, M. Weber, K. Bramstedt, T. Hilbig, R. Thiéblemont, M. Marchand, F. Lefèvre, A. Sarkissian, and S. Bekki, "Solar-iss: a new reference spectrum based on solar/solspec observations", A&A **611**, A1 (2018).

[101] C. Hargreaves, "Anomalous Radiative Transfer Between Closely-Spaced Bodies", Phys. Lett. A **30**, 491–492 (1969).

[102] T. Kralik, P. Hanzelka, M. Zobac, V. Musilova, T. Fort, and M. Horak, "Strong Near-Field Enhancement of Radiative Heat Transfer between Metallic Surfaces", Phys. Rev. Lett. **109**, 224302 (2012).

[103] K. Joulain, J.-P. Mulet, F. Marquier, R. Carminati, and J.-J. Greffet, "Surface electromagnetic waves thermally excited: Radiative heat transfer, coherence properties and Casimir forces revisited in the near field", Surf. Sci. Rep. **57**, 59–112 (2005).

[104] A. I. Volokitin and B. N. J. Persson, "Near-field radiative heat transfer and noncontact friction", Rev. Mod. Phys. **79**, 1291–1329 (2007).

[105] B. Song, Y. Ganjeh, S. Sadat, D. Thompson, A. Fiorino, V. Fernandez-Hurtado, J. Feist, M. T. H. Reid, F. J. Garcia-Vidal, J. C. Cuevas, P. Reddy, and E. Meyhofer, "Enhancement of near-field radiative heat transfer using polar dielectric thin films", Nat. Nanotechnol. **10**, 253–258 (2015).

[106] D. Polder and M. Van Hove, "Theory of Radiative Heat Transfer between Closely Spaced Bodies", Phys. Rev. B **4**, 3303–3314 (1971).

[107] C. W. Gardiner, *Handbook of Stochastic Methods: for Physics, Chemistry and the Natural Sciences*, 3rd (Springer, Berlin, Heidelberg, 2004).

[108] A. Blais, A. L. Grimsmo, S. M. Girvin, and A. Wallraff, "Circuit quantum electrodynamics", Rev. Mod. Phys. **93**, 025005 (2021).

[109] J. Wise, "Theory of heat transfer in nanostructures: microscopic and phenomenological approaches", PhD thesis (Université Grenoble Alpes, 2021).

[110] E. G. Cravalho, C. L. Tien, and R. Caren, "Effect of Small Spacings on Radiative Transfer Between Two Dielectrics", J. Heat Transfer (1967).

[111] G. Domoto, R. Boehm, and C. L. Tien, "Experimental Investigation of Radiative Transfer Between Metallic Surfaces at Tryogenic Temperatures", J. Heat Transfer (1970).

[112] C. Williams and H. Wickramasinghe, "Scanning thermal profiler", Appl. Phys. Lett. **49**, 1587–1589 (1986).

[113] J. B. Xu, K. Läuger, K. Dransfeld, and I. H. Wilson, "Thermal sensors for investigation of heat transfer in scanning probe microscopy", Rev. Sci. Instrum. **65**, 2262–2266 (1994).

[114] W. Müller-Hirsch, A. Kraft, M. T. Hirsch, J. Parisi, and A. Kittel, "Heat transfer in ultrahigh vacuum scanning thermal microscopy", J. Vac. Sci. Technol. A **17**, 1205–1210 (1999).

[115] A. Kittel, W. Müller-Hirsch, J. Parisi, S.-A. Biehs, D. Reddig, and M. Holthaus, "Near-Field Heat Transfer in a Scanning Thermal Microscope", Phys. Rev. Lett. **95**, 224301 (2005).

[116] A. Narayanaswamy, S. Shen, and G. Chen, "Near-field radiative heat transfer between a sphere and a substrate", Phys. Rev. B **78**, 115303 (2008).

[117] S. Shen, A. Narayanaswamy, and G. Chen, "Surface phonon polaritons mediated energy transfer between nanoscale gaps", Nano Lett. **9**, 2909–2913 (2009).

[118] E. Rousseau, A. Siria, G. Jourdan, S. Volz, F. Comin, J. Chevrier, and J.-J. Greffet, "Radiative heat transfer at the nanoscale", Nat. Photonics **3**, 514–517 (2009).

[119] P. J. van Zwol, L. Ranno, and J. Chevrier, "Tuning Near Field Radiative Heat Flux through Surface Excitations with a Metal Insulator Transition", Phys. Rev. Lett. **108**, 234301 (2012).

[120] C. Lucchesi, D. Cakiroglu, J.-P. Perez, T. Taliercio, E. Tournié, P.-O. Chapuis, and R. Vaillon, "Near-Field Thermophotovoltaic Conversion with High Electrical Power Density and Cell Efficiency above 14%", Nano Letters **21**, 4524–4529 (2021).

[121] R. St-Gelais, B. Guha, L. Zhu, S. Fan, and M. Lipson, "Demonstration of Strong Near-Field Radiative Heat Transfer between Integrated Nanostructures", Nano Letters **14**, 6971–6975 (2014).

[122] R. St-Gelais, L. Zhu, S. Fan, and M. Lipson, "Near-field radiative heat transfer between parallel structures in the deep subwavelength regime", Nat. Nanotechnol. **11**, 515–519 (2016).

[123] L. Hu, A. Narayanaswamy, X. Chen, and G. Chen, "Near-field thermal radiation between two closely spaced glass plates exceeding planck's blackbody radiation law", Appl. Phys. Lett. **92**, 133106 (2008).

[124] R. S. Ottens, V. Quetschke, S. Wise, A. A. Alemi, R. Lundock, G. Mueller, D. H. Reitze, D. B. Tanner, and B. F. Whiting, "Near-Field Radiative Heat Transfer between Macroscopic Planar Surfaces", Phys. Rev. Lett. **107**, 014301 (2011).

[125] P. J. van Zwol, S. Thiele, C. Berger, W. A. de Heer, and J. Chevrier, "Nanoscale Radiative Heat Flow due to Surface Plasmons in Graphene and Doped Silicon", Phys. Rev. Lett. **109**, 264301 (2012).

[126] P. Sabbaghi, L. Long, X. Ying, L. Lambert, S. Taylor, C. Messner, and L. Wang, "Super-Planckian radiative heat transfer between macroscale metallic surfaces due to near-field and thin-film effects", J. Appl. Phys. **128**, 025305 (2020).

[127] J. L. Wise, D. M. Basko, and F. W. J. Hekking, "Role of disorder in plasmon-assisted near-field heat transfer between two-dimensional metals", Phys. Rev. B **101**, 205411 (2020).

[128] A. I. Volokitin and B. N. J. Persson, "Radiative heat transfer between nanostructures", Phys. Rev. B **63**, 205404 (2001).

[129] L. M. A. Pascal, H. Courtois, and F. W. J. Hekking, "Circuit approach to photonic heat transport", Phys. Rev. B **83**, 125113 (2011).

[130] A. Andreev, "Thermal conductivity of the intermediate state of superconductors. II", Sov. Phys. JETP **20**, 1490 (1965).

[131] J. T. Peltonen, P. Virtanen, M. Meschke, J. V. Koski, T. T. Heikkilä, and J. P. Pekola, "Thermal Conductance by the Inverse Proximity Effect in a Superconductor", Phys. Rev. Lett. **105**, 097004 (2010).

[132] D. R. Schmidt, R. J. Schoelkopf, and A. N. Cleland, "Photon-Mediated Thermal Relaxation of Electrons in Nanostructures", Phys. Rev. Lett. **93**, 045901 (2004).

[133] A. V. Timofeev, M. Helle, M. Meschke, M. Möttönen, and J. P. Pekola, "Electronic refrigeration at the quantum limit", Phys. Rev. Lett. **102**, 200801 (2009).

[134] J. B. Pendry, "Quantum limits to the flow of information and entropy", J. Phys. A: Math. Gen. **16**, 2161 (1983).

[135] O. Chiatti, J. T. Nicholls, Y. Y. Proskuryakov, N. Lumpkin, I. Farrer, and D. A. Ritchie, "Quantum Thermal Conductance of Electrons in a One-Dimensional Wire", Phys. Rev. Lett. **97**, 056601 (2006).

[136] K. Schwab, E. A. Henriksen, J. M. Worlock, and M. L. Roukes, "Measurement of the quantum of thermal conductance", Nature **404**, 974–977 (2000).

[137] C. S. Yung, D. R. Schmidt, and A. N. Cleland, "Thermal conductance and electron-phonon coupling in mechanically suspended nanostructures", Appl. Phys. Lett. **81**, 31–33 (2002).

[138] O. Maillet, D. Subero, J. T. Peltonen, G. Timossi, T. Proslier, C. B. Winkelmann, H. Courtois, M. Meschke, F. Giazotto, and J. P. Pekola, "Electric field control of radiative heat transfer in a superconducting circuit", Nat. Commun. **11**, 4326 (2020).

[139] M. Partanen, K. Tan, J. Govenius, R. E. Lake, A. Jenei, S. Masuda, M. Mäkelä, M. Silveri, and M. Möttönen, "Quantum-limited heat conduction over macroscopic distances", Nat. Phys. **12**, 460–464 (2016).

[140] K. Joulain, J. Drevillon, Y. Ezzahri, and J. Ordonez-Miranda, "Quantum Thermal Transistor", Phys. Rev. Lett. **116**, 200601 (2016).

[141] M. Majland, K. S. Christensen, and N. T. Zinner, "Quantum thermal transistor in superconducting circuits", Phys. Rev. B **101**, 184510 (2020).

[142] A. Gubaydullin, G. Thomas, D. S. Golubev, D. Lvov, J. T. Peltonen, and J. P. Pekola, "Photonic heat transport in three terminal superconducting circuit", Nat. Commun. **13**, 1552 (2022).

[143] H. Liu, C. Wang, L.-Q. Wang, and J. Ren, "Strong system-bath coupling induces negative differential thermal conductance and heat amplification in nonequilibrium two-qubit systems", Phys. Rev. E **99**, 032114 (2019).

[144] C. Wang, D. Xu, H. Liu, and X. Gao, "Thermal rectification and heat amplification in a nonequilibrium V-type three-level system", Phys. Rev. E **99**, 042102 (2019).

[145] A. Levy and R. Kosloff, "Quantum Absorption Refrigerator", Phys. Rev. Lett. **108**, 070604.

[146] M. Kilgour and D. Segal, "Coherence and decoherence in quantum absorption refrigerators", Phys. Rev. E **98**, 012117 (2018).

[147] G. Thomas, A. Gubaydullin, D. S. Golubev, and J. P. Pekola, "Thermally pumped on-chip maser", Phys. Rev. B **102**, 104503 (2020).

[148] S.-A. Biehs and P. Ben-Abdallah, "Fluctuations of radiative heat exchange between two bodies", Phys. Rev. B **97**, 201406 (2018).

[149] D. S. Golubev and J. P. Pekola, "Statistics of heat exchange between two resistors", Phys. Rev. B **92**, 085412 (2015).

[150] G. Tang and J.-S. Wang, "Heat transfer statistics in extreme-near-field radiation", Phys. Rev. B **98**, 125401 (2018).

[151] L. D. Landau and E. M. Lifshitz, *Statistical Physics: Volume 5 of Course of Theoretical Physics*, Vol. 5 (Butterworth-Heinemann, 1980).

[152] C. Kittel, "Temperature fluctuation: an oxymoron", Phys. Today **41**, 93–93 (1988).

[153] P. Day, I. Hahn, T. C. Chui, A. W. Harter, D. Rowe, and J. A. Lipa, "The Fluctuation-Imposed Limit for Temperature Measurement", J. Low Temp. Phys. **107**, 359–370 (1997).

[154] F. Giazotto, T. T. Heikkilä, A. Luukanen, A. M. Savin, and J. P. Pekola, "Opportunities for mesoscopics in thermometry and refrigeration: physics and applications", Rev. Mod. Phys. **78**, 217–274 (2006).

[155] B. Karimi, F. Brange, P. Samuelsson, and J. P. Pekola, "Reaching the ultimate energy resolution of a quantum detector", Nat. Commun. **11**, 367 (2020).

[156] N. Balabanian and T. A. Bickart, *Electrical Network Theory* (John Wiley & Sons Inc., 1969).

[157] R. Pauli, "Darlington's theorem and complex normalization", Int. J. Circuit Theory Appl. **17**, 429–446 (1989).

[158] M. Wohlers, "On Scattering Matrices Normalized to Active n-Ports at Real Frequencies", IEEE Trans. Circuit Theory **16**, 254–256 (1969).

[159] J.-L. Wan and W.-K. Chen, "On consistency of the complex normalized scattering matrices of multi-port networks", J. Frankl. Inst. **330**, 441–451 (1993).

[160] Y. S. Zhu and W. K. Chen, "On real and complex normalizations", Circuits Syst. Signal Process. **12**, 579–587 (1993).

[161] J. Rahola, "Power waves and conjugate matching", IEEE Trans. Circuits Syst. II, Exp. Briefs **55**, 92–96 (2008).

[162] W.-K. Chen and Q.-Z. Zha, "Factorizations and complex normalization of scattering matrices", in [1991] proceedings of the 34th midwest symposium on circuits and systems (1992), pp. 716–718.

[163] S. Kirchhoff, "Über den Durchgang eines elektrischen Stromes durch eine Ebene, insbesondere durch eine kreisförmige", Ann. Phys. **140**, 497–514 (1845).

[164] B. Yurke and J. S. Denker, "Quantum network theory", Phys. Rev. A **29**, 1419–1437 (1984).

[165] U. Vool and M. Devoret, "Introduction to quantum electromagnetic circuits", Int. J. Circuit Theory Appl. **45**, 897–934 (2017).

[166] M. Henneaux and C. Teitelboim, *Quantization of Gauge Systems* (Princeton University Press, 1992).

[167] M. Sheikh-Jabbari and A. Shirzad, "Boundary conditions as Dirac constraints", Eur. Phys. J. C **19**, 383–390 (2001).

[168] M. Rymarz and D. P. DiVincenzo, "Consistent Quantization of Nearly Singular Superconducting Circuits", Phys. Rev. X **13**, 021017 (2023).

[169] G. Burkard, "Circuit theory for decoherence in superconducting charge qubits", Phys. Rev. B **71**, 144511 (2005).

[170] L. Frunzio, A. Wallraff, D. Schuster, J. Majer, and R. Schoelkopf, "Fabrication and characterization of superconducting circuit QED devices for quantum computation", IEEE Trans. Appl. Supercond. **15**, 860–863 (2005).

[171] A. Bruno, G. de Lange, S. Asaad, K. L. van der Enden, N. K. Langford, and L. DiCarlo, "Reducing intrinsic loss in superconducting resonators by surface treatment and deep etching of silicon substrates", Appl. Phys. Lett. **106**, 182601 (2015).

[172] M. Reagor, W. Pfaff, C. Axline, R. W. Heeres, N. Ofek, K. Sliwa, E. Holland, C. Wang, J. Blumoff, K. Chou, M. J. Hatridge, L. Frunzio, M. H. Devoret, L. Jiang, and R. J. Schoelkopf, "Quantum memory with millisecond coherence in circuit QED", Phys. Rev. B **94**, 014506 (2016).

[173] M. Devoret, S. Girvin, and R. Schoelkopf, "Circuit-qed: how strong can the coupling between a josephson junction atom and a transmission line resonator be?", Ann. Phys. **519**, 767–779 (2007).

[174] R. Landauer, "Electrical transport in open and closed systems", Z. Phys. B Condens. Matter **68**, 217–228 (1987).

[175] T. Ojanen and T. T. Heikkilä, "Photon heat transport in low-dimensional nanostructures", Phys. Rev. B **76**, 073414 (2007).

[176] S. M. Rytov, *Theory of Electric Fluctuations and Thermal Radiation* (Air Force Cambrige Research Center, Bedford, MA, 1953).

[177] S. M. Rytov, Y. A. Kravtsov, and V. I. Tatarskii, *Principles of Statistical Radiophysics* (Springer-Verlag, Berlin Heidelberg, 1989).

[178] G. Bimonte, T. Emig, M. Kardar, and M. Krüger, "Nonequilibrium Fluctuational Quantum Electrodynamics: Heat Radiation, Heat Transfer, and Force", Annu. Rev. Condens. Matter Phys. **8**, 119–143 (2017).

[179] S.-A. Biehs, E. Rousseau, and J.-J. Greffet, "Mesoscopic Description of Radiative Heat Transfer at the Nanoscale", Phys. Rev. Lett. **105**, 234301 (2010).

[180] H. H. Yap and J.-S. Wang, "Radiative heat transfer as a landauer-büttiker problem", Phys. Rev. E **95**, 012126 (2017).

[181] F. Herz, C. Kathmann, and S.-A. Biehs, "General trace formula for heat flux fluctuations", EPL **130**, 44003 (2020).

[182] T. Ojanen and A.-P. Jauho, "Mesoscopic Photon Heat Transistor", Phys. Rev. Lett. **100**, 155902 (2008).

[183] D. M. Pozar, *Microwave Engineering: Theory and Techniques* (John wiley & Sons Inc., 2021).

[184] A. Khondker, M. R. Khan, and A. Anwar, "Transmission line analogy of resonance tunneling phenomena: The generalized impedance concept", J. Appl. Phys. **63**, 5191–5193 (1988).

[185] W. van Haeringen and D. Lenstra, *Analogies in optics and micro electronics* (Kluwer Academic Publishers, Dordrecht, 1990).

[186] P.-O. Chapuis, S. Volz, C. Henkel, K. Joulain, and J.-J. Greffet, "Effects of spatial dispersion in near-field radiative heat transfer between two parallel metallic surfaces", Phys. Rev. B **77**, 035431 (2008).

[187] P.-O. Chapuis, M. Laroche, S. Volz, and J.-J. Greffet, "Near-field induction heating of metallic nanoparticles due to infrared magnetic dipole contribution", Phys. Rev. B **77**, 125402 (2008).

[188] J. L. Wise and D. M. Basko, "Near field versus far field in radiative heat transfer between two-dimensional metals", Phys. Rev. B **103**, 165423 (2021).

[189] Cowley, R.A., "Raman scattering from crystals of the diamond structure", J. Phys. France **26**, 659–667 (1965).

[190] P. G. Klemens, "Anharmonic decay of optical phonons", Phys. Rev. **148**, 845–848 (1966).

[191] M. S. Kushwaha, "The Bond-Bending Force Model (BBFM) for Phonons in β-SiC", Phys. Status Solidi B **111**, 337–340 (1982).

[192] D. H. Lee and J. D. Joannopoulos, "Simple Scheme for Deriving Atomic Force Constants: Application to SiC", Phys. Rev. Lett. **48**, 1846–1849 (1982).

[193] T. Wang, Z. Gui, A. Janotti, C. Ni, and P. Karandikar, "Strong effect of electron-phonon interaction on the lattice thermal conductivity in 3C-SiC", Phys. Rev. Mater. **1**, 034601 (2017).

[194] L. D. Landau and E. M. Lifshitz, *Theory of Elasticity* (Pergamon Press, Oxford, 1975).

[195] G. Catelani and I. L. Aleiner, "Interaction corrections to thermal transport coefficients in disordered metals: the quantum kinetic equation approach", J. Exp. Theor. Phys. **100**, 331–369 (2005).

[196] A. A. Abrikosov, L. P. Gorkov, and I. E. Dzyaloshinski, *Methods of Quantum Field Theory in Statistical Physics*, Revised, Dover Books on Physics (Dover Publications, New York, 1975).

[197] M. Reina, R. Messina, and P. Ben-Abdallah, "Conduction-radiation coupling between two closely separated solids", Phys. Rev. Lett. **125**, 224302 (2020).

[198] M. Reina, R. Messina, and P. Ben-Abdallah, "Strong slowing down of the thermalization of solids interacting in the extreme near field", Phys. Rev. B **104**, L100305 (2021).

[199] P. K. Tien and J. P. Gordon, "Multiphoton Process Observed in the Interaction of Microwave Fields with the Tunneling between Superconductor Films", Phys. Rev. **129**, 647–651 (1963).

[200] M. Moskalets and M. Büttiker, "Floquet scattering theory for current and heat noise in large amplitude adiabatic pumps", Phys. Rev. B **70**, 245305 (2004).

[201] M. V. Moskalets, *Scattering Matrix Approach to Non-Stationary Quantum Transport* (Imperial College Press, London, 2012).

[202] G. B. Lesovik and L. S. Levitov, "Noise in an ac biased junction: Nonstationary Aharonov-Bohm effect", Phys. Rev. Lett. **72**, 538–541 (1994).

[203] R. J. Schoelkopf, A. A. Kozhevnikov, D. E. Prober, and M. J. Rooks, "Observation of "Photon-Assisted" Shot Noise in a Phase-Coherent Conductor", Phys. Rev. Lett. **80**, 2437–2440 (1998).

[204] L.-H. Reydellet, P. Roche, D. C. Glattli, B. Etienne, and Y. Jin, "Quantum Partition Noise of Photon-Created Electron-Hole Pairs", Phys. Rev. Lett. **90**, 176803 (2003).

[205] V. S. Rychkov, M. L. Polianski, and M. Büttiker, "Photon-assisted electron-hole shot noise in multiterminal conductors", Phys. Rev. B **72**, 155326 (2005).

[206] J. Hammer and W. Belzig, "Quantum noise in ac-driven resonant-tunneling double-barrier structures: photon-assisted tunneling versus electron antibunching", Phys. Rev. B **84**, 085419 (2011).

[207] G. Gasse, C. Lupien, and B. Reulet, "Observation of Squeezing in the Electron Quantum Shot Noise of a Tunnel Junction", Phys. Rev. Lett. **111**, 136601 (2013).

[208] H. Zhan, M. Vanevic, and W. Belzig, "Continuous-Variable Entanglement Test in Driven Quantum Contacts", Phys. Rev. Lett. **122**, 236801 (2019).

[209] J.-C. Forgues, C. Lupien, and B. Reulet, "Emission of Microwave Photon Pairs by a Tunnel Junction", Phys. Rev. Lett. **113**, 043602 (2014).

[210] J. Keeling, I. Klich, and L. S. Levitov, "Minimal Excitation States of Electrons in One-Dimensional Wires", Phys. Rev. Lett. **97**, 116403 (2006).

[211] C. Grenier, R. Hervé, E. Bocquillon, F. D. Parmentier, B. Plaçais, J. M. Berroir, G. Fève, and P. Degiovanni, "Single-electron quantum tomography in quantum Hall edge channels", New J. Phys. **13**, 093007 (2011).

[212] J. Dubois, T. Jullien, F. Portier, P. Roche, A. Cavanna, Y. Jin, W. Wegscheider, P. Roulleau, and D. Glattli, "Minimal-excitation states for electron quantum optics using levitons", Nature **502**, 659–663 (2013).

[213] E. Bocquillon, F. D. Parmentier, C. Grenier, J.-M. Berroir, P. Degiovanni, D. C. Glattli, B. Pla çais, A. Cavanna, Y. Jin, and G. Fève, "Electron Quantum Optics: Partitioning Electrons One by One", Phys. Rev. Lett. **108**, 196803 (2012).

[214] E. Bocquillon, V. Freulon, J.-M. Berroir, P. Degiovanni, B. Plaçais, A. Cavanna, Y. Jin, and G. Fève, "Coherence and Indistinguishability of Single Electrons Emitted by Independent Sources", Science **339**, 1054–1057 (2013).

[215] E. Bocquillon, V. Freulon, F. D. Parmentier, J.-M. Berroir, B. Plaçais, C. Wahl, J. Rech, T. Jonckheere, T. Martin, C. Grenier, D. Ferraro, P. Degiovanni, and G. Fève, "Electron quantum optics in ballistic chiral conductors", Ann. Phys. **526**, 1–30 (2014).

[216] J. Rammer, *Quantum Field Theory of Non-Equilibrium States* (Cambridge University Press, 2011).

[217] D. Ferraro, A. Feller, A. Ghibaudo, E. Thibierge, E. Bocquillon, G. Fève, C. Grenier, and P. Degiovanni, "Wigner function approach to single electron coherence in quantum hall edge channels", Phys. Rev. B **88**, 205303 (2013).

[218] T. Jullien, P. Roulleau, B. Roche, A. Cavanna, Y. Jin, and D. Glattli, "Quantum tomography of an electron", Nature **514**, 603–607 (2014).

[219] L. S. Levitov, H. Lee, and G. B. Lesovik, "Electron counting statistics and coherent states of electric current", J. Math. Phys. **37**, 4845–4866 (1996).

[220] T. Rybka, M. Ludwig, M. F. Schmalz, V. Knittel, D. Brida, and A. Leitenstorfer, "Sub-cycle optical phase control of nanotunnelling in the single-electron regime", Nat. Photonics **10**, 667 670 (2016).

[221] M. Ludwig, G. Aguirregabiria, F. Ritzkowsky, T. Rybka, D. C. Marinica, J. Aizpurua, A. G. Borisov, A. Leitenstorfer, and D. Brida, "Sub-femtosecond electron transport in a nanoscale gap", Nat. Phys. **16**, 341–345 (2020).

[222] M. Ludwig, A. K. Kazansky, G. Aguirregabiria, D. C. Marinica, M. Falk, A. Leitenstorfer, D. Brida, J. Aizpurua, and A. G. Borisov, "Active control of ultrafast electron dynamics in plasmonic gaps using an applied bias", Phys. Rev. B **101**, 241412 (2020).

[223] D. A. Ivanov, H. W. Lee, and L. S. Levitov, "Coherent states of alternating current", Phys. Rev. B **56**, 6839–6850 (1997).

[224] M. Acciai, L. Arrachea, and J. Splettstoesser, "Quantum transport phenomena induced by time-dependent fields", arXiv:2505.22472 (2025).

[225] L. Levitov and G. Lesovik, "Charge distribution in quantum shot noise", JETP Lett. **58**, 230–235 (1993).

[226] M. O. Scully and M. S. Zubairy, *Quantum optics* (Cambridge University Press, 1997).

[227] B. Reulet, J. Senzier, and D. E. Prober, "Environmental Effects in the Third Moment of Voltage Fluctuations in a Tunnel Junction", Phys. Rev. Lett. **91**, 196601 (2003).

[228] J. Bylander, T. Duty, and P. Delsing, "Current measurement by real-time counting of single electrons", Nature **434**, 361–364 (2005).

[229] T. Fujisawa, T. Hayashi, R. Tomita, and Y. Hirayama, "Bidirectional Counting of Single Electrons", Science **312**, 1634–1636 (2006).

[230] S. Gustavsson, R. Leturcq, T. Ihn, K. Ensslin, M. Reinwald, and W. Wegscheider, "Measurements of higher-order noise correlations in a quantum dot with a finite bandwidth detector", Phys. Rev. B **75**, 075314 (2007).

[231] W. Belzig and Y. V. Nazarov, "Full Counting Statistics of Electron Transfer between Superconductors", Phys. Rev. Lett. **87**, 197006 (2001).

[232] W. Belzig, "Full Counting Statistics of Superconductor-Normal-Metal Heterostructures", in *Quantum Noise in Mesoscopic Physics*, edited by Y. V. Nazarov (Springer Netherlands, Dordrecht, 2003), pp. 463–496.

[233] M. Kindermann and Y. V. Nazarov, "Interaction Effects on Counting Statistics and the Transmission Distribution", Phys. Rev. Lett. **91**, 136802 (2003).

[234] M. Kindermann, Y. V. Nazarov, and C. W. J. Beenakker, "Feedback of the electromagnetic environment on current and voltage fluctuations out of equilibrium", Phys. Rev. B **69**, 035336 (2004).

[235] J. Tobiska and Y. V. Nazarov, "Inelastic interaction corrections and universal relations for full counting statistics in a quantum contact", Phys. Rev. B **72**, 235328 (2005).

[236] D. C. Ohnmacht, W. Belzig, and J. C. Cuevas, "Full counting statistics of yu-shiba-rusinov bound states", Phys. Rev. Res. **5**, 033176 (2023).

[237] M. Vanević, "Circuit Theory of Charge Transport in Mesoscopic Conductors", PhD thesis (University of Basel, Basel, Switzerland, 2008).

[238] L. S. Levitov and M. Reznikov, "Counting statistics of tunneling current", Phys. Rev. B **70**, 115305 (2004).

[239] K. E. Nagaev, P. Samuelsson, and S. Pilgram, "Cascade approach to current fluctuations in a chaotic cavity", Phys. Rev. B **66**, 195318 (2002).

[240] K. E. Nagaev, "Cascade boltzmann-langevin approach to higher-order current correlations in diffusive metal contacts", Phys. Rev. B **66**, 075334 (2002).

[241] S. Pilgram, A. N. Jordan, E. V. Sukhorukov, and M. Büttiker, "Stochastic Path Integral Formulation of Full Counting Statistics", Phys. Rev. Lett. **90**, 206801 (2003).

[242] A. N. Jordan, E. V. Sukhorukov, and S. Pilgram, "Fluctuation statistics in networks: A stochastic path integral approach", J. Math. Phys. **45**, 4386–4417 (2004).

[243] L. S. Levitov and G. B. Lesovik, "Charge-transport statistics in quantum conductors", JETP Lett. **55**, [Pis'ma v ZhETF 55, 534–537 (1992)], 555–559 (1992).

[244] Y. V. Nazarov, *Quantum Noise in Mesoscopic Physics*, Vol. 97, NATO Science Series II: Mathematics, Physics and Chemistry (Springer Science & Business Media, Dordrecht, 2012).

[245] Y. V. Nazarov, "Novel circuit theory of andreev reflection", Superlattices Microstruct. **25**, 1221–1231 (1999).

[246] I. Snyman and Y. V. Nazarov, "Keldysh action of a multiterminal time-dependent scatterer", Phys. Rev. B **77**, 165118 (2008).

[247] K. D. Usadel, "Generalized diffusion equation for superconducting alloys", Phys. Rev. Lett. **25**, 507–509 (1970).

[248] Y. V. Nazarov, "Block-determinant formalism for an action of a multi-terminal scatterer", Physica E **74**, 561–569 (2015).

[249] M. Büttiker, H. Thomas, and A. Prêtre, "Current partition in multiprobe conductors in the presence of slowly oscillating external potentials", Z. Phys. B **94**, 133–137 (1994).

[250] J. Gabelli and B. Reulet, "Dynamics of Quantum Noise in a Tunnel Junction under ac Excitation", Phys. Rev. Lett. **100**, 026601 (2008).

[251] A. D. Lorenzo and Y. V. Nazarov, "Full Counting Statistics with Spin-Sensitive Detectors Reveals Spin Singlets", Phys. Rev. Lett. **94**, 1 4 (2005).

[252] W. Belzig and M. Vanevic, "Elementary Andreev processes in a driven superconductor–normal metal contact", Physica E Low-Dimens. Syst. Nanostruct. **75**, 22 27 (2016-01).

[253] A. O. Caldeira and A. J. Leggett, "Influence of Dissipation on Quantum Tunneling in Macroscopic Systems", Phys. Rev. Lett. **46**, 211–214 (1981).

[254] M. H. Devoret, D. Esteve, H. Grabert, G.-L. Ingold, H. Pothier, and C. Urbina, "Effect of the electromagnetic environment on the Coulomb blockade in ultrasmall tunnel junctions", Phys. Rev. Lett. **64**, 1824–1827 (1990).

[255] A. A. Odintsov, "Effect of dissipation on the characteristics of small-area tunnel junctions: Application of the polaron model", Zh. Eksp. Teor. Fiz. **94**, [Sov. Phys. JETP 67, 1265 (1988)], 312 (1988).

[256] D. Averin and A. Odintsov, "Macroscopic quantum tunneling of the electric charge in small tunnel junctions", Phys. Lett. A **140**, 251–257 (1989).

[257] J. Clarke and F. K. Wilhelm, "Superconducting quantum bits", Nature **453**, 1031–1042 (2008).

[258] C. Gardiner and P. Zoller, *Quantum Noise: A Handbook of Markovian and Non-Markovian Quantum Stochastic Methods with Applications to Quantum Optics*, Springer Series in Synergetics (Springer, 2004).

[259] R. Horodecki, P. Horodecki, M. Horodecki, and K. Horodecki, "Quantum entanglement", Rev. Mod. Phys. **81**, 865–942 (2009).

[260] C. C. Gerry and P. L. Knight, *Introductory quantum optics* (Cambridge University Press, Cambridge, 2023).

[261] G. Breitenbach, S. Schiller, and J. Mlynek, "Measurement of the quantum states of squeezed light", Nature **387**, 471–475 (1997).

[262] M. Hofheinz, E. M. Weig, M. Ansmann, R. C. Bialczak, E. Lucero, M. Neeley, A. D. O'Connell, H. Wang, J. M. Martinis, and A. N. Cleland, "Generation of Fock states in a superconducting quantum circuit", Nature **454**, 310–314 (2008).

[263] M. Hofheinz, H. Wang, M. Ansmann, R. C. Bialczak, E. Lucero, M. Neeley, A. D. O'connell, D. Sank, J. Wenner, J. M. Martinis, and A. N. Cleland, "Synthesizing arbitrary quantum states in a superconducting resonator", Nature **459**, 546–549 (2009).

[264] C. K. Law and J. H. Eberly, "Arbitrary Control of a Quantum Electromagnetic Field", Phys. Rev. Lett. **76**, 1055–1058 (1996).

[265] A. Lingenfelter, D. Roberts, and A. A. Clerk, "Unconditional Fock state generation using arbitrarily weak photonic nonlinearities", Sci. Adv. **7**, eabj1916 (2021).

[266] T. Yamamoto, K. Inomata, M. Watanabe, K. Matsuba, T. Miyazaki, W. D. Oliver, Y. Nakamura, and J. S. Tsai, "Flux-driven Josephson parametric amplifier", Appl. Phys. Lett. **93**, 042510 (2008).

[267] A. Roy and M. Devoret, "Introduction to parametric amplification of quantum signals with Josephson circuits", C. R. Phys. **17**, 740–755 (2016).

[268] G. Milburn and D. Walls, "Production of squeezed states in a degenerate parametric amplifier", Opt. Commun. **39**, 401–404 (1981).

[269] M. J. Collett and C. W. Gardiner, "Squeezing of intracavity and traveling-wave light fields produced in parametric amplification", Phys. Rev. A **30**, 1386–1391 (1984).

[270] B. Yurke, P. G. Kaminsky, R. E. Miller, E. A. Whittaker, A. D. Smith, A. H. Silver, and R. W. Simon, "Observation of 4.2-K equilibrium-noise squeezing via a Josephson-parametric amplifier", Phys. Rev. Lett. **60**, 764–767 (1988).

[271] R. Movshovich, B. Yurke, P. G. Kaminsky, A. D. Smith, A. H. Silver, R. W. Simon, and M. V. Schneider, "Observation of zero-point noise squeezing via a Josephson-parametric amplifier", Phys. Rev. Lett. **65**, 1419–1422 (1990).

[272] N. Didier, F. Qassemi, and A. Blais, "Perfect squeezing by damping modulation in circuit quantum electrodynamics", Phys. Rev. A **89**, 013820 (2014).

[273] Y. Yin, Y. Chen, D. Sank, P. J. J. O'Malley, T. C. White, R. Barends, J. Kelly, E. Lucero, M. Mariantoni, A. Megrant, C. Neill, A. Vainsencher, J. Wenner, A. N. Korotkov, A. N. Cleland, and J. M. Martinis, "Catch and Release of Microwave Photon States", Phys. Rev. Lett. **110**, 107001 (2013).

[274] R. Dassonneville, R. Assouly, T. Peronnin, A. Clerk, A. Bienfait, and B. Huard, "Dissipative Stabilization of Squeezing Beyond 3 dB in a Microwave Mode", PRX Quantum **2**, 020323 (2021).

[275] P. Xie, X.-c. Wang, J.-w. Wang, X.-k. Li, Y. Zhou, G.-h. Wang, F. Badshah, and Y.-c. Xiong, "Dissipatively stabilized superposition of squeezed coherent states via periodically breaking the qubit inversion symmetry", Phys. Rev. A **109**, 052409 (2024).

[276] F. A. Cárdenas-López, G. Romero, L. Lamata, E. Solano, and J. C. Retamal, "Parity-Assisted Generation of Nonclassical States of Light in Circuit Quantum Electrodynamics", Symmetry **11**, 372 (2019).

[277] R. P. Feynman, R. B. Leighton, and M. Sands, *The feynman lectures on physics, volume iii: quantum mechanics* (Addison-Wesley, Reading, MA, 1965).

[278] P. W. Anderson and J. M. Rowell, "Probable observation of the josephson superconducting tunneling effect", Phys. Rev. Lett. **10**, 230–232 (1963).

[279] S. Shapiro, "Josephson Currents in Superconducting Tunneling: The Effect of Microwaves and Other Observations", Phys. Rev. Lett. **11**, 80–82 (1963).

[280] J. Kadlec and K. Gundlach, "Current-Versus Voltage Source Model in Josephson Effect", Phys. Lett. A **63**, 149–150 (1977).

[281] M. Chauvin, *The josephson effect in atomic contacts; effect josephson dans les contacts atomiques*, 2005.

[282] A. H. Dayem and R. J. Martin, "Quantum Interaction of Microwave Radiation with Tunneling Between Superconductors", Phys. Rev. Lett. **8**, 246–248 (1962).

[283] A. A. Clerk, K. W. Lehnert, P. Bertet, J. R. Petta, and Y. Nakamura, "Hybrid quantum systems with circuit quantum electrodynamics", Nat. Phys. **16**, 257–267 (2020).

[284] L. Bretheau, Ç. Ö. Girit, H. Pothier, D. Esteve, and C. Urbina, "Exciting Andreev pairs in a superconducting atomic contact", Nature **499**, 312–315 (2013).

[285] L. Bretheau, Ç. Ö. Girit, M. Houzet, H. Pothier, D. Esteve, and C. Urbina, "Theory of microwave spectroscopy of Andreev bound states with a josephson junction", Phys. Rev. B **90**, 134506 (2014).

[286] G. Aiello, M. Féchant, A. Morvan, J. Basset, M. Aprili, J. Gabelli, and J. Estève, "Quantum bath engineering of a high impedance microwave mode through quasiparticle tunneling", Nat. Commun. **13**, 7146 (2022).

[287] P. Joyez, "Self-Consistent Dynamics of a Josephson Junction in the Presence of an Arbitrary Environment", Phys. Rev. Lett. **110**, 217003 (2013).

[288] H. Grabert, "Dynamical coulomb blockade of tunnel junctions driven by alternating voltages", Phys. Rev. B **92**, 245433 (2015).

[289] Y. Nazarov, "Full counting statistics and field theory", Ann. Phys. **519**, 720–735 (2007).

[290] J. C. Cuevas and W. Belzig, "Full Counting Statistics of Multiple Andreev Reflections", English, Phys. Rev. Lett. **91**, 187001 (2003).

[291] J. C. Cuevas and W. Belzig, "Dc transport in superconducting point contacts: a full-counting-statistics view", English, Phys. Rev. B **70**, 1404 (2004).

[292] M. Hübler and W. Belzig, "Light emission in delta-T-driven mesoscopic conductors", Phys. Rev. B **107**, 155405 (2023).

[293] M. Hübler, D. M. Basko, and W. Belzig, "Scattering approach to near-field radiative heat transfer", Phys. Rev. B **112**, 165428 (2025).

[294] M. Hübler and W. Belzig, "Full counting statistics of ultrafast quantum transport", Appl. Phys. Lett. **123**, 034006 (2023).

[295] M. Hübler, J. C. Cuevas, and W. Belzig, "Nonclassical photon-assisted transport in superconducting tunnel junctions", Phys. Rev. B **112**, 214501 (2025).